



LASER ASSISTED PRODUCTION OF  
NANOSTRUCTURES FOR BIOMEDICAL  
SENSING APPLICATIONS

submitted in fulfilment of the requirements for the degree of Doctor of  
Philosophy

by Cian Hughes, BSc

Dublin City University, School of Mechanical Engineering

October 2019

Supervisor: Prof Dermot Brabazon

Co-Supervisors: Prof Fiona Regan, Prof Niall Barron - UCD



# Declaration

I hereby certify that this material, which I now submit for assessment on the programme of study leading to the award of PhD is entirely my own work, that I have exercised reasonable care to ensure that the work is original, and does not to the best of my knowledge breach any law of copyright, and has not been taken from the work of others save and to the extent that such work has been cited and acknowledged within the text of my work.

Signed: \_\_\_\_\_ ID No.: \_\_\_\_\_ Date: \_\_\_\_\_



## Publications and Presentations

- List of Published First-Author Papers:
  - Hughes, C.; McCann, R.; Eguileor, J.; Bagga, K.; Groarke, R.; Regan, F.; Brabazon, D. *Opt. Laser Technol.* **2018**, 108, 295.
- List of other Published Papers:
  - “Pulsed laser deposition of plasmonic nanostructured gold on flexible transparent polymers at atmospheric pressure”; McCann, R.; Hughes, C.; Bagga, K.; Stalcup, A.; Vázquez, M.; Brabazon, D. *J. Phys. D. Appl. Phys.* **2017**, 50 (24), 245303.
  - Cruz, J. M.; Hughes, C.; Quilty, B.; Montagnolli, R. N.; Bidoia, E. D. *Waste and Biomass Valorization* **2018**, 9 (4), 613.
  - Ahad, I. U.; Pabijan, J.; Pogoda, K.; Hughes, C.; Bartnik, A.; Fiedorowicz, H.; Lekka, M.; Brabazon, D. *Acta Phys. Pol. A* **2018**, 133 (2), 283.
- List of poster presentations:
  - McCann, R.; Hughes, C.; Freeland, B.; Bagga, K.; Groarke, R.; Stalcup, A.; Vázquez, M.; Brabzon, D.; “*Confined atmospheric pulsed laser deposition: A new route to nanostructured ultrathin films*”, IOP Spring Meeting 2016, February, **2016**, Belfast, Northern Ireland.
  - Hughes, C.; McCann, R.; Bagga, K.; Groarke, R.; Regan, F.; Barron, N.; Brabazon, D.; “*Pulsed laser ablation (PLA) and confined atmospheric-pulsed laser deposition (CA-PLD) based nano-biosensor production*”, Biosensors 2016, May, **2016**, Gothenburg, Sweden.
  - Groarke, R.; Skrobisz, T.; Hughes, C.; McCann, R.; Scigliano, A.; Brabazon, D.; “*Next Generation High Performance Thin Layer Chromatography (HP-TLC) Using Additively*

*Manufactured Acrylate Based Polymer Stationary Phases*”,  
31st International Symposium on Chromatography, Aug –  
Sept, **2016**, Cork, Ireland.

- Hughes, C.; McCann, R.; Ul Ahad, I.; Bagga, K.; Regan, F.; Brabazon, D.; *“Metal Nanostructured Film Deposition on Flexible Polymer”*, 20<sup>th</sup> International ESAFORM Conference, Apr, **2017**, Dublin, Ireland.
- McCann, R.; Hughes, C.; Bagga, K.; Stalcup, A.; Vázquez, M.; Brabazon, D. *“Picosecond Nd:YAG laser ablation of cyclic olefin polymer substrates for sensing platform fabrication”*, ICASS 2015, July, **2015**, Shanghai, PRC.
  
- List of Oral Presentations:
  - Hughes, C.; McCann, R.; Eguileor, J.; Bagga, K.; Groarke, R.; Brabazon, D.; *“Modelling and optimisation of single-step laser-based gold nanostructure deposition with tunable optical properties”*, AMPT 2018, September, **2018**, Dublin, Ireland
  - Hughes, C.; Brabazon, D; *“Development of a Nanobiosensor Using Novel Laser Fabrication Techniques”*, Engineers Ireland “Best Individual Applied Engineering Project” Competition, December **2019**, Dublin, Ireland
  
- List of Awards:
  - Best poster award received at ESAFORM 2017 for the poster “Metal Nanostructured Film Deposition on Flexible Polymer”.
  - Best Presenter and 3<sup>rd</sup> Place in Engineers Ireland 2019 “Best Individual Applied Engineering Project” Competition

## Acknowledgements

To begin I would like to acknowledge the guidance offered by my primary supervisor Prof Dermot Brabazon throughout the course of my studies and research, always being happy to endlessly discuss ideas and offer valuable advice while, importantly, nudging the focus back on target to the goals of the project. Similarly, I would like to acknowledge my co-supervisors, Prof Fiona Regan and Prof Niall Barron for the wealth of advice they offered. There are a million possible avenues of research and without these people I would surely have become hopelessly lost along the way without a map.

I would also like to acknowledge the many wonderful colleagues I've had the pleasure of working with over the past few years. Across their many disciplines and own areas of research, they've always been happy to offer support, ideas and opportunities for discussion when it might help and every one of those is appreciated immensely.

Likewise, I must acknowledge the unbelievable support offered by my friends and family throughout my studies. Without their encouragement and, of course, willingness to put up with me at times I would never have been able to continue to the point of completing this work.

Finally, I would be remiss not to acknowledge the Science Foundation Ireland for funding the first 3 years of this work. Without their contribution there would not even have been a project to work on, and I am thankful for the opportunity they provided to undertake this research.

# Table of Contents

<b>DECLARATION</b> .....	<b>2</b>
<b>PUBLICATIONS AND PRESENTATIONS</b> .....	<b>4</b>
<b>ACKNOWLEDGEMENTS</b> .....	<b>6</b>
<b>GLOSSARY OF ABBREVIATIONS</b> .....	<b>10</b>
<b>GLOSSARY OF TABLES</b> .....	<b>13</b>
<b>GLOSSARY OF FIGURES</b> .....	<b>15</b>
<b>ABSTRACT</b> .....	<b>26</b>
<b>1. INTRODUCTION</b> .....	<b>29</b>
<b>2. LITERATURE REVIEW</b> .....	<b>31</b>
2.1 CANCER RESEARCH .....	31
2.2 AN OVERVIEW OF THE BIOLOGY OF CANCER .....	33
2.2.1 <i>Introduction to Cancer</i> .....	33
2.2.2 <i>A Brief Discussion of the Morphology of Cancerous Cells and the Study of Histology</i> .....	34
2.2.3 <i>Biochemical Differences in Cancerous Cells</i> .....	36
2.2.4 <i>A Discussion of Cancer Biomarkers</i> .....	39
2.2.5 <i>Cancer Antigens</i> .....	42
2.2.6 <i>Genetic Markers</i> .....	44
2.3 DETECTION METHODS .....	45
2.3.1 <i>Quartz Crystal Microbalance (QCM) Biosensors</i> .....	45
2.3.2 <i>Electronic Biosensors</i> .....	46
2.3.3 <i>Field-Effect Transistor (FET) Biosensors</i> .....	48
2.3.4 <i>Surface Plasmon Resonance (SPR)</i> .....	51
2.3.5 <i>Spectroscopic Measurements</i> .....	52
2.3.6 <i>Electrical Percolation (EP) Biosensors</i> .....	53
2.4 DESIGN OF FUNCTIONALISED SURFACES FOR LABEL-FREE BIOSENSING .....	55
2.5 DETECTION MOLECULES .....	56
2.5.1 <i>Antibodies</i> .....	56
2.5.2 <i>DNA Probes</i> .....	58
2.5.3 <i>Nucleic Acid Aptamers</i> .....	59
2.6 SENSOR SURFACES .....	61
2.7 NANOSTRUCTURE FABRICATION TECHNIQUES .....	63

2.7.1 Chemical Deposition.....	63
2.7.2 Nanoimprinting and Nanolithography.....	64
2.7.3 Laser-Based Deposition.....	65
2.7.3 Dewetting.....	67
2.8 NANOPARTICLE COLLOIDS.....	68
2.8.1 Chemical Reduction: Monophasic Reduction Reactions.....	68
2.8.2 Chemical Reduction: Biphasic Reduction Reactions.....	74
2.8.3 Photolysis.....	75
2.8.4 Pulsed Laser Ablation in Liquid (PLAL).....	76
2.9 BIOMICROFLUIDICS.....	78
2.9.1 Fabrication of Microfluidic Systems.....	81
2.10 SUMMARY.....	83
<b>3. DEVELOPMENT OF CONFINED ATMOSPHERIC PULSED-LASER DEPOSITION.....</b>	<b>85</b>
3.1 EXPLORATORY RESEARCH OF THE CAP DEPOSITION PROCESS.....	88
3.2 CAP PROCESS OPTIMISATION STUDIES.....	93
3.2.1 Study 1: Gold Foil Deposition on Glass Substrate.....	93
3.2.1a Study 1: Materials and Equipment.....	93
3.2.1b Study 1: Experimental Methodology.....	94
3.2.1c Study 1: Results and Analysis.....	96
3.2.2 Study 2: Gold Foil Deposition on COP Substrate.....	102
3.2.2a Study 2: Materials and Equipment.....	103
3.2.2b Study 2: Experimental Methodology.....	104
3.2.2c Study 2: Results and Analysis.....	104
3.2.3 Study 3: Target Stage Deposition on COP Substrate.....	107
3.2.3a Study 3: Materials and Equipment.....	107
3.2.3b Study 3: Experimental Methodology.....	108
3.2.3c Study 3: Results and Analysis.....	112
3.3 CONCLUSIONS ON THE CAP DEVELOPMENT PROCESS.....	133
<b>4. DEVELOPMENT OF SENSOR SURFACE FABRICATION METHODS.....</b>	<b>135</b>
4.1 EXPLORATION OF INTERDIGITATED ELECTRODE DESIGNS.....	137
4.2 DEVELOPMENT OF A SQUARE PLATE ELECTRODE.....	147
4.2.1 Methods for Conductivity Enhancement.....	150
4.2.1a Laser Sintering of CAP Films.....	152
4.2.1b Crosslinking Functionalisation of CAP Films.....	157
4.2.1c Comparison of Sintering and Crosslinking Methods.....	162
4.2.2 Development of a Complete Working Electrode.....	163

4.3 DESIGN OF FINAL SENSOR PLATFORM .....	174
<b>5. DEVELOPMENT OF A RAPID, NON-DESTRUCTIVE PARTICLE ENUMERATION TECHNIQUE .....</b>	<b>182</b>
5.1 THE THEORY OF INTERACTIONS BETWEEN LIGHT AND SMALL PARTICLES .....	183
5.1.1 <i>The Scattering of Monochromatic Light by a Single Classical Particle</i> .....	184
5.1.2 <i>The Scattering of Polychromatic Light by a Single Quantum Particle</i> .....	189
5.1.3 <i>The Scattering of Polychromatic Light by Numerous Polydispersed Quantum Particles</i> .....	194
5.1.4 <i>Simplification of Physical Inputs: Expanding Usability to Interdisciplinary Users</i> .....	196
5.2 DESIGN OF THE PARTICLE COUNTING PROGRAM .....	198
5.2.1 <i>Choice of Programming Language</i> .....	199
5.2.2 <i>Translation of Pre-Existing Codebase from FORTRAN77 to Julia and Optimisation</i> .....	202
5.2.3 <i>Overview of the Structure of the Program</i> .....	209
5.2.4 <i>Empirical Verification of Program Accuracy</i> .....	211
5.2.5 <i>Program Compatibility Tests</i> .....	214
5.2.6 <i>Conclusions on the NanoConc Program</i> .....	217
<b>6. EVALUATION OF SENSOR PERFORMANCE .....</b>	<b>219</b>
6.1 TESTING OF ANALYSIS TECHNIQUES .....	221
6.1a <i>Testing of Analysis Techniques: Materials and Equipment</i> .....	221
6.1b <i>Testing of Analysis Techniques: Methodology</i> .....	222
6.1c <i>Testing of Analysis Techniques: Results and Analysis</i> .....	226
6.2 DOSE-RESPONSE CURVE OF SENSOR .....	230
6.1a <i>Dose-Response Curve of Sensor: Materials and Equipment</i> .....	230
6.2b <i>Dose-Response Curve of Sensor: Methodology</i> .....	231
6.2c <i>Dose-Response Curve of Sensor: Results and Analysis</i> .....	232
<b>7. SUMMARY AND CONCLUSIONS .....</b>	<b>248</b>
<b>9. BIBLIOGRAPHY .....</b>	<b>256</b>
<b>9. APPENDICES .....</b>	<b>271</b>

## Glossary of Abbreviations

- AFM - Atomic Force Microscopy
- ANOVA - ANalysis Of Variance
- BRCA1 - BReast CAncer 1
- BRCA2 - BReast CAncer 2
- CAP - Confined Atmospheric Pulsed-laser deposition
- CNT - Classical Nucleation Theory
- COP - Cyclic Olefin Polymer
- CT - Computed Tomography
- CV - Cyclic Voltammetry
- DHEA-S - DeHydroEpiAndrosterone Sulfate
- DLS - Dynamic Light Scattering
- DNA - DeoxyriboNucleic Acid
- DoE - Design of Experiments
- EDL - Electrostatic Double Layer
- EDX - Energy Dispersive X-ray spectroscopy
- EIS - Electrical Impedance Spectroscopy
- ELISA - Enzyme Linked Immuno-Sorbent Assay
- EP - Electron Percolation
- Fab - Fragment antigen-bonding
- FCC - Face-Centered Cubic
- FET - Field-Effect Transistor
- FWHM - Full-Width at Half-Maximum
- IgD - Immunoglobulin D
- IgE - Immunoglobulin E
- IgG - Immunoglobulin G
- IgM - Immunoglobulin M
- ISFET - Ion Sensitive Field Effect Transistor
- JIT - Just-In-Time (compilation)
- LAMP - Loop-mediated isothermal AMPlification

- LIFT - Laser Induced Forward Transfer
- MRI - Magnetic Resonance Imaging
- MS - Mass Spectrometry
- MYC - homo sapiens v-MYC avian myelocytomatosis viral oncogene homolog
- Nd:YAG - Neodymium-Yttrium-Aluminium Garnet
- OES - Optical Emission Spectroscopy
- PCR - Polymerase Chain-Reaction
- PDMS - PolyDiMethylSiloxane
- PEDOT - Poly(3,4-EthyleneDiOxyThiophene)
- PET - Positron Emmision Tomography
- PLAL - Pulsed Laser Ablation in Liquid
- PLD - Pulsed Laser Deposition
- PPM - Parts Per Million
- PPmL - Particles Per milliLitre
- PRF - Pulse Repetition Frequency
- PSA - Prostate Specific Antigen
- PSA3 - Prostate Specific Antigen 3
- PW - Pulse Width
- QCM - Quartz Crystal Microbalance
- SAXS - Small-Angle X-ray Scattering
- SELEX - Systematic Evolution of Ligands by EXponential enrichment
- SEM - Scanning Electron Microscopy
- SERS - Surface-Enhanced Raman Spectroscopy
- SIMD - Single Instruction-Multiple Data
- SNR - Signal-to-Noise Ratio
- SPR - Surface Plasmon Resonance
- ssDNA - single stranded DeoxyriboNucleic Acid
- ssRNA - single-stranded RiboNucleic Acid
- TOAB - TetraOctyl Ammonium Bromide
- UV - UltraViolet

- UV/Vis - UltraViolet/Visible
- VEGF-A - Vascular Endothelial Growth Factor A
- XANES - X-ray Absorption Near Edge Structure
- XRD - X-Ray Diffraction spectroscopy

## Glossary of Tables

Table 1. Tumour biomarkers that see the most widespread clinical use and the purposes for which the cancers they are indicative of (according to the U.S. National Cancer Institute <sup>37</sup> ).....	39
Table 2. The DoE parameters used in the preparation of samples for the process optimisation study and the UV/Vis spectral peak analysis for each of the produced samples. Samples are presented in the randomised order in which they were to be produced. Fields containing “N/A” denote samples for which no plasmonic peak was observed in their UV/Vis spectrum.....	96
Table 3. Processing parameters for each sample produced during this DoE process analysis. ....	110
Table 4. Results of the peak analysis performed on the spectra of the samples produced. This data was gathered from baseline corrected data using an automated peak-picking program. ....	114
Table 5. The results of manual particle sizing analysis ( $\pm\sigma$ indicated, for $n=20$ ). Sizing was performed by randomised fitting of ellipses to SEM imagery.....	117
Table 6. A table of SNR data for all responses measured during this study. SNR was calculated according to equation (2).....	120
Table 7. The ANOVA outputs for each model derived. ANOVA analysis was performed using Design-Expert software.....	122
Table 8. The electrical properties of the sample before and after thiolation, in addition to the difference between them as both a value and a percentage change. This test served as a quick demonstration of a CAP film changing its preproperties responding to surface interaction (a prerequisite for use as a sensor). ....	136

Table 9. The DoE parameters and measured outputs from the linear CAP deposition study. The line width output is to within  $\pm 5 \mu\text{m}$  and contiguity is simply recorded as a simple binary “0” for lines with breakages and “1” for contiguous lines. .... 139

Table 10. A table of the DoE input parameters and the measured response (resistivity) for the post deposition sintering process..... 154

Table 11. A table comparing the nominal, maximum and minimum particles per mL for the standard (as calculated based on the data reported by the supplier) and the output of the nanoconc program. .... 213

Table 12. A table of the ANOVA results for the initially derived fits (complete ANOVA tables are available in Appendix 53 - Appendix 54). These fits suggest predictable changes in sensor properties as a response to the target..... 238

Table 13. A table of the ANOVA results for the initially derived models (complete ANOVA tables are available in Appendix 55 - Appendix 56). These fits suggest predictable changes in sensor properties as a response to the target..... 242

## Glossary of Figures

Figure 1. The number of anticancer drugs approved yearly between 1981 and 2010 <sup>5</sup> .....	32
Figure 2. Histological images of a bladder mass found in a 70 year old patient (published online in a case study by the University of Pittsburgh School of Medicine <sup>24</sup> ).....	36
Figure 3. A schematic of a QCM biosensor system using antibodies as detection molecules. As analyte binds to the detection molecules, the mass of the surface increases thus dampening the oscillation and enabling detection of the analyte. ....	46
Figure 4. Diagrams of the most commonly used electronic biosensor electrode designs, showing a) interdigitated electrodes, b) concentric circle interdigitated electrodes and c) parallel plate electrodes. ....	48
Figure 5. A basic diagram outlining the concept behind the FET detection method. Depending on the polarity of the antigen, the charge on the conductor may increase or decrease, affecting its conductivity. ....	49
Figure 6. A diagram outlining the underlying principle behind an SPR based immunoassay. Note the darker absorbance band in the reflected light, representing a change in spectral intensity at this angle of reflection.....	52
Figure 7. A schematic depicting the proposed mechanism of action of an EP biosensor. It is suggested that the additional steric bulk of the bound target molecule causes the distance between the nanotubes to increase, decreasing the ability of electrons to “percolate” across that gap. ....	54
Figure 8. Illustration of the major methods of protein immobilisation in label-free biosensor development: A) direct covalent capture, which is only possible with suitably reactive surfaces; B) covalent capture via a linker, allowing the linkage of detectors and surfaces unsuitable for	

method A; C) an example of an affinity capture method (in this case, using Protein G to immobilise an antibody). ..... 55

Figure 9. Schematic depicting the appearance of the immunoglobulin isotypes, as well as the orientation in which an antibody binding site binds to an antigen. When the binding site is separated from the rest of the antibody it is usually referred to as a Fab fragment. .... 57

Figure 10. A chart compiled using data from the Web of Science “Search Results Analysis” function. This chart shows the number of papers citing the keyword “aptamer” every year since their first mention. It is clear from this chart that interest in aptamers has grown near exponentially in recent years. .... 60

Figure 11. A diagram of a simple roller-based nanoimprinting setup. This kind of continuous roller nanimprinting method readily allows for the mass production of nanoimprinted polymeric materials. .... 64

Figure 12. The process of photolithographic etching of silicon wafers. This process is used in microprocessor manufacturing<sup>102</sup>. .... 65

Figure 13. A diagram of: a) the conventional PLD technique, the vacuum chamber pictured could be evacuated to a pressure as low as  $10^{-5}$  Torr<sup>103</sup>; and b) the LIFT process, the laser beam scans from left to right ablating the donor film, depositing it in a nanostructured format on the substrate. .... 67

Figure 14. A chemical equation schema outlining the Turkevich Method of nanoparticle synthesis (resulting in a nanoparticle coated with citrate ligands). This process is currently one of the more common methods of nanoparticle production. .... 69

Figure 15. Diagrams of numerous proposed colloidal nanoparticle growth mechanisms where red/blue/grey circles are positive/negative/neutral atoms, gold circles are nanoparticles and green arrows are electrostatic forces on atoms. Each diagram represents: a.) the LaMer burst nucleation model, b.) the Reiss growth by diffusion model, c.) the Chow aggregation

model, d.) the Ostwald ripening model, e.) Polte’s category 2 model (where light blue represents the EDL) and f.) Polte’s category 1 model... 71

Figure 16. Schematic of the effect of a single laser pulse in the PLAL method. In general use, PLAL makes use of repeated pulses such as this to produce a colloid..... 76

Figure 17. Photographs of gold nanoparticle (left) and zinc-based (right) aqueous nanoparticle colloids produced using the PLAL method. .... 77

Figure 18. Illustration of the relationship between the dimensions of a channel and the surface area in contact with its contents. Note how the volume in each case is the same but the smaller channel has greater contacting surface area. This increased surface area presents a significant advantage for biomicrofluidic sensors, as it maximises the interaction between the analyte and the sensor. .... 78

Figure 19. An illustration of Crossflow Filtration separating blood plasma from blood. The gaps in the wall of the channel are small enough to exclude cells from the plasma outlet without excluding proteins and other blood plasma components..... 79

Figure 20. A photograph of a modular microfluidic system developed by Langelier et al. in 2011<sup>155</sup> ..... 80

Figure 21. A schematic of the basic CAP methodology, as applied in section 3.2.1. .... 85

Figure 22. The results of SEM/EDX analysis of the aluminium oxide nanostructures deposited during experimental attempts to deliberately replicate the unintended nanostructure deposition noted during earlier tests with steel showing a) the results of EDX analysis analysis on a single nanostructured cluster and b) a larger scale SEM image showing the variety of structures deposited..... 87

Figure 23. CAP deposited nanostructures comprising of a) gold nanostructures on COP, b) gold nanostructures on glass, c) silver

nanostructures on COP, d) the same silver on COP sample at higher magnification and e) an example of deposited gold nanostructures and the EDX spectrum used to confirm its elemental composition..... 89

Figure 24. The XRD spectrum of a Gold on COP sample deposited using the CAP method. The unidentified peak present is suspected to be due the adhesive tape used to secure the sample. .... 90

Figure 25. Examples of various patterns deposited as nanostructured gold using the CAP technique, including a) a raster scanned 5mm x 5mm square produced for the experiments described in Chapter 4.1, b) a straight line, c) a curve describing a function often referred to as a Farris' Wheel<sup>158</sup> and d) a raster scanned version of the APT group logo..... 92

Figure 26. Images of the two CAP setups used during this stage of the project: a) the original methodology using adhesive tape, found to have low reproducibility and b) the setup that replaced the adhesive tape method, utilising metal clips to apply mechanical pressure. The use of setup b showed a noticeable increase in reproducibility over setup a. .... 95

Figure 27. A photograph of the sample produced at parameters Scan Speed: 10 mm/s, Fluence: 0.79 J/cm<sup>2</sup>, Scan Spacing: 150 μm, Vertical Spacing: 188 μm. The white square in the middle of the glass is the area in which frosting has occurred..... 98

Figure 28. The UV/Vis spectrum of the sample prepared at parameters Scan Speed: 3 mm/s, Fluence: 0.15 J/cm<sup>2</sup>, Scan Spacing: 50 μm, Vertical Spacing: 188 μm. The red line is the corrected baseline to compensate for the background glass peak..... 99

Figure 29. A cross-sectional SEM image of a cracked CAP sample (deposition parameters: Scan Speed: 3 mm/s, Fluence: 0.79 J/cm<sup>2</sup>, Scan Spacing: 150 μm, Vertical Spacing: 0 μm)..... 101

Figure 30. An example of one of the Raman spectra obtained from the samples produced. All showed only these peaks thought to be indicative

of glass, with varying intensities (most likely due to varying degrees of frosting). .....	102
Figure 31. An example of one of the I/V curves obtained from the samples of CAP depositions on a COP substrate. ....	107
Figure 32. A schematic diagram of the “Target Stage” variant of the CAP methodology used during this experiment. This variant of the methodology uses a SLA produced stage to ensure a 50µm gap between the target and substrate. ....	109
Figure 33. Examples of some of the UV/Vis spectra obtained showing a) the spectrum obtained for sample 6 with its local maximum and corrected baseline shown and b) the baseline-corrected spectra of samples 6, 17 and 21 on the same graph, clearly showing their variations in intensity and local maxima. ....	113
Figure 34. Examples of the kinds of features observed during SEM analysis. The samples numbers and processing parameters for each image shown are a) Sample 18 (6 mm/s, 0.221 J/cm <sup>2</sup> , 150 µm), b) Sample 11 (12 mm/s, 0.351 J/cm <sup>2</sup> , 100 µm), c) Sample 20 (12 mm/s, 0.481 J/cm <sup>2</sup> , 150 µm) and d) Sample 4 (18 mm/s, 0.481 J/cm <sup>2</sup> , 50 µm) all obtained at 8380× magnification. ....	116
Figure 35. Contour plots of the particle area (left) and standard deviation of area (right) predicted by the derived models at various scan spacings. ....	125
Figure 36. Normal plot of residuals and predicted vs actual plots for the size (top) and dispersity (bottom) models derived. ....	126
Figure 37 Surface (left) and contour (right) plots of the predicted plasmonic peak positions at scan speeds of (a,b) 6mm/s, (c,d) 12mm/s and (e,f) 18mm/s. Surfaces and contours are colorised by plasmon position.....	128

Figure 38. Normal plot of residuals and predicted vs actual plot for the plasmonic peak position model. .... 129

Figure 39. Surface (left) and contour (right) plot of the plasmonic peak integral as predicted by the model derived. Surface and contour plots are colorised by plasmonic peak integral in  $\text{nm}^2$ . .... 130

Figure 40. The normal plot of residuals and predicted vs actual plot for the plasmonic peak integral model derived. .... 130

Figure 41. A plot of the line described by (7) (red) and the process space examined during this study (grey). The pink area above the line is the area where where the plasmonic peak integral is predicted to begin increasing again. .... 132

Figure 42. Toolpaths for electrode designs deposited on  $25\text{mm}^2$  areas based on the a.) square and b.) circular standard forms of interdigitated electrode designs. These lines describe the paths traced by the laser during CAP deposition of these shapes. .... 138

Figure 43. Optical microscopic images of samples a.) 15, b.) 17, c.) 14 and d.) 8 at the same magnification. Recorded line widths were taken to include all darkened areas along the scan path, to the nearest  $10\mu\text{m}$ . . 139

Figure 44. Microscope images of CAP deposited a) square and b) circular interdigitated electrodes (dimensions  $5\text{mm} \times 5\text{mm}$  and  $5.64\text{mm}$  diameter so that both cover an equal area). Note the LIFT zone gaps highlighted within the green circles. .... 142

Figure 45. Images of several linear deposition tests and their respective LIFT zones. Sample numbers are a.) 10, b.) 17, c.) 11 and d.) 1. As can be seen in image d, a LIFT zone is still present when no visible line was deposited. .... 143

Figure 46. The toolpath prepared for the deposition of the redesigned electrodes. Each electrode is comprised of a single line spiralling towards

the centre with a consistent distance to the other electrode on either side.  
..... 145

Figure 47. Samples produced at scan speed: 17 mm/s, Fluence: 0.671 J/cm<sup>2</sup>. Each of the samples fabricated with these parameters shows a thin, contiguous deposition of spiral electrodes. .... 146

Figure 48. Cross-Sectional SEM analysis of the deposited spiral electrodes. Image b is zoomed in on the edge visible in image a. The spiral shaped channels visible align with the path of the laser, suggesting that they were likely created by the laser during deposition. .... 147

Figure 49. A photograph of a successful gold nanoparticle deposited film produced using a bidirectional raster scan pattern of 5 mm by 5 mm. . 149

Figure 50. Simple diagrams exhibiting how a.) sintering and b.) chemical crosslinking can be used to bridge gaps between deposited particles. These methods were both tested as a possible conductivity enhancing post-processing step. .... 151

Figure 51. A photograph of the modified 4-point probe used during testing. Note the crocodile clip and metal wire being passed through the cooling inlet to ground the stage. .... 152

Figure 52. A diagram of the deposition and sintering process employed during this experiment. A film was first deposited, the sample was then flipped and the now upwards facing film was immediately sintered. .... 153

Figure 53. A diagram of overlapping adjacent scanlines. Adjacent scanlines alternate red/blue and the overlap area is shown as purple. The parameter  $x_0$  denotes the width of the overlap area. .... 156

Figure 54. The molecular structure of benzene-1,4-dithiol (a) and a diagram of the mechanism by which it can transfer charge between surfaces (b). .... 159

Figure 55. A diagram showing the underlying concept behind the functionalisation method employed. Note that the distances between

particles in this example are somewhat exaggerated to demonstrate the underlying principle more clearly..... 160

Figure 56. Pairs of samples taken at the most effective parameter sets for conductivity enhancement compared to untreated CAP samples. Resistivity values for each sample are included. .... 163

Figure 57. A photograph of the proof-of-concept experiment described above. A finished sensor was immersed in PBS and exposed to 6-mercaptophexanol while repeated EIS measurements were taken. Change in EIS demonstrates a measurable response to interactions at the sensor surface..... 164

Figure 58. Plots of the conductometric data obtained before beginning the thiolation test. These tests were performed to confirm the presence of a measurable conductometric response in the sensor. .... 165

Figure 59. Surface and contour plots of the changes in EIS spectra observed over a 24 hour period in the presence of a thiol. The plots on the left are Bode Plots vs. time and on the right are Nyquist plots vs time. Colourbars are on the appropriate side for their plots and are relative to the Z-axes of the plots..... 166

Figure 60. Photographs of the corroded sample discussed above, flaky pieces of the patina that was present and, on the right, the crocodile clip that was used to hold the sample while this corrosion occurred. .... 167

Figure 61. The various design stages of the sensor contacts as they evolved. The sensor contacts gradually evolved from CAP based contacts towards a more complete screen-printing based design. .... 169

Figure 62. A photograph of conductometry tests being performed with a lollipop style sensor. The sensor was immersed in PBS and exposed to 6-mercaptophexanol. EIS measurements were then repeatedly taken, looking for a measurable electrochemical change in response to interactions at the sensor surface..... 171

Figure 63. Chronoamperometry and cyclic voltammetry scans for the 25mm<sup>2</sup> lollipop sensor design. Note that the first and final scans on the CV are plotted in grey. .... 172

Figure 64. Chronoamperometry and cyclic voltammetry scans for the 100mm<sup>2</sup> lollipop sensor design. Note that y axis on the CV is scaled by 10<sup>-3</sup> and that the first and final scans on the CV are plotted in grey. .... 172

Figure 65. Time-resolved EIS spectra for the 10mm lollipop sensor design with thiol added at t=0s. The plots on the left are Bode Plots vs. time and on the right are Nyquist plots vs time. Colourbars are on the appropriate side for their plots and are relative to the Z-axes of the plots. .... 173

Figure 66. The final sensor designs. The golden areas are CAP deposited nanostructures (the sensing surface) and the black areas are conductive carbon ink. On an A4 page, the diagram of the sensors in this figure should match the size of the actual sensors. .... 175

Figure 67. An image of the sensor screen layout designed (top) and the final, finished sensor screen (bottom). .... 177

Figure 68. A photograph of a number of mass produced 25mm<sup>2</sup> biosensors (left) and a closer photograph of a single one of these sensors (right). .... 178

Figure 69. Time-resolved EIS data for the final sensor design with thiol added at t=0. The plots on the left are Bode Plots vs. time and on the right are Nyquist plots vs time. Colourbars are on the appropriate side for their plots and are relative to the Z-axes of the plots. .... 180

Figure 70. A comparison of traditional Single Instruction-Single Dispatch (SISD) computing and Single Instruction-Multiple Dispatch computing. In the example, SISD requires eight ticks to process the array while SIMD can complete the process in only two ticks. .... 206

Figure 71. A high-level flowchart summarising the design of the particle counting program. .... 210

Figure 72. Plots of particles per mL vs % (v/v) of colloid as calculated based on the supplier's specifications (green, with error bands) and as returned by the NanoConc program (red). The output of the program is clearly well within the margin of error for the standard value. .... 214

Figure 73. Photographs of the various steps of sensor fabrication following the screen-printing step. The steps pictured are (a) immersion in 1,4-dithiobenzene, (b) immersion in aqueous AuNP colloid, (c) inoculation with thio-DNA and (d) passivation with 6-mercaptohexanol. .... 224

Figure 74. A photograph of conductometric testing being performed on the final sensor design. Sensors were immersed in PBS and subjected to conductometric testing both before and after inoculation with the target. .... 225

Figure 75. Overlaid graphs of several electrochemical tests for the sensor before (red) and after (green) passivation. Each plot shows a clear change in electrochemical properties following passivation. .... 226

Figure 76. Overlaid graphs of several electrochemical tests for the sensor before (red) and after (green) exposure to c-Myc exon 2. Each plot shows a clear change in electrochemical properties following inoculation with the target. .... 228

Figure 77. Example EIS plots for the sensor exposed to 10  $\mu$ M c-Myc exon 2 (red is before exposure and green is after exposure). There is a clearly visible change in the EIS spectrum for the sensor following inoculation with the target. .... 233

Figure 78. A diagram of the commonly modelled diffusive Randles' circuit. The "W" symbol represents a "Warburg element", a type of constant phase element used to model diffusion in electrodes. .... 234

Figure 79. A diagram of the equivalent circuit found to most closely match the data obtained. Note that it is comprised of 3 Randles' circuits

in parallel, with their elements labelled as being in Randles' circuit 1, 2 or 3 .....	235
Figure 80. The Cook's Distance plot for the initially derived R-Total (diff) model. Note the highlighted outlier, signifying a point that significantly deviates from the observed trend.....	239
Figure 81. A $2\sigma$ confidence ellipse plot for the R-Total (diff) dataset. The grey ellipse denoted the area of the plot wherein samples are less than 2 standard deviations from the trend. The suspected outlier of interest is highlighted in green and is clearly outside the $2\sigma$ confidence range.....	240
Figure 82. The sensor used for the 4um batch 2 datapoint of the dataset (the apparent outlier). An apparent break in the working electrode contact is highlighted with a green circle. This break is the most likely explanation for the unusually large standard deviation of the sample. .	241
Figure 83. The normal plot of residuals and predicted vs actual plots for the R-Total (diff) model described by Equation (59). .....	244
Figure 84. A plot of the empirical R-Total (diff) data obtained and the line described by Equation (59). The fitted line described by this equation aligns well with the empirical data. ....	245
Figure 85. The normal plot of residuals and predicted vs actual plots for the Real Impedance (%diff) model described by Equation (60). .....	246
Figure 86. A plot of the empirical Real Impedance (%diff) data obtained and the line described by the Equation (60). The fitted line described by this equation aligns well with the empirical data. ....	247

# Abstract

## *Laser Assisted Production of Nanostructures for Biomedical Sensing Applications - Cian Hughes*

With the recent rise of nanotechnology, the cutting-edge of biosensor technology has rapidly progressed becoming more sensitive, accurate and higher throughput than ever before. However, if nanoengineered biosensors are to become as ubiquitous as ELISA assays in general diagnostic applications they first must become more cost-effective. Current methods for the fabrication of nanobiosensor platforms generally rely on chemical processes that are expensive, environmentally destructive and often time-consuming. As nanotechnology matures from a new, exciting technology into an everyday, mundane one it must also become more affordable and more environmentally friendly.

It was noted during polymer ablation experiments that (under specific conditions) laser ablation of bulk metals appeared to result in the direct deposition of nanostructures on the polymer. Following this discovery, work began to optimise this technique (referred to as Confined Atmospheric Pulsed-laser deposition, or CAP) for reliable, reproducible nanostructure deposition and the application of this new technique in the fabrication of biosensors. Such a technique would allow for the rapid, green, inexpensive fabrication of nanostructured films, potentially resulting in the design of a biosensor offering many advantages of the current cutting-edge in sensor technology at a price suitable for use in a

Initial experiments explored the capabilities of the CAP technique, discovering suitable metals, substrates and conditions for deposition. Following this, several studies were performed to optimise the technique and search for correlations between processing parameters and the properties of the resulting films. A series of experiments were then performed to adapt this optimised technique to for the deposition of films suitable for biosensor production, such as the direct deposition of interdigitated electrodes. Once a suitable fabrication method had been found, a brief diversion was made to address a difficulty in the characterisation of some reagents needed for that method. This work resulted in the creation of a new, novel, non-destructive technique for particle enumeration in colloidal suspensions.

With the design of the sensor finalised, a number of experiments were then conducted to test the effectiveness of the sensor platform for detecting an example target analyte. These tests resulted in the successful detection of c-Myc exon 2 (a cancer biomarker) and the elucidation of dose-response relationships that enables the developed sensor to be used for quantifying the amount of target present in a sample.





# 1. Introduction

This project was focused on the application of laser processing based nanostructure deposition techniques in the fabrication of sensor platforms. Of the wide variety of potential sensor applications, it was decided to focus on diagnostic sensors for the purposes of cancer detection due to the criticality of the need for such sensor technologies. Herein, the work is presented with the long-term goal of creating a sensor capable of detecting DNA strands that are indicative of cancers in patient blood samples.

Due to the highly cross-disciplinary nature of this project, the first step undertaken was a lengthy literature review (as presented in Section 2), intended to briefly summarize the current state of diagnostic sensor technology, the need for such devices, and design decisions to consider going forward. The next step undertaken was the exploration of the capabilities of the newly discovered deposition technique which was chosen as the focus of this work (Confined Atmospheric Pulsed-laser Deposition or CAP), as presented in Section 3.1. Once the initial boundaries of this technique were established, the focus of the work shifted to the optimisation of the method, and examination of the possibility of exerting control over the deposition process. This work is presented in the rest of Chapter 3.

After the capabilities and controllability of the CAP technique had been defined, work progressed towards adapting this optimised deposition technique for the fabrication of electrodes suitable for use in biosensing applications. This involved processing the CAP surfaces to optimise their conductive properties and iterative proof-of-concept tests based on thiol-surface bonding interactions. This part of the development process and the results obtained from it are presented in Chapter 4.

With the design of the sensor in a roughly finalised state it was apparent that to ensure reproducibility all reagents used in the fabrication process should be properly characterised. An important example of one such reagent is the gold nanoparticle colloid used in a fabrication step. Pulsed Laser Ablation in Liquids (PLAL) was utilised as a method for producing this colloid which could then be used to exert more exacting control over the conductivity of the sensor surface. Characterising a nanoparticle colloid of unknown concentration proved difficult with the equipment available. When attempting to address this characterisation problem it quickly became clear that a new particle enumeration method would be required to characterise this colloid. This new methodology based upon previous work applying the Mie model of particle-photon interactions to UV/Vis spectroscopy was used to create a program (called “NanoConc” herein) that can use UV/Vis spectroscopic data and Dynamic Light Scattering data to measure the number of particles per mL in a colloid. The theory of this methodology and the design fo the program based on it are outlined throughout Chapter 5.

Once these various pieces of work for the project had been completed, tests began on the final sensor platform. Using the c-Myc exon 2 cancer biomarker as an example target, a conductometric sensor response to a target analyte was successfully demonstrated in Section 6.1. Finally, dose-response experiments were performed on the sensor to find a relationship that could be used to quantify the amount of analyte in a sample based on the sensor response. This work, presented in Section 6.2 found that a clear linear relationship between the analyte concentration and the impedance of the sensor, successfully demonstrating its use as a quantitative sensor and thus its future potential use for cancer diagnosis.

## 2. Literature Review

### 2.1 Cancer Research

The field of oncology is one that has steadily gained increased importance over the past century with the rise of modern medicine and the great progress made in the treatment of infectious diseases. During this time, the percentage of fatalities due to diseases such as influenza has decreased<sup>1</sup> and the average life expectancy worldwide has increased<sup>2</sup>, while the percentage of mortalities due to cancer has seen a steady increase to the point that it is now one of the leading causes of death worldwide<sup>3,4</sup>. For this reason, research into methods to help detect and treat cancers in their early stages has become a priority within the scientific community in recent years, as shown by the ever-increasing development of cancer treatments in the pharmaceutical industry (see Figure 1).

Research into combinations of monoclonal antibody based treatments with new chemotherapeutics in the late 20<sup>th</sup> century has led to the development of a number of new, higher efficacy cancer treatments emerging in the early years of the 21<sup>st</sup> century<sup>5</sup>. Thus, the effective detection of cancers has become a critically important issue, particularly as the means to treat and potentially cure such cancers if diagnosed early has become available to us.

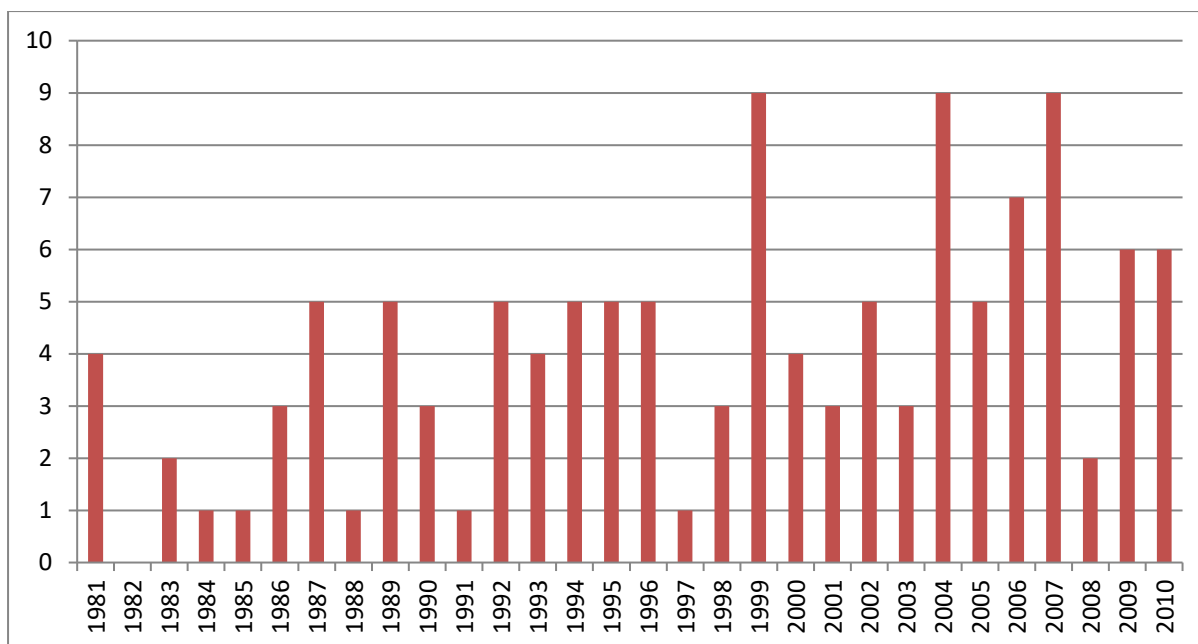


Figure 1. The number of anticancer drugs approved yearly between 1981 and 2010<sup>5</sup>.

The current standard methods for the detection of cancer with any high degree of certainty rely primarily on imaging techniques (such as MRI and PET) followed by a direct biopsy<sup>6</sup>. While blood biomarker tests are also used as a non-invasive supporting test, the risk of a false-positive (or worse, a false-negative), and the high expense of current blood testing methodologies make them a somewhat undesirable primary means of diagnosis. Pharmacoeconomic studies have found even common PSA screening tests are not cost-effective<sup>7</sup>, exhibited by the finding that PSA3 antigen tests had a cost of €450 per patient in Ireland as recently as 2012<sup>8</sup>. Genetic screening offers a much higher degree of certainty than blood biomarker testing, but at an even higher expense despite the many advances provide by genetic studies in recent years<sup>9</sup>.

As biomolecular diagnosis methods have matured, research into non-invasive cancer detection has moved away from specific tests and towards the idea of a screening assay. Such assays allow for cheaper, high-throughput methods of biomarker detection<sup>10</sup>. The term biomarker refers

to biomolecules that are indicative of a disease, in this case cancer. Cheap, high-throughput methodologies offer the exciting prospect of not only fast, affordable cancer screening but the possibility of a greater understanding of the biochemistry of different cancers. This biochemical understanding could potentially lead to further improvements in treatment methods in the future.

For these reasons, this thesis is focused on making contributions to the development of detection techniques with the goals of facilitating a higher throughput and/or lower cost (yet still capable) method for the detection of cancer biomarkers in human blood samples. This review summarises the ideas on which this research has been based, and the examples reported in the literature which provided the impetus to considering the feasibility of the techniques investigated.

## 2.2 An Overview of the Biology of Cancer

### 2.2.1 Introduction to Cancer

Cancer is a disease characterised by the uncontrolled division of cells within a given tissue<sup>11</sup> most often giving rise to a mass of cells referred to as a neoplasm or, more commonly, a tumour. Cancer is usually the result of a change in the biochemistry of a cell that either allows it to divide an infinite number of times (unchecked by the mechanisms that normally prevent this, such as telomere counting), or which causes it to avoid undergoing apoptosis<sup>12</sup>.

The initial formation of cancerous tumours, a process known as tumorigenesis or carcinogenesis<sup>11</sup>, can be due to many factors but is ultimately the result of a genetic change allowing these cancerous behaviours. Factors that are thought to contribute to these changes

include (but are not limited to) epigenetics<sup>13</sup>, chemical exposure<sup>14</sup>, viral<sup>15</sup> or bacterial<sup>16</sup> infection and/or exposure to pollutants<sup>17</sup>.

While tumours themselves can cause a range of health problems, cancerous cells become most dangerous when they undergo metastasis<sup>18</sup>. Metastasis is the process by which malignant cells invade the bloodstream of a patient. Once in the bloodstream, these cells can reach other organs and trigger the formation of new “secondary” tumours in those organs, a process known as colonization<sup>12</sup>. Metastatic cancers have a far higher mortality rate than non-metastatic cancers due to their systemic nature, and are estimated to be responsible for approximately 90% of cancer related deaths<sup>19</sup>.

Cancers have been observed forming from essentially every known human tissue<sup>20</sup> (with the obvious exception of erythrocytes, as they lack a nucleus) and it follows that there are many distinct cancers, each as unique as the cells that they derive from and the mutations that caused them to become cancerous. For this reason, making statements applicable to all cancers can prove extremely difficult. For the purposes of this discussion, however, a focus is placed on a number of specific cancers in an attempt to give a more generalised picture of the biology classically expected from them.

### 2.2.2 A Brief Discussion of the Morphology of Cancerous Cells and the Study of Histology

Histology is a term that refers to the study of tissues and tissue structures with the aid of microscopy. It is one of the primary ways in which many cancers are diagnosed from biopsies. A histological diagnosis requires an expert with years of training to make judgements based on the changes in morphology that occur as cells become cancerous. The study of histology, therefore, has extensively logged a wide variety of

morphological changes observed in cancerous cells that can offer insights into their biology.

One of the defining features of the cells comprising most human tissues is that they are comprised of similar cells with a certain degree of recognizable organization<sup>21</sup>. Cancerous cells, as mentioned before, grow uncontrollably and this trait is visible when biopsy samples are viewed under the microscope. Cancerous cells often appear larger than their non-cancerous counterparts, more crowded or less well defined<sup>22</sup>. And, of course, since they may have metastasised from elsewhere they could even be totally different cells from those nearby, sometimes even to the point of their origins being unidentifiable<sup>23</sup>.

As a result of this, in many cases histology is a difficult method by which to make a definite diagnosis, requiring extensive training and experience to carry out effectively. In cancer biopsies such as the example shown in Figure 2 deciding if a tumour is present can be extremely difficult and this may result in an incorrect judgement by physicians. While these images contain a wealth of information to the trained eye with many years of experience, to the untrained eye they merely appear to be a collection of blobs of various colours, exhibiting the degree of expertise required to make accurate histological diagnoses. In the case study from which Figure 2 was sourced a final diagnosis of clear cell adenocarcinoma (a relatively rare gynecological cancer) was made. Adenocarcinomas are a broadly defined group of malignant epithelial cell tumours of that originate in the glands. This diagnosis was eventually made with the aid of these images (among many others), 10 other histological staining tests, a CT scan, and a patient history highlighting the inherent difficulty of obtaining a reliable diagnosis using the currently favoured methods.

The complexity and inherent difficulty of histological classification of tumours has, historically, been a repeated source of misdiagnoses<sup>25</sup> and can mean that histological diagnoses require a lot of time. These

disadvantages have led to a greater focus on developing a means of cancer diagnosis based instead on biochemical metrics as time has progressed.

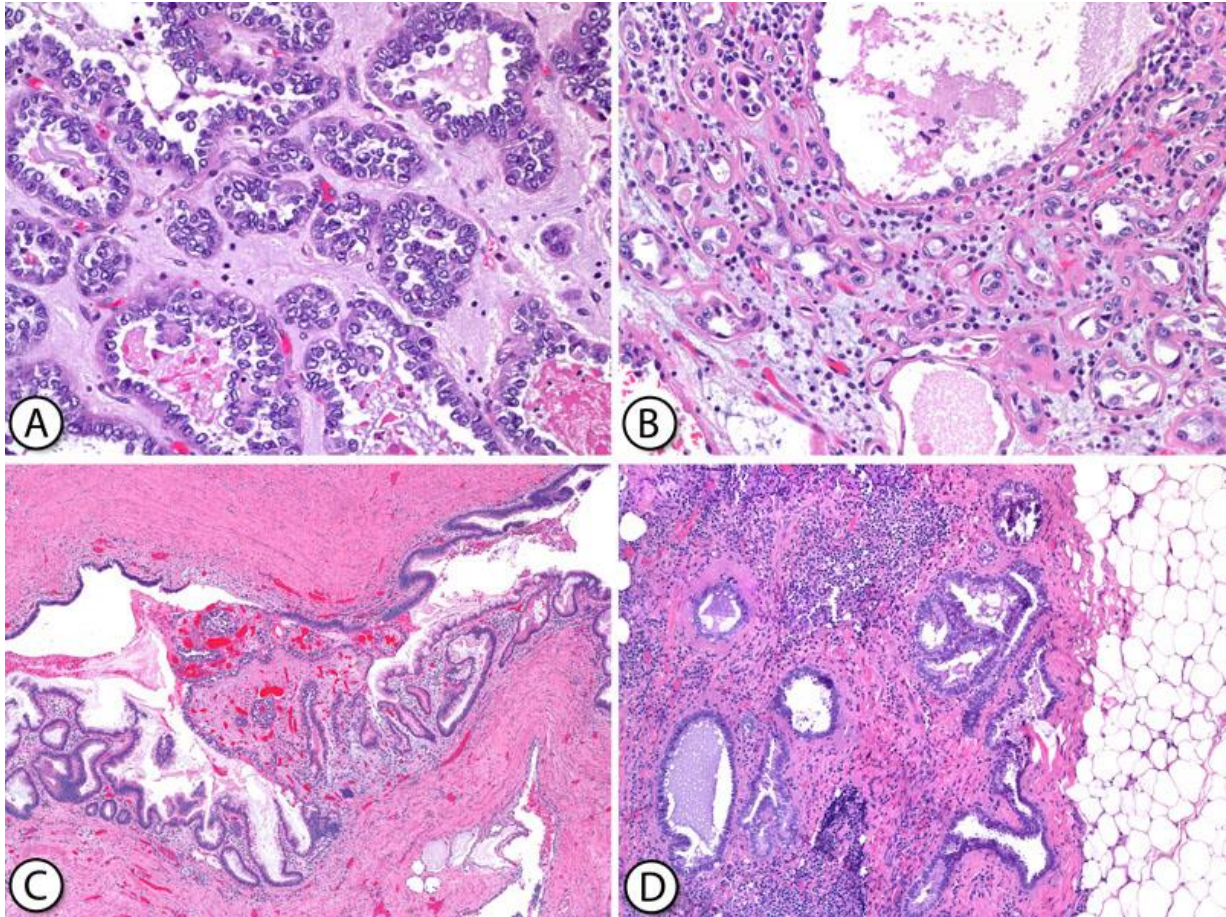


Figure 2. Histological images of a bladder mass found in a 70 year old patient (published online in a case study by the University of Pittsburgh School of Medicine<sup>24</sup>).

### 2.2.3 Biochemical Differences in Cancerous Cells

As early as 1959, it was noted that certain sarcomas displayed a markedly higher level of purines (key building blocks of DNA and RNA) in their cytoplasm<sup>26</sup>. While quite mysterious at the time, this observation makes sense when viewed through the lens of our current understanding of cancers, which posits that many are caused by cells that perpetually replicate<sup>11</sup>. Thus, as cell replication is reliant on DNA synthesis it is logical

to expect that the levels of such DNA building blocks should be elevated in cancer cells. Still, these kinds of observations were the first steps towards unravelling the subtle biochemical differences between cancer cells and healthy cells, an ongoing process that continues to offer prospects for meaningful medical advancement.

While an increase in purine levels is an easily detectable marker, it is also unreliable and non-specific. In recent years, research has focused on discovering specific proteins that may contribute to the disease state of a cancer, and such research has gradually advanced our understanding of these conditions to its current state<sup>27</sup>. These cancer indicating proteins (in addition to some cancer indicating polyglycosides and polynucleotides) are generally referred to in the study of diagnostics as cancer biomarkers<sup>28</sup>. Due to their extremely varied nature discussing specific biomarkers in-depth falls somewhat outside the scope of this review, with however their most important generalised features being discussed in Section 2.2.4.

Currently, areas of particular interest with regard to the biochemistry of cancer are the study of angiogenesis and hypoxic tumour tissues. Angiogenesis is an interesting process by which a tumour creates new blood vessels, for the purpose of sustaining the tumour tissue<sup>11</sup>. This process has caught the interest of researchers because without the materials carried by the blood (such as sugars, oxygen and essential amino acids) even cancer cells are incapable of division. While the biochemical mechanisms underpinning angiogenesis are still a subject of active research, it is generally accepted that these mechanisms are facilitated by the protein known as Vascular Endothelial Growth Factor-A (VEGF-A)<sup>12,29</sup>. This protein is usually responsible for the creation of vital blood vessels during embryonic development, and remains present in cancers capable of angiogenesis. A number of oncogenes (suspected

cancer contributing genes) have been implicated as triggers for the activation of the VEGF-A encoding gene, allowing for its expression<sup>12</sup>.

When a region of a tumour is too far from a blood vessel to receive oxygen from the blood, this region of tissue is referred to as a hypoxic tumour. Hypoxic tumour tissue has been suggested to have many important influences on tumour development. For example, tumour hypoxia has been observed to upregulate the expression of VEGF-A in tumours<sup>12,30</sup>, suggesting that cancers exhibiting this upregulation may have a mechanism to generate new blood vessels through angiogenesis as required to sustain their growth. It has also been suggested that the adverse conditions in hypoxic environments may create selective pressures that promote the growth of cancers with less susceptibility to apoptotic signals<sup>31</sup>, an increased tendency for metastasis and reoccurrence<sup>32</sup> and even an increased resistance to radiation therapy<sup>33</sup>. Further highlighting the changes prevalent in hypoxic tissue are its vastly different responses to chemotherapeutic molecules, for example its increased susceptibility to the effects of  $\delta$ -tocotrienol<sup>34</sup>.  $\delta$ -Tocotrienol is a member of the vitamin-E family of nutrients that has exhibited the ability to reduce tumour growth by inhibiting angiogenesis. Shibata et al.<sup>34</sup> recently published a paper reporting their observation that this compound appeared to have a greater efficacy against hypoxic cancer cells than it exhibited against regular or “normoxic” ones.

Clearly, despite the great progress that has been made in the field of cancer biochemistry since the early discoveries such as those discussed at the beginning of this chapter, there are still many unanswered questions about these diseases. As such, the most useful target protein for accurately diagnosing cancer is a topic that is subject to marked and sudden change as new research is conducted. An ideal biosensor platform would therefore be one that has not only a high degree of specificity for

its target, but which can easily and rapidly have its design tweaked to target a different antigen with comparable specificity.

## 2.2.4 A Discussion of Cancer Biomarkers

The term “cancer biomarker” is used to refer to any molecule that has the possibility of being used as a means of diagnosing cancer. There are a great many cancer biomarkers that could potentially be useful for the reliable diagnosis of cancers. See Table 1 for examples of those currently in use. These include genes, proteins, oligosaccharides and even some lipids<sup>35</sup>. However, the most commonly explored biomarkers tend to be categorized as either an antigen or a gene. Antigens are molecules that are produced by cancer cells that stimulate an immune response from a patient<sup>21</sup>. Cancer genes, on the other hand, are the genetic sequences and traits in the DNA of cancerous cells that contribute to their cancerous nature<sup>36</sup>.

Table 1. Tumour biomarkers that see the most widespread clinical use and the purposes for which the cancers they are indicative of (according to the U.S. National Cancer Institute<sup>37</sup>)

Biomarker	Cancer type	Found in tissue	Clinical use
Anaplastic lymphoma kinase (alk) gene rearrangements	Non-Small Cell Lung Cancer/Anaplastic Large Cell Lymphoma	Tumour	Prognosis/Treatment Determination
$\alpha$ -fetoprotein (afp)	Liver Cancer/Germ Cell Tumours	Blood	Diagnosis (Liver Cancer)/Treatment Determination (Germ Cell)/Prognosis (Germ Cell)

Biomarker	Cancer type	Found in tissue	Clinical use
$\beta_2$ microglobulin (b2m)	Multiple Myeloma/Chronic Lymphocytic Leukemia/some Lymphomas	Blood, Urine and Cerebro-spinal Fluid	Prognosis/Measurement of Response to Treatment
$\beta$ human chorionic gonadotropin (beta-hcg)	Choriocarcinoma/Testicular Cancer	Urine and Blood	Stage Assessment/Prognosis/Measurement Response to Treatment
Bcr-abl fusion gene (philadelphia chromosome)	Chronic Myeloid Leukemia	Blood and Bone Marrow	Diagnosis Confirmation/Disease Monitoring
Braf mutation v600e	Cutaneous Melanoma/Colorectal Cancer	Tumour	Targeted Therapy
Carbohydrate antigen 15-3/carbohydrate antigen 27.29 (ca15-3/ca27.29)	Breast Cancer	Blood	Measurement of Response to Treatment/Test for Recurrence
Carbohydrate antigen 19-9 (ca19-9)	Pancreatic Cancer/Gallbladder Cancer/Bile Duct Cancer/Gastric Cancer	Blood	Measurement of Response to Treatment
Carbohydrate antigen 125 (ca-125)	Ovarian Cancer	Blood	Diagnosis/Measurement of Response to Treatment/Test for Recurrence
Calcitonin	Medullary Thyroid Cancer	Blood	Diagnosis/Measurement of Response to Treatment/Test for Recurrence

Biomarker	Cancer type	Found in tissue	Clinical use
Carcinoembryonic antigen (cea)	Colorectal Cancer/Breast Cancer	Blood	Test for Metastasis (Colorectal Cancer)/Test for Recurrence (Breast Cancer)/Measurement of Response to Treatment (Breast Cancer)
Cluster of differentiation 20 (cd20)	Non-Hodgkin Lymphoma	Blood	Targeted Therapy
Chromogranin a (cga)	Neuroendocrine Tumours	Blood	Diagnosis/Measurement of Response to Treatment/Test for Recurrence
Chromosomes 3, 7, 17, and 9p21	Bladder Cancer	Urine	Test for Recurrence
Cytokeratin fragments 21-1	Lung Cancer	Blood	Test for Recurrence
Epidermal growth factor receptor mutation (egfr mutation)	Non-Small Cell Lung Cancer	Tumour	Targeted Therapy
Fibrinogen	Bladder Cancer	Urine	Monitor Progression/Response to Treatment
Human epididymis protein 4 (he4)	Ovarian Cancer	Blood	Monitor Progression/Test for Recurrence
Epidermal growth factor receptor 2 (her2)	Breast Cancer/Gastric Cancer/Oesophageal Cancer	Tumour	Targeted Therapy
Immunoglobulins	Multiple Myeloma/Waldenström Macroglobulinemia	Blood and Urine	Diagnosis/Measurement of Response to Treatment/Test for Recurrence

Biomarker	Cancer type	Found in tissue	Clinical use
Kit gene	Gastrointestinal Stromal Tumour/Mucosal Melanoma	Tumour	Diagnosis/Treatment Determination
Kirsten rat sarcoma viral oncogene homolog (kras) gene	Colorectal Cancer/Non-Small Cell Lung Cancer	Tumour	Targeted Therapy
Lactate dehydrogenase	Germ Cell Tumours	Blood	Stage Assessment/Prognosis/ Measurement of Response to Treatment
Nuclear matrix protein 22	Bladder Cancer	Urine	Measurement of Response to Treatment
Prostate-specific antigen (psa)	Prostate Cancer	Blood	Diagnosis/Measurement of Response to Treatment/Test for Recurrence
Thyroglobulin	Thyroid Cancer	Blood	Measurement of Response to Treatment/ Test for Recurrence
Urokinase plasminogen activator (upa)	Breast Cancer	Tumour	Prognosis/Determination of Treatment

### 2.2.5 Cancer Antigens

Cancer antigen molecules are molecules that can stimulate an immune response from cancer patients. These molecules are useful as cancer indicators for many reasons but one of the primary reasons is the fact that by triggering an immune response they also stimulate the production

of antibodies that specifically target and bind to these antigens<sup>21</sup>. These antibodies are the basis of most existing cancer detecting assays due to their high specificity for binding with their target antigen. By measuring the interactions between antibodies and antigens it is possible to quantify the amount of antigen that is present<sup>38</sup>, and this is why cancer antigens are among the most studied means of detecting cancers.

An important milestone in the development of antigen based cancer detection has been the widespread use of Prostate-Specific Antigen (PSA) testing in the diagnosis and management of prostate cancer. PSA was first identified in the prostate of dogs in 1972 and by 1980 an assay capable of measuring its levels in human blood serum had been developed<sup>39</sup>. Based on the addition of an anti-PSA antibody and an Enzyme-Linked ImmunoSorbent Assay (ELISA) technique, this method found its way into clinical use within several years and has been seen as one of the gold standards exemplifying the success of antigen based detection. However, it should be noted that in recent years the shortcomings of PSA testing have been noted, in that it lacks the degree of specificity expected from modern diagnostic methods<sup>13</sup>.

In 2007 Polanski and Anderson<sup>35</sup> conducted a study identifying 1,261 candidate proteins that appeared to be indicative of cancers in the human body. Many of these indicators were acknowledged to lack specificity, a problem that was similarly noted with PSA testing. This shortcoming could be overcome though, as the sheer number of these proteins means that by quantifying a number of these biomarkers, greater statistical specificity could be achieved for the detection and distinguishing of cancers. This kind of assay, which achieves statistical specificity by measuring multiple biomarkers, is referred to as a “multiplex” assay<sup>40</sup>. In addition, of the 1,261 possible targets a total of 274 were known to occur in the blood plasma lending further credibility to the possibility that an

antigen based multiplex assay could allow for the relatively non-invasive diagnosis of cancers from patient blood samples.

### 2.2.6 Genetic Markers

With the recent developments in rapid, affordable gene sequencing and the astounding progress in the understanding of genetics in the last 20 years a lot of interest has been directed towards the potential for the direct detection of the underlying genetic causes of cancers and, as a result, genetic indicators of the disease. While the theory behind this research had been in place since the discovery of oncogenes in 1979<sup>41</sup>, the high cost of sequencing proved a great impediment to progress. Even though sequencing has now become more affordable, the field of oncogenetics is still in its infancy relative to the study of antigen based immunoassays. It appears, however, to show great promise for application in diagnostics<sup>42</sup>.

One of the most well-known and well-studied oncogenes are the BRCA1/2 genes, which is indicative of a high risk for breast cancer in female patients. The first of these genes (BRCA1) was identified in 1994<sup>36</sup> and they are tumour suppressing genes that are particularly prone to mutation and, as a result, loss of function. By 1999 a relatively simple test for the BRCA1/2 genes had been devised<sup>43</sup>, and in recent years such testing has become relatively affordable. This test is now seeing use for determining the cancer risk in female patients with a family history of breast cancer<sup>44</sup>. In addition, such testing is under investigation as a means to determine the most effective treatment for breast cancer patients, as evidence has been found that cancers testing positive for BRCA mutations are also more responsive to platinum based chemotherapeutic treatments<sup>45</sup>.

It seems likely that in the future the field of oncogenetics could prove revolutionary to cancer diagnosis and treatment, even though it is still in

its early days. Associations like those noted for BRCA mutations have begun to be observed more frequently in recent years, and research into these associations and their use in medicine has intensified<sup>46</sup>. One of the more well-understood cancers, prostate cancer, has become somewhat of a focus for oncogenetics<sup>13</sup>, attempting to further the understanding of the disease built up since the discovery of the PSA protein. Some recent work has produced interesting results, such as a test that uses mutations in 13 genes to predict the prognosis of prostate cancer patients with an impressive amount of accuracy<sup>47</sup>. Despite all this, cancer indicating genes remain the more poorly understood of the types of cancer indicators discussed in this chapter when compared to antigenic biomarkers and this fact should be considered when deciding which offers a more reliable sensor platform.

## 2.3 Detection Methods

### 2.3.1 Quartz Crystal Microbalance (QCM) Biosensors

The Quartz Crystal Microbalance (QCM) is one of the earliest and most studied examples of a label-free sensing system, having been first described as early as 1964 by William H. King<sup>48</sup>. QCM make use of the piezoelectric properties of quartz ( $\text{SiO}_2$ ) crystals, exploiting the fact that they oscillate at high frequencies when an electric current is passed through them, resulting in detectable acoustic vibrations. The frequency of this oscillation is affected by interactions occurring at the surface of the crystal<sup>49</sup>. With the introduction of a detection molecule (as shown in Figure 3) this surface interaction can be enhanced via molecular interactions, increasing the observed dampening and shift of the oscillation frequency of the crystal.

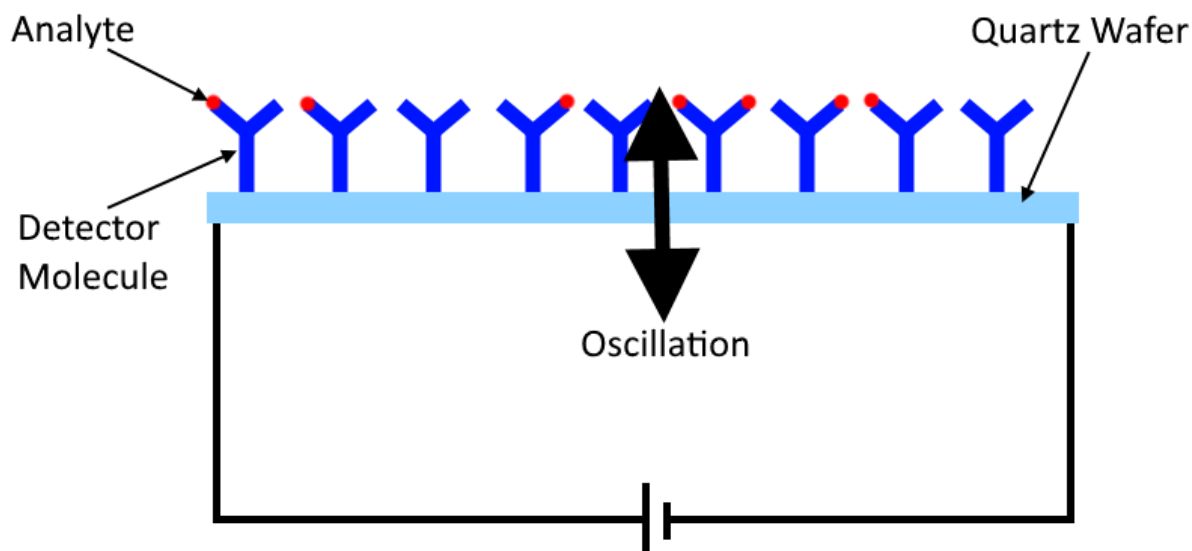


Figure 3. A schematic of a QCM biosensor system using antibodies as detection molecules. As analyte binds to the detection molecules, the mass of the surface increases thus dampening the oscillation and enabling detection of the analyte.

### 2.3.2 Electronic Biosensors

Electronic biosensors can detect analytes using a wide variety of methods but all are based on the same core concept. In each case, detection is achieved by measuring changes in the electronic properties of the sensor (for example, its conductivity) in response to interactions occurring at the surface of the material. Due to the importance of such properties in almost every aspect of modern technology there are many ways to quantify changes in the various electronic properties of a material. However, the most commonly used methods for measuring these changes in sensing applications are chronoamperometry, chronopotentiometry, Cyclic Voltammetry (CV), and Electrochemical Impedance Spectroscopy (EIS)<sup>50</sup>.

Chronoamperometry and chronopotentiometry are among the simpler techniques that can be used in electronic biosensing. During chronoamperometry, the current across the sensing element is measured over time while a constant or square wave potential is applied to it.

Conversely, in the case of chronopotentiometry, the voltage across the sensing element is measured while a constant or square wave current is applied.

Cyclic voltammetry is, to an extent, similar to chronoamperometry but uses a different potential waveform to extract more information from the sensor. In CV, the voltage applied to the sensing element is varied over time in a cycling triangle wave while the resulting current is measured. This results in a graph of current vs voltage with features that offer a wealth of detailed information regarding the chemical equilibria of reactions and interactions taking place at the sensing element<sup>50,51</sup>.

EIS is decidedly more complex than the other techniques discussed herein, but offers the ability to measure all of the major electronic properties in the sensing element at once<sup>50</sup>. This density of data makes it ideal for biosensing applications, increasing accuracy by offering the ability to measure the effect of receptor-analyte interactions on multiple electronic properties in a single test. EIS works by varying the potential across the sensing element in a sinusoidal waveform and measuring the current. The frequency of the waveform potential is then varied across a range and the current at each frequency is recorded resulting in a graph of current vs frequency. Via various mathematical manipulations of this resulting graph (for example the creation of a Nyquist plot, Bode impedance plot, or Kramers-Kronig transform) a wealth of electrochemical data can be obtained for the examination of the interactions occurring at the sensor surface<sup>52</sup>.

One common feature of most electronic biosensor designs is the shape of the electrodes comprising the sensing element. One typically used design is the “Interdigitated Electrodes” sensing element<sup>50,53,54</sup>, comprised of multiple straight, connected, parallel lines for each electrode, interleaved to maximise cathode-anode interaction (as shown in Figure 4a). A variant of the interdigitated electrode that has seen use in some applications is

that of the concentric circle interdigitated electrode<sup>55</sup> (shown in Figure 4b). This design fits slightly more electrode surface into a given area than the standard interdigitated electrode design. An alternative sensor design is the simpler parallel plate electrode design which is often employed with a tightly defined distance between the electrode plates (as shown in Figure 4c).

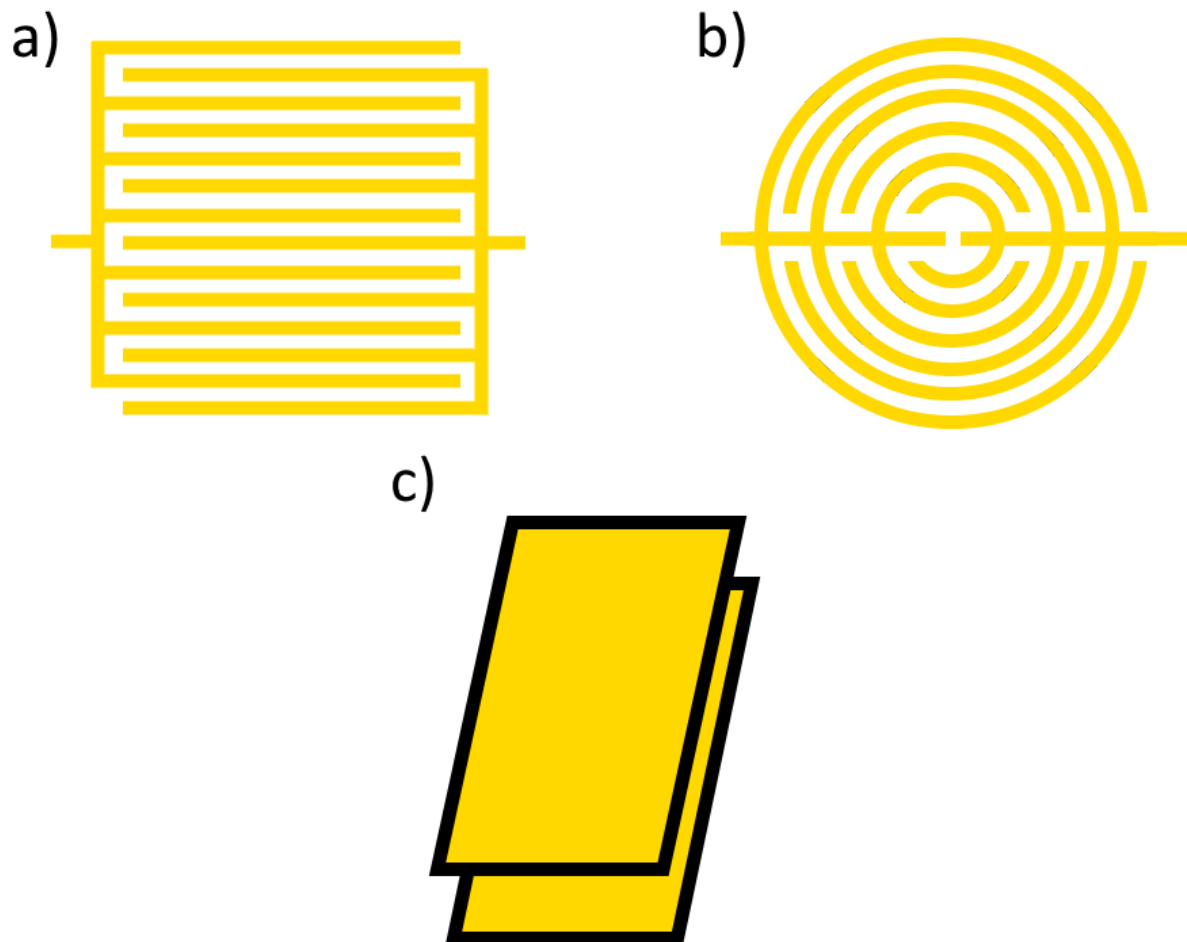


Figure 4. Diagrams of the most commonly used electronic biosensor electrode designs, showing a) interdigitated electrodes, b) concentric circle interdigitated electrodes and c) parallel plate electrodes.

### 2.3.3 Field-Effect Transistor (FET) Biosensors

One possible means of biomarker quantification for a straightforward, robust biosensing platform would be the possibility of indirectly

measuring the shift in electron density of the antibody as it binds to the antigen. It seems reasonable to think that a probable means to achieve this could be by the direct measurement of the effect that such changes in electron density (as illustrated in Figure 5) would have on the immobilisation media chosen for the sensor. By using a semiconductive immobilisation medium, the changes in the dipole moment of the antibody as it binds may interact with the distribution of electrons and electron holes, this influencing the resistivity of the surface.

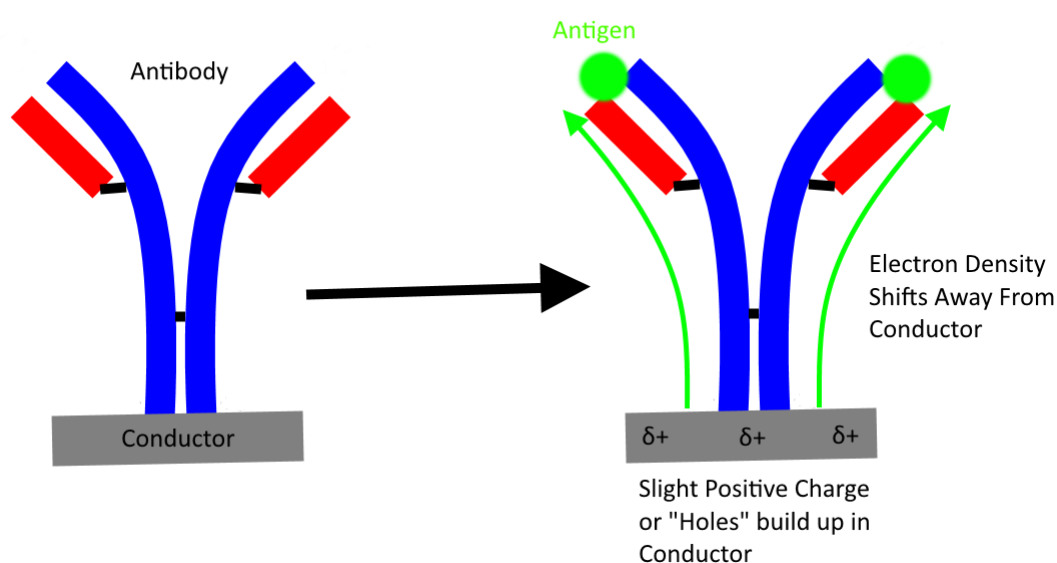


Figure 5. A basic diagram outlining the concept behind the FET detection method. Depending on the polarity of the antigen, the charge on the conductor may increase or decrease, affecting its conductivity.

This idea has been explored in the field of biosensing technology in recent years, and such devices have been termed “Field-Effect Transistors”<sup>56</sup>. Field-effect transistors have been developed for a variety of applications including for use as biosensors<sup>56</sup>, as pH sensing platforms<sup>54</sup> and as more generalised ion detecting sensors<sup>57</sup>. Such pH measuring and ion quantifying FETs are referred to collectively as “Ion Sensitive Field-Effect Transistors”, or ISFETs.

The detection characteristics of FETs are tailored by changing the ligand molecule attached to the surface. Fundamentally, by appropriately selecting a ligand that undergoes a change in polarity or dipole moment when subjected to the target conditions, the extent of those conditions can be measured by the FET platform. If we examine the explanatory diagram in Figure 5 the ligand shown is an antibody (thus allowing for the detection of the target antigen), but for other systems this antibody may be replaced with a different molecule. For example, in the pH sensitive ISFET developed by Gou et al.<sup>54</sup> the semiconductive single-walled carbon nanotubes in the FET system are coated with (but not covalently bonded to) poly(aminoanthracene), a polymer which accepts protons becoming more positively charged in more acidic environments. Furthermore, with regards to biosensors, such biologically active platforms are not limited to the scope of antibodies, with Wang et al.<sup>58</sup> having published a paper that uses a surface functionalized with aptamers (which will be discussed further in Chapter 2.5.3) to detect dehydro-epi-androsterone sulfate (DHEA-S), an important metabolic biomarker in the field of endocrinology. However, throughout all these differing ligands and applications the core theory remains constant, that the change in the dipole moment of the ligand influences the conductive properties of the semiconductor on which it is immobilised.

Often, the semiconductive surface used in the construction of a field-effect transistor is comprised of single-walled carbon nanotubes<sup>56</sup> or any other kind of nanowire<sup>59</sup>. It seems a logical assumption to think that this technique should use nanowires due to their large surface area enabling many antibodies to be coated and immobilised onto the wire, thus allowing the small effects of these antibody-antigen interactions to have a large cumulative effect along the length of the wire. The use of nanowires also has the advantage of limiting the ability of detection molecules immobilised in the desired orientation from contorting to adopt a flat-on or side-on orientation, as their rigidity would prevent them from twisting

far enough to interact with the nanowire (unlike in the case of a flat surface). Detection molecule in flat-on and side-on orientations reduce the sensitivity of the sensor because in these orientations the sensor surface can block the active site of the detection molecule<sup>60</sup>.

#### 2.3.4 Surface Plasmon Resonance (SPR)

Surface plasmon resonance is a technique whereby reflected electromagnetic waves are used to measure the resonance of the free electrons in a conductive medium<sup>38</sup>. This medium is typically a metallic conductor but can also be a semiconductor<sup>61</sup>. This technique is probably the most common means of label-free quantification in biosensors for many reasons, one of which is that it bears many similarities to the kinds of photospectroscopic techniques that have been established in the fields of chemistry and physics for centuries.

A surface plasmon resonance based sensor works by shining a monochromatic plane-polarised incident ray of infrared light into a prism that is in contact with the functionalised conductive surface (see Figure 6). The ray then reflects off the conductive surface and the angles at which it reflects are measured. The angles at which it does not reflect the incident light are related to the total mass of the material bound to the surface<sup>38</sup>. Thus, in the case of an antibody functionalised surface the angle at which this absorbance band occurs can be used to calculate the amount of antigen present. The use of SPR in biosensing applications is well established and, as a result, is one of the more commonly used methods of detection for label-free biosensor development<sup>61-64</sup>.

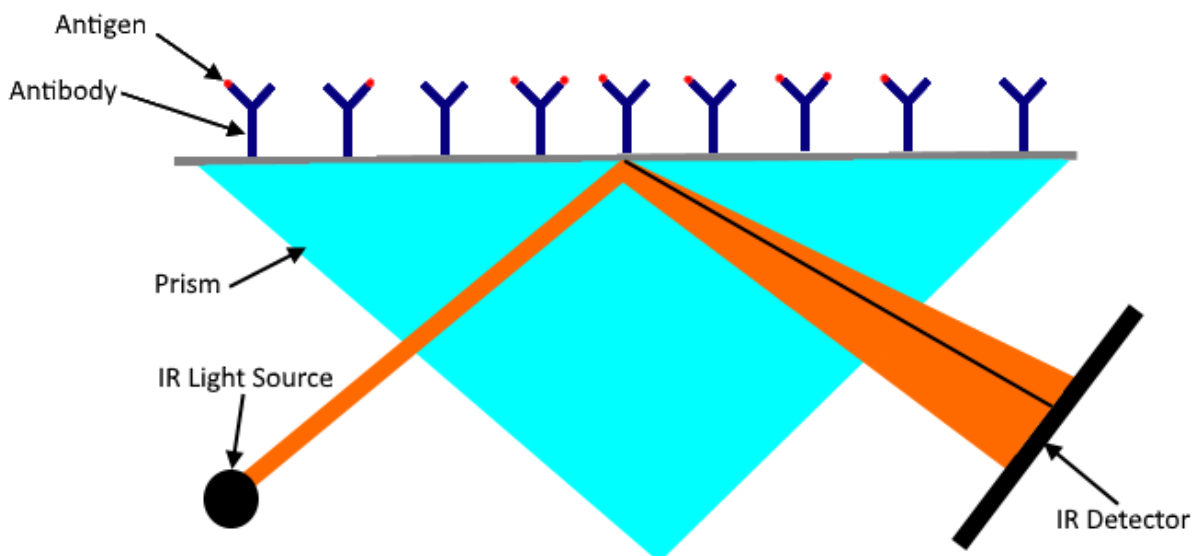


Figure 6. A diagram outlining the underlying principle behind an SPR based immunoassay. Note the darker absorbance band in the reflected light, representing a change in spectral intensity at this angle of reflection.

Finally, it should be noted that it has been observed that the sensitivity of SPR biosensors can be greatly enhanced by the preparation of a “sandwich-style” biosensor<sup>53</sup>. These biosensors work by the addition of nanoparticle derived labels to the sample that bind to the antigen once it has already bound to the sensor surface. While this style of assay does have the disadvantage of not being label-free, there are cases where the enhanced sensitivity it offers could prove extremely beneficial for biosensing applications.

### 2.3.5 Spectroscopic Measurements

As a comparison to techniques such as FET and SPR, the centuries old approach of the determination of the concentration of analytes by photospectroscopic measurements may also be utilized. Depending on the spectral properties of the sensor surface the use of UV/Vis spectroscopy<sup>65</sup>, infrared spectroscopy<sup>66</sup>, Raman spectroscopy<sup>66</sup> or potentially even the relatively unexplored techniques of microwave or radio spectroscopy<sup>67</sup> could provide accurate measurement of the amount

of adsorbed antigen by the well-established method of measuring the shift in spectroscopic features once the antigen and antibody have bound to each other<sup>65</sup>.

### 2.3.6 Electrical Percolation (EP) Biosensors

In addition to the numerous label-free biosensor designs already discussed, one method that has seen a relatively small amount of exploration is the “Electrical Percolation Biosensor”. The only currently published (to the author’s knowledge) design for an electrical percolation (EP) biosensor<sup>56</sup> shares similarities with many FETs on a molecular level, being comprised of carbon nanotubes coated in antibodies. However, its proposed mechanism of action differs somewhat from that of an FET<sup>56</sup>. Current FET biosensors usually make use of a single functionalised carbon nanotube in the form of a “quantum wire”. The referenced EP biosensor, however, makes use of a matrix of multiple functionalised nanotubes. Once the target molecule is introduced the matrix expands as the antibodies bind to the target molecule, decreasing its ability to carry electrical current (See Figure 7)<sup>56</sup>.

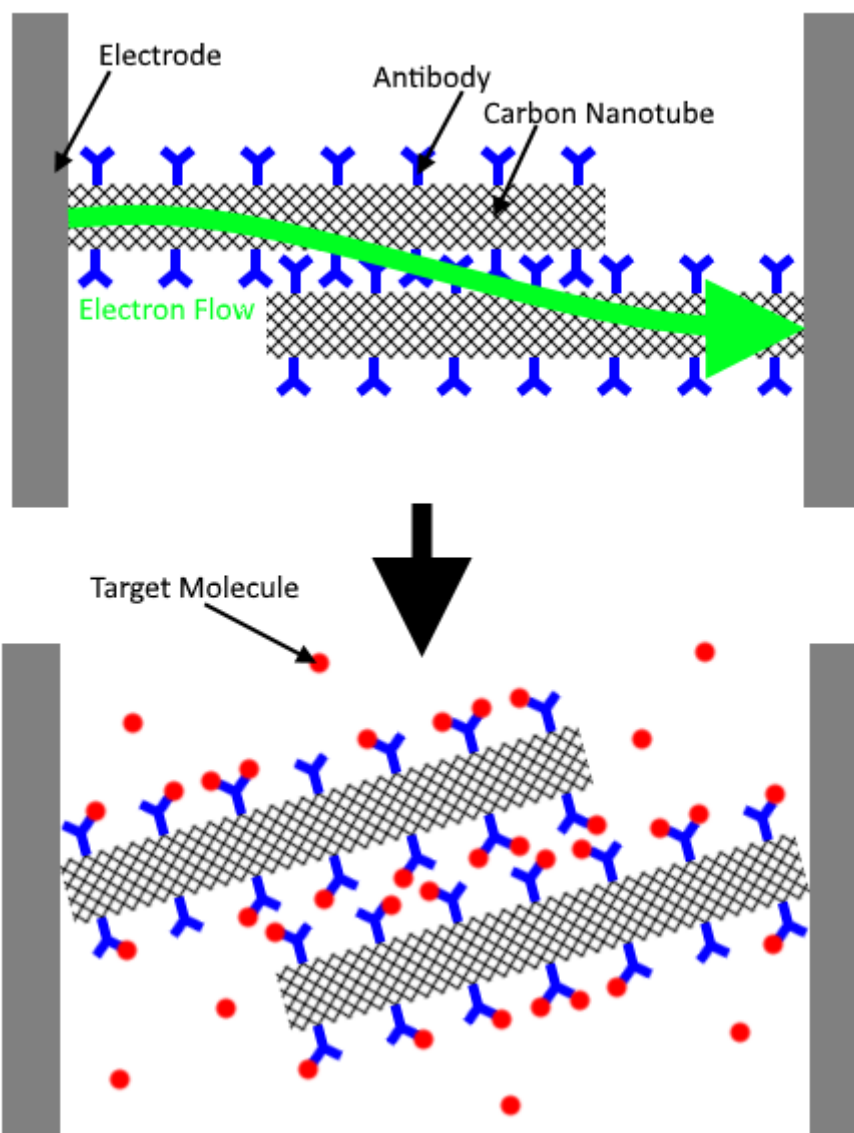


Figure 7. A schematic depicting the proposed mechanism of action of an EP biosensor. It is suggested that the additional steric bulk of the bound target molecule causes the distance between the nanotubes to increase, decreasing the ability of electrons to “percolate” across that gap.

The scarcity of publications utilizing this biosensor design should be noted, and its examination is far behind that of the more established methods above. Despite this, consideration of the EP sensor serves to highlight the potential importance of supramolecular interactions in the design of a biosensing platform.

## 2.4 Design of Functionalised Surfaces for Label-Free Biosensing

The design of label-free biosensing platforms generally relies on the immobilisation of a detection molecule (generally an antibody, DNA probe or aptamer) on a solid surface. This immobilisation most commonly takes one of two forms: covalent capture or affinity capture<sup>38,58</sup>. Covalent capture involves the covalent linkage of a detector to a surface (either directly or via the use of a linker molecule) while affinity capture relies on non-covalent interactions such as hydrogen bonding to immobilise the detector, often using biomolecules such as protein G and protein A for this purpose<sup>68,69</sup> (see Figure 8). While covalent capture can minimise degradation of the biosensor over time (due to the strength of the covalent bond), affinity capture allows for easier orientation specific binding<sup>38,68</sup> which ensures that detection molecules are captured in an orientation allowing for maximum binding efficiency (a task that is often difficult using covalent capture). As such, the selection of a suitable capture technique depends largely on the intended application of the biosensor.

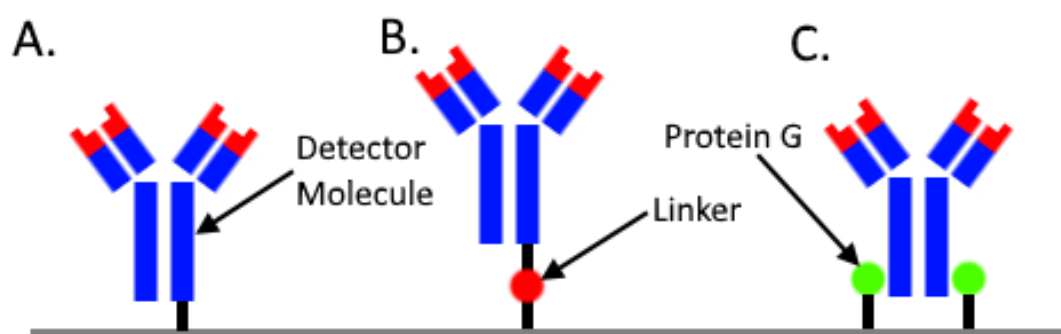


Figure 8. Illustration of the major methods of protein immobilisation in label-free biosensor development: A) direct covalent capture, which is only possible with suitably reactive surfaces; B) covalent capture via a linker, allowing the

linkage of detectors and surfaces unsuitable for method A; C) an example of an affinity capture method (in this case, using Protein G to immobilise an antibody).

## 2.5 Detection Molecules

### 2.5.1 Antibodies

The most studied and most reliable means for the quantification of cancer biomarkers is based on the interactions between antibodies and antigens. Antibodies are proteins produced by the immune system that bind to specific molecules. The molecules that they bind to are termed “antigens” and these antigens are usually the product of a disease state<sup>21</sup>. In the case of cancer, these antigens are usually proteins that are upregulated (meaning they trigger their production in greater amounts) by the cancer disease state or modified proteins resulting from oncogenetic mutations<sup>35</sup>.

Antibodies (also known as immunoglobulins) all have a unique binding region that targets their antigen but the rest of the protein generally has a distinctive Y-shape or some variation thereof<sup>21</sup>. They are classified into isotypes of immunoglobulins<sup>70</sup> (written as Ig for short), these are IgG, IgE, IgD, non-secretory IgA, secretory IgA and IgM. While IgG, IgE, IgD and non-secretory IgA all share the simpler Y-shape of the monomeric immunoglobulins, secretory IgA is dimeric (appearing as two Y-shapes end-to-end) and IgM is pentameric (appearing as five Y-shapes arranged as the points of a five-pointed star, see Figure 9). The most common isotype of antibody is the IgG isotype<sup>71</sup>, it has the highest affinity for its antigens<sup>70</sup> and, as a result, most antibodies commonly used in assays belong to this isotype.

The specific interaction of the protein and the antigen occurs at the top of the upwards pointing arms of the Y-shape, and these regions can be

produced in isolation from the rest of the molecule<sup>72</sup>. These fragments are known as Fab fragments, and see some use in immunoassay development as some of their properties (such as decreased molecular mass and volume) can sometimes prove advantageous<sup>72</sup>. In most cases however, the whole antibody is used simply because it is generally a significantly cheaper alternative.

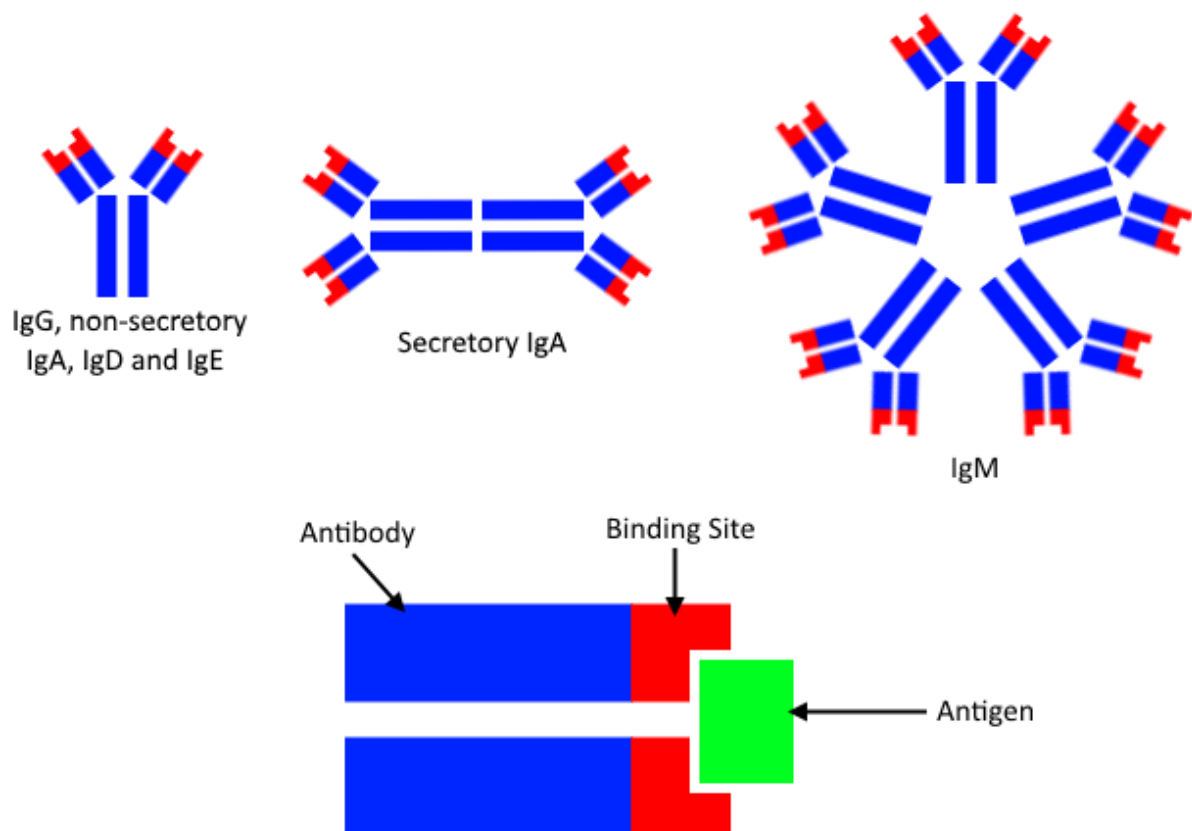


Figure 9. Schematic depicting the appearance of the immunoglobulin isotypes, as well as the orientation in which an antibody binding site binds to an antigen. When the binding site is separated from the rest of the antibody it is usually referred to as a Fab fragment.

A reusable antibody based assay requires the “immobilisation” of an antibody, i.e. the bonding of it to a surface to ensure that the antibody required for testing is not removed by the testing process. There are a

great variety of ways to do this including covalent bonding, adsorption and the use of a protein linker<sup>68</sup>. Some more complex methods use combinations of numerous biomolecules to ensure the proper, upright orientation of the antibodies when they are bonded<sup>73</sup>. However, in most cases this is not entirely necessary and the simplest, most robust way to immobilise an antibody onto a surface is through covalent bonding, usually via epoxidation of the surface<sup>74</sup>.

While many immobilised antibody based immunoassays have been developed (such as the now commonplace Enzyme-Linked ImmunoSorbent Assay or “ELISA” platform, for example the commercially available Vironostika® brand marketed by Biomérieux Diagnostics<sup>75</sup>), few are reusable and almost all require the use of a “label”, which is an added molecule intended to aid in the detection of the antibody-antigen interaction. A reusable, label-free assay would offer the advantage of a far cheaper, more efficient assay option. As a result of this, the detection methods for immunoassays discussed below are aimed towards the possible development of such a system.

### 2.5.2 DNA Probes

An alternative to the detection of cancers via antibody antigen interactions is the possibility of detection by interactions between genes and complimentary DNA strands. These detectors are based on similar principles to the antigen and antibody based sensors described above but rather than relying on amino acid based interactions they rely on the interactions of single stranded DNA on the sensor surface forming double stranded DNA with loose DNA fragments from the sample. Such biosensors have been investigated extensively using SPR based detection<sup>64</sup> in particular. Complementary DNA interaction based sensors would offer the possibility of detecting the causes of a cancer at their source, with a high sensitivity and selectivity but suffer from the disadvantage that samples used for this technique require several hours

of preparation via PCR<sup>64</sup>. The new DNA amplification technique of LAMP<sup>76</sup> could potentially replace PCR in this application, but LAMP has the drawback that it can only be used effectively on specific DNA sequences, thus limiting the scope of a LAMP assisted DNA biosensor significantly. These drawbacks mean that, currently, DNA detection based biosensors remain somewhat less attractive for clinical applications than antibody based sensors.

### 2.5.3 Nucleic Acid Aptamers

Aptamers are oligonucleotides (and sometimes polypeptides) with the ability to bind to target molecules with a high degree of specificity<sup>77</sup>. For the purposes of this discussion, the focus will be limited to nucleic acid aptamers because they are more commonly used in biosensors<sup>78</sup>. Despite their classification as nucleic acids, the mechanism by which aptamers function is more akin to that of antibodies than DNA probes. Like antibodies, they bind to targets as a result of how their tertiary structure orients their functional groups and the key distinction between antibodies and nucleic acid aptamers is that the aptamers are polypeptides. As a result of this similarity, aptamers are already being investigated for a variety of clinical applications<sup>79,80</sup>. As such, aptamers can often be applied to fulfil many of the same roles in biosensors that antibodies can. With regards to research into label free biosensors, aptamers have been applied to both SPR based platforms<sup>81</sup> and FET based platforms<sup>58,82</sup> with the observed results being comparable to those observed from antibodies, further highlighting the similarities between these classes of biomolecules.

Aptamers have, so far, not seen the same widespread clinical use that monoclonal antibodies have enjoyed. There appear to be no definitive reasons for this other than the fact that antibodies have been around longer, and therefore, one might speculate that the incentive to develop aptamer based technologies was small because this niche had already

been filled. A number of reviews have been published recently that have begun to argue that aptamers offer several key advantages over antibodies that have become more evident as the necessary technologies have matured<sup>78,79,83</sup>. These advantages include greater performance in sensors (selectivity, affinity, etc.), more stability, more easily manipulated chemistries and (in the case of their use as drugs) greater bioavailability<sup>78,79,83</sup>. In addition, the use of specialised aptamer development techniques such as “Systematic Evolution of Ligands by EXponential enrichment” (SELEX) allow for the rapid, automated development of new aptamers for specific targets in a fraction of the time required to develop a new antibody<sup>84,85</sup>. Finally, because aptamers are comprised of relatively short ssRNA and ssDNA strands rather than large polypeptides they are usually cheaper to mass produce than their antibody counterparts<sup>80</sup>. For these reasons, the study of aptamers has seen significant increase in recent years, see Figure 10.

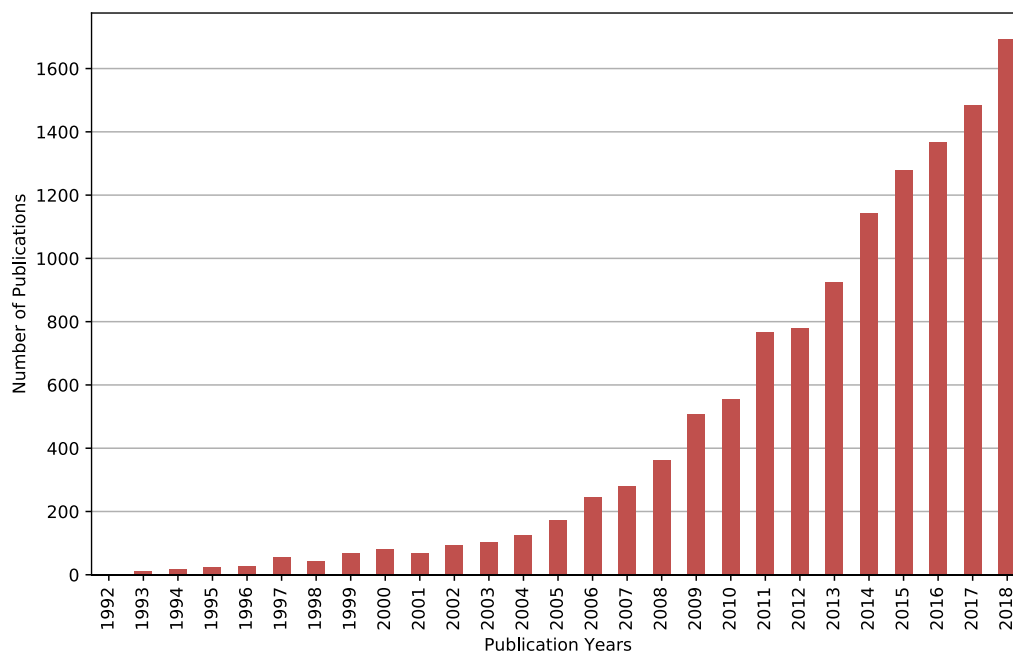


Figure 10. A chart compiled using data from the Web of Science “Search Results Analysis” function. This chart shows the number of papers citing the keyword

“aptamer” every year since their first mention. It is clear from this chart that interest in aptamers has grown near exponentially in recent years.

## 2.6 Sensor Surfaces

Due to the prevalence of SPR, electronic and FET based biosensors sensor surfaces used in the development of label-free biosensors are quite often conductive or semiconductive in nature<sup>58,61,64</sup>. As such, many sensors tend to be based on gold due to its high conductivity and the ease with which it can be covalently bonded to thiols<sup>81</sup>. However, there are many alternative possibilities to consider for different applications and these will be discussed below.

In the development of SPR based biosensors research has begun to move away from the use of planar gold film in favour of nanoengineered materials. Some more recent designs have incorporated the use of gold nanorods and gold nanodots<sup>63</sup> instead, attempting to increase the sensitivity of SPR assays by increasing the surface area of the sensor surface. Similarly, attempts have been made to develop nanoimprinting methods that would allow for the enhancement of SPR sensor surface area<sup>86</sup>. Gold, however, is not the only metal to have been explored for use in SPR based biosensors, with alternatives such as chromium plated silver also seeing use<sup>87</sup>.

Unsurprisingly, electronic biosensor development has advanced in much the same direction as SPR biosensors by favouring the use nanostructured materials, presumably also to maximise the surface area available on which sensor-analyte interactions can occur. In another parallel to the development of SPR biosensors, many electronic biosensors have continued to make extensive use of gold as their sensor surface<sup>50</sup> due to its favourable electronic properties and ease of functionalisation<sup>88</sup>. Despite the ubiquity of nanostructured gold based electrode designs within this field, there has also been a large amount of research into

alternative materials that are suitable to be used as sensor surfaces in electrochemical biosensors such as conductive polymers<sup>89</sup> (e.g. polypyrrole) or nanocomposite materials<sup>90</sup>. When compared with gold nanostructure based sensors the more common alternatives generally offer less sensitivity<sup>91</sup> but have the advantage of being significantly cheaper to manufacture.

While SPR based and electronic sensors are mostly confined to the use of conductive materials as a sensor surface, FET biosensors rely on the use of semiconductors. Due to their importance to the modern electronics industry new semiconductive materials are constantly under development offering a range of potential material to be explored for use in FET biosensors. While most of the existing FET systems in the literature appear to be based on the use of quantum wires, a number of more recent papers appear to have shifted towards the use of a graphene based quantum well<sup>58,82</sup>. This kind of quantum well system has the advantage of being easier to prepare than a system based on quantum wires but suffers from the disadvantage that the monolayer graphene currently used in their construction is currently quite expensive to produce.

As a result of the problems associated with monolayer graphene based FET biosensors a number of alternative semiconductors have been investigated. Traditionally, silicon semiconductors have dominated the field of electronics and as a result silicon has been explored as a potentially suitable material. Similar to carbon nanotubes, a system based on silicon quantum wires has been demonstrated to give the desired effect<sup>59</sup> and a silicon wafer based FET biosensor has, in fact, been designed recently<sup>92</sup>, making use of a molybdenum disulphide coating to affinity capture DNA probes on its surface.

Other materials that have been explored as alternatives are semiconductive and conductive polymers such as polyaniline<sup>93,94</sup> and polypyrrole<sup>93</sup>. These materials have the significant advantage of being

extremely cheap relative to other materials studied. Another conducting polymer that has seen extensive application in other biomedical devices<sup>95</sup> but is relatively understudied as a polymer for use in FET biosensors is poly(3,4-ethylenedioxythiophene)<sup>96</sup> (often referred to as PEDOT). These semiconductive polymers have all been shown to be applicable in FET biosensors and have the significant advantage of generally being cheaper than other gold based and nanoparticle based alternatives currently available.

## 2.7 Nanostructure Fabrication Techniques

### 2.7.1 Chemical Deposition

Chemical based methods for nanostructure deposition usually rely on metal ion based redox reactions, growing the desired nanostructures by reducing metal ions out of solution<sup>97-99</sup>. Often this is achieved via electrochemical means, using the deposition substrate as an electrode in a circuit passed through an electrolytic cell containing ionic species of the desired metal<sup>97</sup>. It is also possible to deposit structures with different morphologies using a chemical reduction method, such as reaction with a lewis base<sup>98</sup>. Due to factors discussed in Section 2.6, nanostructures intended for biosensing applications would most often be comprised of gold. While chemical deposition of gold is possible, it is often deposited from a chloroauric acid solution<sup>99</sup>. The preparation of chloroauric acid involves the dissolution of gold in the superacid "Aqua Regia", a reagent that is extremely damaging to the environment and which raises major safety concerns for handling. As a result, chemical deposition based biosensing platforms would be quite difficult to manufacture on a large scale without either implementing major measures to ensure personal and environmental safety.

## 2.7.2 Nanoimprinting and Nanolithography

Nanoimprinting and nanolithography are examples of subtractive methods of nanostructure fabrication. Perhaps the simplest of these methods, nanoimprinting creates nanostructures through the use of a mechanical mold<sup>100</sup>. Commonly, nanoimprinting involves placing this mold in UV-initiated polymer resin and using a UV lamp to cure this resin in the shape of the pattern on the mold<sup>101</sup> (Figure 11). While this technique has the advantage of being easily scalable and relatively inexpensive it does, however, suffer from the drawback of being largely limited to use in the fabrication of nanostructured polymers making it somewhat of a niche technology in the field of biosensor research.

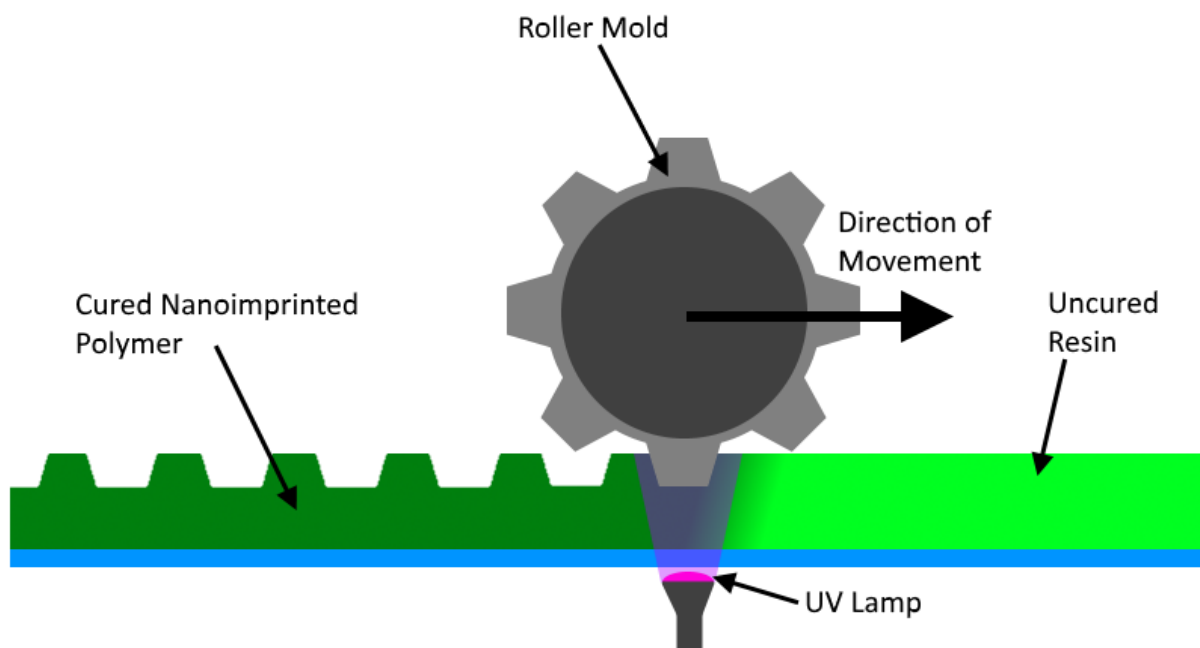


Figure 11. A diagram of a simple roller-based nanoimprinting setup. This kind of continuous roller nanimprinting method readily allows for the mass production of nanoimprinted polymeric materials.

Nanolithography is the use of photolithography in the preparation of nanoscale structures. Photolithography is a technique whereby a pattern is etched into a substrate surface by the creation of a protective “resist” that leaves the desired pattern exposed followed by the chemical

destruction of the exposed substrate<sup>102</sup>. This resist is usually prepared by photocuring, using opaque regions on a transparent sheet to prevent curing in the pattern desired for the etching phase<sup>102</sup>. During the nanolithography process (Figure 12), the surface of the wafer is first oxidized, producing a thin layer of silicon dioxide. Then, the wafer is coated with a UV curable liquid photoresist before a glass plate with a pattern is used to cure the photoresist. The unexposed, still liquid photoresist is then washed away with a developer, leaving a solid resist coating. The exposed silicon dioxide is then etched away using an ammonium fluoride/hydrofluoric acid solution. Finally, the photoresist is removed using sulphuric acid, leaving an open microscale channel.

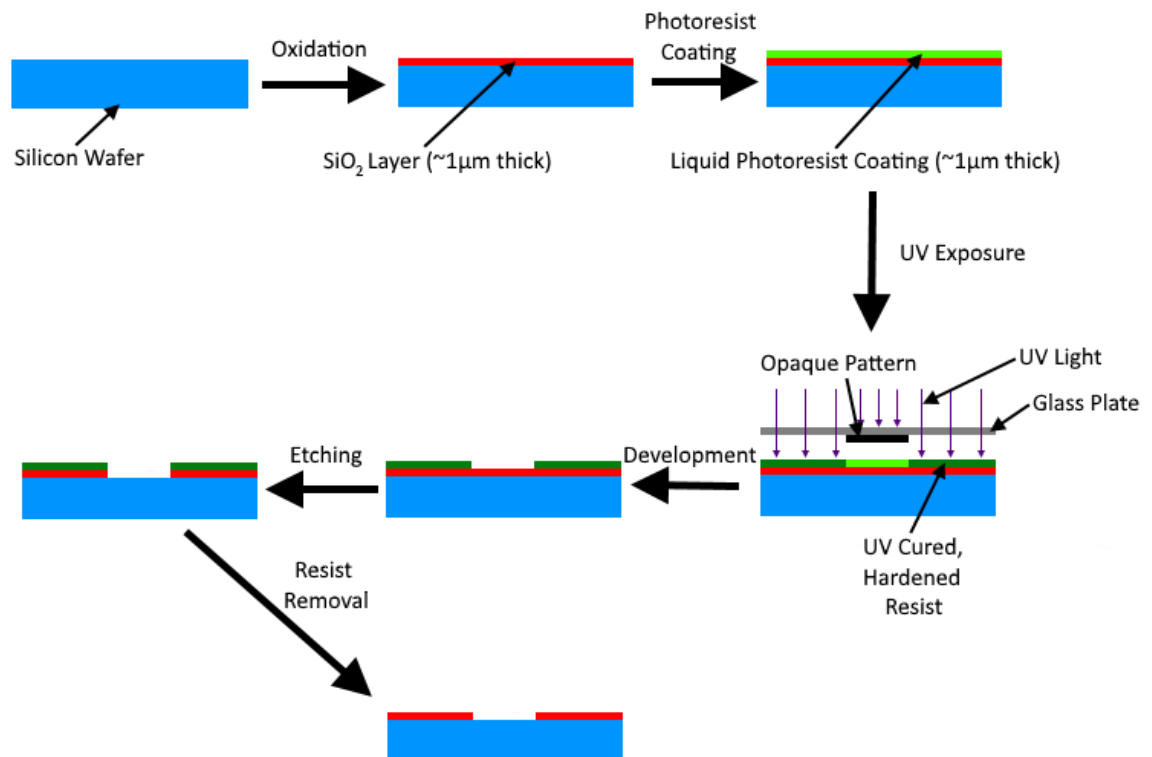


Figure 12. The process of photolithographic etching of silicon wafers. This process is used in microprocessor manufacturing<sup>102</sup>.

### 2.7.3 Laser-Based Deposition

Laser-based deposition techniques are attractive options for the fabrication of nanostructured surfaces due to their environmental

friendliness and avoidance of the use of dangerous reagents. These techniques generally rely on the condensation of nanostructures from an ablation plume produced by a laser pulse<sup>103,104</sup>. The most extensively studied laser-based deposition technique is Pulsed Laser Deposition (PLD)<sup>103,105</sup> (Figure 13a). This technique allows for the creation of highly homogenous nanostructure films with very controllable morphologies and as a result this technique has received a lot of interest in the research community. However, it also is a technique that must be performed in an extremely low-pressure vacuum environment and can take several hours to deposit a reasonably thick nanoparticle film. This makes the process of PLD difficult to scale-up to mass scale production. In response to this barrier to the industrial scale-up of PLD, a number of atmospheric equivalents have been developed with the one that has attracted the most interest being Laser-Induced Forward Transfer (LIFT)<sup>106,107</sup> (Figure 13b). LIFT makes use of lasers with higher pulse frequencies to ablate a donor film forward onto the desired deposition substrate. This technique has the benefit of being able to be performed in atmospheric conditions (unlike conventional PLD) and in a fraction of the time (often minutes or seconds). The drawback of LIFT is that the shorter pulse width “femtosecond” lasers generally used in this technique are comparatively more expensive than the more common nanosecond and picosecond lasers used in conventional PLD.

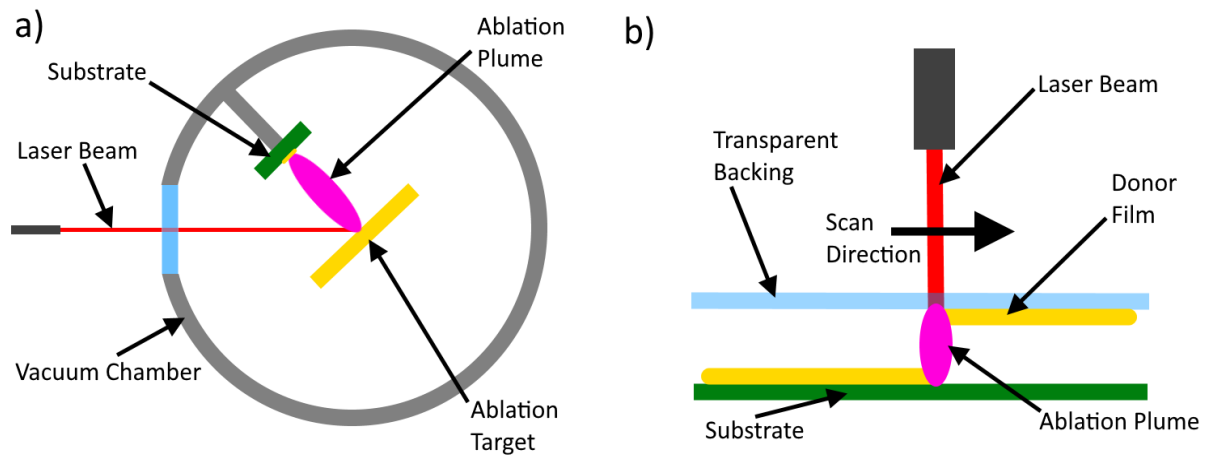


Figure 13. A diagram of: a) the conventional PLD technique, the vacuum chamber pictured could be evacuated to a pressure as low as  $10^{-5}$  Torr<sup>103</sup>; and b) the LIFT process, the laser beam scans from left to right ablating the donor film, depositing it in a nanostructured format on the substrate.

### 2.7.3 Dewetting

Contrasting with section 2.7.2 above, there are other laser-assisted nanostructure fabrication methods that are not deposition based. Of these, one of the most widely used is the direct laser irradiation of metal thin films on a substrate in a process known as dewetting<sup>108-110</sup>. In the dewetting process a thin metal film is rapidly melted, resolidifying into a nanostructure surface. Because the dewetting technique is able to be performed in atmosphere and without the necessity of a femtosecond laser this technique has been widely studied and as a result is quite well understood. As a result, this technique can offer a high degree of morphological control when compared with other methodologies<sup>111</sup>. However, this technique is of course not without its disadvantages. As the process requires rapid heating/cooling of the metal film it therefore requires that the film be placed on a thin substrate with a maximum thickness of several hundred nanometers and a high melting point<sup>108</sup>. For this reason, some of the most commonly used substrates are inexpensive wafers of Si and SiO<sub>2</sub><sup>108-110</sup> although many versions of the process

absolutely require the use of far more expensive materials such as c-plane sapphire<sup>112</sup>.

## 2.8 Nanoparticle Colloids

In the fabrication and functionalisation of nanostructured surfaces nanoparticle colloids are often used as a readily available source of nanostructured material<sup>53,113</sup>. A colloid is a dispersed suspension of particles with a diameter of less than 500nm<sup>114</sup>. Generally, these colloids are aqueous and there are many methods for their preparation. Depending on the method of production, nanoparticles may be functionalised (with bound ligands on their surface) or unfunctionalized nanoparticles (referred to as “bare” nanoparticles) may be synthesised. In addition to this classification, colloids are also classified as either “lyophilic” (meaning their particles prefer to stay dispersed in their solvent) or “lyophobic” (meaning their particles prefer not to stay dispersed in their solvent)<sup>114</sup>. Lyophobic mixtures will only remain stable for a certain amount of time before their particles begin to aggregate and crash out of the colloid and for this reason lyophobic colloids are often “stabilised” by functionalising their particles with a molecule that increases their affinity for the solvent<sup>114</sup>. The primary methods for metal nanoparticle colloid preparation will be discussed in this section.

### 2.8.1 Chemical Reduction: Monophasic Reduction Reactions

The most common way to synthesise metal nanoparticles (and thus the most important to discuss) is the reduction of a solution of a high oxidation-state reagent containing the desired metal. By reducing the metal ions in solution and controlling the conditions of the reaction particles of various sizes and shapes can be produced. By introducing a “capping agent” to the reaction (a molecule that binds to the produced

particles), the rate of particle growth can be inhibited by steric hindrance. Perhaps the earliest example of such a chemical reduction synthesis method is the “Turkevich Method”, wherein hot chloroauric acid solution ( $\text{HAuCl}_4$ , a solution of gold in aqua regia) is reduced by the addition of sodium citrate ( $\text{Na}_3\text{C}_6\text{H}_5\text{O}_7$ ) yielding a nanoparticle colloid with particle sizes ranging from 10-20nm<sup>88,115,116</sup> (Figure 14). In this method, sodium citrate serves as both the reducing agent and the capping agent for the reaction, making it a relatively simple example of a chemical reduction based nanoparticle synthesis method. The citrate ligands left on the nanoparticle also serve to stabilise the colloid, resulting in a lyophilic dispersion.

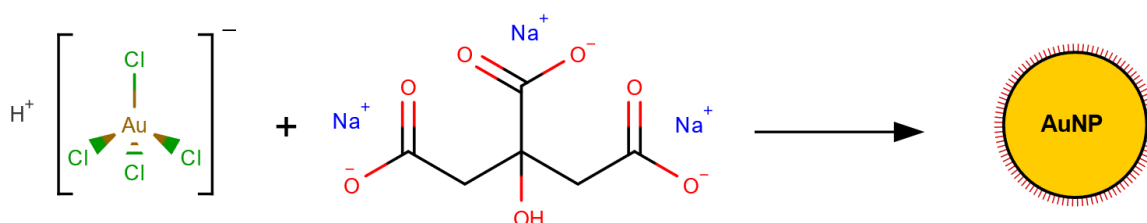


Figure 14. A chemical equation schema outlining the Turkevich Method of nanoparticle synthesis (resulting in a nanoparticle coated with citrate ligands). This process is currently one of the more common methods of nanoparticle production.

This method was later refined further to allow for a degree of particle size control in the 15-150nm range in what is known as the “Turkevich-Frens Method”. This was achieved by varying the stoichiometric of the original Turkevich reaction, allowing for particle size control by changing the chloroauric acid to citrate ratio<sup>117</sup>.

While the redox chemistry of the Turkevich method is quite straightforward, the exact mechanism of the reaction has been a subject of debate since its initial discovery. Early research by LaMer to elucidate the specifics of the mechanism of this reaction concluded that the

process appeared to be described well by the application of Classical Nucleation Theory (CNT) to nanoparticle growth, a variant of nucleation referred to as “burst nucleation”<sup>118-120</sup> (Figure 15a). In a nucleation based growth model, the process first begins with primary nucleation (wherein nucleation centres spontaneously form throughout the solution) followed by secondary nucleation (wherein the unstable species around the nucleation centre react with it thus causing it to grow)<sup>114</sup>. However, it was later found that the kinetics of the Turkevich reaction were inexplicable within the framework of the LaMer model<sup>118,121</sup>. As an alternative to CNT, Reiss proposed a “Growth by Diffusion” model in 1951<sup>122</sup>. In the growth by diffusion model, reduced atoms diffuse throughout the reaction medium via Brownian motion and only become part of a particle once they move within a certain distance of an existing particle<sup>122,123</sup> (Figure 15b). Although the growth by diffusion model appeared to explain some of the discrepancies in the CNT model, its prediction of monodispersed particle size was clearly only true in niche cases, leaving many questions regarding the reaction kinetics. A number of competing extensions to the LaMer model were developed, such as (for example) the model proposed by Chow et al in which it was proposed that the reaction was better described by the inclusion of a reversible aggregation/deaggregation reaction for the particles during their growth by nucleation<sup>124</sup> (Figure 15c). In addition to aggregation/deaggregation models such as the Chow model, several models proposed that “Ostwald ripening” (a precipitation mechanism whereby colloiddally unstable smaller particles aggregate onto more stable larger particles, Figure 15d) was the primary mode of nanoparticle growth rather than nucleation<sup>118,121,125</sup>.

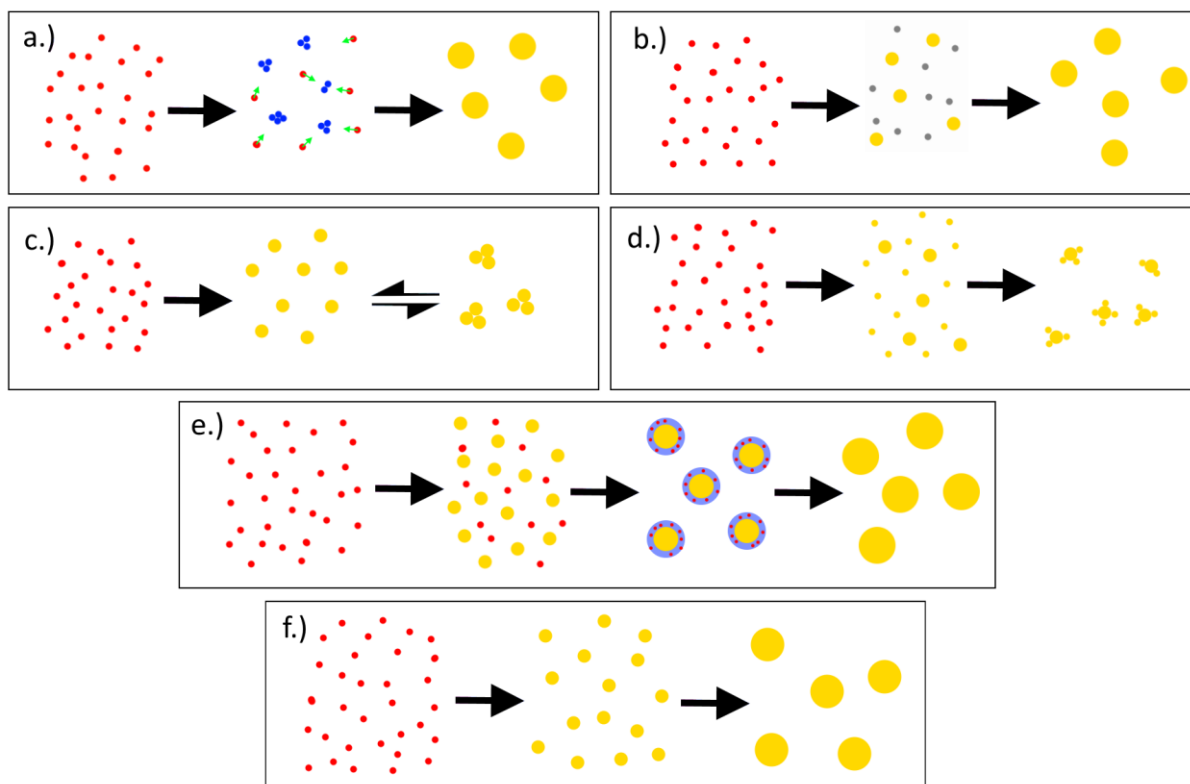


Figure 15. Diagrams of numerous proposed colloidal nanoparticle growth mechanisms where red/blue/grey circles are positive/negative/neutral atoms, gold circles are nanoparticles and green arrows are electrostatic forces on atoms. Each diagram represents: a.) the LaMer burst nucleation model, b.) the Reiss growth by diffusion model, c.) the Chow aggregation model, d.) the Ostwald ripening model, e.) Polte's category 2 model (where light blue represents the EDL) and f.) Polte's category 1 model.

Beginning in 2010, Jörg Polte and colleagues began a series of experiments attempting to discern the true mechanism of the Turkevich reaction. They began their enquiries by using Small-Angle X-Ray Scattering (SAXS), X-ray Absorption Near Edge Structure (XANES) and UV/Vis spectroscopy to examine the reaction kinetics. These experiments strongly suggested that the reaction begins with a rapid nucleation step and a competing coalescence or aggregation step of some kind<sup>126</sup>, that it proceeds according to a 4 step process<sup>127</sup> and that the 4<sup>th</sup> step of this process is not a result of aggregation<sup>128</sup>. At this early stage, the following reaction steps were proposed:

1. Formation of nanoclusters by burst nucleation
2. Either Coalescence or Ostwald Ripening
3. Diffusion Based Growth
4. Faster growth via an unknown mechanism (speculated to be some form of autocatalytic reduction at nanoparticle surfaces)

Based on these findings, later experiments sought to distinguish between the possible mechanisms of Step 2 and to discern the process underlying Step 4. By examining the formation of silver nanoparticles in glass<sup>129</sup> (which severely hampers the movement of clusters larger than an atom) it was found that the resulting metal nanoclusters were stable and that the reaction kinetics were similar to those expected for the above mechanism. This finding implied that Ostwald ripening was unlikely to be responsible for step 2. Finally, observations made using UV/Vis spectroscopy suggest that step 4 cannot be due to the absorption of gold ions<sup>130</sup>. Although this does leave the exact nature of step 4 elusive, it does very much narrow down the range of possible processes by which it might proceed. Polte also notes that based on the elucidated mechanism thus far (for steps 1-3) the observed changes in colloid colour would not seem to make sense if they were simply based on increases in particle size and that it might thus be speculated that this change is due to dielectric interactions near the particle surface<sup>118</sup>. It is understood that the high density of negative charge in metallic or metalloid nanoparticles attracts positive ions to their surface, giving rise to an Electrostatic Double-Layer (EDL)<sup>131</sup> and based on this idea and the available evidence and observations Polte has hypothesised that as the particles grow during step 3 their electron density begins forming an EDL. As the most readily available positive ions in solution would be (in the case of the Turkevich reaction)  $\text{Au}^{3+}$  ions this causes these ions to build up in high concentration around the particle as it continues to grow by a diffusive growth mechanism. Finally, once step 4 is reached, Polte suggests that the  $\text{Au}^{3+}$  ions in the EDL likely begin to get reduced, causing the particle

to grow at the extremely high rate observed without aggregation or the direct absorption of gold ions<sup>131</sup>. Taking this hypothesis as the best proposed explanation would suggest that the steps of the Turkevich reaction proceed as follows (Figure 15e):

1. Formation of nanoclusters by burst nucleation
2. Coalescence of nanoclusters
3. Diffusion based growth and formation of EDL
4. Reduction of and resulting coalescence of ions in the EDL

With a plausible and well-reasoned hypothetical mechanism for the Turkevich reaction proposed, it then becomes necessary to offer an explanation for the kinetics of the many chemical reduction based reactions that deviate from these “Turkevich-esque” kinetics. For example, the commonly used alternative method of the reduction of chloroauric acid using sodium borohydride ( $\text{NaBH}_4$ ) instead of sodium citrate (as is used in the Turkevich reaction) clearly deviates from the kinetics of the traditional Turkevich reaction. This reaction instead appears to proceed via a far simpler mechanism wherein burst nucleation occurs followed by coalescence similar to steps 1 and 2 of the Turkevich method<sup>131</sup>. Polte refers to this simpler mechanism as a “Category 1” synthesis (Figure 15f), while referring to the Turkevich style mechanism as “Category 2”. The key difference in category 1 syntheses is that during step 1 the reducing agent is used up completely before proceeding to step 2.

Examining the kinetics of these categories it is clear that in a category 1 synthesis the rate of growth via nucleation must exceed the rate of growth due to coalescence, thus creating conditions in which nucleative reduction proceeds to completion before coalescence becomes the dominant mechanism of growth (the point at which it transitions from step 1 to step 2). In contrast, it is evident that as a category 2 synthesis transitions from step 1 to step 2 some reducing agent still remains, giving rise to the conditions allowing for it to eventually resume

nucleative reduction in step 4<sup>131</sup>. Thus, as the rate of aggregation is primarily determined by colloidal stability, it thus stands to reason that this parameter should strongly influence whether a reaction is category 1 or category 2. The other important in this determination is the rate of reduction, which is obviously primarily dependent on the strength of the reducing agent and the redox potential of the oxidised metal species.

Considering the available evidence, these hypotheses offered by Polte et al. appear to offer the most plausible mechanism for the Turkevich reaction and, similarly, the most plausible framework for the understanding of monophasic metal nanoparticle colloid syntheses.

## 2.8.2 Chemical Reduction: Biphasic Reduction Reactions

As the study of nanoparticle colloids has advanced the control of nanoparticle size and colloid dispersity has been a key driver for the development of new synthesis methods. As the development of new synthesis methods continued eventually the benefits of biphasic reactions in colloid synthesis were discovered. The first of these biphasic methods popularised was the “Brust-Schiffrin Method” of synthesis<sup>132</sup>. In the Brust-Schiffrin reaction chloroauric acid is reduced with sodium borohydride similar to a variant of the Turkevich method discussed in Section 2.8.1. However, the Brust-Schiffrin reaction takes place in a biphasic toluene/water solvent and makes use of TetraOctyl Ammonium Bromide (TOAB) and a thioalkane (such as dodecanethiol) as a phase-transfer catalyst and capping agent respectively. Despite its initial similarities to a Turkevich style reaction with a borohydride reducing agent the Brust-Schiffrin reaction has the advantage of being a room temperature reaction resulting instead in the production of very small thiolate functionalised nanoparticles with sizes in the 2-5nm range<sup>88,115</sup>. These advantages of biphasic syntheses are somewhat offset by the disadvantage that purification of a colloid prepared by this method is often more complex than for simpler monophasic equivalents (for example, the Brust-Schiffrin

method results in a colloid that requires Soxhlet extraction for purification).

Despite the usefulness of the Brust-Schiffrin method and its growing importance it remains a somewhat niche method for colloid preparation relative to the ubiquity of monophasic Turkevich style reactions. As such, its exact mechanism is still a subject of great uncertainty and debate<sup>132,133</sup>.

### 2.8.3 Photolysis

Photolysis (that is, the splitting of molecules using photons) offers an interesting alternative to chemical reduction methodologies for the synthesis of nanoparticle colloids. In most photolytic colloid syntheses a solution of a metal complex or salt is dissolved in a solvent and is exposed to a photon source of a specific wavelength. This methodology has been used in the production of a variety of nanoparticles using ultraviolet<sup>134,135</sup>, microwave<sup>136,137</sup> and gamma<sup>134,138</sup> radiation. These methodologies have proven versatile proving capable of producing particles as small as 0.5nm<sup>135</sup> from materials as varied as gold<sup>135</sup>, silver<sup>136,137</sup>, palladium<sup>134</sup>, iron-platinum alloy<sup>135</sup> and iron oxyhydroxide<sup>138</sup>.

Importantly, the mechanisms of these photolysis reactions appear to differ between cases where UV or microwave radiation is used and cases where gamma radiation is used. In UV and microwave photolysis reactions, the dissolved metal species is commonly a metal complex<sup>134-137</sup>, suggesting the photolysis occurs through a simple ligand dissociation reaction wherein the energy is provided by the incident photons. In contrast, gamma photolysis reactions are commonly performed using metal salts<sup>134,138</sup>, suggesting that this type of photolysis occurs via the lysis of water molecules to produce hydroxyl radicals that subsequently reduce the metal ions present<sup>138</sup>. Likely, this difference is primarily due to the differing energies of each type of photon, as microwaves and UV rays are

too low energy to split water atoms while gamma radiation has the energy to achieve this.

#### 2.8.4 Pulsed Laser Ablation in Liquid (PLAL)

Since its discovery there has been growing interest in the development of the Pulsed Laser Ablation in Liquid (PLAL) method as a simple, rapid and environmentally friendly methodology for the production of bare nanoparticle colloids<sup>139,140</sup>. This methodology involves placing a metal sample in a solvent (usually water) and ablating the metal with repeated pulses of an incident laser beam<sup>139-142</sup> (Figure 16).

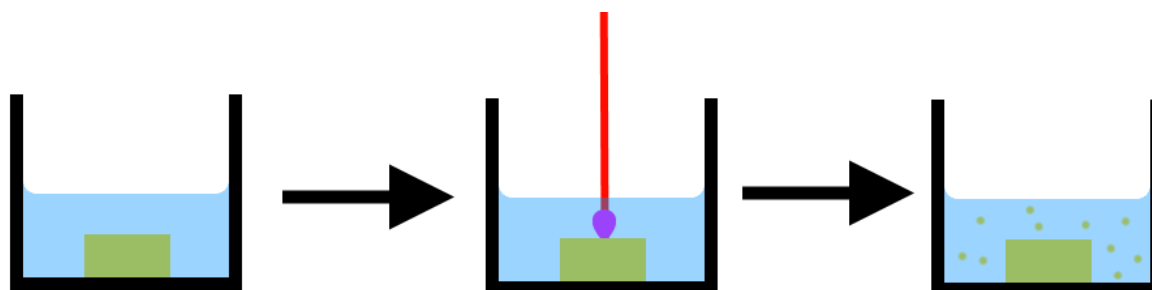


Figure 16. Schematic of the effect of a single laser pulse in the PLAL method. In general use, PLAL makes use of repeated pulses such as this to produce a colloid.

In the mechanism of the PLAL reaction the laser produces a plasma plume at the surface of the metal target, which is subsequently cooled and compressed by the surrounding liquid resulting in the formation of nanoparticles<sup>143,144</sup>. This technique has been proven to be a highly versatile synthetic method, allowing for the facile production of colloids from a wide variety of materials including gold<sup>141,145</sup>, silver<sup>145</sup>, platinum<sup>141</sup>, palladium<sup>142</sup>, carbon<sup>140</sup>, silicon<sup>139</sup>, aluminium<sup>146</sup>, zinc<sup>143</sup> and zinc oxide<sup>143</sup> among many others<sup>146</sup>. The diameter of the resulting particles is also controllable within a range (the size of which dependent on the properties of the specific material) by the introduction of suitable ligands to the liquid<sup>147</sup>, by varying its pH<sup>148</sup> and by varying the fluence of the incident

laser beam<sup>148</sup>. In general it has been found that the pH of the liquid is inversely proportional to the size of the nanoparticles produced and that fluence is directly proportional to particle size.



Figure 17. Photographs of gold nanoparticle (left) and zinc-based (right) aqueous nanoparticle colloids produced using the PLAL method.

The PLAL technique generally produces stable colloids with a high degree of clarity ideal for spectroscopic testing applications (Figure 17). In addition to the versatility and controllability of the PLAL methodology it is also one of the few methods of nanoparticle synthesis that is readily and safely scalable. The technique has been applied in continuous flow multigram nanoparticle production platforms<sup>149</sup> and has even been used in pilot-scale platforms producing particles at a rate of up to 400g/hour<sup>141</sup>. Thus based on this proven scalability and the inexpensive, fast and green nature of the method it seems likely that PLAL will

continue to grow in importance as a nanoparticle production technique over time.

## 2.9 Biomicrofluidics

Microfluidics is the science of developing systems for the control of the flow of liquids in micron-scale channels<sup>150</sup>. The study of microfluidics is often applied to microfluidic chips for the design of novel sensor platforms, separation platforms, preconcentration of analytes and a wide variety of other applications. Microfluidic techniques have seen increased use in recent times due to the many advantages they offer over traditional systems. They generally require less analyte than traditional systems, are more compact and offer greatly enhanced sensitivities. This is largely because the ratio of sample volume to surface area in contact with the sensor is significantly increased on such a small scale<sup>150</sup> (see Figure 18). The term “biomicrofluidics” refers to the application of microfluidics to solve biological problems, most often the use of microfluidics in the development of biological sensors.

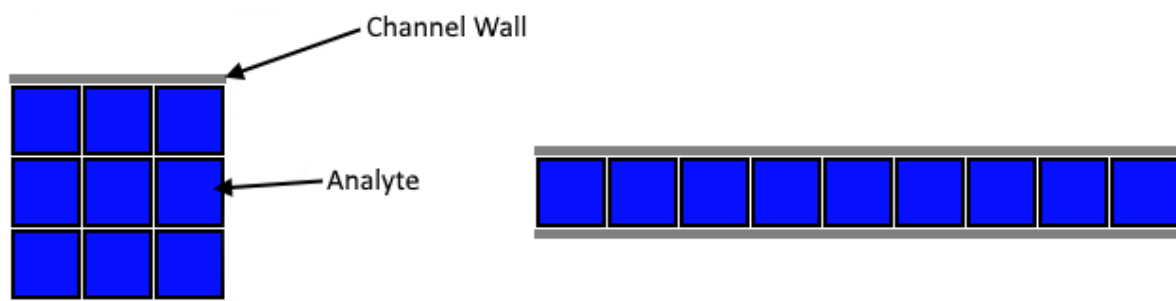


Figure 18. Illustration of the relationship between the dimensions of a channel and the surface area in contact with its contents. Note how the volume in each

case is the same but the smaller channel has greater contacting surface area. This increased surface area presents a significant advantage for biomicrofluidic sensors, as it maximises the interaction between the analyte and the sensor.

Microfluidic platforms are quite often created in the form of a chip<sup>150,151</sup>, and often offer a compact system allowing for the performance of tests normally carried out in a laboratory. Many chips can be placed in sequence or designed with complex architectures performing many functions, leading to the use of the popular term “lab-on-a-chip” to describe them.

While the use of biomicrofluidics in the development of a biosensing platform offer the obvious advantage of allowing increased sensitivity it also may offer other benefits in the form of simplifying sample preparation. One interesting development that occurred recently which may have relevance to this project is the design of microfluidic chips capable of separating blood plasma from cells<sup>152,153</sup>, a process normally performed using the more expensive and time-consuming method of centrifugation. The simpler of these systems<sup>152</sup> is based on crossflow filtration (see Figure 19), which has the advantage that it will not get clogged with repeated use, whereas the other design<sup>153</sup> uses gradual filtration, trading this reusability for a greater separation efficiency.

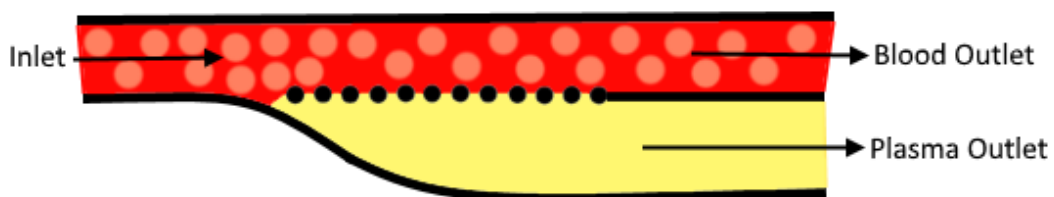


Figure 19. An illustration of Crossflow Filtration separating blood plasma from blood. The gaps in the wall of the channel are small enough to exclude cells from the plasma outlet without excluding proteins and other blood plasma components.

Components such as the filtering apparatus discussed above may be desirable for certain applications but unnecessary for others. Microfluidic components are often expensive and, as a result, some researchers have given consideration to the possibility of modular microfluidic systems<sup>154,155</sup> (Figure 20), allowing for the easy removal, rearrangement and replacement of components in a microfluidic system. Such platforms offer a great degree of versatility with a given set of components, greatly simplifying the design of new experiments and allowing for rapid prototyping.

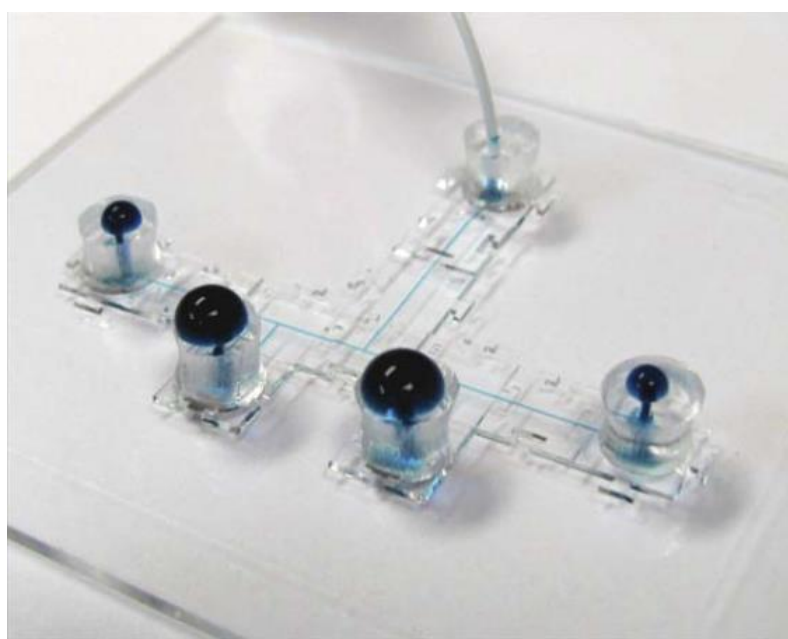


Figure 20. A photograph of a modular microfluidic system developed by Langelier et al. in 2011<sup>155</sup>

In addition, quite a lot of research has been dedicated to reducing the inherent cost of microfluidic systems, with a lot of focus in recent years being placed on the prospect of microfluidic devices fabricated using 3D printing technology<sup>151</sup>. 3D printing is a technique that readily allows for the cheap, fast, precise and automated production of microfluidic devices and components (most commonly made from PDMS, though many other polymers have been used), further increasing the attractiveness of

microfluidic techniques. The applications of 3D printing in microfluidics have ranged from the printing of individual components to the printing of entire chips, allowing for unprecedented ease in the production of new prototypes for biomicrofluidic applications<sup>151</sup>.

### 2.9.1 Fabrication of Microfluidic Systems

The most common method currently used in the fabrication of microscale systems is the well-established technique of lithography. There are a number of variations on lithographic techniques (with the most common being photolithography, discussed in Chapter 2.7.2) and the development of lithography has thus far been primarily driven by developments in integrated circuit technology<sup>102</sup>, fuelling the microprocessor revolution and the ongoing miniaturization of computer technology.

When photolithography is used in the fabrication of microfluidic channels it creates “open channels”, channels with only three walls<sup>150</sup>. Often, open channels are perfectly suitable for microfluidic applications because they still exhibit the capillary action that allows liquids to flow through a microfluidic system. However, there are many applications for which “closed channels” are more desirable, requiring a fourth channel wall (such as in pressurised microfluidic systems). To produce closed channels one common technique is the addition of a “bonding step” to the standard photolithographic procedure, a step in which the etched surface is bonded to another surface to create a closed channel<sup>156</sup>. It should be noted, for the sake of comparison, that this is a step that 3D printing techniques avoid, reducing the likelihood of leakage in 3D printed closed channels relative to their photolithographically produced counterparts<sup>156</sup>.

In addition to standard photolithography, a number of alternative processes have been extensively explored in an attempt to increase the resolution of lithographic techniques. These processes are often referred to as “Next-Generation Lithography” and include X-Ray lithography<sup>102</sup>,

extreme UV lithography<sup>102</sup>, charged particle lithography<sup>102</sup> and nanoimprint lithography<sup>86</sup>.

While discussing the topic of lithography when applied to microfluidics it should also be noted that there has been some interest in exploring the capabilities of the 3D printing method known as stereolithography for the creation of microfluidic channels in recent years<sup>156</sup>. Stereolithography makes use of a scanning laser that is shone into a container of photocurable resin. The laser cures the resin and thus builds up the structure layer-by-layer. Most 3D-printed microfluidic systems (such as those discussed in the previous section) are based on the use of this technique due to its high resolution relative to other 3D printing methods. Of course, while the 3D printing of microfluidic devices has great potential for the future it is by no means commonplace at present.

While photolithography has long been the dominant method for the preparation of microfluidic devices there are currently several techniques being developed with the aim of improving upon it. Techniques such as micromilling<sup>157</sup> (the direct mechanical cutting of a channel using a microscale drill-bit) could make the process more straightforward and applicable to a wider range of materials, while techniques such as stereolithography could make the process cheaper and quicker. Gradually these techniques may become the standard for the fabrication of microfluidic devices, next-generation lithography might allow for the progression towards “nanofluidics”, or perhaps a new technique entirely might arise. At present, however, photolithography remains a widely accepted standard method for microfluidic channel production.

## 2.10 Summary

Based on the information presented thus far, it is clear that the possibility of a low-cost, reusable, label-free biomicrofluidic sensor platform is an extremely attractive one. Although such a platform has so far been difficult to create, significant progress has been made towards this goal in recent years. A variety of relatively new detection methods being developed (such as various conductometric, FET and SPR platforms) and a large amount of research into microfluidic sensors has been reported. Based on this previous work, it seems that exploring the possibility of a microfluidic conductometry based sensor could potentially yield such a platform, achieving the goals of rapid fabrication, low cost and high sensitivity. The development of techniques allowing for low-cost nanofabrication is one possible path to the development of such a platform. Alternatively, the possible use of new organic semiconducting materials combined with conjugated antibodies or aptamers as discussed above may also allow for the easy production of such platforms and thus allow the technique to be readily exploited in a biomicrofluidic sensor.

In addition, although genetically based diagnosis techniques are currently less developed when compared to the more established antibody or aptamer based diagnosis techniques (with some difficulties such as the possible requirement for preconcentration via PCR or LAMP) this is likely not to continue to be the case due to the extensive research effort working towards geneticall based diagnostics. The further maturing of genetic technology can be expected overcome these minor disadvantages in time, causing biosensor development to favour gene based detection techniques. As such the applicability of a biosensor fabrication method to miDNA and miRNA detection should also be examined further, as these

analytes may prove to be the most direct and reliable means of diagnosis in the future.

### 3. Development of Confined Atmospheric Pulsed-Laser Deposition

As discussed in section 2.7, laser based nanostructure deposition techniques have proven to offer many advantages over other deposition methods. Despite this, their widescale use has thus far been hindered by their requirement for the use of expensive equipment such as femtosecond pulse-width laser platforms and extremely low-pressure vacuum chambers. Early in the course of this project, a series of experiments performed hinted at the possibility of an interesting new laser-based method for the deposition of nanostructures. As the project progressed, this discovery was gradually refined into the Confined Atmospheric Pulsed-Laser deposition (CAP) methodology (outlined in Figure 21).

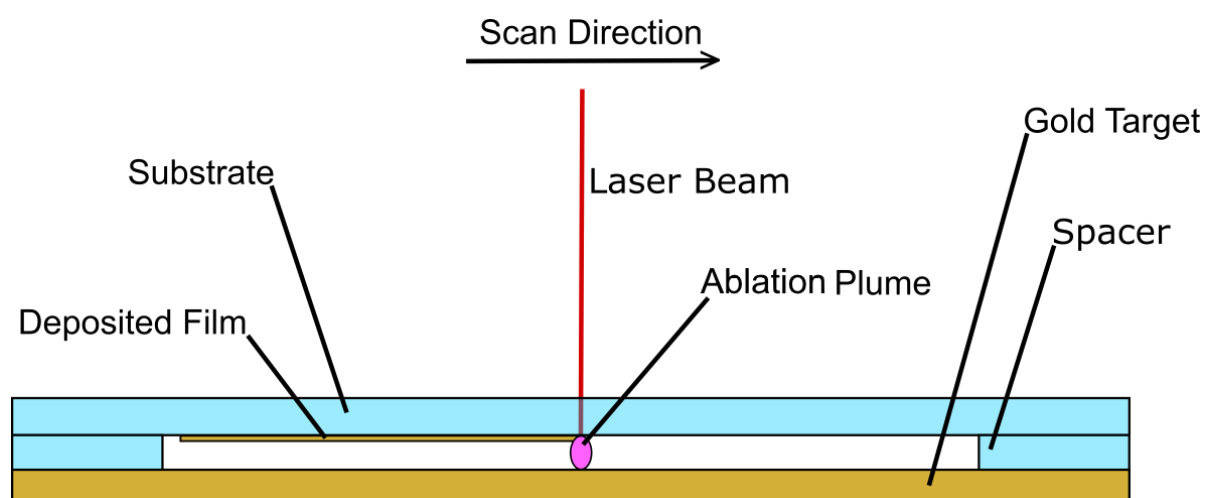


Figure 21. A schematic of the basic CAP methodology, as applied in section 3.2.1.

The initial discovery of the technique was based on an anomalous result during an unrelated polymer ablation test. During laser ablation tests on a Cyclic Olefin Polymer (COP) sheet using a relatively low-cost picosecond pulse-width 1064nm 4W Neodymium-Yttrium Aluminium Garnet (Nd:YAG)

laser at atmospheric pressure it was noted that some samples were left with a grey discolouration on their underside. This discolouration was observed in samples where the target stage was adjusted so that the focal point of the laser was at the surface of the steel backing plate to which the polymer was temporarily affixed for ease of handling. Scanning Electron Microscopy (SEM) images of the discoloured undersides of these sheets found what appeared to be nanoparticles on their surfaces. Energy-Dispersive X-Ray (EDX) spectroscopy of these apparent nanoparticles showed that they were most likely comprised of a steel alloy with a composition comparable to that of the backing plate, suggesting that the laser had ablated the backing plate and deposited these nanoparticles on the COP. Minor visible damage to the surface of the steel backing plate supported this hypothesis, as potential evidence of the material removed by ablation. Following these observations a more deliberate test was conducted to test this hypothesis by attempting to use the above methodology to instead deposit aluminium nanoparticles, by replacing the steel backing plate with an aluminium one. From SEM analysis of the film deposited nanoparticles were observed (Figure 22) and EDX analysis of the resulting structures suggested the structures to be comprised primarily of aluminium oxide, agreeing with the hypothesised mechanism of deposition. Based on these observations, it was decided that this potential deposition method would be worth further investigation as a possible method for the laser based deposition of nanostructures without the disadvantageous need for a more costly and temperamental femtosecond laser or a vacuum chamber as used in conventional Pulsed Laser Deposition (PLD).

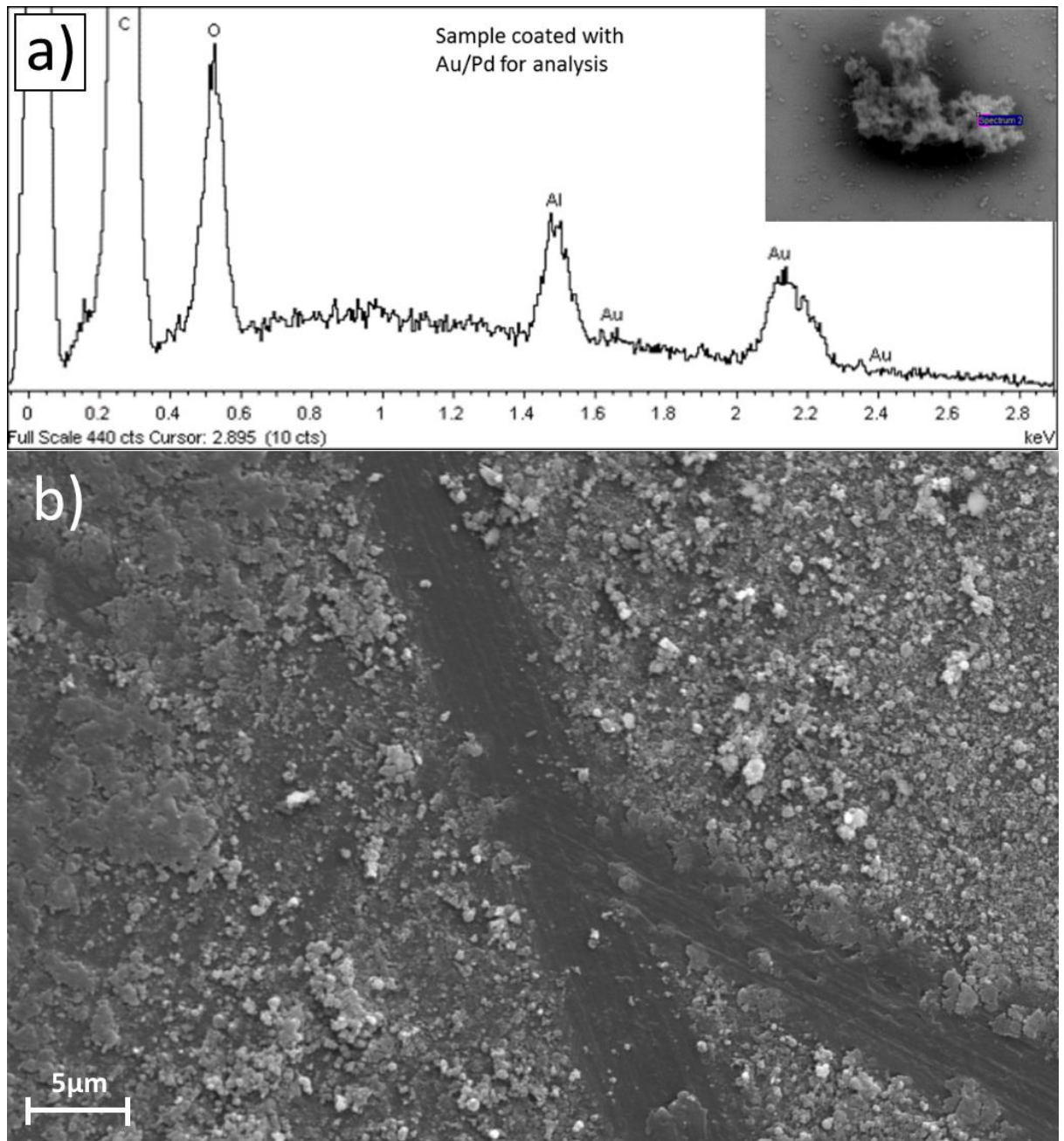


Figure 22. The results of SEM/EDX analysis of the aluminium oxide nanostructures deposited during experimental attempts to deliberately replicate the unintended nanostructure deposition noted during earlier tests with steel showing a) the results of EDX analysis analysis on a single nanostructured cluster and b) a larger scale SEM image showing the variety of structures deposited.

## 3.1 Exploratory Research of the CAP Deposition Process

Before more quantitative optimisation studies were performed to examine this technique, it was decided that more qualitative exploratory research should be undertaken to assess its capabilities, limitations and potential factors that could allow for process control. With the eventual goal of applying this technique to biosensor production in mind, this exploratory research began by focussing on the possibility of gold and silver nanostructure deposition. These metals were chosen due to their ability to be easily functionalised via thiolation, as well as their optical and electrical properties, which offer many advantages in biosensor production. Successful nanostructure deposition was observed for both materials (Figure 23a, c and d). Successful attempts were also made to perform CAP deposition onto a glass substrate instead of COP, as the resulting film would be more comparable to those currently used as the standard in SPR biosensing (Figure 23b).

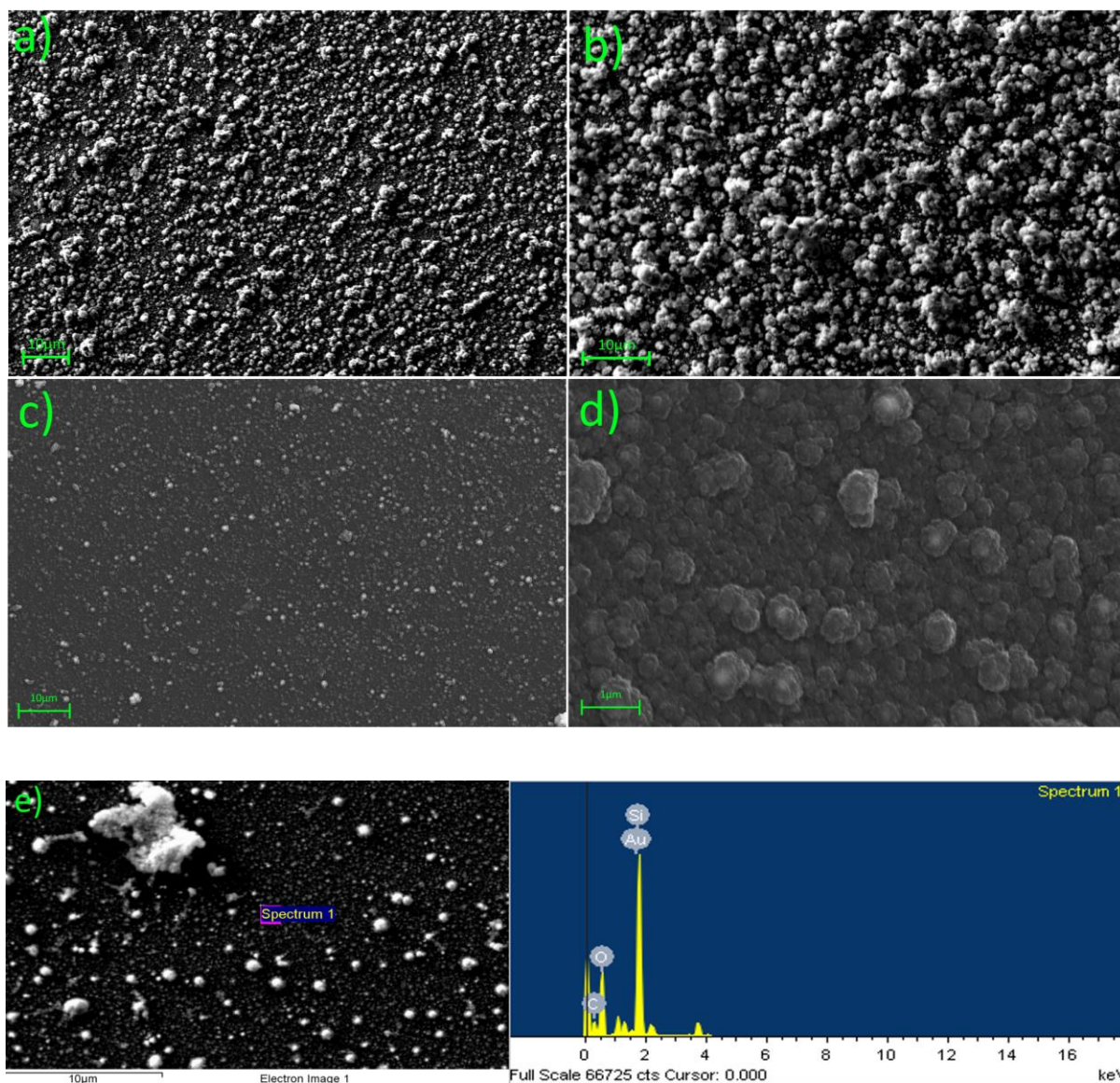


Figure 23. CAP deposited nanostructures comprising of a) gold nanostructures on COP, b) gold nanostructures on glass, c) silver nanostructures on COP, d) the same silver on COP sample at higher magnification and e) an example of deposited gold nanostructures and the EDX spectrum used to confirm its elemental composition.

To confirm the elemental composition of the nanostructures deposited, an X-Ray Diffraction test was performed for one of the gold nanostructure depositions on COP. This XRD spectrum (Figure 24) confirmed the presence of a Face-Centered Cubic (FCC) crystal structure with scattering

angles that match those reported for gold, confirming the successful deposition of the metal using the CAP method.

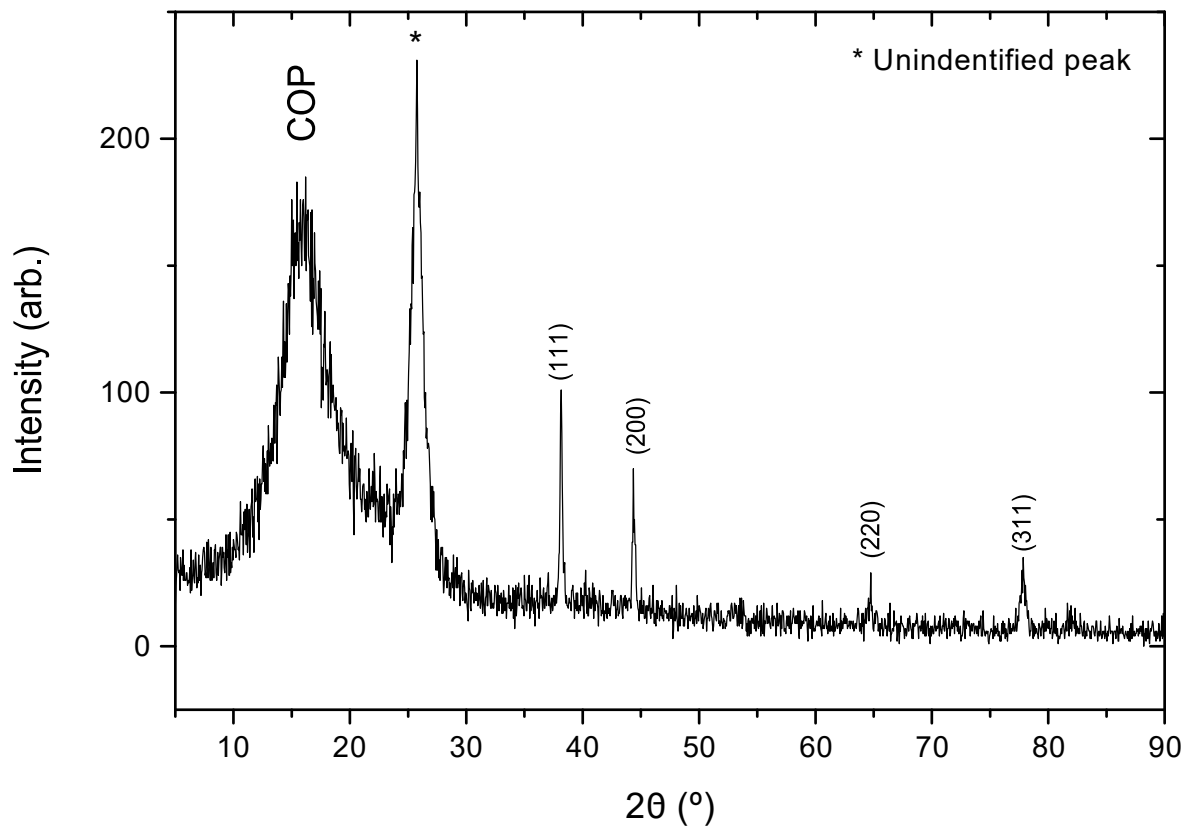


Figure 24. The XRD spectrum of a Gold on COP sample deposited using the CAP method. The unidentified peak present is suspected to be due the adhesive tape used to secure the sample.

Several interesting observations were made during the course of this investigation. Firstly, it was noted that CAP deposition occurred only within specific fluence ranges, and these fluence values were subsequently used in the selection of values for the process optimisation study, see section 4.1. It was also noted that the use of a “spacer” (a piece of material that creates a gap between the ablation target and the deposition substrate) resulted in lighter depositions but more homogenous films (a concept examined in greater detail in section 4.1).

Experiments were also performed to determine the macroscale capabilities of the CAP process, such as the different micrometre-centimetre scale patterns formed with the structures during deposition. This larger scale control is important as it would have an influence on the kinds of sensors that CAP deposition is capable of creating. The first samples produced (such as those shown in Figure 23) had a 5mm x 5mm square pattern (Figure 25a), having been deposited by a unidirectionally raster scanned laser beam. Further experiments successfully carried out the deposition of nanostructured films in a straight, linear form (Figure 25b) and a complex, mathematically defined curved line (Figure 25c). These experiments show the capability of CAP to deposit a vectorizable shape, as they exhibit the ability of the process to deposit in both straight lines and lines with complex curvatures. Based on the observation that different scan speeds affected the apparent colour of the resulting film, an experiment was performed to deposit a film showing a monochrome result using a rastered ".tiff" file format image (see Figure 25d), where the scan speed across each pixel was varied based on its grayscale value. The success of each of these experiments suggests that the CAP methodology is capable of exerting a high degree of control over the larger scale shape of the deposited nanoparticle film, affording a versatility which would be useful for the fabrication of various kinds of biosensing platforms.

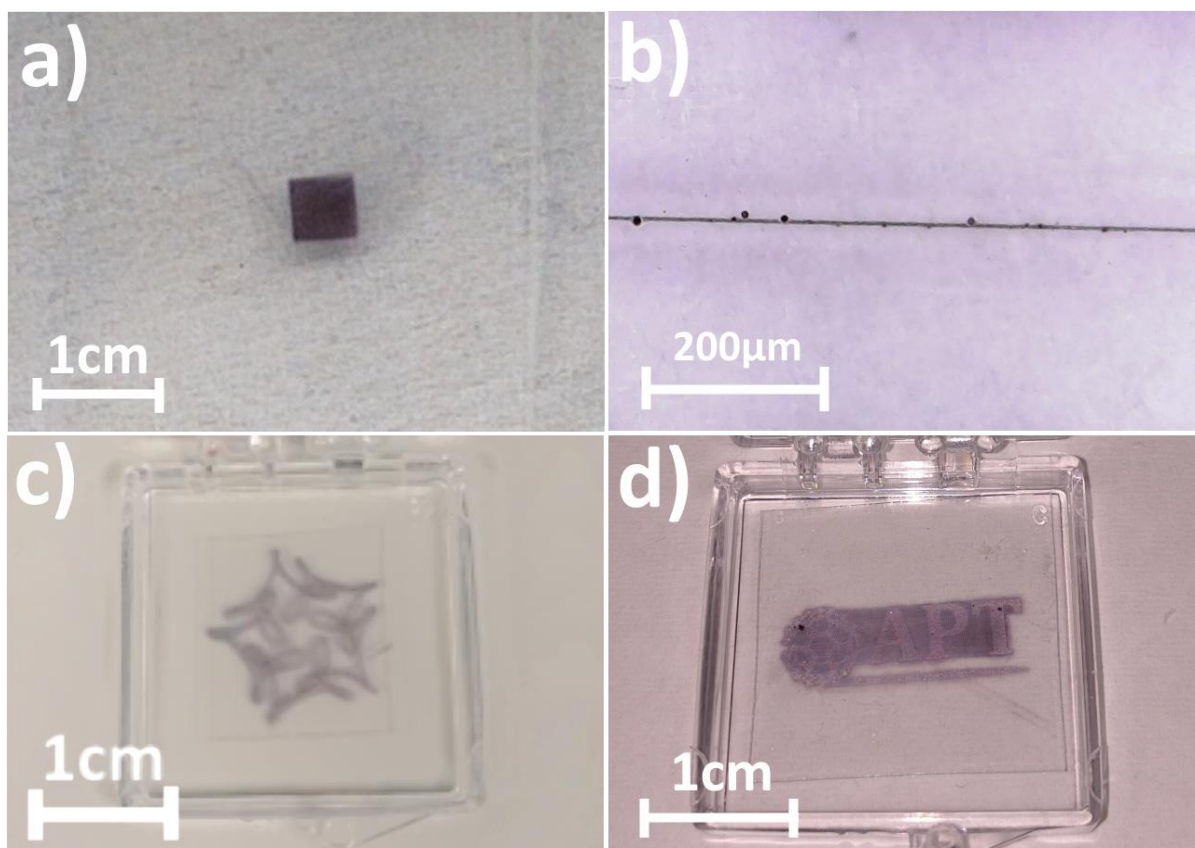


Figure 25. Examples of various patterns deposited as nanostructured gold using the CAP technique, including a) a raster scanned 5mm x 5mm square produced for the experiments described in Chapter 4.1, b) a straight line, c) a curve describing a function often referred to as a Farris' Wheel<sup>158</sup> and d) a raster scanned version of the APT group logo.

In addition to these investigations of CAP, an experiment was performed to test the possibility of a liquid based variant of the technique. It was hypothesised that by placing a liquid in the space between the ablation target and the substrate, a cavitation bubble may be created similar to that produced in the PLAL method of nanoparticle colloid synthesis. In PLAL the ablation plume exists within a cavitation bubble, that has a uniform pressure applied upon it by the surrounding liquid<sup>142</sup>. These uniform, high pressure (relative to a gaseous environment) conditions result in the condensation of nanoparticles with a narrow size distribution when compared to other nanoparticle production methods. In an attempt to confer this advantage of PLAL onto the CAP methodology, a droplet of

water was placed on the ablation target before the deposition substrate was placed in contact with it. The ablation was then performed as normal for CAP deposition. However, following this no significant deposition was observed on the substrate, and it was decided that work should therefore focus on optimising the existing, gaseous variant of the technique.

## 3.2 CAP Process Optimisation Studies

### 3.2.1 Study 1: Gold Foil Deposition on Glass Substrate

Based on the results of the various experiments described in Section 3.1, the basic methodology for the CAP process was devised as shown in Figure 21 at the beginning of this chapter. Following this, process optimisation experiments began. Initial experiments in the optimisation of the CAP process were performed using a simple setup comprising of a glass deposition substrate mechanically affixed to a gold foil ablation target, with the use of a spacer as required. These experiments were performed to discover relationships between the deposition parameters used and the properties of the resulting film, as well as to refine the CAP methodology to maximise its reproducibility.

#### *3.2.1a Study 1: Materials and Equipment*

Clear glass microscope slides were used as the deposition substrate (VWR, IE). A 10 mm × 10 mm × 0.188 mm, 99.9% pure gold metal ablation target was prepared from a sputtering target (Agar Scientific, UK). This target piece was then affixed to an ablation stage, machined from aluminium alloy 2011. All depositions were performed with a 1064 nm diode-pumped, solid state neodymium-doped yttrium aluminium garnet (Nd:YAG) laser. This laser was operated in TEM00 mode, producing a beam with a Gaussian profile and a spot diameter of 140 µm at the focus. This beam was pulsed at a PRF of 10 kHz and with a pulse width of

700 ps. This laser beam was rastered across the target during sample production using a 2D scanning galvanometer (Raylase SS- 12, Germany). The target position in the beam waist was controlled using an M-404 4PD nano-position stage (PI, Germany).

The samples produced were characterised via UV-Vis spectroscopy (Agilent, Cary 50, USA). Samples were carbon coated using a Scancoat Six (Edwards, UK) with carbon evaporation accessory at a pressure of  $10^{-4}$  bar for examination via Scanning Electron Microscopy (SEM) using an Evo LS15 (Carl Zeiss AG). Image analysis on the SEM images obtained was carried out using Fiji image analysis software.

Design of Experiments (DoE) and data analysis was performed with the aid of StatEase Design-Expert and Origin Pro 2016 software packages respectively. Parameters to be examined in the DoE were the laser fluence, the laser scan speed and the raster scan spacing.

### *3.2.1b Study 1: Experimental Methodology*

When first attempting to produce sample batches for this optimisation study, it was noted that samples produced at the same processing parameters had a high degree of qualitative variance (high variation in the shade and intensity of visible colour). It was suspected that this may be due to inconsistencies in the preparation of the ablation target and substrate arising from the use of manually applied adhesive tape when securing the substrate. To remove this inconsistent element, a new experimental setup was designed to make use of mechanically applied pressure to secure the substrate instead of adhesive tape (Figure 26). This new setup was then used in preparation of samples for this initial optimisation study.

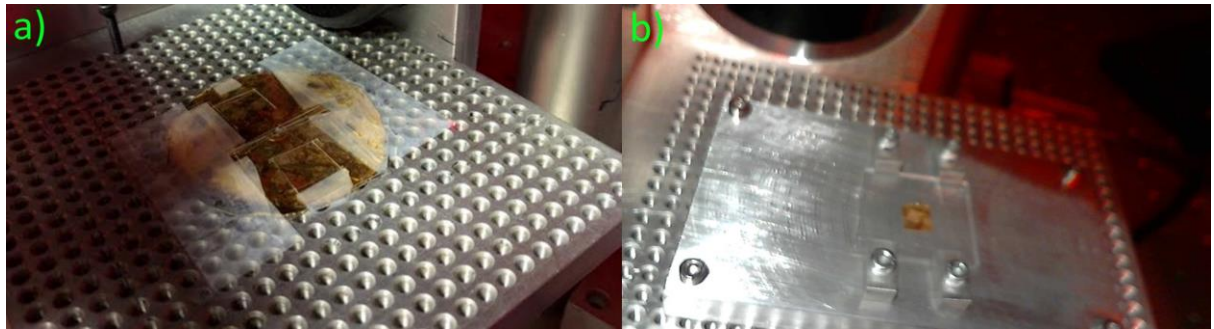


Figure 26. Images of the two CAP setups used during this stage of the project:  
a) the original methodology using adhesive tape, found to have low reproducibility and b) the setup that replaced the adhesive tape method, utilising metal clips to apply mechanical pressure. The use of setup b showed a noticeable increase in reproducibility over setup a.

During the experiments described in Section 3.1, several parameters were identified as potentially controllable factors in determining the characteristics of the deposited film. These parameters were the speed at which the laser is raster scanned across the target (referred to as the “Scan Speed, in mm/s), the fluence received by the target due to the incident laser (referred to simply as the “Fluence”, in J/cm<sup>2</sup>), the distance between each of the raster scanned lines (referred to as the “Scan Spacing”, in  $\mu\text{m}$ ) and the height of the gap created between the target and the deposition substrate by the spacer (referred to as the “Vertical Spacing”, in  $\mu\text{m}$ ). These values were varied across ranges that were determined based on those in which CAP deposition was observed in earlier experiments. All depositions were carried out with a Pulse-Repetition Frequency (PRF) of 10kHz and a Pulse Width (PW) of 3.5 $\mu\text{s}$  unless specifically stated otherwise as these were the default values for the laser. The laser spot used had a Gaussian profile, due to the configuration of the laser optics. Using StatEase Design-Expert 7 statistical analysis software<sup>159</sup>, a Design of Experiments (DoE) parameter table was generated using a 3 parameter and 3 level factorial design and samples were produced in a randomised run order according to this table. A number of measurements were carried out on the resulting samples

including UV/Vis spectral analysis, SEM microscopy and film thickness measurement.

### 3.2.1c Study 1: Results and Analysis

Following their fabrication according to the DOE described in Section 3.2.1a the samples were analysed to gather the relevant data (Table 2).

Table 2. The DoE parameters used in the preparation of samples for the process optimisation study and the UV/Vis spectral peak analysis for each of the produced samples. Samples are presented in the randomised order in which they were to be produced. Fields containing “N/A” denote samples for which no plasmonic peak was observed in their UV/Vis spectrum.

Scan Speed (mm/s)	Fluence (J/cm <sup>2</sup> )	Scan Spacing (μm)	Vertical Spacing (μm)	Plasmon Peak Wavelength (nm)	Plasmon Peak Integrated Area	Plasmon Peak FWHM (nm)
10.00	0.15	150.00	0.00	597.042	32.5929	266.311
3.00	0.15	150.00	0.00	559.978	12.8691	142.941
3.00	0.79	150.00	0.00	544.998	1.13489	61.288
3.00	0.79	50.00	0.00	N/A	N/A	N/A
10.00	0.15	50.00	0.00	543.947	3.40791	92.0225
3.00	0.79	50.00	0.00	N/A	N/A	N/A
10.00	0.79	50.00	0.00	562.968	20.1839	101.892
3.00	0.15	50.00	0.00	N/A	N/A	N/A
6.50	0.47	100.00	0.00	579.074	16.3804	162.438
6.50	0.47	100.00	0.00	559.978	22.4512	191.387
6.50	0.47	100.00	0.00	582.05	7.60601	140.978
10.00	0.79	150.00	0.00	562.071	13.1768	131.198
6.50	0.47	100.00	0.00	552.045	20.6664	111.774
3.00	0.15	50.00	0.00	578	87.25	1.95267
3.00	0.79	150.00	0.00	655.973	126.637	7.63006

Scan Speed (mm/s)	Fluence (J/cm <sup>2</sup> )	Scan Spacing (μm)	Vertical Spacing (μm)	Plasmon Peak Wave-length (nm)	Plasmon Peak Integrated Area	Plasmon Peak FWHM (nm)
3.00	0.15	150.00	0.00	619.936	129.93	262.813
10.00	0.15	150.00	0.00	585.023	54.5076	260.026
10.00	0.79	150.00	0.00	565.059	4.59685	144.615
10.00	0.15	50.00	0.00	653.932	183.589	280.678
10.00	0.79	50.00	0.00	646.049	150.444	291.547
10.00	0.15	150.00	188.00	540.944	31.1953	312.174
3.00	0.15	150.00	188.00	532.975	2.13467	85.1913
3.00	0.79	150.00	188.00	529.061	4.79808	107.211
3.00	0.79	50.00	188.00	N/A	N/A	N/A
10.00	0.15	50.00	188.00	540.944	29.1299	280.876
3.00	0.79	50.00	188.00	N/A	N/A	N/A
10.00	0.79	50.00	188.00	N/A	N/A	N/A
3.00	0.15	50.00	188.00	549.048	14.5928	183.255
6.50	0.47	100.00	188.00	540.944	3.40068	144.991
6.50	0.47	100.00	188.00	550.996	3.93699	134.335
6.50	0.47	100.00	188.00	537.037	7.15681	187.323
10.00	0.79	150.00	188.00	N/A	N/A	N/A
6.50	0.47	100.00	188.00	537.938	3.45829	83.4013
3.00	0.15	50.00	188.00	524.992	14.5649	97.6693
3.00	0.79	150.00	188.00	529.965	5.12684	102.577
3.00	0.15	150.00	188.00	534.931	20.9332	198.415
10.00	0.15	150.00	188.00	540.944	19.2778	364.415
10.00	0.79	150.00	188.00	540.944	27.2005	311.957
10.00	0.15	50.00	188.00	550.996	5.21424	123.639
10.00	0.79	50.00	188.00	543.046	6.99216	140.1

Table 2 shows that most of the samples produced resulted in the appearance of a plasmonically active film. Plasmonically inactive samples were noted to be those for which there was evidence of interactions between the glass and the incident laser beam. This evidence appeared in the form of visible damage to the glass substrate (a well-known effect referred to as “frosting” in the glass-processing industry<sup>160</sup>, Figure 27). The specific reasons causing frosting to occur in these tests have not yet been determined with certainty.



Figure 27. A photograph of the sample produced at parameters Scan Speed: 10 mm/s, Fluence: 0.79 J/cm<sup>2</sup>, Scan Spacing: 150 μm, Vertical Spacing: 188 μm. The white square in the middle of the glass is the area in which frosting has occurred.

The UV/Vis spectra (Figure 28) obtained were analysed using Origin Pro 2016 analysis software, using a semi-automated peak picking algorithm to baseline correct each peak and obtain the local maximum, the integrated area under the peak and the Full Width at Half-Maximum (FWHM) measurement.

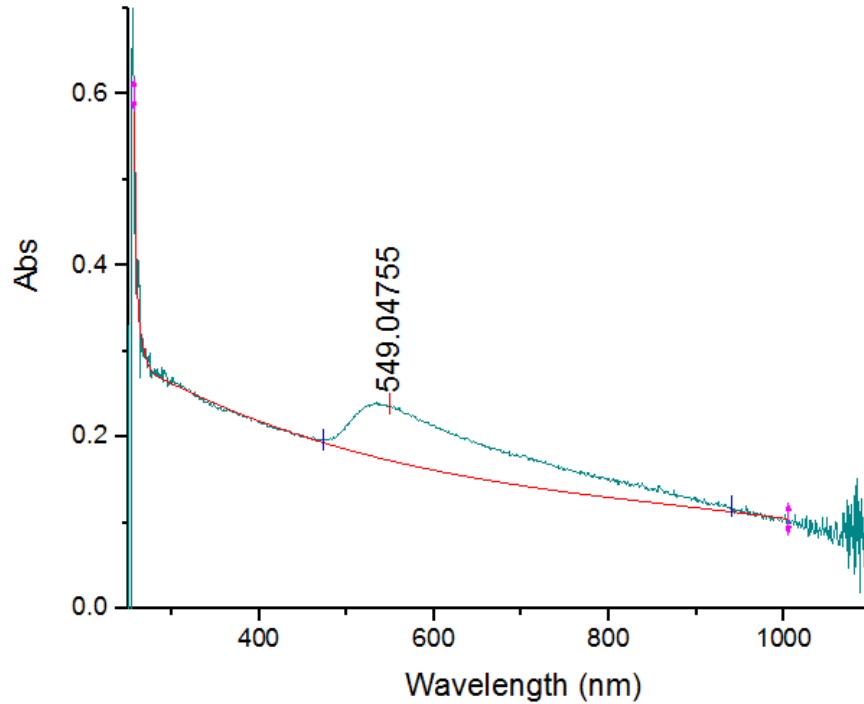


Figure 28. The UV/Vis spectrum of the sample prepared at parameters Scan Speed: 3 mm/s, Fluence: 0.15 J/cm<sup>2</sup>, Scan Spacing: 50 μm, Vertical Spacing: 188 μm. The red line is the corrected baseline to compensate for the background glass peak.

Analysis of this peak data (not including failed depositions) showed some evidence of several potentially significant correlations. However, there was only a single significant model found obtainable with a percentage coefficient of variation of less than 40% suggesting a large degree of inconsistency in the films produced. This model showed an apparent relationship between all processing parameters and the FWHM of the resulting plasmonic peaks. The collected data can be described by the mathematical model (1) with an R<sup>2</sup> correlation coefficient of 0.59.

$$\text{FWHM} = 39.02v - 144.77F + 1.91x + 1.42h - 0.20vh - 0.011xh - 0.18vx + 0.0019hvx - 143.28867 \quad (1)$$

This equation attempts to describe the FWHM in terms of the scan speed (v), fluence (F), scan spacing (x) and the vertical spacing (h).

The existence of this correlation suggested that further optimisation of the technique to reduce its inconsistencies could allow for the derivation of a more accurate formula describing the effect of the CAP process on the plasmonic properties of the resulting film.

SEM analysis showed successful deposition of the nanostructures, as expected based on earlier tests and observations. No relationship was found between the measured particle size or the qualitative morphological properties of the nanostructures formed and their processing parameters at this stage.

A large number of experiments were performed in an attempt measure the thickness of the films deposited. The experimental techniques utilised to obtain this value include Atomic Force Microscopy (AFM), profilometry, interferometry and ellipsometry. However, none of these attempts at measurement proved successful. In the case of AFM, profilometry and interferometry it is likely that the lack of success was due to the deposition area having boundaries that gradually slope down towards the substrate, rather than having a clearly defined step<sup>161</sup>. In the case of ellipsometry it is likely the optical properties of the films differ significantly enough from bulk gold films or more consistent gold nanoparticle films such that the established models for ellipsometric thickness measurement no longer apply. To overcome these difficulties, it was decided that a cross-sectional SEM would be used to measure the thickness of a sample, see Figure 29. This SEM image suggested the average film thickness for the sample selected was between approximately 3 $\mu\text{m}$  and 5 $\mu\text{m}$ .

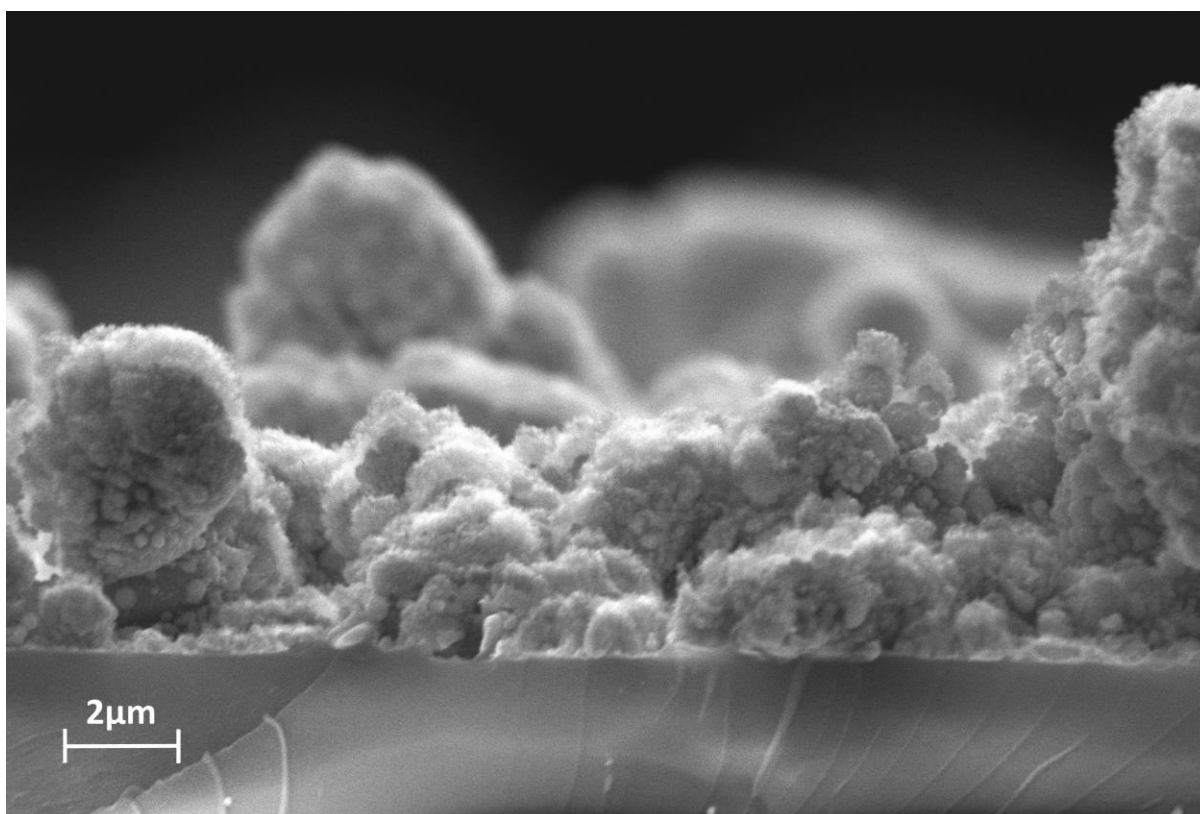


Figure 29. A cross-sectional SEM image of a cracked CAP sample (deposition parameters: Scan Speed: 3 mm/s, Fluence: 0.79 J/cm<sup>2</sup>, Scan Spacing: 150 μm, Vertical Spacing: 0 μm).

In addition to allowing for the approximation of the film-thickness, this cross-sectional SEM image also gives an interesting perspective on the nanostructures being deposited, showing them to resemble tree-like structures and appearing to have a high surface area, aggregating with the top-down SEM images already shown.

By this point it was decided that a second optimisation would need to be performed (detailed in Section 3.2.2) due to the high degree of variance in the samples produced (as discussed earlier in this chapter).

Finally, based on the consideration of the possibility of potentially using these films as Surface-Enhanced Raman Spectroscopy (SERS) substrates, each sample was examined using Raman microscopy (Figure 30). This confirmed the expected outcome that no peaks were visible in any of the

spectra other than those that would be expected of the glass substrate. As such, it was concluded that these films may have applications in SERS analysis as the gold nanostructures deposited do not appear to produce any significant background peaks that would interfere with the technique.

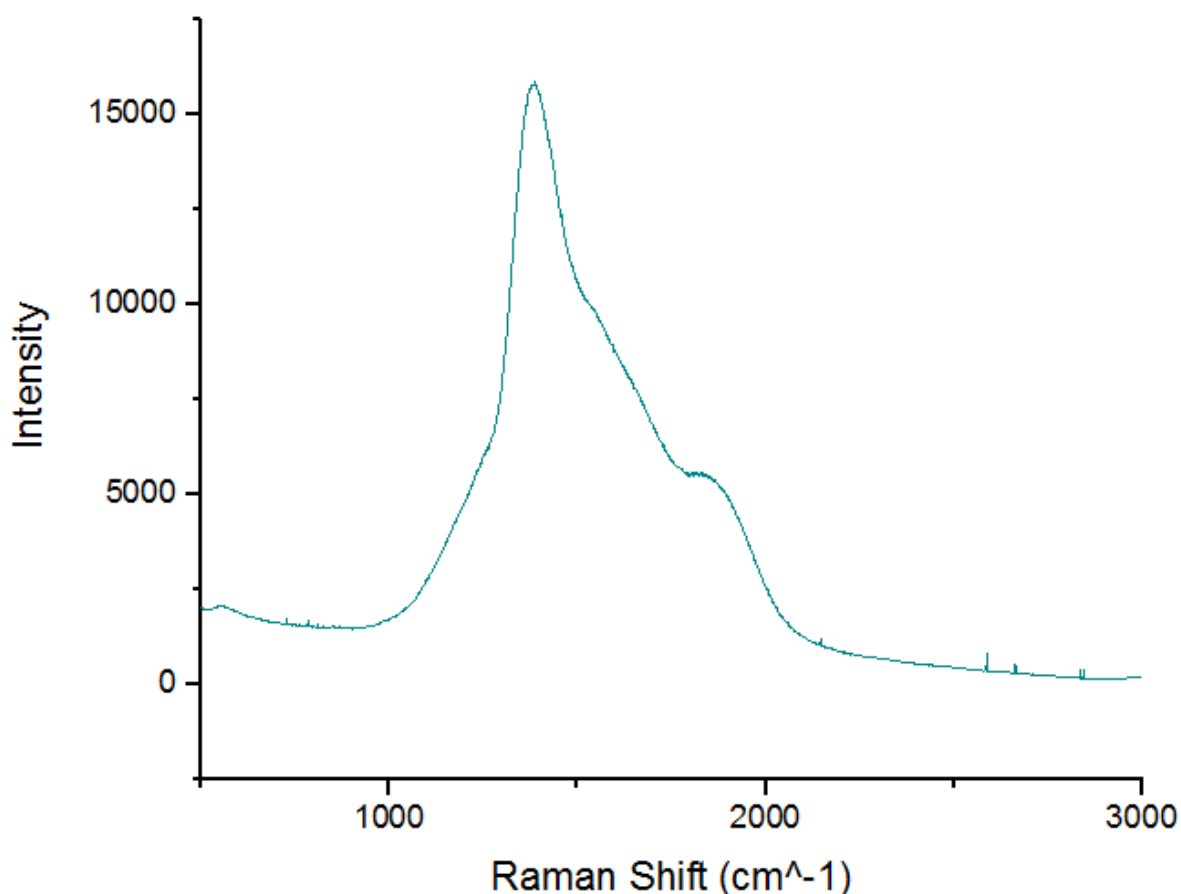


Figure 30. An example of one of the Raman spectra obtained from the samples produced. All showed only these peaks thought to be indicative of glass, with varying intensities (most likely due to varying degrees of frosting).

### 3.2.2 Study 2: Gold Foil Deposition on COP Substrate

Due to the problems introduced into the study described in Section 3.1 by unexpected frosting effects, it was decided to repeat this study using a material that would not be subject to frosting effects. For this reason, it was decided to repeat Study 1 using COP as a substrate instead of glass. It was expected that the high optical transparency of COP at the

wavelength of the laser beam and its properties as a polymer would make similar frosting effects extremely unlikely to hamper such a repeat experiment.

### *3.2.2a Study 2: Materials and Equipment*

ZeonorFilm ZF14-188 (Zeon Chemical L.P. Japan) Cyclic Olefin Polymer (COP) was used as the substrate. A 10 mm × 10 mm × 0.188 mm, 99.9% pure gold metal ablation target was prepared from a sputtering target (Agar Scientific, UK). This target piece was then affixed to an ablation stage, machined from aluminium alloy 2011. All depositions were performed with a 1064 nm diode-pumped, solid state neodymium-doped yttrium aluminium garnet (Nd:YAG) laser. This laser was operated in TEM<sub>00</sub> mode, producing a beam with a Gaussian profile and a spot diameter of 140 μm at the focus. This beam was pulsed at a PRF of 10 kHz and with a pulse width of 700 ps. This laser beam was rastered across the target during sample production using a 2D scanning galvanometer (Raylase SS-12, Germany). The target position in the beam waist was controlled using an M-404 4PD nano-position stage (PI, Germany).

The samples produced were characterised via UV-Vis spectroscopy (Agilent, Cary 50, USA). Samples were carbon coated using a Scancoat Six (Edwards, UK) with carbon evaporation accessory at a pressure of 10<sup>-4</sup> bar for examination via Scanning Electron Microscopy (SEM) using an Evo LS15 (Carl Zeiss AG). Image analysis on the SEM images obtained was carried out using Fiji image analysis software.

Design of Experiments (DoE) and data analysis was performed with the aid of StatEase Design-Expert and Origin Pro 2016 software packages respectively. Parameters to be examined in the DoE were the laser fluence, the laser scan speed and the raster scan spacing.

### *3.2.2b Study 2: Experimental Methodology*

As this experiment was intended to be a repeat of Study 1 using COP instead of glass it was decided that the samples for Study 2 should be prepared according to the same DoE and response table as in Section 3.2.1 (Table 2). It was, however, decided that no attempts would be made to measure film thickness. This measurement was excluded as the only method that had proven effective for this measurement in Study 1 (cross sectional SEM imaging) was only possible on glass due to its brittleness. The flexibility of COP made clean cracking of the substrate and coating difficult to achieve.

As a final modification to the methodology of Study 1, it was decided that this experiment should include conductometric measurements to begin evaluating the feasibility of using these films as the basis for a conductometric sensor platform. To perform these measurements, a 4-point Hall Effect instrument (BioRad HL5500) was used at room temperature.

### *3.2.2c Study 2: Results and Analysis*

While the sample set for this study was successfully produced and the preliminary data analysis was completed, it was quickly discovered that the data would not be particularly useful as a final quantitative model. This was primarily due to a problem with equipment calibration. The laser used for the production of this sample set was found, during later maintenance, to be producing an incident beam with a far lower power than it had been the last time it was measured. Subsequent tests found the power output of the laser to be highly variable, and this was suspected to be due to the failure of an aging component. As such, there could be no certainty that the fluence values reported in the recorded data were accurate and it was decided that the study would need to be repeated once again, with methodological modifications to compensate

for this discrepancy in laser power output (see section 3.2.3). However, while this rendered the quantitative data from this dataset somewhat unusable it was decided to use this invalidated COP sample set to better adapt our CAP methodology for deposition on COP rather than glass.

The first distinction that was noted between CAP on glass and CAP on COP using the methodology from Section 3.2.1a was that the flexibility of COP made the placement of the sample with a consistent vertical gap between the sample and substrate somewhat challenging. When using the setup shown in Figure 26b, the locking mechanism generally caused the COP to bow upwards at its middle unless extreme care was taken during setup. This introduced a possible source of error that was not present when glass was used as the deposition substrate and, thus, it was decided that a new CAP setup should be designed specifically for the use of a COP substrate.

During examination of the samples obtained, it was found that some samples for which deposition was expected to have occurred showed no evidence of deposition. To confirm if this was due to the discrepancies in laser power or due to the change in substrate, several tests were performed attempting to carry out depositions in the same conditions for both COP and glass. This experiment confirmed that the conditions in which reliable deposition can be achieved are different for each of the two substrates. As such, it was decided that new deposition parameters would need to be selected for the next study performed, to ensure a thorough examination of the process being optimised.

It was noted during conductometry testing that the films appeared to give an unexpected, non-ohmic response (Figure 31). When this I/V curve data was plotted on a graph the plotted line did not pass through the origin and had a negative slope. When performing the same measurement on raw COP the same effect was not observed, and the raw COP clearly behaved like an insulator. This difference between raw COP and COP

following CAP deposition suggests that the deposited nanostructures have, indeed formed a conductive film. However, due to the nature of the I/V curves obtained from these films, it is difficult to make any concrete conclusions about their conductive properties. These unexpected I/V curves were hypothesised to be potentially due to several factors. However, it is suspected that the most likely primary reason the line did not pass through the origin was due to the fact that the 4-point probe used does not ground the sample itself causing the samples to exhibit a floating potential. In future, this effect may be avoidable with the modification of the instrument used to better ground the sample stage. There are several possible reasons that the line in the I/V plot shown might have a negative slope, but it is suspected that the most likely reason is due to current arcing through the air in the tiny gaps between the deposited nanostructures. This hypothesis is based on the well-documented observation that gas-discharge tubes generally exhibit a similar negatively sloped I/V curve<sup>162</sup>. While this effect does mean the resistivity of the film was unable to be determined it would also confirm that the film is conductive, which is an advantage for its use in a biosensing platform. This arcing through the air should not be an issue in the end application, as biosensing tests would be performed on in an aqueous environment.

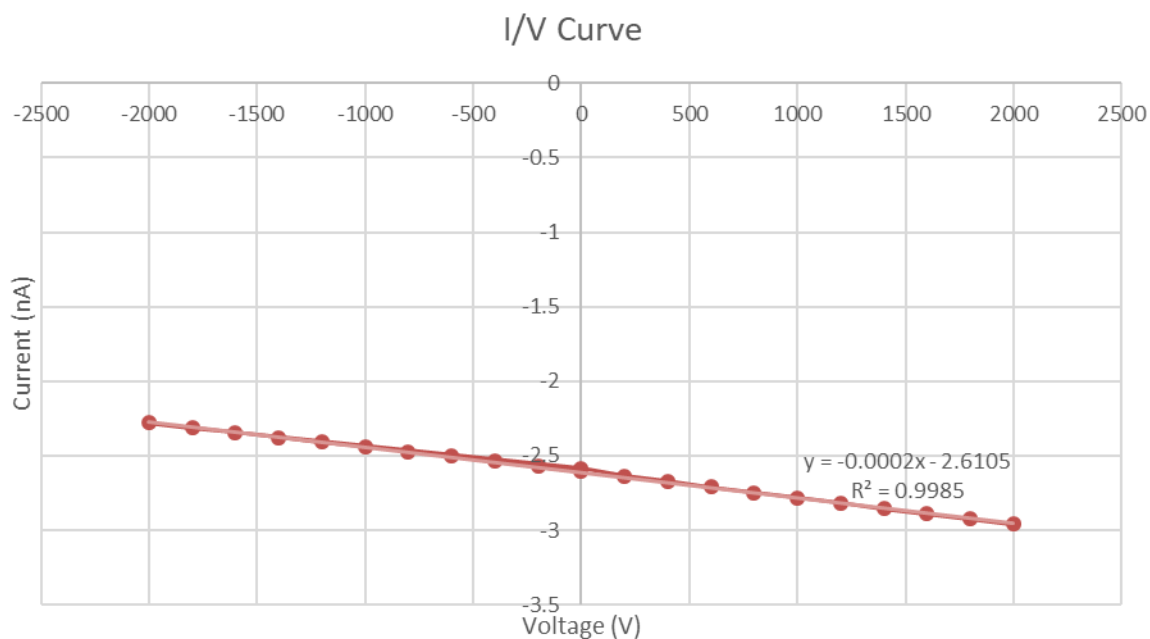


Figure 31. An example of one of the I/V curves obtained from the samples of CAP depositions on a COP substrate.

### 3.2.3 Study 3: Target Stage Deposition on COP Substrate

For the reasons outlined in Section 3.2.2 above, the CAP methodology described in Figure 26b was found to be less applicable to CAP deposition on a flexible COP substrate. Thus, the methodology used in Study 3 was arranged to account for this. In addition, the methodology was further modified to maximise the reliability of depositions and to include in-situ measurements to account for the previously discussed drift in laser parameters.

#### 3.2.3a Study 3: Materials and Equipment

ZeonorFilm ZF14-188 (Zeon Chemical L.P. Japan) Cyclic Olefin Polymer (COP) was used as the substrate. A 10 mm × 10 mm × 0.188 mm, 99.9% pure gold metal ablation target was prepared from a sputtering target (Agar Scientific, UK). This target piece was then affixed to an ablation stage, fabricated using PlasClear photopolymer resin and a Freeform Pico

(Asiga, CA, USA) 3D printer. All depositions were performed with a 1064 nm diode-pumped, solid state neodymium-doped yttrium aluminium garnet (Nd:YAG) laser. This laser was operated in TEM00 mode, producing a beam with a Gaussian profile and a spot diameter of 140  $\mu\text{m}$  at the focus. This beam was pulsed at a PRF of 10 kHz and with a pulse width of 700 ps. This laser beam was rastered across the target during sample production using a 2D scanning galvanometer (Raylase SS- 12, Germany). The target position in the beam waist was controlled using an M-404 4PD nano-position stage (PI, Germany).

The samples produced were characterised via UV-Vis spectroscopy (Agilent, Cary 50, USA). Samples were carbon coated using a Scancoat Six (Edwards, UK) with carbon evaporation accessory at a pressure of  $10^{-4}$  bar for examination via Scanning Electron Microscopy (SEM) using an Evo LS15 (Carl Zeiss AG). Image analysis on the SEM images obtained was carried out using Fiji image analysis software.

Design of Experiments (DoE) and data analysis was performed with the aid of StatEase Design-Expert and Origin Pro 2016 software packages respectively. Parameters to be examined in the DoE were the laser fluence, the laser scan speed and the raster scan spacing.

### *3.2.3b Study 3: Experimental Methodology*

As a result of this, a modified methodology was designed specifically for nanostructure deposition on COP. This modified methodology (Figure 32) avoids the bowing observed using previous methods by adhesively affixing the target to the bottom of a recessed region in the surface of a larger piece, henceforth referred to as the “target stage”. This target stage was 3D printed from PlasClear resin using an Asiga Freeform Pico stereolithography system, to allow for the fabrication of a stage with high dimensional precision. From the previous experiments using a COP substrate the amount of deposition was found to be low when using a

188 $\mu\text{m}$  gap and very inconsistent when using a 0 $\mu\text{m}$  gap. Following a review of existing literature on single-shot atmospheric laser deposition techniques comparable to CAP, it was found that a gap of 50  $\mu\text{m}$ <sup>163</sup> should be sufficient to create the desired plasma confinement effect while avoiding the inconsistencies observed using the 0  $\mu\text{m}$  gap. As such, the recessed region of the target stage was designed to have a depth equal to the thickness of the gold foil target plus 50  $\mu\text{m}$ , thus creating a 50  $\mu\text{m}$  gap between the target and COP deposition substrate.

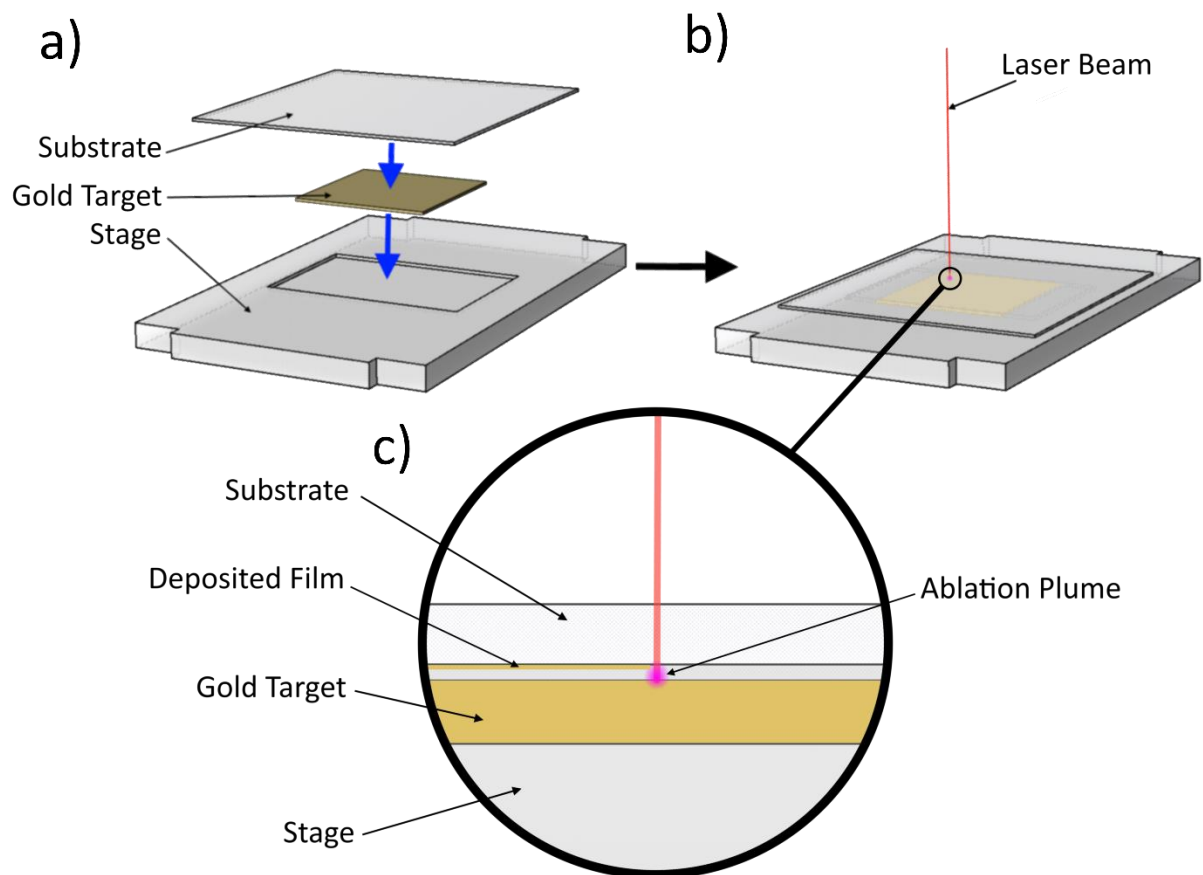


Figure 32. A schematic diagram of the “Target Stage” variant of the CAP methodology used during this experiment. This variant of the methodology uses a SLA produced stage to ensure a 50 $\mu\text{m}$  gap between the target and substrate.

Following the discovery of the instability of the laser setup to be used (as described in Section 3.2.2) it was decided that regular laser power and focal point measurements would be necessary to confirm the reliability of

the fluence values recorded. Thus, as samples were produced a focal point measurement and several power measurements were performed approximately every half an hour to ensure that the power output curve and focal point of the laser were consistent during sample production. If the focal point or power output curve of the laser was found to have changed, the samples produced since the previous measurement were deemed unusable for the purposes of this study. In this way, a sample set was prepared in which the production parameters of each sample would be as prescribed from the DoE analysis of the CAP process. A new DoE table was generated, using parameter ranges found during the experiments described in Section 3.2.2 to be suitable for reliable CAP deposition (see Table 3). This DoE table was based on a 2-level factorial design and samples were prepared in duplicate to examine process precision.

Table 3. Processing parameters for each sample produced during this DoE process analysis.

Sample no.	Fluence (J/cm <sup>2</sup> )	Scan Speed (mm/s)	Scan Spacing (μm)
1	0.221	6	50
2	0.221	18	50
3	0.481	6	50
4	0.481	18	50
5	0.221	6	150
6	0.221	18	150
7	0.481	6	150

Sample no.	Fluence (J/cm <sup>2</sup> )	Scan Speed (mm/s)	Scan Spacing (μm)
8	0.481	18	150
9	0.351	12	100
10	0.351	12	100
11	0.351	12	100
12	0.351	12	100
13	0.351	12	100
14	0.221	6	50
15	0.221	18	50
16	0.481	6	50
17	0.481	18	50
18	0.221	6	150
19	0.221	18	150
20	0.481	12	150
21	0.481	12	150
22	0.351	12	100
23	0.351	12	100
24	0.351	12	100
25	0.351	12	100

Sample no.	Fluence (J/cm <sup>2</sup> )	Scan Speed (mm/s)	Scan Spacing (μm)
26	0.351	12	100

### *3.2.3c Study 3: Results and Analysis*

Once the sample set was produced, they were first subjected to UV/Vis spectroscopic analysis. All samples produced had clearly discernible plasmonic peaks visible in their UV/Vis spectra, suggesting successful deposition of gold in all cases. The plasmonic peaks observed in the spectra of the samples produced showed clear variations in the wavelengths of their local maxima and intensities as shown in Figure 33.

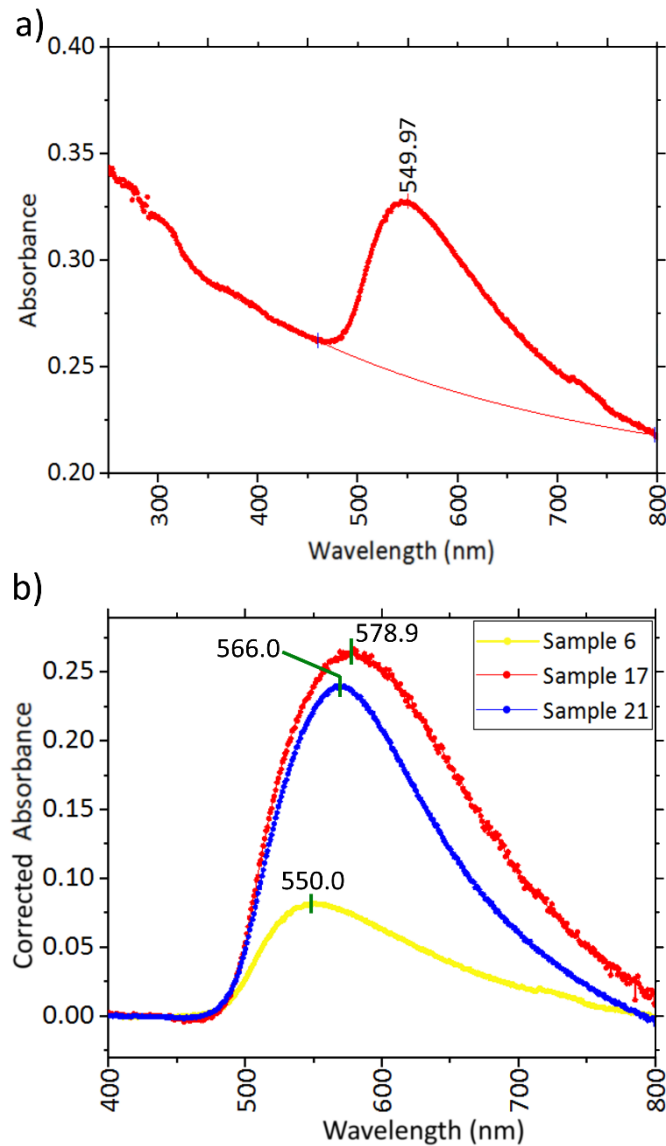


Figure 33. Examples of some of the UV/Vis spectra obtained showing a) the spectrum obtained for sample 6 with its local maximum and corrected baseline shown and b) the baseline-corrected spectra of samples 6, 17 and 21 on the same graph, clearly showing their variations in intensity and local maxima.

As with the previous studies, the features of these spectra were then analysed using baseline correction and a semi-automated peak analysis algorithm to determine the characteristics of the plasmonic peak. The features obtained include the local maximum of the plasmon peak for each sample (henceforth referred to as the “Plasmonic Peak Wavelength”),

the area under this peak as calculated by integration (henceforth referred to as the “Plasmonic Peak Integral”) and the FWHM of the peak (Table 4).

Table 4. Results of the peak analysis performed on the spectra of the samples produced. This data was gathered from baseline corrected data using an automated peak-picking program.

Sample no.	Plasmonic Peak Wavelength (nm)	Plasmonic Peak Integral	Plasmon Peak FWHM (nm)
1	561	28.1	160
2	568	26.3	151
3	570	47.7	146
4	576	40.9	170
5	551	11.1	147
6	550	12.3	138
7	572	35.6	163
8	574	26.1	152
9	568	21.8	161
10	571	23.3	164
11	568	22.3	164
12	577	49.9	225
13	576	30.4	193
14	562	33.1	161
15	559	15.6	151
16	564	38.9	146
17	579	45.1	163
18	559	18.5	154
19	557	21.2	150
20	578	42.7	169
21	566	34.5	134
22	568	29.8	155
23	568	33.5	142
24	570	32.5	151
25	568	25.0	146
26	572	28.8	164

The plasmonic peak found for each of the samples obtained had maxima ranging from approximately 550 nm to 580 nm, with a broad, uneven shape appearing to taper more steeply towards zero on the shorter wavelength side of the peak than on the longer wavelength side. This observation is confirmed by comparing the values of the minima with the median value of the local maxima, which was found to be 555 nm. The local minima on the shorter wavelength side of the peak were noted to generally occur at approximately 450 nm (a difference of 105 nm from the median maximum), while that of the longer wavelength side generally occurred at approximately 800 nm (245 nm from the median maximum).

Following this, the samples were examined using SEM. This characterisation step was performed last as it required the samples to be carbon coated and, thus, renders samples unusable for other tests afterwards. Successful nanostructure deposition was observed in all samples during this characterisation step, and the resulting images (Figure 34) were then qualitatively examined as discussed below before being analysed using Fiji image processing software<sup>164</sup>.

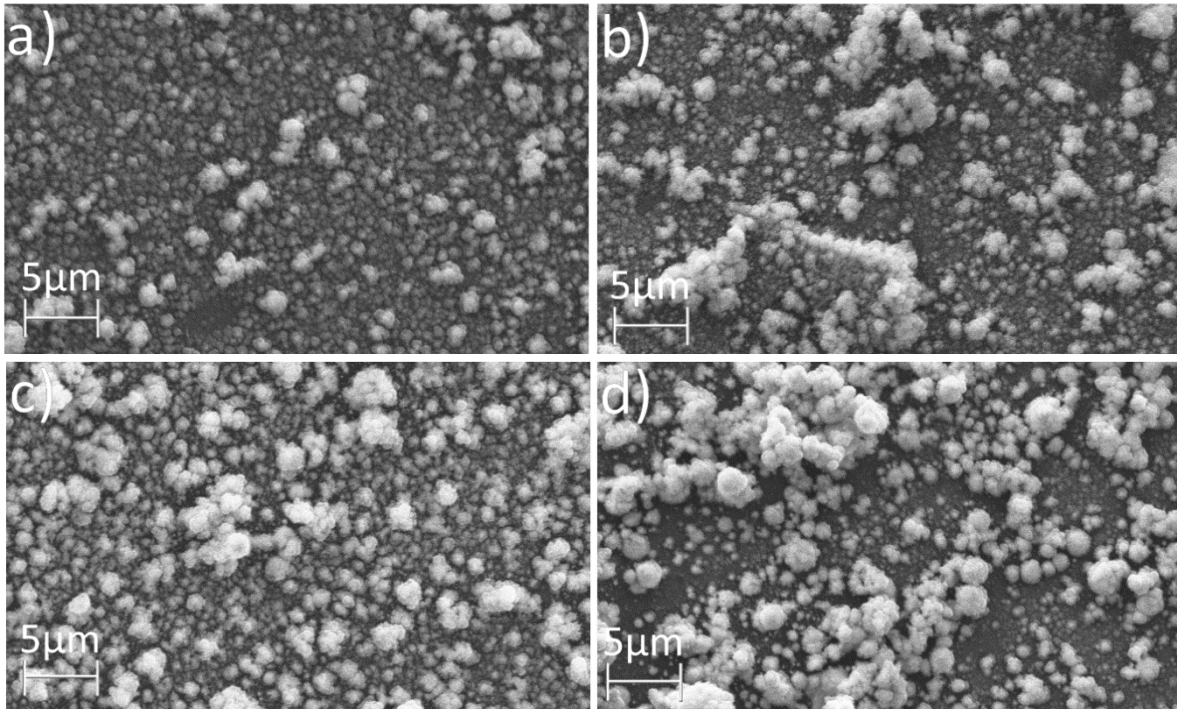


Figure 34. Examples of the kinds of features observed during SEM analysis. The samples numbers and processing parameters for each image shown are a) Sample 18 (6 mm/s, 0.221 J/cm<sup>2</sup>, 150 μm), b) Sample 11 (12 mm/s, 0.351 J/cm<sup>2</sup>, 100 μm), c) Sample 20 (12 mm/s, 0.481 J/cm<sup>2</sup>, 150 μm) and d) Sample 4 (18 mm/s, 0.481 J/cm<sup>2</sup>, 50 μm) all obtained at 8380× magnification.

As can be seen in Figure 34, many of the samples produced showed clear differences in the kinds of nanostructures deposited and the images therein were selected to best exhibit some of these differences. For example, Figure 34a is an example of a more homogenous film than most others obtained, showing less large scale aggregation of particles and melting than comparable samples. This is starkly contrasted with Figure 34b, which clearly shows some larger aggregates dispersed throughout the film, and Figure 34c, which shows a film that appears to be comprised primarily of aggregates. Figure 34d is distinct from the other 3 presented in that it also contains larger spheroidal microparticles in addition to the nanostructures and microaggregates present in Figure 34a, b and c. These structures are hypothesised to be the result of laser sintering of the deposited microaggregates to form a single, large spherical

microparticles<sup>165</sup>. When examining the SEM images obtained there was no clearly discernible relationship between the processing parameters selected and the apparent homogeneity of the resulting film. This is also true of conventional PLD<sup>105</sup>, reinforcing the hypothesis that the mechanism of CAP is related to the mechanism of conventional PLD.

All SEM images obtained were analysed using manual particle sizing by the use of best-fit ellipses. The particles to be sized were selected using a script that placed 20 points on the image at random, and particles on which points were placed were then measured. For each particle, the major axis, minor axis, area and eccentricity of the best-fit ellipse was recorded and these measurements were compiled to calculate the average dimensions of particles generated at each set of processing parameters (Table 5). Standard deviations were also calculated, and serve as a way to quantify the dispersity of the particle films deposited.

Table 5. The results of manual particle sizing analysis ( $\pm\sigma$  indicated, for  $n=20$ ). Sizing was performed by randomised fitting of ellipses to SEM imagery.

Sample	Avg Minor Axis (nm)	Avg Major Axis (nm)	Avg Cross-Sectional Area (nm <sup>2</sup> )	Avg Eccentricity
1	223 $\pm$ 56	277 $\pm$ 80	206656 $\pm$ 114236	0.51 $\pm$ 0.24
2	147 $\pm$ 38	178 $\pm$ 51	87605 $\pm$ 49284	0.46 $\pm$ 0.27
3	207 $\pm$ 52	237 $\pm$ 62	162682 $\pm$ 86446	0.36 $\pm$ 0.29
4	235 $\pm$ 60	279 $\pm$ 72	217593 $\pm$ 109501	0.44 $\pm$ 0.26
5	218 $\pm$ 54	259 $\pm$ 74	188430 $\pm$ 99363	0.45 $\pm$ 0.25
6	213 $\pm$ 49	256 $\pm$ 58	178859 $\pm$ 88137	0.48 $\pm$ 0.25

Sample	Avg Minor Axis (nm)	Avg Major Axis (nm)	Avg Cross-Sectional Area (nm <sup>2</sup> )	Avg Eccentricity
7	190 ± 51	211 ± 56	134316 ± 77813	0.31 ± 0.28
8	235 ± 89	267 ± 101	223402 ± 210179	0.35 ± 0.28
9	265 ± 89	326 ± 113	300751 ± 205286	0.52 ± 0.20
10	246 ± 76	292 ± 90	243338 ± 143070	0.40 ± 0.30
11	325 ± 130	393 ± 153	458533 ± 429958	0.50 ± 0.23
12	250 ± 77	290 ± 80	244364 ± 135750	0.40 ± 0.29
13	232 ± 74	269 ± 81	212695 ± 126095	0.40 ± 0.29
14	275 ± 111	315 ± 130	314306 ± 251533	0.36 ± 0.28
15	279 ± 89	317 ± 100	303490 ± 185652	0.37 ± 0.27
16	255 ± 97	302 ± 118	275351 ± 241689	0.44 ± 0.26
17	237 ± 114	279 ± 124	249940 ± 248796	0.46 ± 0.25
18	212 ± 56	252 ± 72	178973 ± 104235	0.42 ± 0.29
19	179 ± 50	214 ± 61	128846 ± 71535	0.44 ± 0.27
20	203 ± 38	239 ± 50	157441 ± 61204	0.41 ± 0.28
21	229 ± 77	270 ± 91	214174 ± 141208	0.44 ± 0.27
22	201 ± 46	235 ± 52	154822 ± 67590	0.41 ± 0.28

Sample	Avg Minor Axis (nm)	Avg Major Axis (nm)	Avg Cross-Sectional Area (nm <sup>2</sup> )	Avg Eccentricity
23	317 ± 88	375 ± 102	398039 ± 231149	0.49 ± 0.19
24	227 ± 57	262 ± 63	196858 ± 103835	0.37 ± 0.29
25	194 ± 44	226 ± 53	143565 ± 67644	0.41 ± 0.28
26	230 ± 69	287 ± 89	223061 ± 131796	0.51 ± 0.25

Statistical analysis of the data presented in Table 4 and Table 5 began with an examination of the Signal-to-Noise Ratio (SNR) for each output. By examining the SNR for each dataset it was possible to quantify how much of each response measured was likely to be due purely to random statistical noise. A higher SNR generally implies that statistical noise contributed less to the measurements and therefore that the measurement of a parameter was more accurate. During SNR analysis, the most important step is the selection of a suitable SNR formula for the analysis. There are several commonly used SNR formulae and different fields generally use different ones as standard depending upon their needs. The fields of image processing and spectroscopic analysis (in addition to its parent field of analytical chemistry) generally use a formula known as the “True SNR Formula”<sup>166-168</sup> (2) or variants thereof. As the analysis presented here falls within these fields it was therefore decided that this SNR formula is most appropriate. When using this formula for SNR, the resulting value is in decibels (dBs). From a cursory examination of (2) it is clear that at a value of 0 dB the response due to signal is equal to the response due to noise and therefore that a negative SNR implies the response is primarily due to noise and a positive value implies it is primarily due to signal. As such, it seems reasonable that any response

with a negative or negligible SNR should be disregarded as simply statistical noise.

$$SNR = 10 \left( \log_{10} \frac{\mu}{\sigma} \right) \quad (2)$$

Based on this formula, the SNR for each response measured was calculated and collimated into Table 6. This analysis showed the highest SNR for the plasmonic peak position and the lowest SNR for the area standard deviation. All responses were found to have an SNR of greater than 2, suggesting that they are primarily due to signal and should therefore all be subjected to further analysis.

Table 6. A table of SNR data for all responses measured during this study. SNR was calculated according to equation (2).

	Mean Signal	Standard Deviation	Signal-to-Noise Ratio (dB)
<b>Plasmonic Peak Position (nm)</b>	567.403	7.780	18.629
<b>Plasmonic Peak Integral</b>	29.802	10.379	4.581
<b>Plasmonic Peak FWHM (nm)</b>	158.542	18.137	9.416
<b>Average Minor Axis (nm)</b>	231.732	39.342	7.701
<b>Minor Axis Standard Deviation (nm)</b>	70.416	24.714	4.547
<b>Average Major Axis (nm)</b>	273.232	47.588	7.590
<b>Major Axis Standard Deviation (nm)</b>	83.740	27.564	4.826

	Mean Signal	Standard Deviation	Signal-to-Noise Ratio (dB)
<b>Average Area (nm<sup>2</sup>)</b>	223003.431	82828.358	4.301
<b>Area Standard Deviation (nm<sup>2</sup>)</b>	145499.342	85472.142	2.310
<b>Average Eccentricity</b>	0.427	0.0553	8.879
<b>Eccentricity Standard Deviation</b>	0.265	0.0266	9.978

Following this, each dataset was analysed using Design-Expert software<sup>159</sup> to search for statistically significant mathematical relationships from which a model might be derived. The Design-Expert software package offers a wide variety of methods for rapid regression analysis, thus allowing the researcher to apply many regression techniques to a dataset without the prohibitive time investment of manual regression analysis. Because of this, it is an ideal tool to use when searching for predictive models describing processes, such in this DoE analysis. During this analysis, 4 statistically significant mathematical models were derived describing how process parameters influence the properties of the deposited films, and the Analysis of Variance (ANOVA) results for these models are presented in Table 7 (complete ANOVA tables are available in Appendix 1 - Appendix 4).

Table 7. The ANOVA outputs for each model derived. ANOVA analysis was performed using Design-Expert software.

<b>Response</b>	<b>Degrees of Freedom</b>	<b>Adjusted R<sup>2</sup></b>	<b>Predicted R<sup>2</sup></b>	<b>Adequate Precision</b>	<b>F Value</b>
<b>Particle Area</b>	<b>7</b>	<b>0.4952</b>	<b>0.2850</b>	<b>8.682</b>	<b>4.50</b>
<b>Area Standard Deviation</b>	<b>7</b>	<b>0.4985</b>	<b>0.3312</b>	<b>8.021</b>	<b>4.55</b>
<b>Plasmonic Peak Position</b>	<b>5</b>	<b>0.5922</b>	<b>0.4085</b>	<b>9.528</b>	<b>8.26</b>
<b>Plasmonic Peak Integral</b>	<b>2</b>	<b>0.5990</b>	<b>0.5380</b>	<b>12.440</b>	<b>19.67</b>

As can be seen in Table 7, ANOVA analysis of the data obtained produced 4 statistically significant mathematical models. The models derived from SEM data both have an adjusted R<sup>2</sup> of approximately 0.5 while the models produced from UV/Vis data both have an adjusted R<sup>2</sup> of approximately 0.6. An adequate precision of at least 4 is generally required to determine that a model is statistically significant and applicable in reality<sup>169</sup>. Each model derived has an adequate precision of at least 8, suggesting that they should be applicable in process control. While the F values for each model are within the statistically significant range it is particularly notable that the F value for the plasmonic peak interval (19.67) is quite large, suggesting it is likely the most statistically significant model derived.

Interestingly, despite the significantly higher SNR of the plasmonic peak position data relative to the plasmonic peak integral (18.63 dB and 4.581 dB respectively, according to Table 6) the integral model has a far higher

F value. Considering the high adequate precision of the peak position model it is unlikely that this is due to poor correlation. As such, it seems plausible to suggest this lowering of statistical significance may be due to the nature of the modelling techniques used by the Design-Expert software. When deriving a model for peak position it was found that scan speed has no statistically significant contribution to the peak position output. However, it was also found that the interaction between scan speed and spacing did have a statistically significant contribution to this. As Design-Expert makes use of a hierarchical modelling system for the derivation of quantitatively predictive models it was thus required that scan speed be included in the model derived despite its lack of statistical significance. This included independent variable seems likely to be the source of the relatively low (but still strongly statistically significant) F value within the context of the other SNR and ANOVA data available.

For the other models derived (particle area, area standard deviation and plasmonic peak integral) the SNR values are reasonable for the derivation of a model but not as high as for the peak position data suggesting that the observed variance in these datasets (evident from the  $R^2$  values) are likely due to simple statistical noise. The noise in these datasets could be further reduced by expanding the process space to be examined or increasing the number of repetitions for each sample but for the purposes of this work these ANOVA analyses were deemed to have acceptable accuracy.

Of the models derived, the first ones were those pertaining to the morphological characteristics of the resulting film (that being particle size and dispersity). The first morphological model derived (3) during this study describes the cross-sectional area of the deposited particles ( $A_{np}$ , a proxy for particle size as observed by SEM) in terms of the scan speed ( $v$ ), fluence ( $F$ ) and scan spacing ( $x$ ) (note: the notation  $E^x$  is used to represent the exponent  $\times 10^x$  for the sake of clarity).

$$A_{np} = (-1.32E^{-4}\nu - 5.18E^{-3}F - 1.52E^{-5}x + 4.15E^{-4}\nu F - 1.95E^{-6}\nu x + 6.04E^{-5}Fx - 5.62E^{-6}\nu Fx + 3.30E^{-3})^{-2} \quad (3)$$

This model (3) suggests that the primary factor determining particle size is the fluence of the incident beam and that it is also influenced to a lesser extent by scan speed and scan spacing. It also suggests that there are many interactions between all of these parameters, including a statistically significant complex interaction between all 3 parameters (as shown by the  $\nu Fx$  parameter in the equation).

The second morphological model derived (4) describes the standard deviation of the cross-sectional area of the particles ( $\sigma_A$ , a proxy for the dispersity of the particles) in terms of the same parameters as above.

$$\sigma_A = (-7.23E^{-4}\nu - 0.044F - 1.15E^{-4}x + 2.39E^{-3}\nu F + 1.21E^{-5}\nu x + 5.11E^{-4}Fx - 3.69E^{-5}\nu Fx + 0.029)^{-3} \quad (4)$$

Similar to the model for particle size (3), the dispersity model (4) is influenced by fluence, scan speed, scan spacing and complex interactions between all of these parameters. Plotting these models as contour plots clearly shows the wide variance in the shape of the surface plots for particle size and particle dispersity dependent on the input parameters above (Figure 35). Examining these plots, a trend is also immediately evident suggesting that greater fluence generally results in a larger particle size within the film.

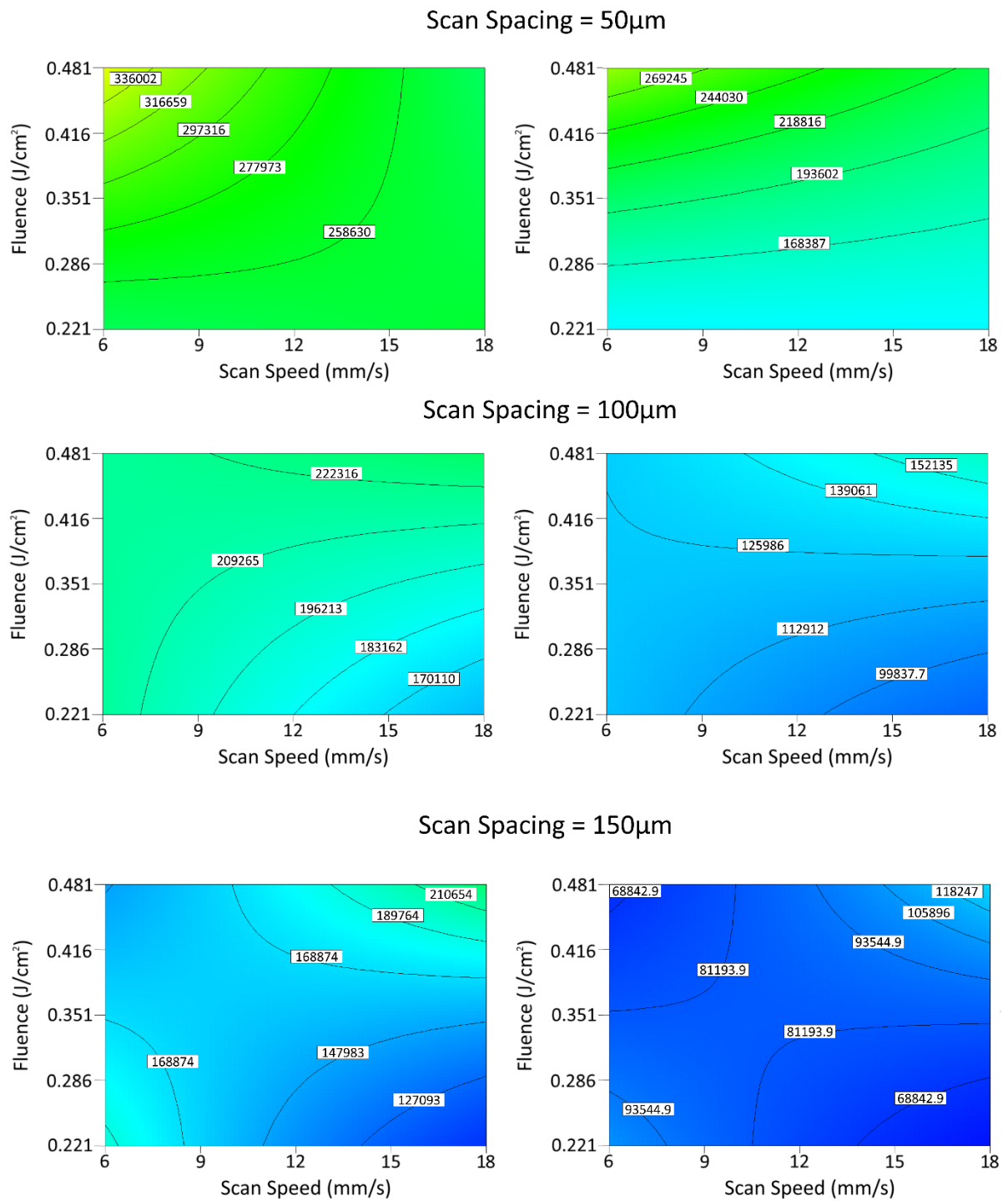


Figure 35. Contour plots of the particle area (left) and standard deviation of area (right) predicted by the derived models at various scan spacings.

Finally, to evaluate accuracy of these models a normal plot of residuals and predicted vs actual plot of each was prepared (Figure 36). From these

plots it can be seen that the empirical measurements largely conform to those predicted by the model and that the deviations from the predicted model are normally distributed. The normal distribution of these deviations from the predicted values suggests that they are primarily due to statistical noise, which agrees with the conclusions drawn above based on Table 6 and Table 7.

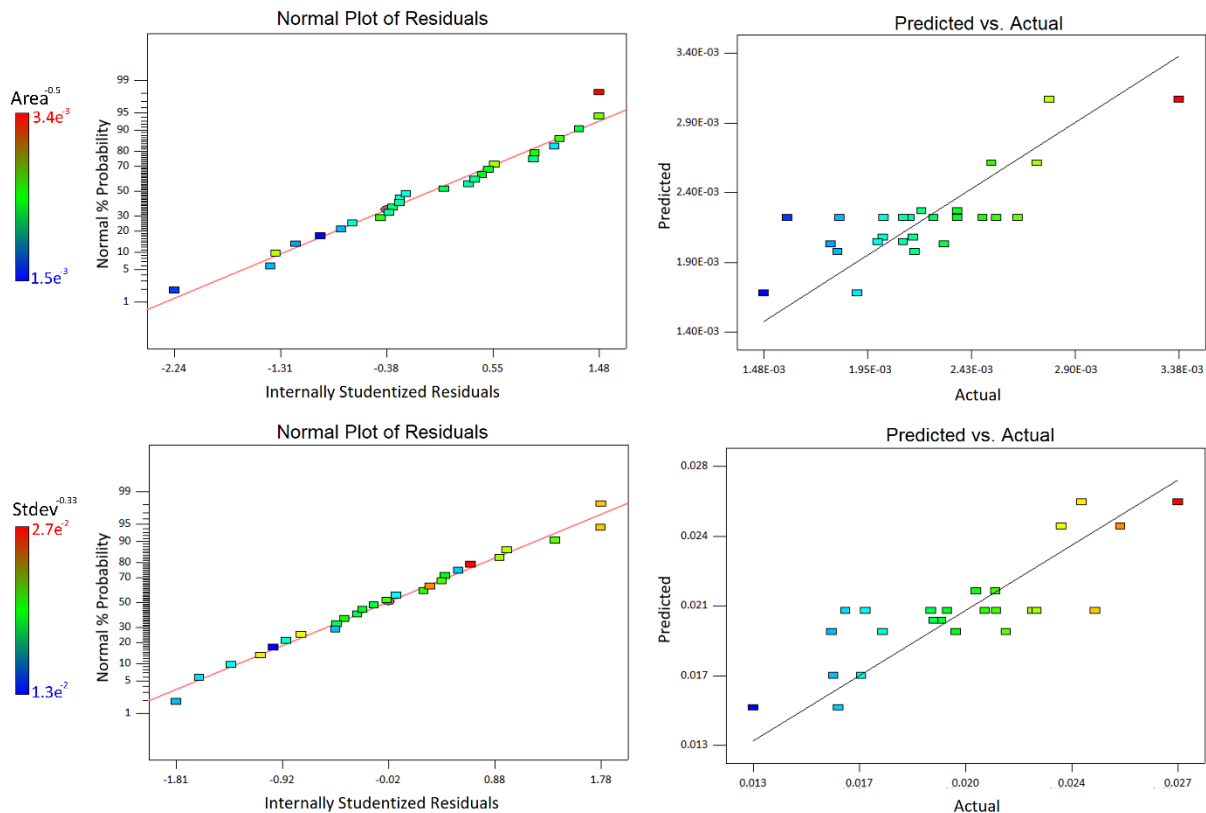


Figure 36. Normal plot of residuals and predicted vs actual plots for the size (top) and dispersity (bottom) models derived.

The derivation of models describing the plasmonic properties of the films followed a similar path to the derivation of the morphological models. The first plasmonic model derived (5) described the plasmonic peak position ( $\lambda_p$ ) of the films produced in terms of the scan speed ( $v$ ), fluence ( $F$ ) and scan spacing ( $x$ ) (5).

$$\lambda_p = 0.91\nu + 21.1F - 0.06x - 0.008\nu x + 0.003Fx + 553.05 \quad (5)$$

Based on this formula it can be seen that fluence is the primary factor determining the plasmonic wavelength of the films produced. When examining a contour plot and surface plot for this model (Figure 37) it is clear that greater fluence generally results in a longer plasmonic wavelength. Assuming that the deposited particles behave similarly to other nanoparticle films<sup>170</sup> this suggests that higher fluence results in the production of larger particles. This observation agrees with trends noted in the previous models above (Figure 35), further reinforcing these proposed models.

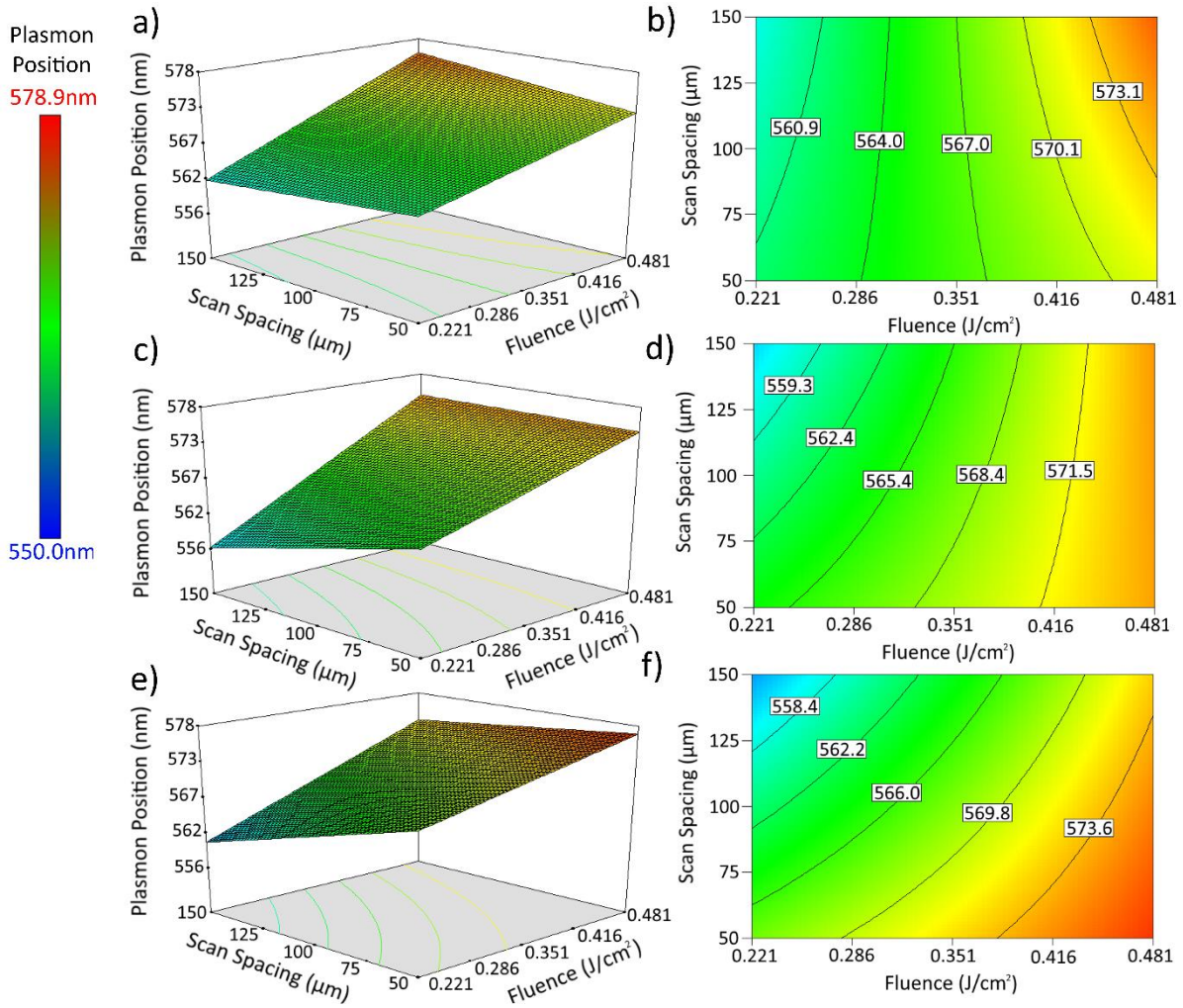


Figure 37 Surface (left) and contour (right) plots of the predicted plasmonic peak positions at scan speeds of (a,b) 6mm/s, (c,d) 12mm/s and (e,f) 18mm/s. Surfaces and contours are coloured by plasmon position.

The actual vs predicted plot for this model (Figure 38) shows that the predicted values largely agree with the actual values for this property. Interestingly, although the normal plot of residuals for this model (Figure 38) suggests that its variance is mostly due to noise but shows a very slight “S-curve” shape, suggesting a very slightly bimodal distribution. A slight bimodal distribution would suggest that some parameters are not being modelled in the ideal way, agreeing with the hypothesised explanation for the unusually low adequate precision value (Table 7) relative to what would be expected based on its SNR (Table 6). Despite

this, the bimodality appears to only be very slight, implying the residuals are at least approximately normally distributed.

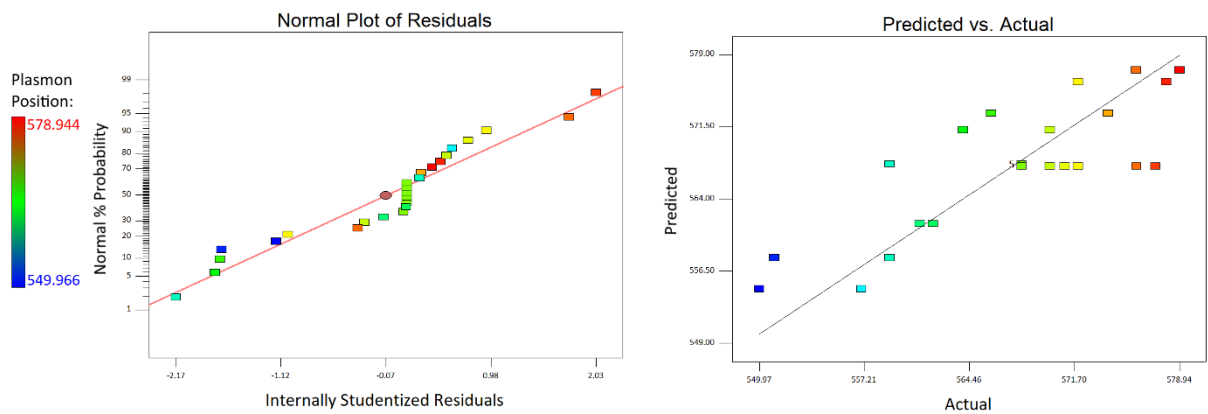


Figure 38. Normal plot of residuals and predicted vs actual plot for the plasmonic peak position model.

The last model produced describes the plasmonic peak integral ( $A_p$ , the area under the peak) in terms of only the fluence ( $F$ ) and scan spacing ( $x$ ) (6). This equation also suggests that the most significant parameter in determining this property of the film is the fluence imparted.

$$A_p = 44.36F^2 + 0.000081x^2 + 52.34F - 0.070x - 0.12Fx + 15.44 \quad (6)$$

This model appears to suggest a squared relationship between fluence and peak integral, in addition to a squared relationship between scan spacing and peak integral. A surface plot of this model (Figure 39) shows that it implies that greater fluence and lower scan spacing result in increased plasmonic peak integral within the process space. This makes sense if we assume that a thicker or more dense film (as would be intuitively expected at greater fluences or lower scan spacings) results in a greater plasmonic peak integral. Such an assumption would be expected to hold true for any monodisperse or low dispersity film<sup>171</sup>.

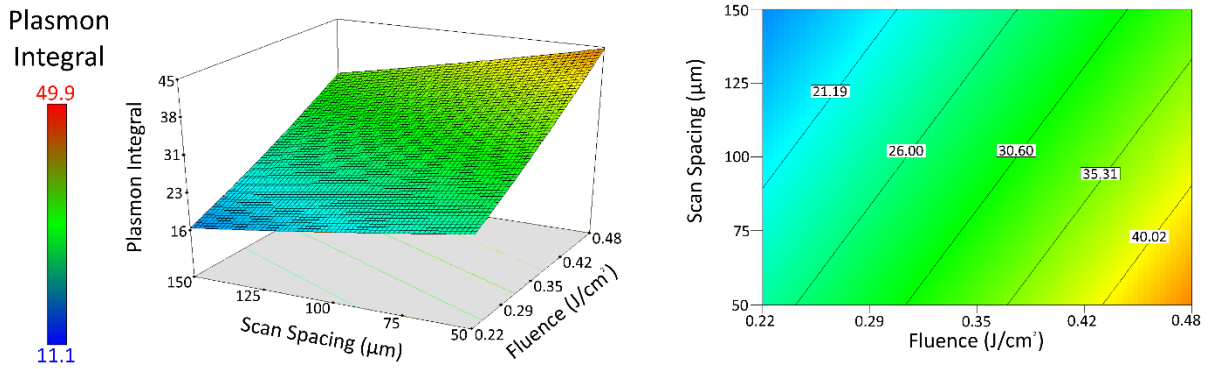


Figure 39. Surface (left) and contour (right) plot of the plasmonic peak integral as predicted by the model derived. Surface and contour plots are colorised by plasmonic peak integral in  $\text{nm}^2$ .

Similar to the other models derived, the validity of the plasmonic peak integral model was verified by plotting a normal plot of residuals and predicted vs actual graph (Figure 40). These plots showed that the predicted values largely agreed with those empirically observed within the process space examined. Despite this general agreement a single outlying measurement was found that deviated from the mathematically predicted value (Sample 12, clearly noticeable as far from the rest of the points in both plots). However, as this measurement was only one of ten repetitions for that same parameter set it was deemed a simple statistical outlier within the dataset.

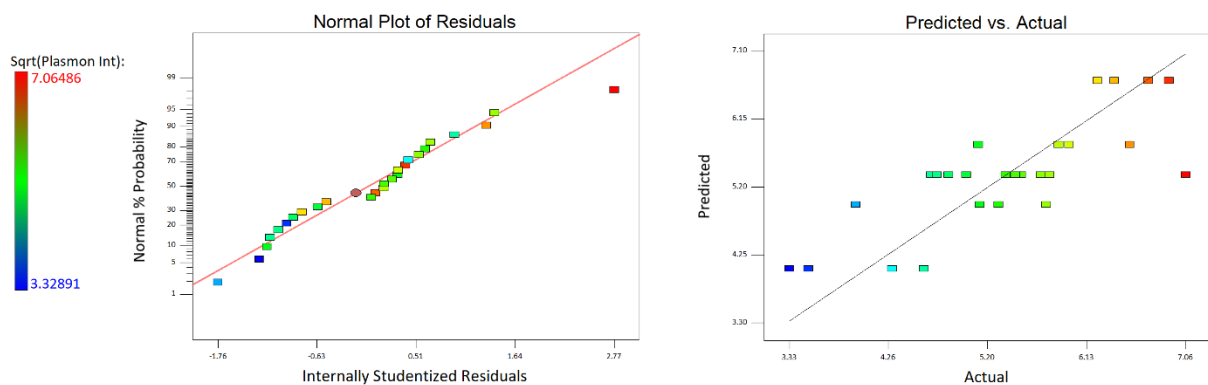


Figure 40. The normal plot of residuals and predicted vs actual plot for the plasmonic peak integral model derived.

Interestingly, upon close examination of the plasmonic peak integral model (6) it is clear that the derived surface has parabolic curvature. Thus, this implies that at a low enough fluence or high enough scan spacing the plasmonic peak integral should begin to increase again. Intuitively speaking, this assertion that large scan spacing should result in a large plasmonic integral seems strange on its face and as a result it likely indicates that the derived model is only a reasonably accurate approximation within a certain range of parameters. From the equation presented (6) it is possible to derive a formula (7) describing the line upon which the predicted minima sit (the “line of minima”), and therefore the line beyond which the integral is expected to begin increasing again.

$$A_p = 44.36F^2 + 0.000081x^2 + 52.34F - 0.070x - 0.12Fx + 15.44 \quad (6)$$

$$\frac{dA_p}{dx} = 0.000162x - 0.12F - 0.07$$

$$\text{let } \frac{dA_p}{dx} := 0$$

$$\Rightarrow 0.000162x - 0.12F - 0.07 = 0$$

$$\Rightarrow x = 740.740740740741F + 432.098765432099$$

$$\Rightarrow x = \frac{600F + 350}{0.81} \quad (7)$$

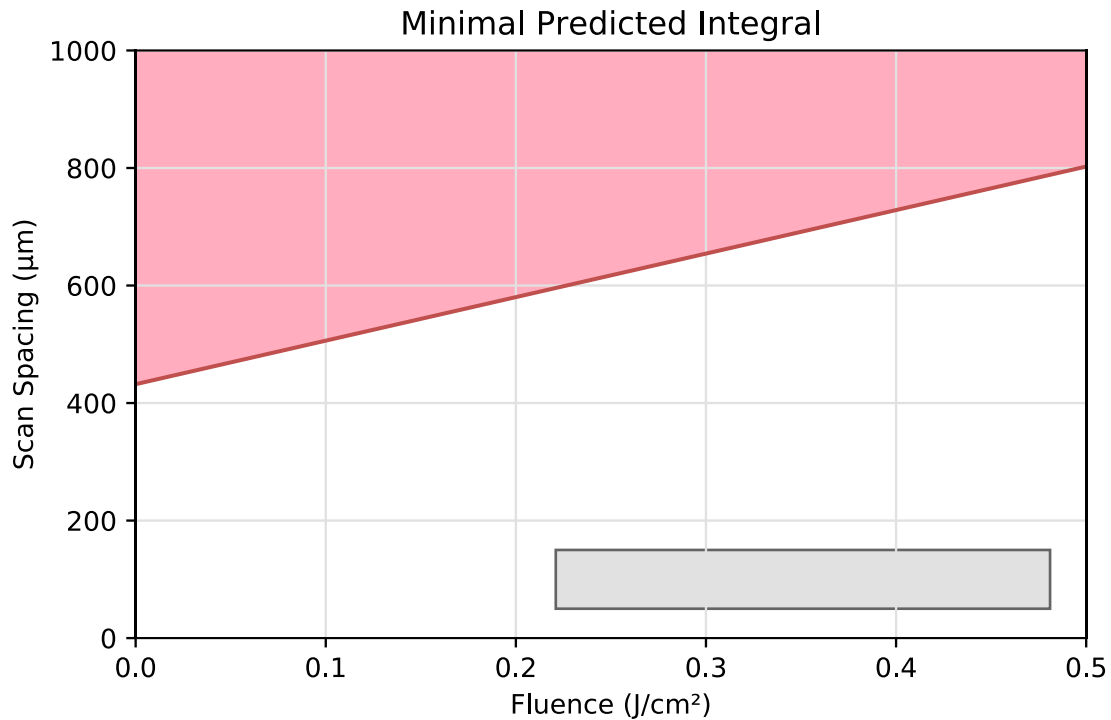


Figure 41. A plot of the line described by (7) (red) and the process space examined during this study (grey). The pink area above the line is the area where where the plasmonic peak integral is predicted to begin increasing again.

As can be seen in Figure 41 the process space examined falls well within the space wherein the trend predicted by the derived model behaves as would be intuitively expected. However, for scan spacings above a certain range (highlighted on the graph) the resulting plasmonic peak integral would be expected to counterintuitively begin increasing again. This would imply that a scan spacing of, for example, 1 m would result in an absurdly high intensity plasmonic peak which goes against the trend that might intuitively be expected. Thus, it should be stated that the derived model likely begins to deviate greatly from reality as the parameters move further outside the process space examined and that further refinement of can likely significantly expand the range over which the model can be applied. As such, future work examining the limits of this model and aiming to further refine it might begin by evaluating the validity of this

unexpected prediction through the production and characterisation of samples whose parameters fall above the line of minima.

### 3.3 Conclusions on the CAP Development Process

As the refinement of CAP progressed from the initial discovery of the process (Section 3.1) to its current form (Section 3.2.3), it has been developed into a reliably reproducible and predictable technique. Furthermore, although the current models are useful for the fabrication of nanostructured surfaces it is clear that there is much room for further refinement of the process to allow for an even greater degree of control and usability. The early exploration of the process (Section 3.1) shows that despite the emphasis placed on gold on COP during these studies the process is applicable to a wide variety of metals and substrates, offering many potential avenues for future research into uses for the methodology. In addition, the somewhat novel capability of CAP to allow for the easy deposition of surfaces with a complex macroscale shape suggests potential applicability in the development of novel types of flexible circuitry and similar applications.

The data gathered during the course of development offers insights into possible mechanisms for the process, which is an important aspect of learning to better control it. As discussed in Section 3.2.3 the results of the study support the hypothesis that the CAP mechanism is similar to the mechanism of conventional PLD methodologies, with the distinction of the exponentially smaller target-substrate distance required in the CAP methodology likely being primarily accounted for by the effects of plasma confinement. Future work on the elucidation of a mechanism for the CAP process would likely benefit greatly from the application of Optical Emission Spectroscopy (OES) of the plume during ablation to examine the plasma dynamics during the CAP process<sup>163,172</sup>.

In the final study performed, four reliably predictive statistically significant models were derived describing relationships between the process parameters and the resulting properties of the films deposited (Section 3.2.3). These models allowed for the reliable prediction of particle size (3), particle dispersity (4), plasmonic peak position (5) and plasmonic peak area (6) based on the fluence, scan spacing and scan speed within the process space being examined. Outside the process space these models may or may not continue to hold true and future work should focus on expanding the predictable process space of the CAP methodology. An example of a potentially necessary future refinement to these models is discussed in Section 3.2.3. As noted, there are some indications that far outside the process space examined the plasmonic peak area model (6) may begin to break down and we can mathematically derive a scan spacing range beyond which the results become quite counterintuitive (see Equation (7) and Figure 41). However, despite this, the models have been shown to be statistically significant and reliably predictive within the parameter ranges tested and for the purposes of this work they are therefore considered to be completely sufficient.

## 4. Development of Sensor Surface Fabrication Methods

Following the studies outlined in Section 3 (which were intended to build a functional understanding of the CAP process, how to reliably carry out CAP deposition and the properties of the films it produces) a series of experiments were performed to begin applying this technique to biosensor fabrication.

Based on the information presented in Chapter 2, it was decided that electronic biosensing methods would likely prove the most reliable way to readily utilise the deposited films in a sensor platform. To confirm this, a quick proof-of-concept experiment was devised to demonstrate the conductometric response of a CAP deposited film to a surface interaction. As discussed in Section 2.6 gold nanostructures are commonly functionalised via thiolation as this is among the simplest methods available. Thiol groups spontaneously form covalent bonds with gold atoms in a reaction readily exploitable for the functionalisation of gold nanoparticles. This chemical reaction between a gold surface and a thiol in solution is commonly applied in the functionalisation of biosensors. This thiolation reaction should also provide a measurable conductometric response in the gold surface and this response is easily measurable and varies with the chemistry of the thiol used<sup>173</sup>. As a result this thiolation reaction provides an easy way to demonstrate a conductometric response in the films deposited. Based on this an experiment was designed to examine the interaction of CAP deposited nanostructured gold films and the readily available thiol 2-mercaptoethanol.

Due to the limitations of the 4-point conductometric probe used at this stage of the work (discussed in Section 3.2.2b) the initial proof-of-concept tests were performed on a sample comprised of a nanostructured gold

film deposited on a glass substrate, rather than COP. In an initial experiment, a nanostructured gold film was deposited on glass according to a set of parameters previously found to result in thick depositions on glass (Section 4.1), these parameters were: scan speed: 3 mm/s, fluence: 0.79 J/cm<sup>2</sup>, scan spacing: 150 μm and vertical spacing: 0 μm. The conductivity of this sample was then measured using the 4-point conductometric probe (Table 8). A droplet of 2-mercaptoethanol was then placed on this surface for 10 minutes, before the sample was thoroughly rinsed with deionised water followed by ethanol to ensure the removal of any unbonded thiol and left to dry before further testing. The conductivity of this sample was then measured again (Table 8).

Table 8. The electrical properties of the sample before and after thiolation, in addition to the difference between them as both a value and a percentage change. This test served as a quick demonstration of a CAP film changing its preoperties responding to surface interaction (a prerequisite for use as a sensor).

Measurement	Resistivity (mΩ · cm)	Hall Mobility (cm <sup>2</sup> /(V · s))	Hall Coefficient (m <sup>2</sup> /C)
<b>Before Thiolation</b>	1.267	0.275	-0.000348
<b>After Thiolation</b>	1.884	0.097	-0.000183
<b>Difference</b>	+0.62 (+48.7%)	-0.178 (-64.8%)	+0.000165 (+47.5%)

As can be seen from the data presented in Table 8, the thiolation of the nanostructured surface produced a significant change in its electrical properties, resulting in a 48.7% increase in the resistivity of the film. The hall mobility and hall coefficient of the film also changed significantly, exhibiting a 64.8% decrease and 47.5% increase respectively. This

suggests that the resistivity change resulting from the thiolation of the surface is due to changes in the mobility and density of charge carrying species in the metal film<sup>174</sup>. This is likely due to the bonding interactions occurring between the gold and sulfur atoms, drawing valence electrons from the electron sea of the metallic film and thus reducing their density throughout as has been observed in other gold nanostructures<sup>175</sup>. This behaviour reinforces the hypothesis that these films have potential applications in the fabrication of electronic sensor platforms, as it shows their significant electronic response to interaction occurring at the metallic surface of the film.

Following this result suggesting the potential efficacy of CAP films as an immobilization surface for electronic sensor platforms, work began on applying this method in the fabrication of electrodes on COP suitable for such a sensor while work also began on the acquisition of a more suitable conductometer for biosensing purposes.

## 4.1 Exploration of Interdigitated Electrode Designs

As discussed in Section 2.3.2, the design of electronic biosensor platforms tends to favour the “Interdigitated Electrode” design, wherein the each individual electrode is comprised of a series of intertwined linear pieces. Based on this convention and the reasoning behind it, initial work on the fabrication of sensor surfaces via the CAP methodology focused on the deposition of similar interdigitated electrode designs. By making use of the capability of the CAP process to draw complex shapes based on toolpaths (Section 3.1, Figure 25) several toolpaths were prepared (as .dxf files) for the single-step deposition of interdigitated electrode sensors (Figure 42).

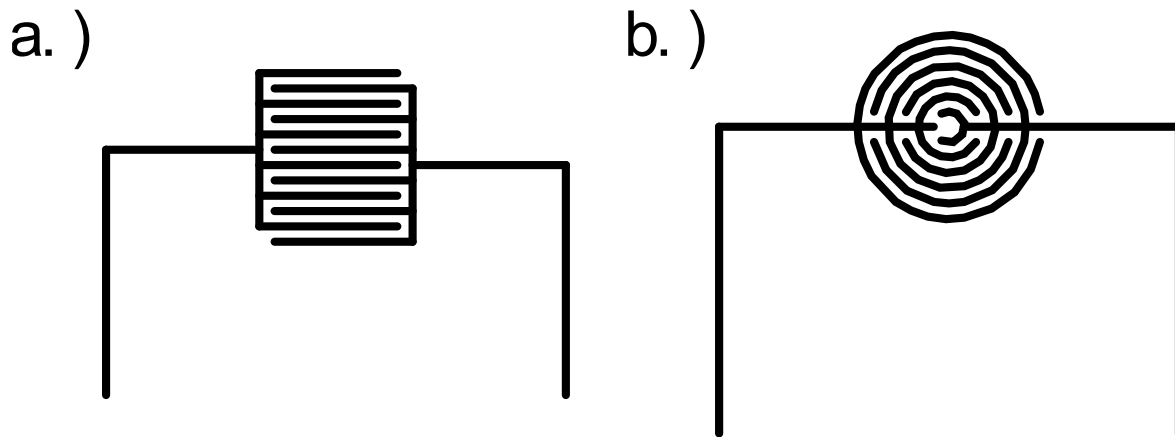


Figure 42. Toolpaths for electrode designs deposited on  $25\text{mm}^2$  areas based on the a.) square and b.) circular standard forms of interdigitated electrode designs. These lines describe the paths traced by the laser during CAP deposition of these shapes.

To achieve a successful deposition of interdigitated electrodes, a rudimentary understanding of the behaviour of CAP specifically applied to linear depositions would be required. To begin understanding this behaviour, an initial study was planned based on the simple deposition of numerous straight lines on a COP substrate using the same semi-optimised methodology applied in Section 3.2.3 (to easily allow for variation of the vertical spacing parameter). Using this methodology, A number of lines were deposited (Figure 43) according to a DoE model (similar to the studies performed in Section 3) and these lines were then examined with optical microscopy to measure their thickness (in microns) and contiguity (Table 9). Contiguity was recorded as a binary value of 1 for a contiguous line and 0 for a line with clearly observable gaps along it.

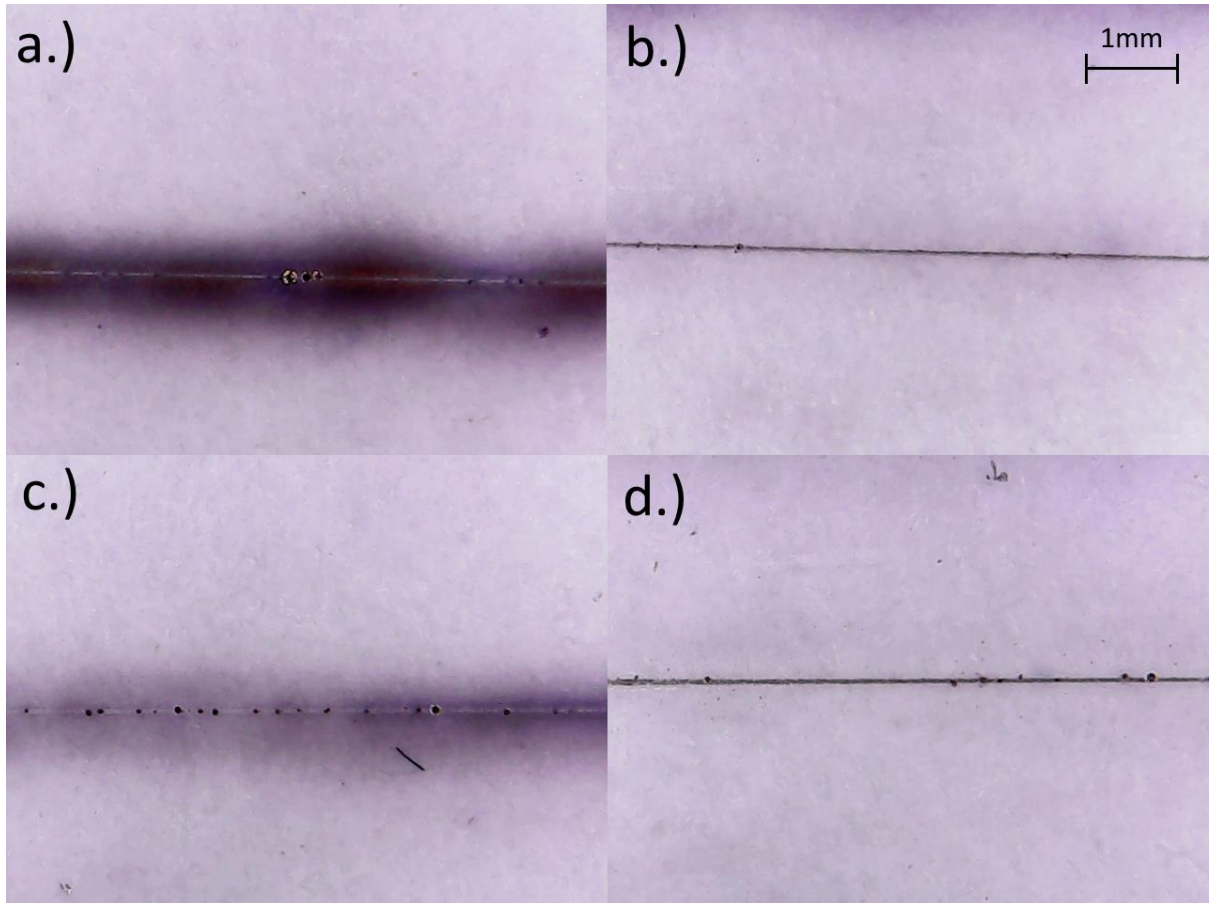


Figure 43. Optical microscopic images of samples a.) 15, b.) 17, c.) 14 and d.) 8 at the same magnification. Recorded line widths were taken to include all darkened areas along the scan path, to the nearest 10 $\mu$ m.

Table 9. The DoE parameters and measured outputs from the linear CAP deposition study. The line width output is to within  $\pm 5 \mu$ m and contiguity is simply recorded as a simple binary “0” for lines with breakages and “1” for contiguous lines.

Sample number	Fluence (J/cm <sup>2</sup> )	Scan Speed (mm/s)	Vertical Spacing ( $\mu$ m)	Line Width ( $\mu$ m)	Contiguity
1	0.151	18.00	0	200	0
2	0.151	10.00	188	200	0
3	0.151	18.00	188	400	0

Sample number	Fluence (J/cm <sup>2</sup> )	Scan Speed (mm/s)	Vertical Spacing (μm)	Line Width (μm)	Contiguity
4	0.151	10.00	0	300	0
5	0.793	18.00	188	350	0
6	0.793	2.00	188	40	0
7	0.582	2.00	0	40	1
8	0.582	2.00	188	50	1
9	0.582	10.00	188	30	0
10	0.582	10.00	0	40	0
11	0.793	2.00	0	350	0
12	0.582	18.00	188	40	0
13	0.582	18.00	0	300	0
14	0.151	2.00	188	750	0
15	0.151	2.00	0	900	0
16	0.793	18.00	0	50	1
17	0.793	10.00	0	40	1
18	0.793	10.00	188	220	0

Despite this DoE study, no strong correlations were found describing how to optimise the process for the deposition of contiguous lines. In the absence of a reliably predictive model to aid in the process of optimisation, the deposition of thin, contiguous electrodes would need to be optimised by different means. This optimisation was performed by simply selecting parameters known to give acceptable results from the study and then varying the parameters individually by small amounts and selecting those found to result in the most desirable and reproducible characteristics for further iterative testing. By gradually improving the depositions until no changes could be made without observing worse

results a local optimum would eventually be found, similar to the mathematical concept of a “Hill-Climbing Algorithm”.

As testing began, these initial attempts to deposit such electrodes directly via the CAP methodology resulted in the discovery of an interesting limitation to the CAP deposition of linear features. As can be seen in Figure 44, attempts to directly deposit interdigitated electrodes resulted in the appearance of numerous gaps that would make the electrodes unsuitable for sensing purposes. It was also noted that these gaps tended to appear mostly where a laser scanned across a previously deposited line. As such, it was hypothesised that this was probably due to the laser ablating the already deposited nanostructures from the polymer back onto the target, an effect similar to that observed in the LIFT process. Based on this hypothesis, these gaps were henceforth be referred to as the “LIFT zone” of the deposited lines. These gaps in the deposited electrodes proved to be a hindrance to the conductivity of the electrodes, thus causing them to be unsuitable for the desired application.

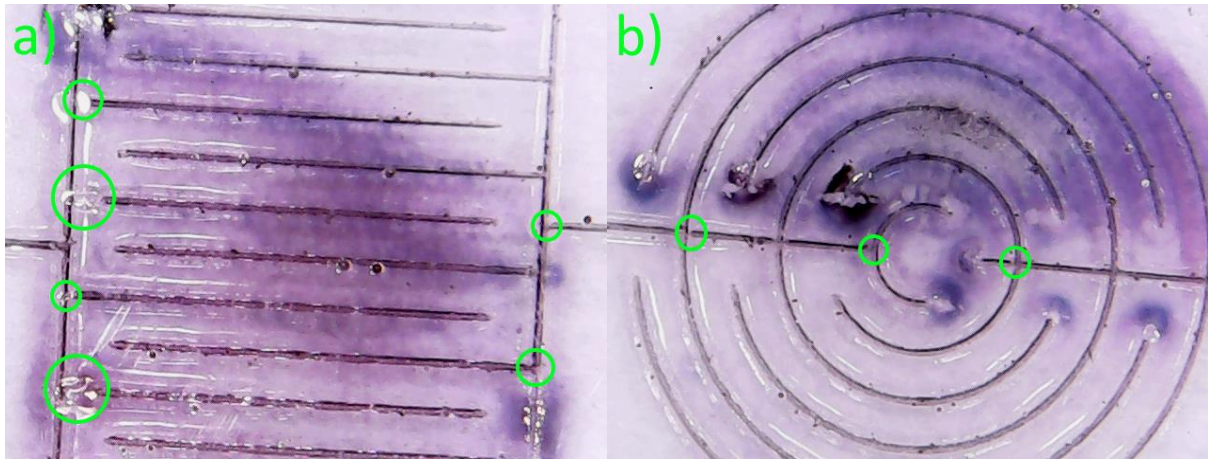


Figure 44. Microscope images of CAP deposited a) square and b) circular interdigitated electrodes (dimensions 5mm x 5mm and 5.64mm diameter so that both cover an equal area). Note the LIFT zone gaps highlighted within the green circles.

Once this phenomenon was observed, an experiment was planned to determine if the effect could be mitigated or not. For this experiment, large CAP surfaces (2 rectangles of approximately 5 mm x 100 mm, one for the samples at each vertical spacing) were deposited and the laser was then scanned across this already deposited surface. The lines were deposited parallel to the short edge on every pass and the laser parameters for each pass were selected according to Table 9 (previously used to examine linear CAP deposition). Upon examination of the samples it was noted that the deposited lines generally fell somewhere on a spectrum of deposition types as exhibited in Figure 45. The first type observed was the thin, contiguous line with a large LIFT zone (Figure 45a), gradually giving way to lines with an equally large LIFT zone and clearly visible breakages (Figure 45b). Other samples appeared as lines of almost no deposition but still with a large LIFT zone (Figure 45c) finally giving way to samples with no deposition present at all but a clearly defined, small LIFT zone (Figure 45d). All examples in Figure 45 are at a vertical spacing of 0  $\mu\text{m}$ , but the same trend was noted in the samples at a spacing of 188  $\mu\text{m}$ . The clear trend on display in the samples suggested

that as fluence is reduced and scan speed is increased the LIFT zone for the deposited line eventually begins to decrease. However, these tests also suggested that the process crosses into a range wherein no contiguous line is deposited long before the LIFT zone begins to shrink. Based on this observation, it was decided that the deposition of a thin contiguous line was not likely and that if it was possible the time required to optimise for these conditions would be excessive. As a result, it was decided that the electrode design should instead be adapted to consist of a single line to simply avoid the LIFT zone problem entirely.

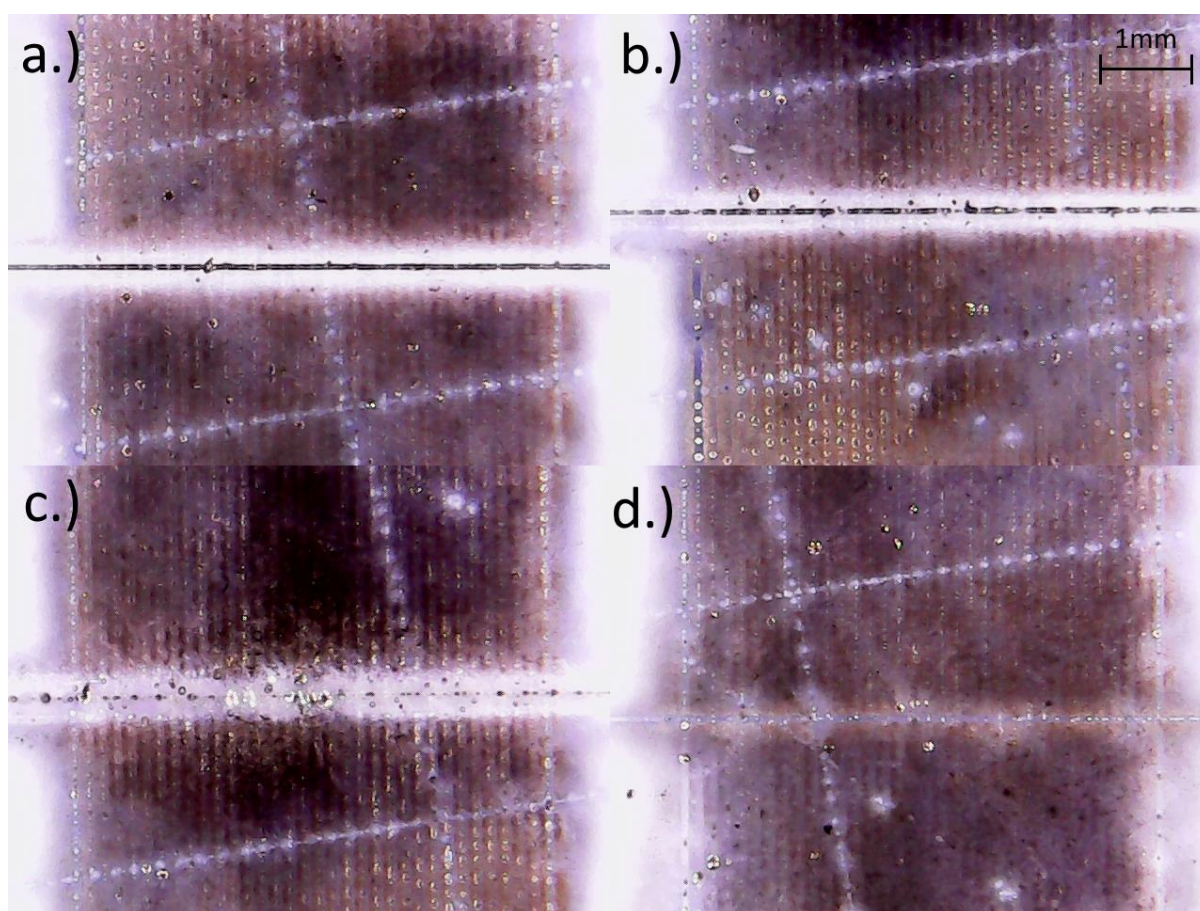


Figure 45. Images of several linear deposition tests and their respective LIFT zones. Sample numbers are a.) 10, b.) 17, c.) 11 and d.) 1. As can be seen in image d, a LIFT zone is still present when no visible line was deposited.

Considering the aim of the interdigitated electrode design (to allow maximum surface interaction between electrodes in as compact a space

as possible) while bearing in mind the requirement for the deposition of a single continuous line for each electrode, it was eventually decided that the most logical design was to deposit a pair of tightly interlocking spirals as electrodes (Figure 46, henceforth referred to as “spiral electrodes”). Using this design the space in which the electrode is deposited would be used efficiently, the electrodes would each be deposited as a single line and the cathode and anode should be close enough to easily interact with each other. In addition to increasing their ability to interact with one another, minimizing the distance between the electrodes also allows the interlocking spiral electrodes to be longer, increasing the exposed area that can participate in these interactions between electrodes and allowing for functionalisation with more detection molecule. During the previous studies the observed LIFT zone was generally found to extend no further than approximately 50 $\mu\text{m}$  from the deposited lines. The deposited lines were also found to generally have a thickness below 40 $\mu\text{m}$  when a contiguous, well-defined line was deposited. Based on these pieces of information, it was extrapolated that the minimum possible distance between the electrodes to ensure that they are both outside the LIFT zone of the other should be approximately 90  $\mu\text{m}$ . As such it was decided to deposit the electrodes with a centre line gap of 100  $\mu\text{m}$  between each spiral, to allow some space for errors and inaccuracies.

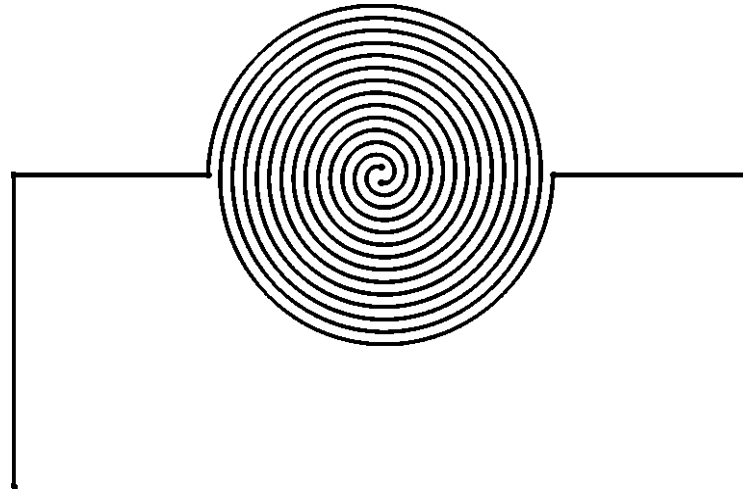


Figure 46. The toolpath prepared for the deposition of the redesigned electrodes. Each electrode is comprised of a single line spiralling towards the centre with a consistent distance to the other electrode on either side.

Following the preparation of this design, numerous tests were made attempting to deposit these spiral electrodes on COP. These depositions were performed using the more optimised CAP setup from the experiment described in section 4.3, thus using a  $50\mu\text{m}$  gap. This setup was used due to the fact it had proven in previous experiments to give the most reproducible results when compared with the other setups used. Following the deposition of several straight lines at various parameters, a parameter set was found that appeared to give reliable, thin, contiguous depositions (scan speed:  $18\text{ mm/s}$ , fluence:  $0.665\text{ J/cm}^2$ ) and this was selected as the starting point for the optimisation process. The optimisation process then proceeded through iterative incremental adjustment, as previously described in the linear deposition tests. Following the examination of samples produced in triplicate at 11 different parameter sets, each making small adjustments to the deposition parameters, a set of parameters was found that resulted in a thin, contiguous deposition in all 3 repetitions (Figure 47).

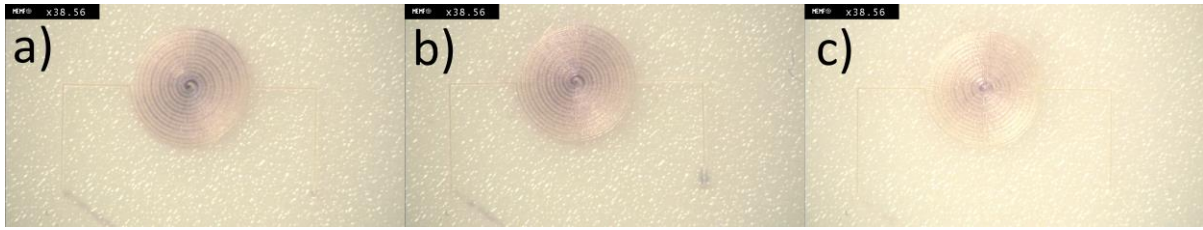


Figure 47. Samples produced at scan speed: 17 mm/s, Fluence: 0.671 J/cm<sup>2</sup>. Each of the samples fabricated with these parameters shows a thin, contiguous deposition of spiral electrodes.

The samples visible in Figure 47 were produced at a scan speed of 17 mm/s, fluence of 0.671 J/cm<sup>2</sup>. These parameters allowed for the reproducible fabrication of spiral electrodes, with the only visible imperfection being the small gap visible in the bottom right corner of sample b. This imperfection is at the beginning of the toolpath and is therefore likely due to the laser output having not yet stabilised (its output can be somewhat inconsistent for the first few seconds after it is engaged).

Following the production of these electrodes, a conductometer more suitable for sensor testing (a Gamry Interface 1000 Potentiostat) was obtained and a precursory attempt was made to utilise the bare electrode samples to perform a CV measurement. This first attempt showed lower than expected conductivity. It was hypothesised that the reason for this may be due to the laser etching a channel in the polymer during the deposition step. This was further evidenced by the fact that past attempts at conductivity measurements using a 5mm x 5mm square deposition were successful, and CV attempts with the same samples also proved successful. To examine this hypothesised explanation, the sample used in the failed CV experiment was used in a cross-sectional SEM experiment, as shown in Figure 48.

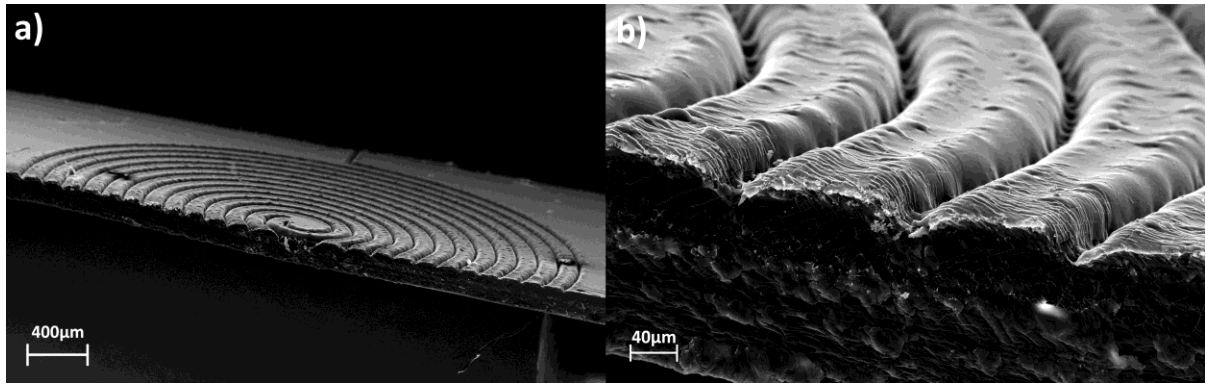


Figure 48. Cross-Sectional SEM analysis of the deposited spiral electrodes. Image b is zoomed in on the edge visible in image a. The spiral shaped channels visible align with the path of the laser, suggesting that they were likely created by the laser during deposition.

As can be seen in Figure 48, the CAP deposition of spiral electrodes also resulted in the etching of deep channels that would make it difficult to establish an electrical contact with the electrodes. Based on this discovery, it was concluded that to further pursue this fabrication method in the face of such obstacles would likely take an inordinate amount of time, and thus that future designs should simply focus on improving the simpler square surface electrodes that had already proven to give a measurable conductometric signal. As the CAP technique is further developed in the future these interdigitated electrode designs may eventually be worth revisiting, as these early results do show potential for this fabrication method. However, at this relatively early stage of its development it is evident that the CAP technique is not yet mature enough to allow for the facile fabrication of such sensors.

## 4.2 Development of a Square Plate Electrode

As the project progressed, the focus of development shifted away from the ambitious interdigitated electrode inspired designs towards simpler

square plate electrodes. This was largely due to the emergent difficulties of interdigitated electrode deposition, as previously discussed.

As discussed at the beginning of Section 4 (and shown in the data in Table 8) early proof of concept tests demonstrated the desired conductometric response to surface interactions in a CAP deposited film. This early test was constrained to being performed with a surface deposited on a glass backing due to the limitations of the equipment available at the time but it demonstrates that a simple 5mm x 5mm square CAP film would likely be suitable as a basis for a conductometric sensor with further development. To achieve this goal, the deposited film should ideally be optimised to fulfill several conditions. These desired conditions for sensor development were:

- Minimum particle size: to maximise surface area
- Minimum polydispersity: to ensure minimum particle size (extremely large polydispersity at low peak particle size would still contain excessively large particles)
- Minimum interparticle distance: to maximise conductivity
- Maximum deposition thickness: to maximise surface area and sensor loading capacity, and minimise interparticle distance

To optimise for these parameters, we can apply several trends strongly established in Section 3.2.3. These trends are that:

- Lower scan spacing and higher fluence generally results in thicker films (based on the plasmonic integral model)
- At 50 $\mu\text{m}$  and high fluence, greater scan speed generally results in smaller particle size and lower polydispersity

Based on these observations, it was decided that samples should be produced at 50 $\mu\text{m}$  scan spacing, 18mm/s scan speed and the maximum achievable fluence of 0.79J/cm<sup>2</sup> with a PRF of 10kHz and a pulse width of

3.5 $\mu$ s. Although this fluence is somewhat outside the process space for which the applied model was decided that it was necessary to use the maximum possible fluence of the laser (following its repairs) to maximise film thickness and to work on the assumption that the previously established general trends would likely hold true if only one parameter was outside the process space. Initially, this combination of parameters was found to result in an unreliable deposition but it was noted that a large amount of particulates were produced during these failed depositions and that thin diagonal lines were left on the substrate. As a result of this observation it was hypothesised that the failed depositions were possibly due to the same “LIFT zone” effect discussed in Section 4.1, occurring as the laser moved from the end of each line to the beginning of the next one. Based on this assertion, the laser scanning pattern was changed to a bidirectional raster scan pattern and this was found result in a reliable deposition (Figure 49).

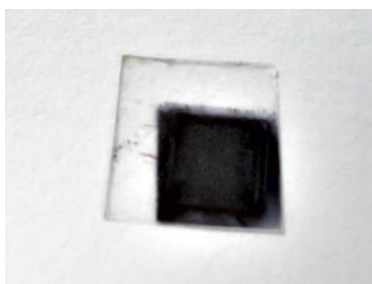


Figure 49. A photograph of a successful gold nanoparticle deposit film produced using a bidirectional raster scan pattern of 5 mm by 5 mm.

Following the successful deposition of these surfaces testing with the potentiometer found that the samples had unusually low conductivity despite the clearly thick deposition layer. As no model was available to optimise the conductivity of samples (due to problems discussed in Section 3.2.2 with the instrumentation available) it was decided at this point that a method was needed to reliably increase the conductivity of the fabricated surfaces, thus ensuring that conductive samples could be obtained regardless of the deposition parameters used.

To solve the conductivity problem noted it was first necessary to identify the possible reason for the observed low conductivities. As gold nanoparticles are well established to be conductive, the most immediately obvious hypothesized reason for low conductivity for a gold nanoparticle film would be lack of contact between deposited nanoparticles. With this hypothesis in mind, two possible solutions were proposed and tested.

#### 4.2.1 Methods for Conductivity Enhancement

The first possible solution was to laser sinter the deposited nanostructures immediately after deposition (Figure 50a). By melting the particles like this adjacent particles would be allowed to fuse with each other, decreasing the number of gaps and thus increasing the rate of electron percolation through the surface. If successful, this proposed solution has the advantage of being simple, straightforward, rapid and inexpensive. However, it would also likely have the major disadvantage of reducing the overall surface area of the sample because fused particles would have a lower surface area to volume ratio.

The second possible solution was to crosslink the adjacent particles with a conductive crosslinker of some kind (Figure 50b). By linking particles together with a suitably long conductive crosslinker electrons would be able to bridge any gaps in the film with minimal resistance, thus also increasing the rate of electron percolation without the need for a surface area reduction. This method would, however, likely increase the complexity and cost of any fabrication method. To mitigate this, the crosslinker should ideally be inexpensive and the chemistry used in the crosslinking process should be straightforward.

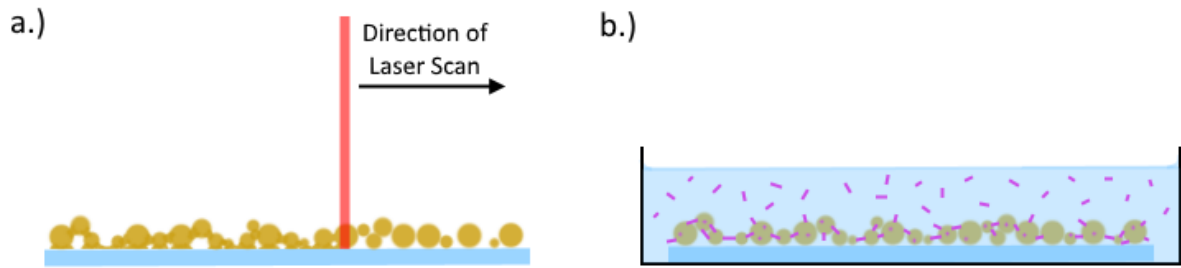


Figure 50. Simple diagrams exhibiting how a.) sintering and b.) chemical crosslinking can be used to bridge gaps between deposited particles. These methods were both tested as a possible conductivity enhancing post-processing step.

To test both of these proposed mechanisms for conductivity enhancement a reliable method of solid state conductometric testing would first be required. It was decided that a 4-point conductometric probe would be ideally suited for these tests, but as discussed in Section 3.2.2b the only such instrument available appeared to have grounding problems and would need to be modified to include a ground if more reliable data was to be obtained. Based on this, permission was obtained to make a minor modification to the instrument to ground the stage (Figure 51) and tests then began to examine the effectiveness of the two proposed methods for conductivity enhancement.

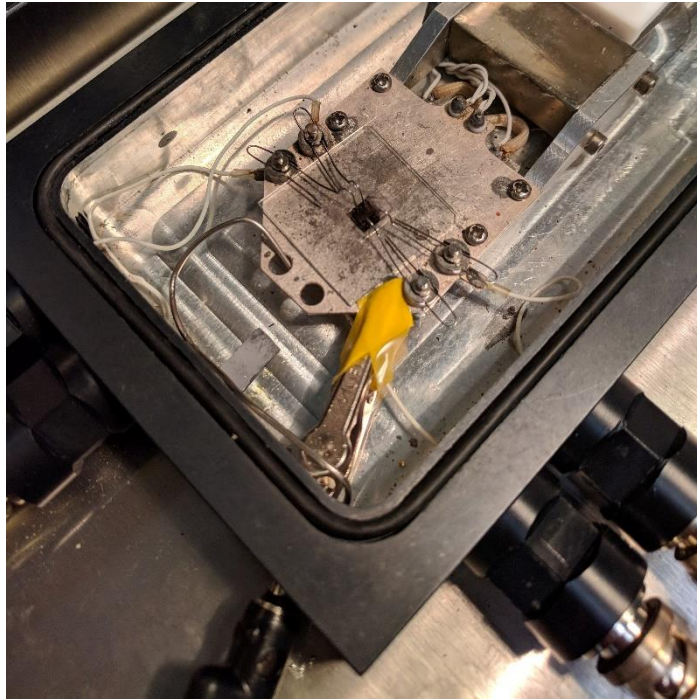


Figure 51. A photograph of the modified 4-point probe used during testing. Note the crocodile clip and metal wire being passed through the cooling inlet to ground the stage.

#### *4.2.1a Laser Sintering of CAP Films*

The method employed for the post deposition sintering of CAP deposited surfaces was kept relatively straightforward to allow for ease of manufacture. On the laser stage, immediately following deposition the sample was flipped, the stage height was changed and the laser was then scanned over the surface according to the desired sintering parameters (Figure 52). This method allowed for the rapid processing of samples and would be relatively simple to scale up to production scale in future work.

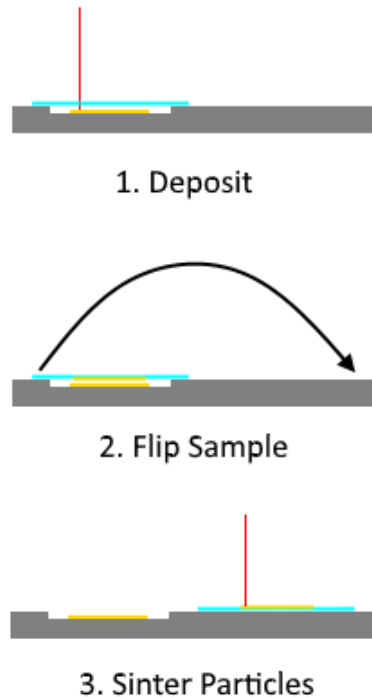


Figure 52. A diagram of the deposition and sintering process employed during this experiment. A film was first deposited, the sample was then flipped and the now upwards facing film was immediately sintered.

Initial tests to evaluate the efficacy of sintering as a conductivity enhancement method showed some slight conductivity enhancement, but no immediately obvious trends affecting the conductivity of the resulting sample. As such, it was decided that the quickest way to examine the factors determining conductivity and repeatability for this technique would best be evaluated using a simple DoE (Table 10) of input parameters, using only resistivity as an output parameter. In this experiment, the power output of the laser was fixed at its maximum (which is 1.22W at 10 kHz PRF) and the laser was defocused to increase/decrease the spot size. As the size of the laser spot was varied, it was decided that overlap percentage would be more relevant than directly measured scan spacing in this case because the size of the spot was no longer fixed as in earlier experiments. For the sake of this experiment, the overlap value used was a simple overlap of adjacent

scanlines (described by the Formula (10)) instead of a more accurate overlap value (described by the Formula (12)) and the reasons for this decision are discussed below.

Table 10. A table of the DoE input parameters and the measured response (resistivity) for the post deposition sintering process.

Sample number	Spot Size ( $\mu\text{m}$ )	Overlap (%)	Scan Speed (mm/s)	Resistivity ( $\Omega$ /sheet)
1	300.00	30.00	30.00	1.32E+9
2	300.00	70.00	10.00	6.66E+9
3	200.00	50.00	20.00	2.13E+9
4	100.00	30.00	30.00	1.52E+10
5	200.00	50.00	20.00	1.39E+6
6	100.00	70.00	10.00	7.28E+11
7	300.00	30.00	10.00	2.45E+8
8	300.00	30.00	10.00	1.86E+5
9	100.00	30.00	30.00	8.73E+9
10	300.00	30.00	10.00	6.70E+10
11	300.00	70.00	30.00	1.63E+7
12	300.00	70.00	10.00	4.48E+8
13	100.00	70.00	10.00	1.86E+10
14	200.00	50.00	20.00	5.59E+7
15	100.00	70.00	10.00	1.31E+8
16	100.00	70.00	30.00	6.58E+9
17	100.00	30.00	10.00	4.12E+10
18	100.00	30.00	10.00	4.48E+9

For pulsed laser setups, overlap between consecutive pulse is often calculated using a simple formula<sup>176</sup> ((8) or, as can be readily derived, (9) where  $L$  = distance between pulses in  $\mu\text{m}$ ,  $d_s$  = spot diameter in  $\mu\text{m}$ ,  $v$  = scan speed in mm/s and  $f$  = PRF in kHz).

$$\text{Consecutive Pulse Overlap}(\%) = \left(1 - \frac{L}{d_s}\right) \times 100 \quad (8)$$

$$L = \frac{v}{f}$$

$$\Rightarrow \text{Consecutive Pulse Overlap}(\%) = \left(1 - \frac{v}{fd_s}\right) \times 100 \quad (9)$$

In the experiment described however, this standard definition for overlap is not sufficient. This is because the laser spot is being raster scanned across the surface at scan spacings lower than the diameter of the defocused laser spots to ensure complete coverage of the surface during sintering. As such, the overlap of imparted fluence will also be dependant on the overlap between scanlines. As can be seen from (Figure 53) the overlap between scanlines can be readily calculated by treating the areas irradiated by each line as rectangular (which they should approximately be). Based on this supposition, an equation for adjacent line overlap can be derived (10).

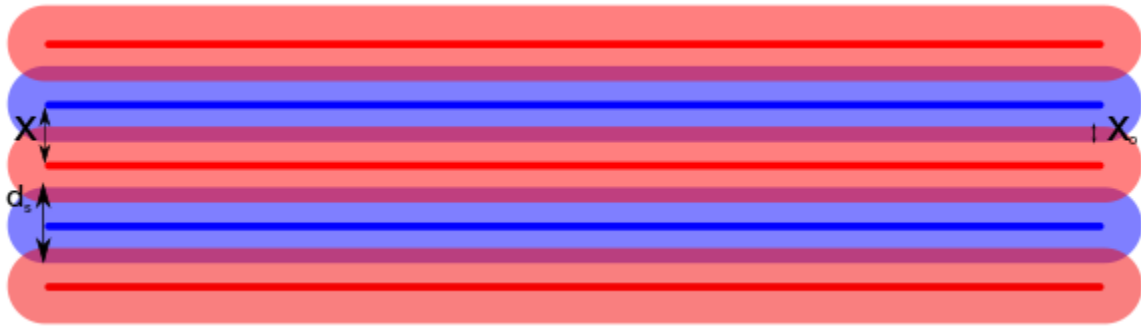


Figure 53. A diagram of overlapping adjacent scanlines. Adjacent scanlines alternate red/blue and the overlap area is shown as purple. The parameter  $x_o$  denotes the width of the overlap area.

$$x_o = 2 \left( \frac{d_s}{2} \right) - x$$

$$\Rightarrow x_o = d_s - x$$

$$\text{Adjacent Scanline Overlap}(\%) = \left( \frac{2x_o}{d_s} \right) \times 100$$

$$\Rightarrow \text{Adjacent Scanline Overlap}(\%) = \left( \frac{2(d_s - x)}{d_s} \right) \times 100$$

$$\Rightarrow \text{Adjacent Scanline Overlap}(\%) = \left( 2 - \frac{x}{d_s} \right) \times 100 \quad (10)$$

By multiplying these overlap percentages (as decimals), it is possible to derive a good approximation for total overlap for this experimental method (11). Based on this, a rather more complicated formula (12) can then be derived for overall overlap percentage that does not simplify further well.

$$\text{Overlap}(\%) = \frac{\text{Consecutive Pulse Overlap}(\%)}{100} \times \frac{\text{Adjacent Scanline Overlap}(\%)}{100} \times 100 \quad (11)$$

$$\Rightarrow \text{Overlap}(\%) = \left(1 - \frac{v}{fd_s}\right) \times \left(2 - \frac{x}{d_s}\right) \times 100 \quad (12)$$

The use of this overlap value was decided against because of the complexity of deriving suitable input parameters using a formula such as (12) and the increased resulting experimental complexity of the study. It was decided that a much more reliable and simpler approach would be to use the adjacent scanline overlap percentage value (10) and record the scan speed to control the input parameters of the sintering process. This would vary total overlap percentage, but would still result in the derivation of a model suitable for sintering process control.

Table 10 shows evidence that at certain process parameters conductivity enhancement via sintering is possible. Despite this, examination of the resulting data using Design-Expert 7<sup>159</sup> showed no statistically significant trends were discernible in the dataset. This would make the process difficult to optimize for maximum effectiveness and reproducibility. This lack of reproducibility in the dataset is further reinforced by its extremely low signal-to-noise ratio (as calculated using the true-SNR formula (2)) of -7.173 dB. This extremely low SNR value suggests that an important parameter in the sintering process may not be accounted for or that process control requires precision that is unachievable with the laser setup being used. Thus, it was decided to shift focus to the functionalization based conductivity enhancement method going forward.

#### *4.2.1b Crosslinking Functionalisation of CAP Films*

To enhance the conductivity of the sensor surfaces using functionalisation a suitable nanostructure crosslinker would first be required. It can be surmised based on an application of some principles of supramolecular chemistry that a desirable crosslinker should have the following properties:

- Charge transfer and conductivity: a suitable crosslinker should be able to transfer charge to and from the surface and conduct charge through its molecular structure
- Homodifunctionality: a suitable crosslinker should be homodifunctional, i.e. it should have two identical functional groups at each end capable of bonding to and transferring charge to/from the surface
- Rigidity: a suitable crosslinker should be rigid, so that its second binding functional group does not simply bind to the same surface as its first functional group
- Long or expandable length: a suitable crosslinker should be long enough to span any small gaps in the surface or should be capable of being stretched to such lengths
- Ease of availability: Although not absolutely vital, the crosslinker should ideally be readily available to keep the cost and complexity of sensor fabrication low

After some consideration, it was decided that the crosslinker that best fit these criteria the most would be benzene-1,4-dithiol (Figure 54), which has every desired property with the exception of length.

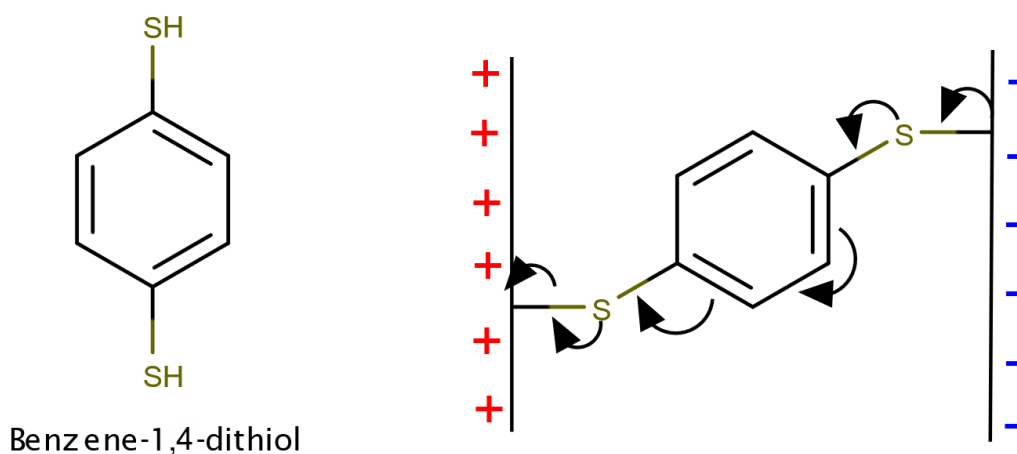


Figure 54. The molecular structure of benzene-1,4-dithiol (a) and a diagram of the mechanism by which it can transfer charge between surfaces (b).

A method was devised to compensate for this shortcoming of having a fixed, short length based on the ease of bonding thiol groups to gold surfaces. By repeatedly exposing of a sensor surface to alternating samples of crosslinker followed by a gold nanoparticle colloid a daisy-chain of nanoparticles should gradually form extending from the sensor surface. As these daisy chains extend they should eventually come into contact or even crosslink, allowing current to bridge any gaps in the sensor surface (Figure 55). This method of crosslinking also has the added advantage of increasing the surface area to volume ratio of the sample, as the daisy-chained nanoparticles are also suitable to serve as part of the sensing surface. This, in turn, would be have a positive effect on the sensitivity of any final biosensor produced using this method.

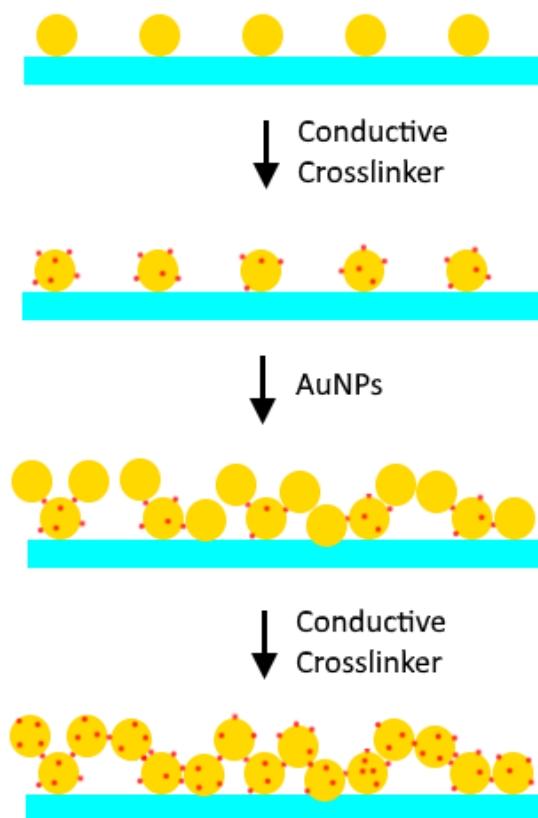


Figure 55. A diagram showing the underlying concept behind the functionalisation method employed. Note that the distances between particles in this example are somewhat exaggerated to demonstrate the underlying principle more clearly.

For testing purposes, it was identified that the most straightforward parameters that could be used to control this process were the time for which the sample was exposed to each reagent, and the number of times the exposure process was repeated. For these tests, a saturated aqueous solution of 1,4-dithiobenzene was used as the crosslinking solution and an aqueous gold nanoparticle colloid produced using PLAL. Despite the relatively low solubility of 1,4-dithiobenzene in water an aqueous solution was used for ease of process scaleup and because water is a more environmentally friendly solvent than most more effective organic solvents. The PLAL method for colloid production was a process-scale continuous flow setup currently being developed by my colleague Brian

Freeland that allowed for the rapid, large scale production of colloids with low dispersity and a small particle size. This readily available and inexpensive source of gold colloid did, however, have the disadvantage of having limited characterisation due to the limitations of the available instrumentation. Although UV/Vis and Dynamic Light Scattering (DLS) particle sizing data was available no particle count was possible as the only available particle enumeration techniques in-house were destructive to the sample. As particle count data is somewhat important to the future reproducibility of this process this problem was addressed through the development of a new, non-destructive particle enumeration method and this method is presented and discussed in Chapter 5.

By producing a number of samples and testing various exposure times and number of repeated exposures it was quickly found that almost all samples showed a significant increase in conductivity when processed in this fashion. As such, it was decided that there was no need for precise optimisation and tests proceeded simply using this method as initially tested. It was, however, found that for exposure times greater than 5 minutes and for more exposures than 3 the conductivity enhancement observed was far less pronounced. Because of this diminishing return, it was decided that future samples would be given 3 exposure repetitions each of 5 minutes length. The functionalisation method used from this point onwards was as follows:

1. Sample was rinsed with IPA
2. Sample was exposed to saturated aqueous 1,6-dithiobenzene crosslinker solution for 5 minutes
3. Sample was rinsed with IPA followed by deionised water
4. Sample was exposed to aqueous gold nanoparticle colloid of unknown concentration (this problem will be addressed in Section 5) for 5 minutes
5. Sample was rinsed with IPA followed by deionised water

6. Steps 2 to 5 were repeated 2 further times

This method generally resulted in the production of a sample with a sheet resistivity of between approximately  $4\text{E}+4 \text{ } \Omega/\text{sheet}$  and  $5\text{E}+4 \text{ } \Omega/\text{sheet}$  compared to an unfunctionalized resistivity of  $>1\text{E}+10 \text{ } \Omega/\text{sheet}$ , a resistivity decrease on the order of millions.

#### *4.2.1c Comparison of Sintering and Crosslinking Methods*

Comparing each method at this point (Figure 56), it seemed evident that while both conductivity enhancement methods appear to be effective to some extent the functionalisation method was simpler, more reliable and even has some added benefits for the purposes of sensor fabrication. Based on this observation, it was decided that future sensor development would benefit from focussing on the development of chemically functionalisation based sensor surfaces rather than sintering based surfaces.

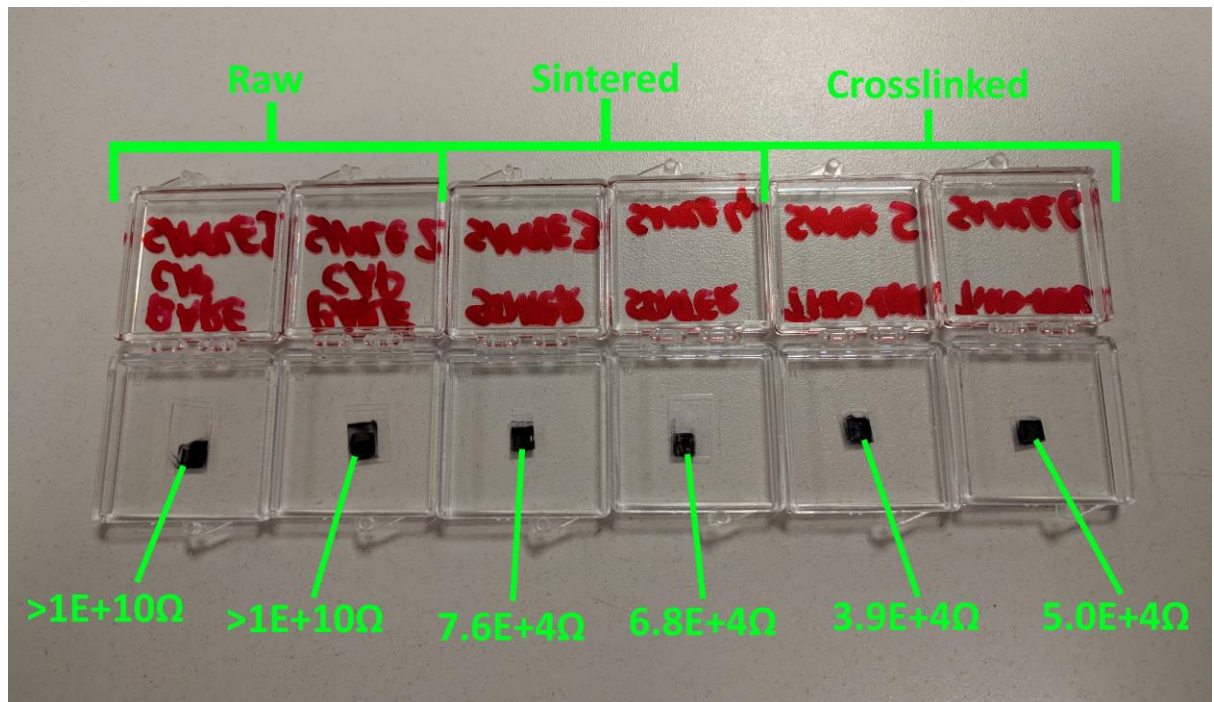


Figure 56. Pairs of samples taken at the most effective parameter sets for conductivity enhancement compared to untreated CAP samples. Resistivity values for each sample are included.

#### 4.2.2 Development of a Complete Working Electrode

To confirm the suitability of the conductivity-enhanced sensor surfaces for biosensing tests a simple proof-of-concept test was devised. For this test, the sensor would be contacted by a crocodile clip and placed in approximately 80 ml of a solution of Phosphate-Buffered Saline (PBS) as this solution is a common biological standard for mimicking the homeostatic conditions of living tissue in biosensor testing<sup>58,61,94,177,178</sup>.



Figure 57. A photograph of the proof-of-concept experiment described above. A finished sensor was immersed in PBS and exposed to 6-mercaptohexanol while repeated EIS measurements were taken. Change in EIS demonstrates a measurable response to interactions at the sensor surface.

The sample was then subjected to some preliminary conductometric tests in PBS with a glassy carbon counter-electrode and a silver chloride reference electrode (Figure 57) at which point several tests were quickly performed to confirm that a measurable conductometric response was present (Figure 58). Following this confirmation of a measurable conductometric signal, 250  $\mu\text{L}$  of a thiol (6-mercaptohexanol) was then added to the solution and the sample was then repeatedly subjected to EIS testing every 10 minutes for 24 hours, to measure the electrochemical response of the sensor surface over time (time resolved EIS, Figure 59).

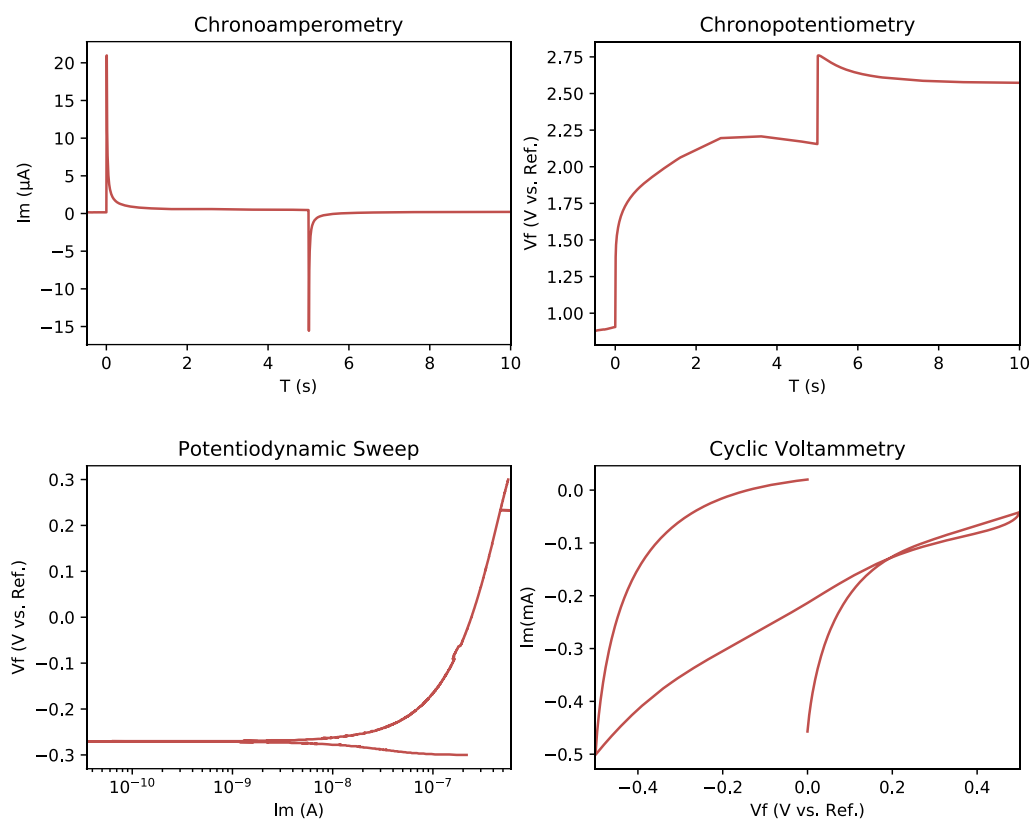


Figure 58. Plots of the conductometric data obtained before beginning the thiolation test. These tests were performed to confirm the presence of a measurable conductometric response in the sensor.

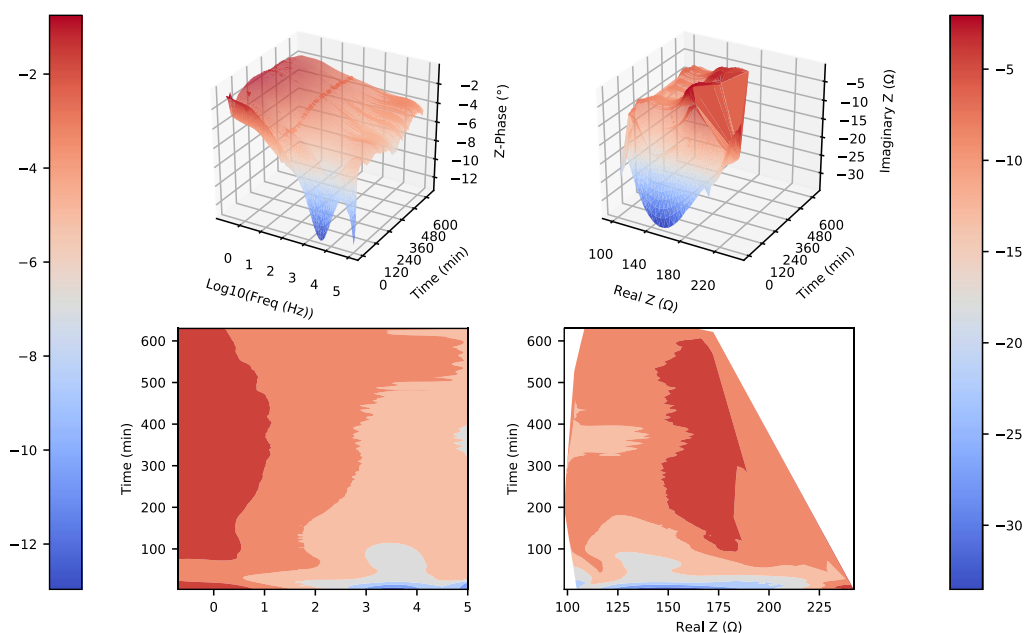


Figure 59. Surface and contour plots of the changes in EIS spectra observed over a 24 hour period in the presence of a thiol. The plots on the left are Bode Plots vs. time and on the right are Nyquist plots vs time. Colourbars are on the appropriate side for their plots and are relative to the Z-axes of the plots.

Upon returning to recover the experimental data, it was found that a extreme corrosion (Figure 60) had occurred on the crocodile clip and that the experiment had aborted after ten and a half hours (as can be seen in Figure 57 as the time axis does not extend to 24 hours). Upon reviewing the pre-test data (Figure 58) it was immediately clear that the data appeared to give early indications that corrosion was extremely likely to have been occurring. In particular, an extreme drift between cycles and eventual automated abort was noted in the CV scan. When this data was first obtained, it was thought that this drift and abort may be due to instability in the sensor surface and it was decided to proceed with other more time consuming tests and diagnose the issue later. However in the retrospective light of this time resolved EIS result corrosion seems the most likely culprit. Interestingly, this occurred despite a deliberate effort

to avoid having the crocodile clip contacting the testing solution. Of course, in an aqueous solution the meniscus where the sensor contacts the solution is quite large and this adhesion of water to the surface makes avoiding contact between the crocodile clip and solution extremely difficult.

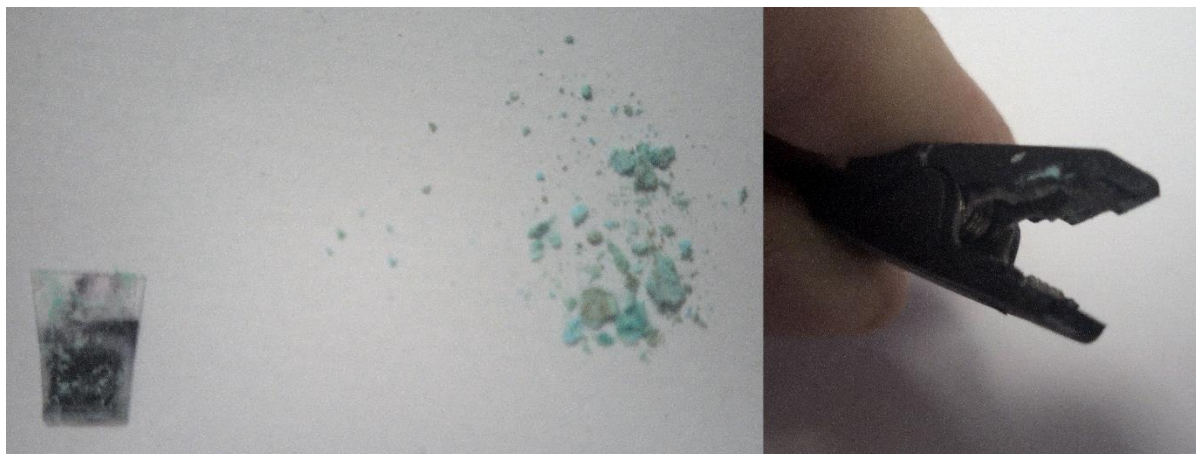


Figure 60. Photographs of the corroded sample discussed above, flaky pieces of the patina that was present and, on the right, the crocodile clip that was used to hold the sample while this corrosion occurred.

With the exception of this unexpected difficulty, the initial test for a conductometric response to a surface interaction with a small molecule appeared to have been promising. It is clear that within the first 10-20 minutes of the test an extreme change was observed in the EIS spectrum obtained. It was difficult to be certain whether this was due to corrosion or the desired sensor response but it is possible to briefly evaluate which is the most likely culprit. The crocodile clip used in the test appeared to be comprised of a common white metal suggesting it was either steel or aluminium. With this in mind, the green color of the oxidised metal produced strongly suggests that the crocodile clip is far more likely to be made of steel than aluminium. The corrosion of steel is a well studied topic, and it is known that the electrochemical corrosion of steel generally proceeds according to first-order or second-order reaction kinetics<sup>179</sup>. This suggests that a corrosion reaction would be expected to proceed

according to a linear or parabolic curve relative to time thus creating a linear or parabolic decay curve if we track the maximum of a decaying peak in a Bode or Nyquist plot. However, if we observe the decay behaviour of a single peak in Figure 59 (for example the large, clearly visible one that stretches between the  $10^3$  and  $10^4$  Hz frequency) it appears to decay logarithmically rather than linearly or parabolically. This would suggest that the initial big change in EIS characteristics was likely not due to corrosion and so, by process of elimination, is likely caused by surface interactions. Despite this deduction the lack of certainty meant that the test would need to be repeated using a different method designed to prevent any kind of contact between the crocodile clip and the testing solution.

It was decided that the simplest way to avoid this difficulty in future would be to create a contact that would allow for the crocodile clip to contact the sensor an appreciable distance from the test solution. The most obvious way to achieve this would be to simply deposit a stalk and contact plate with CAP during the initial deposition process (Figure 61, Design 1). Although this design seems obvious attempts at producing it found that it did not result in a contiguous deposition. It was quite clear that breakages were occurring specifically at points where sudden 90 degree turns were required in the middle of the length of the previous row. An example of such an area would be the point where the stalk contacted the main sensor plate. It was suspected that this may be due to the increased resident time of the laser as the galvanometer switches from horizontal scanning to vertical scanning. This longer resident time appeared to be creating a "LIFT Zone" similar to that discussed in Section 4.1. Iterating on this design, a new toolpath was created that allowed for the deposition of a similar sensor design without the need for any 90 degree turns (Figure 61, Design 2). While this deposition was successful and contiguous, the sensor itself gave almost no signal when connected to the potentiostat. This could be due to many variables that appear exist

in this kind of deposition that are constants in the more well understood square deposition method, such as the length of each scanline for example. With this result noted, the focus of contact fabrication shifted from the use of a CAP based contact fabrication method to a more proven method.

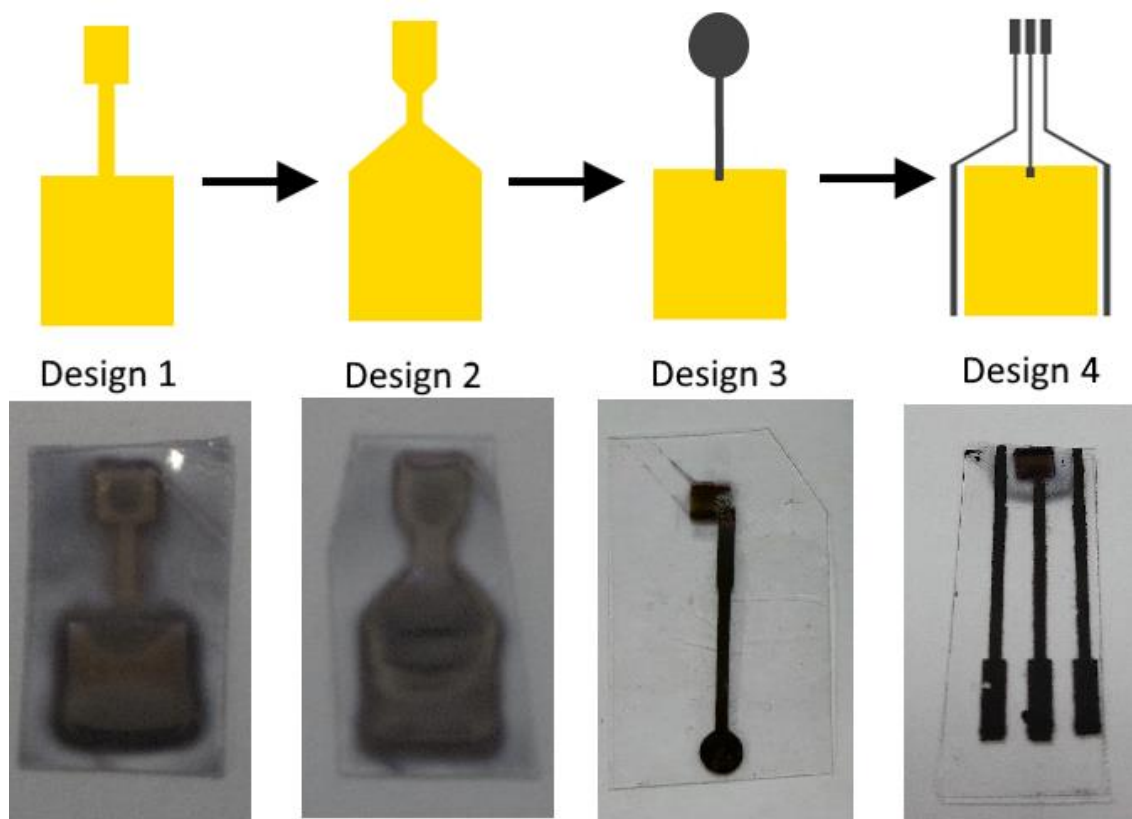


Figure 61. The various design stages of the sensor contacts as they evolved. The sensor contacts gradually evolved from CAP based contacts towards a more complete screen-printing based design.

One readily available method for sensor fabrication in common use today is the screen printing of conductive metallic inks. The screen printing technique is a simple methodology widely used in industry wherein an ink is forced through gaps in a fabric screen (like a stencil) to be impregnated onto the underlying surface. Such screen printed electrodes are generally simple, rapid and cheap to fabricate with the significant disadvantage of not being comprised of nanostructures and, therefore, having far lower

surface area for sensor surface interactions. CAP, by contrast, allows for the rapid, inexpensive fabrication of nanostructured biosensors with the drawback of being difficult to optimise (as seen above where a small change in conditions made the current optimised parameters ineffective). While both methodologies have their drawbacks they can be used to mitigate each others flaws. By CAP depositing a simple, square sensor surface (as can be done very reliably at this point) and then screen printing a contact for that surface these complementary techniques can be applied to fabricate a sensor design that is nanostructured while still being simple, rapid and cheap to fabricate.

For this application, the screen printing ink required would ideally be an inert ink that will not be functionalised by the conductivity enhancement method developed in Section 4.2.1. A container of conductive carbon ink sourced from Ercon (Ercon E3178 Carbon Ink) was acquired for this reason. A carbon based conductive ink should not undergo the same thio-functionalisation reaction as the sensor surface, unlike the other noble-metal based inks commonly used in these kinds of applications. To begin testing, a simple design based on a pre-existing screen was used. The screen allowed for the printing of “lollipop” shaped sensors, and would be used to print a long stalk contacting the CAP deposited sensing surface with a large circular disk at the opposing end onto which the crocodile clip could readily make contact (Figure 61, Design 3).

For testing purposes, 2 separate lollipop-style sensors were prepared. One used a 5mm x 5mm (25mm<sup>2</sup>) sensing surface similar to those used in testing so far and the other used a 10mm x 10mm (100mm<sup>2</sup>) sensing surface. A 100mm<sup>2</sup> surface was also used simply because there was a concern that the 25mm<sup>2</sup> surface may be too small to accurately align below the sensor screen for printing. While alignment proved difficult a contact was successfully printed for both sensor designs (Figure 62).



Figure 62. A photograph of conductometry tests being performed with a lollipop style sensor. The sensor was immersed in PBS and exposed to 6-mercaptohexanol. EIS measurements were then repeatedly taken, looking for a measurable electrochemical change in response to interactions at the sensor surface.

The conductometry data obtained for these samples (chronoamperometry to confirm that a signal is present and a CV to check for the same corrosion problems noted in the first test (Figure 63 for the 25mm<sup>2</sup> sample and Figure 64 for the 100mm<sup>2</sup> sample). Both samples clearly gave a response in the chronoamperometry test and their CV curves completed and showed no significant drift between scans.

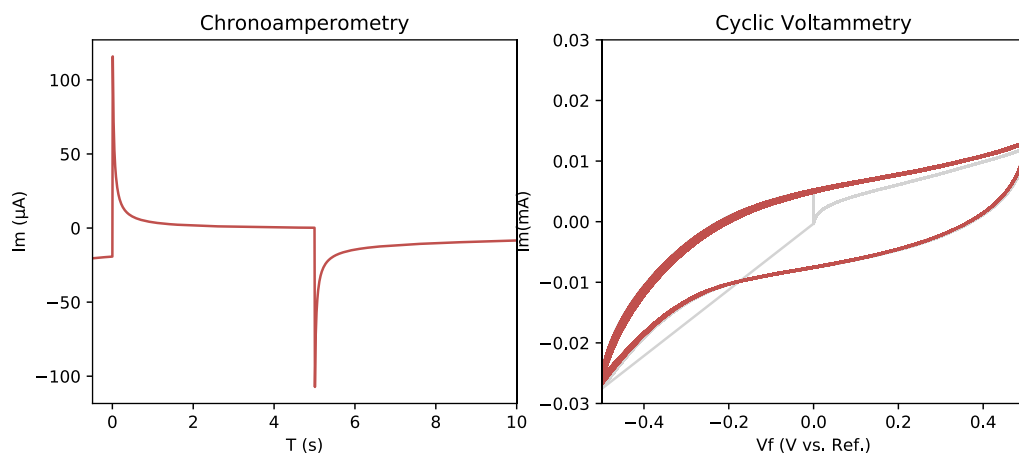


Figure 63. Chronoamperometry and cyclic voltammetry scans for the 25mm<sup>2</sup> lollipop sensor design. Note that the first and final scans on the CV are plotted in grey.

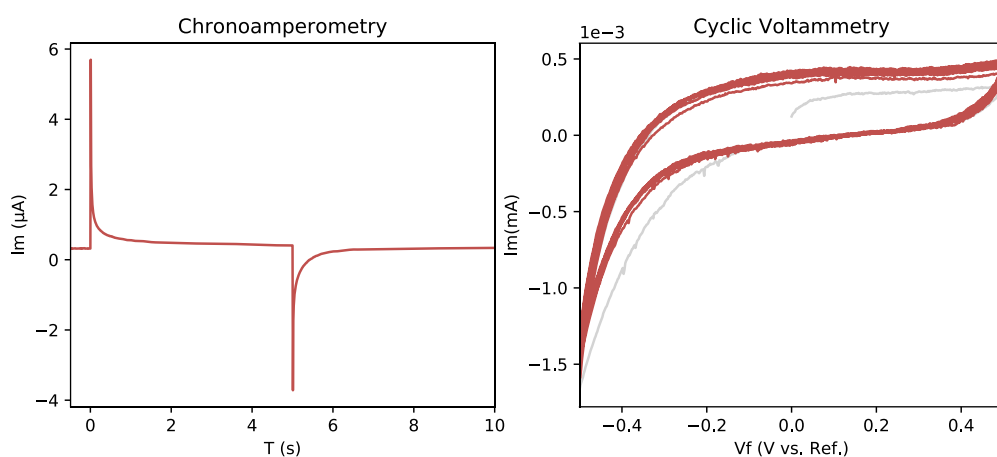


Figure 64. Chronoamperometry and cyclic voltammetry scans for the 100mm<sup>2</sup> slollipop sensor design. Note that y axis on the CV is scaed by  $10^{-3}$  and that the first and final scans on the CV are plotted in grey.

Based on this apparent improvement over the previous design a time-resolved EIS test was prepared. The 100 mm<sup>2</sup> sensor was used for this time-resolved EIS test as it was still unclear at this point whether or not accurate screen-printing of contacts for a 25 mm<sup>2</sup> sensor would be achievable with future, more precise sensor designs. As previous tests showed a strongly suspected response to the dissolved thiol within an

hour this time resolved EIS was performed by performing EIS scans as regularly as the instrument was capable of for 60 minutes. These EIS spectra were then collated into a single time-resolved spectrum (Figure 65). From this time resolved EIS plot, it is quite clear that some kind of interaction occurred at approximately the 15 minute mark. As no corrosion was observed at the end of the test and the crocodile clip was noted to have remained with over 2.5 cm of clearance between it and the surface of the testing solution it is reasonable to conclude that this event is the binding of 6-mercaptohexanol to the sensor surface. Based on this positive result, work then began to create a final sensor design.

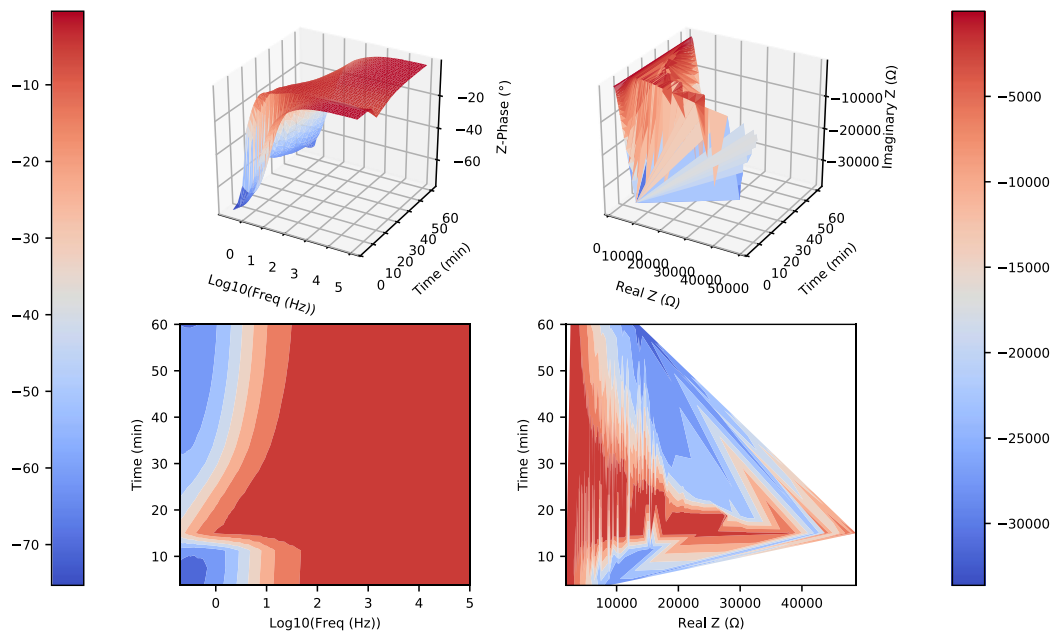


Figure 65. Time-resolved EIS spectra for the 10mm lollipop sensor design with thiol added at  $t=0s$ . The plots on the left are Bode Plots vs. time and on the right are Nyquist plots vs time. Colourbars are on the appropriate side for their plots and are relative to the Z-axes of the plots.

## 4.3 Design of Final Sensor Platform

In preparing a final sensor design the decision was made that any sensor produced should, ideally, conform to any pre-existing standard for sensor apparatus as this would make the design easily able to be tested and used by other researchers or even in a clinical setting. After checking the stock listings of multiple suppliers of sensors it was found that the most commonly used design is one wherein each of the three electrodes in the sensor trace back to 3 parallel contacts (as illustrated in Figure 61, Design 4). In such designs, the central contact is usually for the working electrode (the one with the sensing surface) while the left and right are for the counter-electrode and reference electrode. Such sensors are generally slotted into a stage with contacts that hold it in place for testing. Although the exact scale of these electrodes tends to vary somewhat this design does make it extremely easy to fabricate adapters for fitting sensors to differently sized instruments. It was decided that the exact stage to be used (and thus, the sensors to be used as a template) would be that manufactured by Gamry, as they also manufactured the potentiometer being used for testing.

During the design of a final sensor another important factor to consider was the choice of reference electrode material. A standard in electrochemical testing and sensor testing is the use of a silver (I) chloride reference electrode. However, despite extensive searching through literature dating back to texts as early and foundational as those published in the 1920s<sup>180,181</sup> to find the justification for this choice a stated explanation of exactly why this material became the standard has remained surprisingly elusive. Despite the difficulty of finding the specific reasoning for the use of silver chloride the generally stated requirements for a good reference electrode material are stability and a known

electrode potential. Therefore, presumably, any sufficiently stable material would be usable as an internally consistent reference electrode in a sensor setup. As such, considering the relative stability of carbon based electrodes the most obvious material for a reference electrode in our CAP based screen printed sensor design would be the carbon ink already being used in the contacts and counter electrode. This would greatly simplify the fabrication process and keep costs low. Based on this, it was decided that the design would use a screen printed counter electrode consisting of the same ink as the rest of the screen-printed components of the sensor.

Based on the criteria discussed above 2 sensor designs (Figure 66) were prepared, one for the 25 mm<sup>2</sup> sensor surface and one for the 100 mm<sup>2</sup> sensor surface. These designs consisted of sensor contacts capable of fitting into the gamry sensor stage to be used and incorporated a reference electrode and counter electrode all to be printed from conductive carbon ink in a single pass.

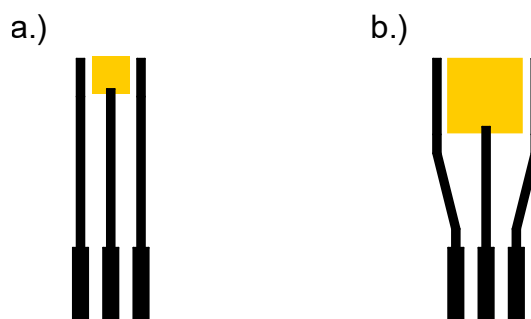


Figure 66. The final sensor designs. The golden areas are CAP deposited nanostructures (the sensing surface) and the black areas are conductive carbon ink. On an A4 page, the diagram of the sensors in this figure should match the size of the actual sensors.

For the contact printing step of the manufacturing process, the shapes of the black areas in Figure 66 would need to be cut from a fabric screen that would then be used as a screen in the screen-printing process. As the minimum size that a screen can be manufactured at is approximately the

size of an A4 page, placing only one of each sensor on the screen would leave a lot of unused space and wasted ink. To make maximum use of resources a design for the screen was created that consisted of a pattern of as many of each sensor as could reliably be fit in an area that can be covered by a single print pass (Figure 67). By doing this, the production of many sensors in parallel was also made possible, thus allowing for the rapid, inexpensive mass production of sensors. A screen based on this design was created (Figure 67) and this screen was used in all sensor manufacture beyond this point.

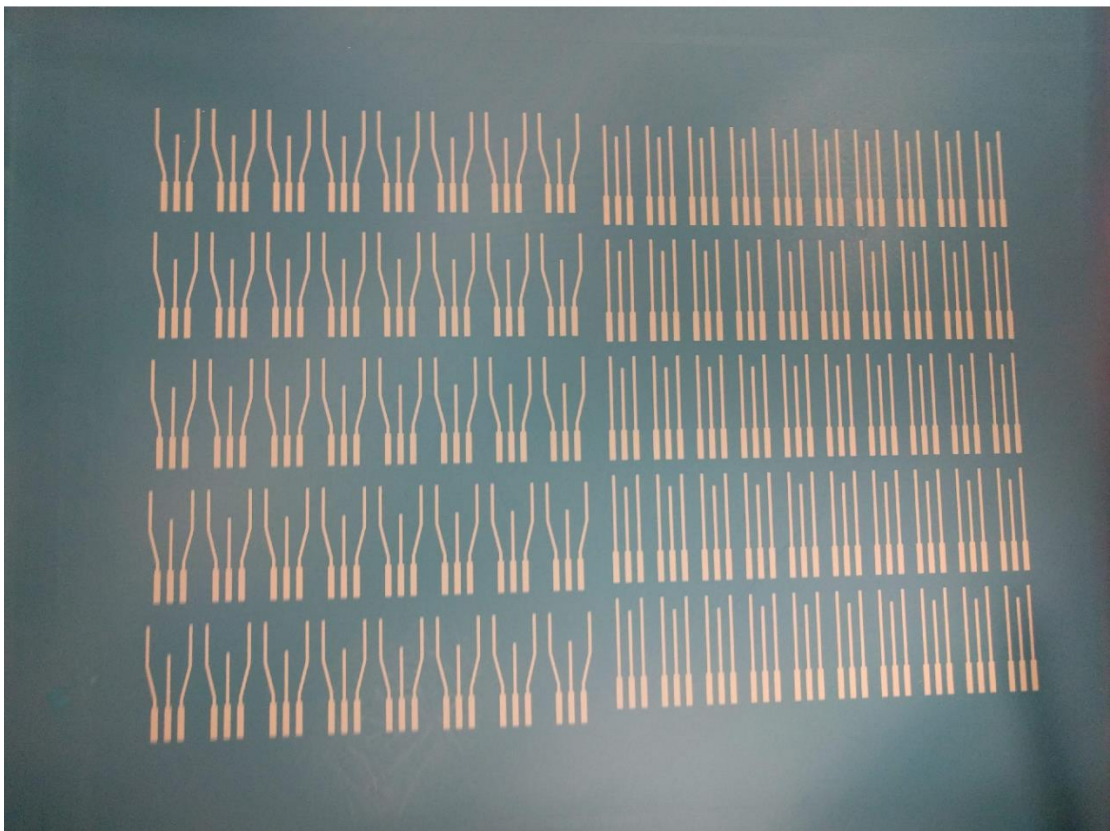
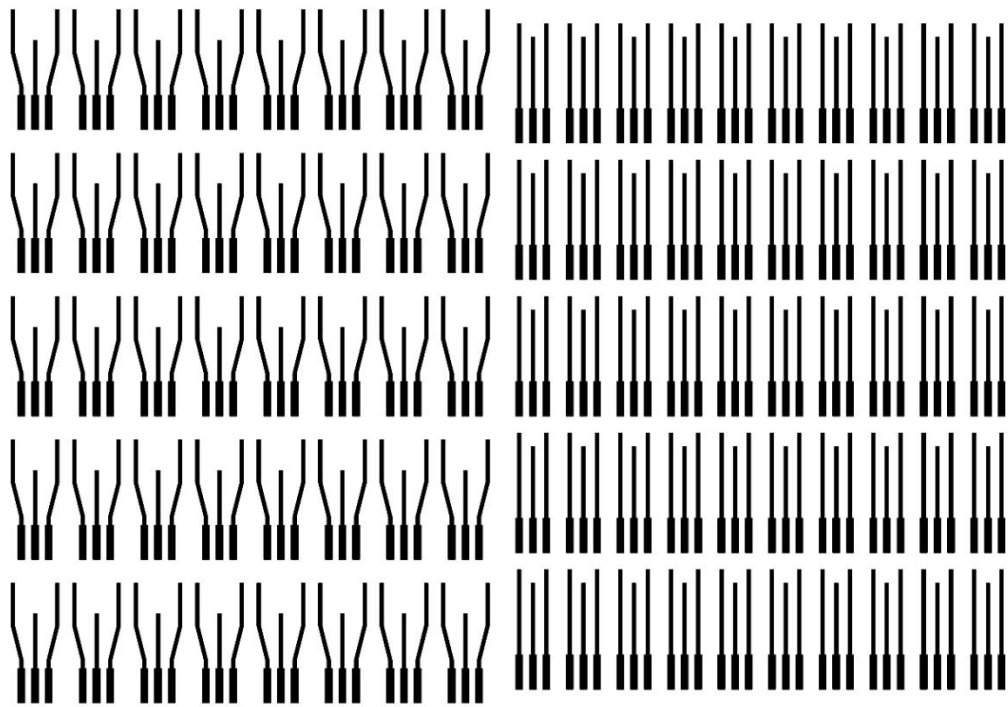


Figure 67. An image of the sensor screen layout designed (top) and the final, finished sensor screen (bottom).

When attempting practice runs of screen printing it was found that accurately aligning the screen for the printing of 25 mm<sup>2</sup> electrodes was possible with the use of an affixed, pre-printed page as a guide and the careful alignment of COP strips with appropriately spaced CAP deposited surfaces along their length. By using this design, it was possible to manufacture several hundred unfunctionalised sensor surfaces within only a single day and with only a single person (Figure 68). These surfaces could then go on to be processed as described in Section 4.2.1 to enhance their conductivity and finally to be functionalised as biosensors.



Figure 68. A photograph of a number of mass produced 25mm<sup>2</sup> biosensors (left) and a closer photograph of a single one of these sensors (right).

To test that these newly designed sensors reacted to thiols as previously demonstrated with earlier designs another time-resolved EIS experiment was performed. The sensor was first crosslinked (Section 4.2.1) as with

earlier tests and then placed in the standardised stage discussed earlier. The sensor was then submerged in a small volume of PBS testing solution before a thiol (6-mercaptohexanol) was added and the sensor was repeatedly subjected to EIS tests for half an hour (as previous tests have shown that the response appears to happen long before the 30 minute mark). In the resulting data the Nyquist plot was noted to be unusually noisy, and the reasons for this were unknown. However, based on the data in the Bode plot it was decided that this unusual Nyquist plot could be addressed at a later date if it was found to reoccur in later tests. At this point in testing, the Bode plot provided sufficient evidence to suggest the efficacy of this sensor design in detecting surface interactions. In this Bode plot it is quite noticeable that the clear peak between around  $1E0.5$  Hz and  $1E2.5$  Hz on the bode plot rapidly disappears within the first 5 minutes of testing. This is strong evidence of a measurable signal from the thiol bonding to the sensing surface. Interestingly, if we compare this data to that present in Figure 65 we see that the apparent change in EIS spectrum observed in Figure 61 did not take place for approximately 10 minutes. The reason for this difference in time could be due to several factors such as the differing area of the sensor but seems most likely to be due to the differing volume of the testing solution. In Figure 65 a separate reference electrode and counter electrode were used, necessitating the use of a larger container for the testing solution. In addition, each electrode had to be clamped into a suitable position for testing, increasing the radius of the required container. This significant difference in volume seems the most likely source of the discrepancy, as the thiol would take far longer to homogeneously disperse throughout the solution in the previous experiment.

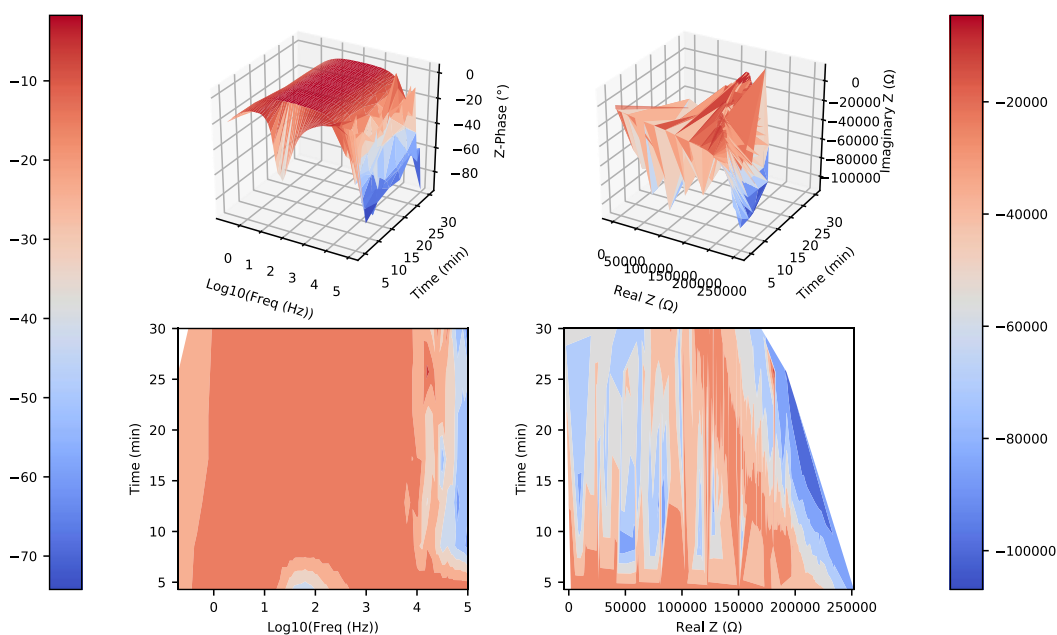


Figure 69. Time-resolved EIS data for the final sensor design with thiol added at  $t=0$ . The plots on the left are Bode Plots vs. time and on the right are Nyquist plots vs time. Colourbars are on the appropriate side for their plots and are relative to the Z-axes of the plots.

Following this promising test result it was concluded that this design would likely be sufficient for use in future biosensor tests. Based on this, the steps involved in the final sensor fabrication method to be used would be:

- CAP deposition of gold on COP
- Screen printing of contacts and counter/reference electrodes
- Crosslinking of nanostructures on sensor surface by:
  - Exposure to dithiobenzene for 5 minutes
  - Exposure to PLAL produced AuNP colloid for 5 minutes
  - Exposure to dithiobenzene for 5 minutes
  - Exposure to PLAL produced AuNP colloid for 5 minutes
- Functionalisation with a thiolated biomolecule

- Passivation with suitable reagent (e.g. 6-mercaptohexanol)

Under normal industry conditions, all of these steps with the exception of one would be inexpensive and green. However, in most modern industrial settings the production of the required AuNP colloid would be quite expensive and environmentally unfriendly lessening the intended positive aspect of this design as an inexpensive, green fabrication method.

Thankfully, the ready availability of producing colloids via PLAL in the laboratory and the ongoing, rapidly proceeding work to scale this process up to an industrial scale have made the use of such colloids an option without resulting in an expensive, environmentally harmful process.

## 5. Development of a Rapid, Non-Destructive Particle Enumeration Technique

As development continued throughout the work programme presented in Chapter 4, it became apparent that the most effective biosensing platform would likely be fabricated with the aid of a PLAL produced nanoparticle colloid. This posed few problems in terms of equipment or expense as PLAL is a simple process that can be performed on the same laser used herein for CAP depositions and the current state of PLAL research on-site allows for near mass-production of colloids. However, the easy characterisation of these colloids was somewhat more problematic. Currently, the process actively monitors DLS particle size data UV/Vis spectroscopic data. While these characterisation methods are useful for monitoring particle size and relative particle concentration for colloids of the same particle size and dispersity they offered no way to get an absolute concentration in the form of a Particles-Per-milliLitre (PPmL) or Parts-Per-Million (PPM) count. To ensure reproducibility of the fabrication process being developed an absolute particle count would be absolutely vital. Measurement of absolute particle count would be possible with common, destructive particle-counting methods (such as, for example, Mass Spectrometry<sup>182</sup> (MS) ) but the use of a destructive method would, obviously, result in the destruction of the colloid sample which is not yet being produced on a sufficient scale as to be quite so disposable. Frustratingly, in literature non-destructive particle counting methods appear far less widespread than their destructive counterparts and generally seem to require specialist equipment that was not available on-site. However, it was thought that obtaining an accurate particle count non-destructively should be possible using the readily available DLS and UV/Vis data from the colloid production in conjunction with appropriate application of some well understood quantum mechanics. If possible, this method could also potentially yield a way to exert some control over the

colloid concentration in the production process, thus further increasing the reproducibility of the sensor fabrication method being developed. Based on this, work began to develop a methodology for obtaining a PPmL count for colloids from simple DLS and UV/Vis data. This methodology would then be applied in the form of a program capable of carrying out the required computation.

## 5.1 The Theory of Interactions Between Light and Small Particles

It is generally understood that the most significant factors influencing the interactions of metal nanoparticle colloids with ultraviolet and visible light are: the material, shape and size of the nanoparticles; the electrochemical properties of the solvent; and the degree of aggregation among the dispersed particles<sup>128,183,184</sup>. These factors combined determine the intensity with which particles absorb light of a given wavelength. Thus, it would be expected (and proven true by the literature on the topic<sup>185</sup>) that these colloids should obey the Beer-Lambert law of molar absorptivity (13) at a given wavelength.

$$A = \epsilon_{ext}cl \quad (13)$$

In this equation, the absorption (A) is calculated based on the molar extinction coefficient ( $\epsilon_{ext}$ ), the concentration of the particles in molarity (c) and the length of the path of the light as it passes through the sample (l). Of course, although concentration in this formula is generally recalculated in moles the conversion of this value into a ppml or ppm value is quite trivial. This law makes the assumption that the turbidity of the liquid is low which, given the extremely obvious clarity of the colloids produced via PLAL (for reference on this return to Figure 17, page 77), is

a safe assumption in the intended use case. Based on this formula, it is quite clear that any method allowing for the enumeration of particles in a colloid from its UV/Vis spectrum will need to be able to calculate the expected extinction coefficient for a colloid at a given wavelength or even at a range of wavelengths.

With this goal in mind this section will outline the theoretical aspects of performing such a calculation before proceeding to combine these aspects into a single methodology and applying them in a program to algorithmically solve the problem presented.

### 5.1.1 The Scattering of Monochromatic Light by a Single Classical Particle

In any examination of literature pertaining to the physics of interactions between particles and light the researcher will inevitably be quick to discover the work of Craig Bohren and Donald Huffman as seminal researchers in this area. First published in 1940, their book “Absorption and Scattering of Light by Small Particles”<sup>183</sup> is a reoccurring reference in the bibliographies of nanophotonics papers to this day. This book outlines the theoretical underpinnings of how small particles interact with light based on the Mie model, including the calculation of their expected attenuation coefficients from first principles. While not a complete model, it has acted as a comprehensive starting point on which later nanophotonics work was firmly built.

In the Mie model of light scattering the particle is treated as a weighted average of infinitely many vector spherical harmonics of electromagnetic waves, each of which scatters light with a different intensity<sup>183,186</sup>. This theory is therefore ideal for applying to extremely small, spherical, plasmonically active metal particles as the plasmonic electrons that dominate their interaction with light behave as spherical waves throughout the particle. The mathematical underpinnings of this theory

are quite complex and the most dense theoretical aspects of the model are not pertinent to the project being undertaken. However, a cursory knowledge of the final formulae used is beneficial to understanding the design of the final program and how this program can be optimally adapted for the intended use so an extremely brief overview of these formulae will be beneficial<sup>183,186</sup>.

The previously mentioned average of vector spherical harmonics has components (Equations (14) and (15)) which can be expressed as the solution to an infinite series. That infinite series is comprised of numerous subcomponents (Equations (16) - (26)) and the derivation of these series and their many subcomponents are quite intimidating. For this reason, it makes sense within the scope of this project to leave aside the daunting (and theoretically opaque) derivation of this infinite series formula and to more closely examine the specifics of the simplified version that will be applied in the final program. In the interest of providing a more complete picture of the model, however, the unsimplified formulae are presented below (albeit extricated from their derivations as they occupy over 100 pages of the text they are sourced from<sup>183</sup>).

$$E_s = \sum_{n=1}^{\infty} E_n (i a_n N_{eln}^{(3)} - b_n M_{oln}^{(3)}) \quad (14)$$

$$H_s = \frac{k}{\omega \mu} \sum_{n=1}^{\infty} E_n (i b_n N_{oln}^{(3)} - b_n M_{eln}^{(3)}) \quad (15)$$

Where:

$$E_n = i^n E_0 \frac{2n + 1}{n(n + 1)} \quad (16)$$

$$a_n = \frac{\mu m^2 j_n(mx) [x j_n(x)]' - \mu_l j_n(x) [m x j_n(mx)]'}{\mu m^2 j_n(mx) [x h_n^{(l)}(x)]' - \mu_l h_n^{(l)}(x) [m x j_n(mx)]'} \quad (17)$$

$$b_n = \frac{\mu_l m^2 j_n(mx) [x j_n(x)]' - \mu j_n(x) [m x j_n(mx)]'}{\mu_l m^2 j_n(mx) [x h_n^{(l)}(x)]' - \mu h_n^{(l)}(x) [m x j_n(mx)]'} \quad (18)$$

$$N_{e1n} = \cos \phi n(n+1) \sin \theta \pi_n(\cos \theta) \frac{z_n(\rho)}{\rho} \hat{e}_r + \cos \phi \tau_n(\cos \theta) \frac{[\rho z_n(\rho)]'}{\rho} \hat{e}_\theta - \sin \phi \pi_n(\cos \theta) \frac{[\rho z_n(\rho)]'}{\rho} \hat{e}_\phi \quad (19)$$

$$M_{o1n} = \cos \phi \pi_n(\cos \theta) z_n(\rho) \hat{e}_\theta - \sin \phi \tau_n(\cos \theta) z_n(\rho) \hat{e}_\phi \quad (20)$$

$$N_{o1n} = \sin \phi n(n+1) \sin \theta \pi_n(\cos \theta) \frac{z_n(\rho)}{\rho} \hat{e}_r + \sin \phi \tau_n(\cos \theta) \frac{[\rho z_n(\rho)]'}{\rho} \hat{e}_\theta + \cos \phi \pi_n(\cos \theta) \frac{[\rho z_n(\rho)]'}{\rho} \hat{e}_\phi \quad (21)$$

$$M_{e1n} = -\sin \phi \pi_n(\cos \theta) z_n(\rho) \hat{e}_\theta - \cos \phi \tau_n(\cos \theta) z_n(\rho) \hat{e}_\phi \quad (22)$$

$$\pi_n = \frac{2n-1}{n-1} \mu \pi_{n-1} - \frac{n}{n-1} \pi_{n-2} \quad (23)$$

$$\tau_n = n \mu \pi_n - (n+1) \pi_{n-1} \quad (24)$$

$$\rho = kr \quad (25)$$

$$k = \sqrt{\omega^2 \epsilon \mu} \quad (26)$$

The equations and notation above are explained in far more depth (and with far more competency than would be possible for the author of this text) in Chapter 4 of Bohren and Huffman's book on the topic<sup>183</sup>, and the notation used follows generally accepted notational standards for theoretical physics. As such, the component  $\phi$  denotes the magnetic flux,  $\theta$  denotes the angle in a polar coordinate system,  $r$  denotes amplitude of the wave at that angle and  $\omega$  denotes the angular frequency of the wave,

while  $\epsilon$  denotes the permittivity and  $\mu$  denotes the permeability of the sphere scattering the light. The component  $\mu_i$  similarly refers to the permeability of the liquid medium the particle is suspended within. In non-standard notation (to avoid conflicting symbols)  $x$  is the radius of the particle and  $m$  is the relative refractive index between the particle and the medium. The functions  $j$  and  $z$  denote spherical Bessel functions, and the sub and superscript notations attached to these functions are standard notations denoting the specific Bessel functions used (Bessel derived an extensive glossary of differing kinds of these functions, each separately identified by these notations). Each value denoted by  $\hat{e}$  is an orthonormal basis vector in the coordinate system centered on the particle, the specific geometries of which are explained in Chapter 3.2 of Bohren and Huffman's book<sup>183</sup>.

Of note among the derived formulae are Equations (17) and (18), which are known as the "scattering coefficients". As suggested by their name, the scattering coefficients are of vital importance in the calculation of the degree of scattering the particle will cause. However, attempts to straightforwardly apply this equation result in extremely long computation times due to the emergence of a logarithmic component to the equation<sup>187</sup>. One way to simplify the equation somewhat and avoid this problem of computational complexity is to assume the permeability of the particle and the surrounding medium are approximately equal and then apply two of the Riccati-Bessel functions (Equations (27) and (28)) to the existing Bessel functions. Although this assumption of equal permeabilities may seem dubious at first the resulting formula has been tested and found to be quite accurate in practical use<sup>184,188</sup> suggesting the effect of differing permeabilities is, in practice, negligible. The resulting simplified formulae (Equations (29) and (30)) can then be more easily applied in a computational method for the calculation of the extinction coefficient.

$$\psi_n(\rho) = \rho j_n(\rho) \quad (27)$$

$$\xi_n(\rho) = \rho h_n^{(1)}(\rho) \quad (28)$$

$$a_n = \frac{m\psi_n(mx)\psi_n'(x) - \psi_n(x)\psi_n'(mx)}{m\psi_n(mx)\xi_n'(x) - m\xi_n(x)\psi_n'(mx)} \quad (29)$$

$$b_n = \frac{\psi_n(mx)\psi_n'(x) - m\psi_n(x)\psi_n'(mx)}{\psi_n(mx)\xi_n'(x) - m\xi_n(x)\psi_n'(mx)} \quad (30)$$

At this point, the scattering coefficients have been simplified but the calculation of  $E_s$  and  $H_s$  (the components of the overall infinite series of spherical electromagnetic waves possible within the particle) are still quite complex and computationally expensive due to the various vector spherical harmonics that still comprise their formulae ( $M_{e1n}$ ,  $M_{o1n}$ ,  $N_{e1n}$  and  $N_{o1n}$ ). By further applying the Riccati-Bessel functions and treating the particle as a 2d cross-section of a sphere (for details on how this is done see Bohren and Huffman<sup>183</sup>, page 102-104) the formulae for  $E_s$  and  $H_s$  can be significantly simplified to yield far more computationally simple formulae describing the scattering cross section ( $C_{sca}$ , Equation (31)) and the extinction cross section ( $C_{ext}$ , Equation (32)) where “Re” is a function that gives the real components of a complex number. The treatment of the particle as a simple 2d cross section is logically justified in scenarios where the rays of incident light striking the particle are parallel, such as when performing a UV/Vis spectrometry experiment. The extinction cross section can then be readily converted to an extinction efficiency ( $Q_{ext}$ , Equation (33)) which can then be readily converted to an extinction coefficient ( $A$ , Equation (34))

$$C_{sca} = \frac{2\pi}{k^2} \sum_{n=1}^{\infty} (2n+1) (|a_n|^2 + |b_n|^2) \quad (31)$$

$$C_{ext} = \frac{2\pi}{k^2} \sum_{n=1}^{\infty} (2n + 1) \operatorname{Re}\{a_n + b_n\} \quad (32)$$

$$Q_{ext} = \frac{C_{ext}}{\pi a^2} \quad (33)$$

$$A = \frac{\pi R^2 Q_{ext} d_0}{2.303} \quad (34)$$

Equation (34) when combined with Equations (33), (32) and (23) through (30) now offers us a mathematical way to calculate the absorbance of a single particle at a single wavelength according to Bohren and Huffman's method<sup>183</sup>. Bohren and Huffman further go on to also derive a method for the calculation of the scattering matrix for the particle in monochromatic light but this methodology is not needed for our purposes. While this methodology is useful in allowing for the accurate and rapid calculation of Mie scattering parameters in niche cases (such as in a spectrometer) it is not without fundamental shortcomings. Most significantly, as the Mie model in general has been shown to have inaccuracies in extremely small nanoscale particles due to quantum effects it does not account for because of its treatment of particles as classical objects<sup>189</sup>. For this reason, later work focused on the expansion of this methodology to make it applicable to particles with more quantum behaviour and to make it applicable in cases with incident polychromatic light sources.

### 5.1.2 The Scattering of Polychromatic Light by a Single Quantum Particle

As previously discussed, the work of Bohren and Huffman in the practical application of the Mie model served as an important stepping stone to many of our modern characterisation techniques used in nanotechnology research. As it was originally published in 1940, the simplifications outlined in Section 5.1.1 were present to allow for the calculation of the

parameters by hand. However, in a later edition of the same book the authors included a highly influential computer program written in FORTRAN77 that performed these calculations using the same simplified methodology described above. This was likely to allow for rapid calculation due to the extremely limited speed of computers at the time. As technology improved, various more computationally expensive methods for performing this calculation with greater accuracy arose. However, Bohren and Huffman's FORTRAN77 code continued to be used in cases where rapid, reasonably accurate calculations were more desirable than slow, extremely precise ones. One such case is in the expansion of Mie scattering calculations to also be applicable to polychromatic incident light rays. This was the focus of the research of Haiss et al in 2007 who expanded Bohren and Huffman's method to be applicable to this situation<sup>184</sup>.

The extenuation made by Haiss et al. to Bohren and Huffman's method involves the simple idea of iteratively repeating their methodology at various wavelength so generate a predicted UV/Vis spectrum for a single particle. This was made possible simply by the advancement of computer technology between 1983 (the original publishing date of Bohren and Huffman's FORTRAN77 code) and 2007. By using Bohren and Huffman's method Haiss et al. were able to perform a Mie scattering calculation thousands of times in only a few seconds using the technology of their time. Despite this major advantage, the original method does, however, have its limitations (as discussed at the end of Section 5.1.1) that make it somewhat more inaccurate in the context of modern day nanotechnology. Rather than resort to the use of a more computationally expensive methodology Haiss et al. devised a simple calculation that can compensate for some of these shortcomings based on the earlier theoretical work of Kreigig and vonFragstein.

In the 1969 Kreibig and vonFragstein<sup>189</sup> examined the deviations of the optical properties of 2.4nm to 21 nm diameter silver nanoparticles from the properties predicted by the classical Mie theory. They found that deviations appeared to begin happening once the diameter of the particle decreased below the mean free path (that is, the average distance that can be travelled before a collision according to the Drude model) of the conductance electrons in the bulk metal. Kreibig and vonFragstein postulate that this is because once the particle diameter decreases below the mean free path of the electrons it effectively bounces off the outer surface of the particle and back inside it<sup>189</sup>. Strictly speaking, of course, a quantum nanoparticle has no such hard “surface” and electrons that stray outside the particle would simply be attracted back towards the particle centre by electromagnetism. However, as the measurable “outer surface” of a particle should coincide with the maximum distance from the particle centre at which you are likely to find electrons this treatment of the particles as bouncing or colliding with an “outer surface” provides a good approximation of the effects of extremely small diameter particles on the mean free path of conductance electrons. To examine how this might influence the interactions between a particle and light we first need to examine how electrons affect the macroscale properties of metals and then we can extend that model to include these surface collisions.

In the Drude model of electron conduction, electrons are generally treated as particles that conduct throughout a metal until they eventually collide with a metal ion and bounce off of it<sup>190</sup>. Of course, similar to the description above describing these “collisions” as such is an oversimplification. However, given that the deflections of electrons by metal ions behave for all intents and purposes as “collisions” where the electrons “bounce” off ions the mathematics of this model provide a very good approximation of reality. As described above, the Drude model considers how often these collisions occur, in the form of the “mean free path” ( $d_i$ ), or the average distance travelled between collisions. In this

model electrons are also generally treated as having a constant average velocity referred to as the “Fermi velocity” of the metal ( $v_f$ ). Based on fundamental classical mechanics it is trivial to surmise the this Fermi velocity is related to the mean free path by the Equation (35) where  $\tau_f$  is the mean free time, the average time between collisions.

$$d_f = v_f \tau_f \quad (35)$$

Furthermore, it is similarly obvious that the mean free time can be converted to a frequency value by simply inverting it as shown in Equation (36), yielding a value known as the “collision frequency” ( $\omega_0$ ).

$$\omega_0 = \frac{1}{\tau_f} \quad (36)$$

By using this collision frequency value in conjunction with a property of the metal known as its “plasma frequency” ( $\omega_p$ , the calculation of which will be discussed later but for now it is only relevant to know it is fixed for any given metal) it is then possible to derive a formula describing the relative permittivity of the metal as a function of the angular frequency of the incoming electromagnetic radiation ( $\omega$ ) (Equation (37)<sup>189</sup>). This equation is divided into contributions made by conduction electrons ( $A_n$ , Equations (38) and (39)) and contributions made by bound electrons ( $B_n$ ). However, as the bound electrons are already confined within atoms and this have no mean free path we can ignore them for the sake of clarity as they have no relevance to the problem at hand.

$$\varepsilon(\omega) = (A_1 + B_1) + (A_2 + B_2)i \quad (37)$$

$$A_1 = 1 - \frac{\omega_p^2}{(\omega^2 + \omega_0^2)} \quad (38)$$

$$A_2 = \frac{\omega_p^2 \omega_0}{\omega(\omega^2 + \omega_0^2)} \quad (39)$$

Based on this, it is quite clear that any factor which might affect the mean free path consequently affects the collision frequency, thus changing the relative permittivity of the metal. If we briefly reconsider Equation (26) in previous Section 5.1.1 it is clear that this change in permittivity would affect the Mie scattering parameters of the particle, and thus that a change to mean free path of the particle would change the UV/Vis spectrum of the particle.

Now, with a clear grasp of the reason why the Mie model appears to break down below the mean free path length of the particle we can return to considering the original problem of expanding the applicability of Bohren and Huffman's algorithm to include such particles. The solution used by Haiss et al is elegantly straightforward. By simply adjusting the collision frequency to also account for surface collisions and recalculating the corrected permittivity it is possible to account for this mean free path effect<sup>184</sup>. This adjustment of collision frequency is carried out according to Equations (40) and (41) (where  $\omega_a$  is the frequency of collisions with atoms,  $x$  is the radius of the particle,  $\omega_0$  is the overall collision frequency and  $\omega_s$  is the frequency of collisions with surfaces).

$$\omega_a = \frac{x}{v_f} \quad (40)$$

$$\omega_0 = \omega_a + \omega_s \quad (41)$$

Using this method, Haiss et al managed to dramatically increase the accuracy of Bohren and Huffman's model for particles with a radius below their bulk mean free path without producing an appreciable increase in the complexity of computing the result. Because it keeps computational complexity low in this way, this method ideally suited expand upon by iteratively applying it predict the spectrum of a broadly polydispersed

particle mixture (more like real nanoparticle mixtures encountered in practice).

### 5.1.3 The Scattering of Polychromatic Light by Numerous Polydispersed Quantum Particles

To allow for the type of colloidal particle enumeration from simple UV/Vis data that the project required it was decided to build further upon the work of Bohren and Huffman<sup>183</sup> and Haiss et al.<sup>130</sup> described in Sections 5.1.1 and 5.1.2 respectively. With this in mind the next step is clearly to expand the applicability of the Haiss et al method from the prediction of the UV/Vis spectrum for single sized particles to the prediction of the UV/Vis spectrum for complex mixtures of variously sized particles as this is the state of most colloidal solutions in real-world practical usage.

To achieve this, a methodology was devised to combine multiple spectra for differently sized particles into an expected spectrum for the mixture. It is well understood (as exemplified by the Beer-Lambert law, Equation (13)) that spectrum intensity is directly proportional to the number of fluorophores present. It thus logically follows that for a mixture of fluorophores at a given wavelength creating a mean extinction coefficient weighted by the relative amounts of each fluorophore present (normalised to a total of 1) should result in an expected extinction coefficient for the mixture as a whole (Equation (42) , where  $c$  is the concentration of the fluorophore and  $n$  is the number of fluorophores present). This principle can obviously also be applied to an spectrum as a mathematical function (Equation (43)). Note that in this equation  $\lambda$  (the wavelength of the incident light) is used interchangeably with  $\omega$  (the angular frequency of light) as they can be readily interconverted using Equation (44), where  $c$  is the speed of light.

$$\overline{Q_{ext}} = \frac{\sum_{i=1}^n \hat{c}_i \times Q_i}{\sum_{i=1}^n Q_i} \quad (42)$$

$$\overline{Q_{ext}}(\lambda) = \frac{\sum_{i=1}^n \hat{c}_i \times Q_i(\lambda)}{\sum_{i=1}^n Q_i(\lambda)} \quad (43)$$

$$\lambda = \frac{2\pi c}{\omega} \quad (44)$$

In applying this concept to colloidal mixtures, it makes sense to treat each differently sized particle present as a different fluorophore due to their different spectral properties. By substituting the mathematical functions of the previous models (Equation (33) and all of its various subcomponents including the corrections in Section 5.1.2) into a weighted mean formula it is possible to derive an equation theoretically describing the predicted extinction spectrum for any polydispersed colloid of nanoparticles with a homogenous unimetallic composition (Equation (45), where  $r$  is the radius of the particle and  $m$  is the number of particle sizes present).

$$\overline{Q_{ext}}(\lambda) = \sum_{i=1}^m \frac{\sum_{j=1}^n \hat{c}_j \times Q_j(\lambda, r_i)}{\sum_{j=1}^n Q_j(\lambda, r_i)} \quad (45)$$

A weighted mean extinction spectrum such as this should, theoretically, allow for the facile calculation of a ppm particle count from the UV/Vis spectrum of the colloid. However, as can be seen the derivation of such a spectrum requires the experimenter to know the relative amounts of each particle size present in the colloid. Thankfully, this data is readily obtainable using the DLS measurement, which is also non-destructive and readily available similar to UV/Vis spectroscopy. And so, we have devised a framework using Equation (43) (and all of its various subcomponents) in conjunction with UV/Vis spectroscopy and DLS measurement that should

make it possible to easily and non-destructively count the number of particles in a colloid using readily available equipment.

#### 5.1.4 Simplification of Physical Inputs: Expanding Usability to Interdisciplinary Users

While expanding upon previous work to make this theory applicable in everyday usage is beneficial it has limited usefulness if the barrier to entry for a researcher using it is an understanding of quantum theory. With this in mind it was decided that while a new program leveraging this methodology was being created it should also be expanded to become as accessible to researchers from various disciplines as possible. Examining the formulae so far it rapidly becomes clear that the primary difficulty for the unfamiliar user attempting to use them would be the input parameters. Many of the input parameters used in this calculation require a degree of knowledge in quantum theory to calculate in the first place, thus rendering the programs unusable to any with no knowledge of the subject. Many of these values are relatively straightforward to calculate from first principles with reasonable accuracy for a simple unimetallic material (these formulae are easily accessible in solid-state physics textbooks such as, for example, Ashcroft and Mermin<sup>190</sup>). Therefore, they could easily be abstracted into various more readily understandable parameters which could then be used to calculate the more complex required inputs. Doing this should dramatically lower the barrier to entry for usage of the program, thus making this useful program far more usable by researchers from a wide variety of disciplines. The specific input parameters that were identified as being unnecessarily difficult to calculate for the unfamiliar user were the plasma frequency ( $\omega_p$ ), the collision frequency ( $\omega_0$ ) and the Fermi velocity ( $v_f$ ) of the material.

To calculate each of these values from first principles we first need to find the free electron density ( $n_e$ ) of the metal. Using Avogadro's constant ( $N_0$ )

in addition to the valence ( $Z$ ), density ( $\rho_m$ ) and atomic mass ( $m_a$ ) of the metal the free electron density can be calculated using Equation (46).

$$n_e = \frac{N_0 Z \rho_m}{m_a} \quad (46)$$

The calculation of the plasma frequency for a metal can be carried out using Equation (47) where  $r_s$  is the electron sphere radius and  $a_0$  is the Bohr radius. Likewise, the electron sphere radius can be calculated according to Equation (48).

$$\omega_p = 2\pi \times 11.44E15 \times \left(\frac{r_s}{a_0}\right)^{-\frac{3}{2}} \quad (47)$$

$$r_s = \sqrt[3]{\frac{3}{4\pi n_e}} \quad (48)$$

The collision frequency calculation follows Equation (49) where  $\rho$  is the resistivity of the metal,  $q_e$  is the elementary charge and  $m_c$  is the mass of the charge carrying species (note that in the case of metals this will almost always be equal to the mass of the electron,  $m_e$ ).

$$\omega_c = \frac{q_e^2 n_e \rho}{m_c} \quad (49)$$

Lastly, the Fermi velocity is calculable using Equations (50) and (51) where  $\hbar$  is the reduced Planck constant and  $k_F$  is the Fermi vector of the metal.

$$v_F = \frac{\hbar k_F}{m_c} \quad (50)$$

$$k_F = \sqrt[3]{3n_e\pi^2} \quad (51)$$

By using these formulae, the required values can be automatically calculated from the much more readily available and generally understood values of a metals density, atomic mass, resistivity and valence significantly reducing the level of theoretical understanding required to effectively utilise the program.

Despite this convenience, it is important to note that in certain circumstances these formulae will begin to break down. Most notably, metals with significant relativistic effects (such as gold<sup>191</sup> or mercury<sup>192</sup>) would be expected to begin to deviate significantly from these formulae as their electrons behave as though they have a greater mass<sup>193</sup>. For this reason, it may in be necessary to manually input values in some edge cases. For now, this option has been left available to the user in the program and corrections for relativistic effects may be added at a later date.

## 5.2 Design of the Particle Counting Program

To effectively make use of the maths described throughout Section 5.1 a program was developed to rapidly perform the computations required. The rapid calculation of a result was determined to be desirable as it would greatly increase the potential applications of the methodology. For example, sufficient speed of calculation would allow for real-time process monitoring in colloidal synthesis processes or for the methodology to be further expanded in future as a subcomponent of a more complex program. To that end, the specific model discussed above was chosen as a relatively simple and computationally inexpensive algorithm for this calculation. As briefly mentioned in the previous section the models make

several simplifying assumptions to reduce the computational complexity of the calculation but these assumptions are valid in the intended use-case for the program.

### 5.2.1 Choice of Programming Language

The first consideration in designing a program is the choice of programming language. As originally written, the programs of Bohren and Huffman<sup>183</sup> and Haiss et al<sup>130</sup> (on which submodules of this program were based) were written in FORTAN77, a language which is largely based on FORTRAN (one of the first programming languages ever devised). Despite its many revolutionary features and its undoubtably brilliant design for its time FORTRAN was originally developed in 1954 as a language intended for punch-card programming<sup>194</sup> and, as such, is not very intuitive to use in a modern setting. For example it lacks the convenience of modern branching in the form of loops and iterative blocks, heavily relying instead on unwieldy arithmetic IF statements and GOTO labelling. It also lacks many features considered essential in modern languages such as functions and module imports, instead incorporating “SUBROUTINES” which conceptually act as a hybrid of functions and imported modules. These features, particularly the heavy reliance on GOTO statements can make FORTRAN notoriously difficult to debug<sup>194</sup>. The language has, of course, continued to be updated and many of these problems have been addressed in the modern descendant of FORTRAN (such as Fortran 2018). The language still sees continual updates and improvements as it still has many uses in the running of legacy code and in ultra-high performance computing due to its now highly optimised design with 60 years of incremental optimisation behind it. Despite these updates the language is still quite archaic and is still challenging to use and debug for a modern user due to many of its key features having their roots in this early language designed for use in a very different era of computing.

The natural first idea when attempting to create this new program was to simply update the existing code and incorporate it into the new program as a subroutine. However, this immediately proved difficult. Attempts to compile both sets of code with both the GNU fortran compiler (known as gfortran) and the Intel Fortran Compiler (known as ifort) were immediately met with errors. Attempts were made to update the code for compatibility with a modern compiler and to incorporate it into submodules to no avail. After resolving several errors only to create several more it was quickly realised that the time required to make the pre-existing code usable would be significant due to the sheer unhelpfulness of the gfortran compilers error messages (likely stemming back to the aforementioned, notable difficulty of debugging this language). Based on this observation, it was clear that the required time investment to update the code and create a usable program in this already largely outdated language was likely not worth it. It was decided that it would be more productive to completely reimplement the algorithms in a more modern programming language. This would allow for it to be more easily modified, maintained and understood by a modern user, while also helping to future-proof the language if Fortran gradually becomes supplanted by more modern high-performance parallel-computing languages such as OpenCL and CUDA.

In deciding upon a programming language to use, the primary consideration was that of performance. As previously mentioned, being able to perform the required calculations in a shorter time period would make the resulting program potentially more useful. Another factor to consider was the ease of reading and writing the code, as the easier a language is to understand the easier it is to maintain or modify the code. Lastly it was important that the language have broad compatibility and interoperability between platforms and other programs, as this allows for the code to be more easily incorporated into other programs. When writing of high-performance code languages such as Fortran, C and C++

are the current gold standards for high performance computing. These statically compiled languages are extremely fast, broadly compatible and generally interoperable with other languages. However, as previously discussed in the context of Fortran these languages can be quite problematic to debug and understand as a tradeoff for their high performance. On the opposite end of the spectrum are more modern, interpreted languages such as Python and R which are ubiquitous in data science. These languages are easy to quickly write and understand programs in and are also very broadly compatible and interoperable but they are quite slow in comparison with the languages previously mentioned. Modified versions python incorporating Just-In-Time (JIT) compilers such as PyPy and Numba offer a significant increase in performance for the language but come at the cost of reduced compatibility and interoperability, thus harming their usefulness. After considering many of these options, the decision was eventually made to use a language named “Julia” as the primary language for this program.

The Julia programming language is a relatively new open-source programming language maintained by Julia Computing, Inc. The language was created in 2012 and it sees small but growing use in high performance computing applications. This language fits all of the requirements laid out in the previous paragraph offering high-performance, wide compatibility and interoperability and a simple, python-like syntax. The language is able to achieve all of this as it has been designed from the ground up with the express intention of offering a language suitable for high-performance without the compromises that were necessary in past eras of computer technology<sup>195</sup>. Julia is designed to take advantage of parallel computing using syntactically simple macros that indicate to the compile how best to parallelize certain tasks. The language also has a broad range of compatibility across most common operating systems and computer architectures. It is also natively interoperable with all of the languages discussed in the previous

paragraph, even being able to call code written in C, Fortran or Python natively from inside a body of Julia code further increasing its broad compatibility. These features coupled with its simple, easy to understand syntax make it ideal for use in applications such as the development of scientific programs which aim to be made up of fast, adaptable code that can easily be modified by researchers without a background in programming.

## 5.2.2 Translation of Pre-Existing Codebase from FORTRAN77 to Julia and Optimisation

The process of incorporating the algorithms of Bohren and Huffman and Haiss et al into a more modern program first begin with a direct translation of the code from FORTRAN77 into Julia. Many of the fundamental keywords of FORTRAN77 are also present in Julia, making direct translation possible if familiar with both languages. For example, the Julia language has “@goto” and “@label” macros (which is unusual for such a modern language) that functionally behave similarly to the GOTO in FORTRAN77. As an example, a loop in FORTRAN77 that takes the values in an 8 element long input array (called “INPUTARRAY” here) and changes the values of an output array (called “OUTPUTARRAY” here) to be their squares would be written as:

```
100  I = 0
110  I = I + 1
120  OUTPUTARRAY(I) = INPUTARRAY(I) ** 2
130  IF (I .LT. 8) THEN
140     GOTO 110
150  END IF
```

While in Julia, a simple direct translation of this could would be written as:

```
i = 0
@label loopstart
```

```

i = i + 1
OutputArray[i] = InputArray[i] ^ 2
if (i < 8)
    @goto loopstart
end

```

Despite this relative ease of direct translation, one difficulty in translating the code was FORTRAN77s unusual use of arithmetic IF statements. Usually, in programming, an “if statement” evaluates a comparison and executes a specific block of code only if the comparison is true as seen in the examples above. However, “arithmetic if” was a feature in some early programming languages wherein the if statement takes the result of an expression compares its result to zero. The arithmetic if then performs a goto jump to one of 3 labels depending on whether the value of the second number is less than, equal to, or greater than zero. For example, an arithmetic if in FORTRAN77 that simply writes if an integer (called “I”) is less than, equal to or greater than 5 then writes the value of I would be written as follows:

```

100  IF (I - 5) 110,130,150
110  WRITE(*,*) "I is less than 5"
120  GOTO 170
130  WRITE(*,*) "I is equal to 5"
140  GOTO 170
150  WRITE(*,*) "I is greater than 5"
160  GOTO 170
170  WRITE(*,*) I

```

This arithmetic IF is rather unique to pre 1995 FORTRAN based languages and thus is not present natively in Julia. To allow for direct translation, this arithmetic if statement was initially emulated using 3 separate normal “if” statements representing each possible outcome of the arithmetic IF. Using this method, the code above can be directly translated as:

```

if i < 5 @goto a end
if i == 5 @goto b end
if i > 5 @goto c end
@label a
println("i is less than 5")
@goto d
@label b
println("i is equal to 5")
@goto d
@label c
println("i is greater than 5")
@goto d
@label d
println(i)

```

With this method for the emulation of arithmetic IF it was possible to proceed with the translation of the program. By translating keywords into their Julia equivalents and making minor changes to account for the differences in syntax and programming paradigm between the languages it was possible to create a direct, naïve, unoptimised translation from FORTRAN77 to Julia as a starting point.

Following this, the first step in creating sensible Julia code rather than a clumsy translation was to replace the complex labyrinth of if statements, @gotos and @labels with modern branching code-blocks. For instance, in the example code earlier demonstrating the translation of code to square each element in an array the structure involving an if statement that conditionally executes an @goto makes far more sense in the form of a “for” loop. An example of this code being reimplemented as a for loop would be written as follows:

```

for i in 1:8
    OutputArray[i] = InputArray[i] ^2
end

```

By reimplementing the old FORTRAN77 code in this more modern fashion, the code thus becomes far more readable and comprehensible to the programmer, allowing for better understanding of program flow and the identification of ways to optimise it.

To begin the process of optimising the program, minor changes were first performed. The first of these changes was to statically declare variables (Julia variables can be either static or dynamic, with static variables giving higher performance) and to optimise datatypes to reduce memory footprint and processing overhead (e.g. switching an unnecessary Int64 for an Int8 or UInt32, or replacing lists that don't require mutation with tuples). Other minor optimisations were to combine multiple calculations into single larger calculations (reducing the number of variable assignments being performed) and disabling bounds-checking where possible.

Next, optimisation was performed by replacing archaic programming practices with more efficient modern ones. One major example of such an optimisation was to reduce the memory footprint of the program by replacing fixed size arrays with ones capable of dynamic allocation. These dynamically allocated arrays were then able to be grown using a simple push function as demonstrated below for our example case:

```
for x in InputArray
    push!(OutputArray, x ^ 2)
end
```

In certain cases optimisation was further possible by the replacement of for loops with comprehensions or vectorised array calculation, as these structures allow the compiler to carry out further mathematical optimisations at runtime. Returning to our example case of a loop to square an array, these loops would be suitable for optimisation with comprehensions but would not be well suited to demonstrating vector

array calculations. Reimplementing the loop as a list comprehension would result in the following expression:

```
OutputArray = [x^2 for x in InputArray]
```

After these optimisations were complete, work then began to effectively parallelise the program to further increase the speed of computation. Initial parallelisation attempts were performed by parallelising loops and array operations wherever possible using Single Instruction-Multiple Dispatch (SIMD) parallelisation. SIMD parallelisation is a simple way to parallelise highly repetitive array operations and loops by having each available CPU core carry out the same operation on different elements of the array (Figure 70).

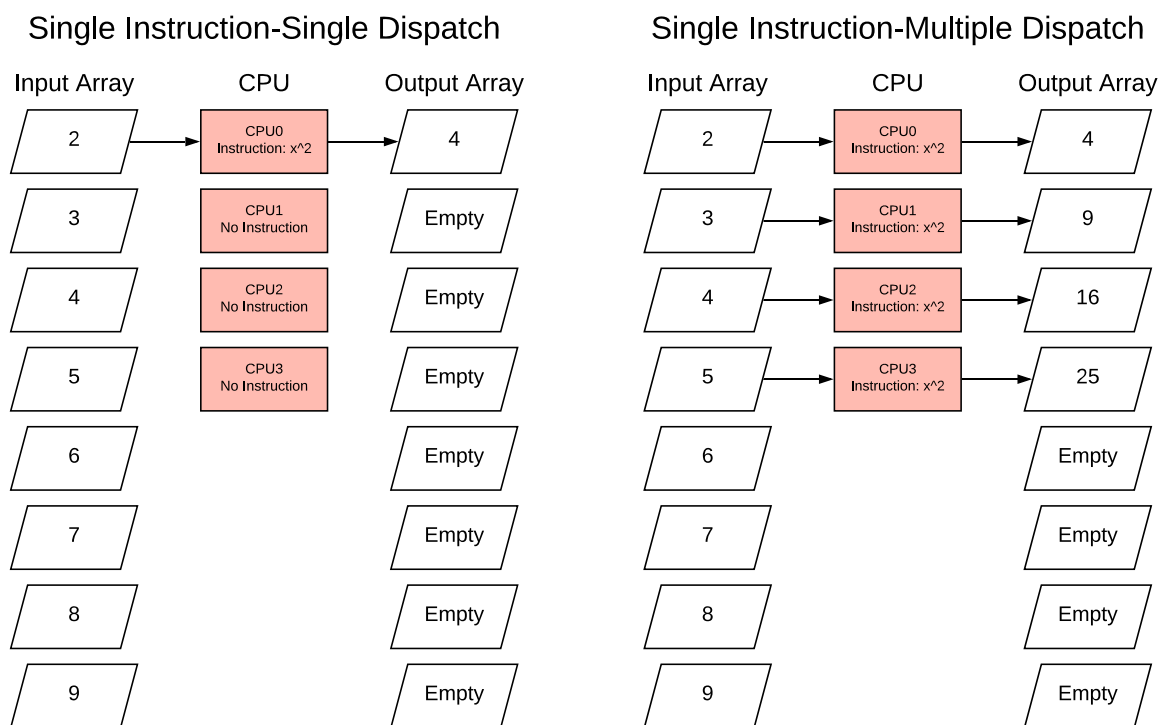


Figure 70. A comparison of traditional Single Instruction-Single Dispatch (SISD) computing and Single Instruction-Multiple Dispatch computing. In the example, SISD requires eight ticks to process the array while SIMD can complete the process in only two ticks.

In Julia, SIMD parallelisation can be readily achieved through the use of a simple macro. For example, the SISD operation in Figure 70 is the normal “for loop” structure we used earlier in this section. To remind the reader, this for loop would be written as:

```
for x in InputArray
    push!(OutputArray, x ^ 2)
end
```

Converting this loop to an SIMD variant of the same operation is as simple as adding an “@SIMD” macro before the start of the loop. Modifying the code above to be carried out as an SIMD operation is as simple as writing the following:

```
@simd for x in InputArray
    push!(OutputArray, x ^ 2)
end
```

SIMD execution does, however, have its limitations. The most significant limitation is that it is unsafe to use on arrays where elements are derived from previous elements in the array. This is due to the fact that such arrays are inherently sequential, that is to say that in such arrays it is impossible to calculate the value of element 4 (for example) until elements 1, 2 and/or 3 are finished first. Despite this limitation its ease of implementation and the fact it was suitable for use on many of the arrays in the program make SIMD parallelisation a powerful method for performing this calculation more quickly. Of all optimisations performed this simple form of SIMD parallelisation gave the most significant performance increase, on average more than halving the time required to perform calculations on the computer used for testing.

Further parallelisation outside of loops and array operations were performed by restructuring the code into blocks of calculations that do not influence one another. By grouping completely independent calculations together, they could be easily parallelised using synchronous parallelisation, wherein each processor is given a different instruction and the CPU waits until all processors finish their tasks before queueing new instructions.

The final major optimisation performed was to solve a bottleneck caused by the simple linear interpolation algorithm. In Haiss et al's algorithm (which exists within a function named "qbare"), there is a step where linear interpolation is performed on the permittivity spectrum given as an input. This step is necessary to estimate the expected permittivity at wavelengths between datapoints on the spectrum. This linear interpolation algorithm is extremely simple, making it readily understandable but also making it quite slow relative to more mathematically efficient but complex algorithms for this task. Thankfully, using a modern programming language such as Julia it is quite simple to replace this simple, naïve interpolation algorithm with a far better optimised one from a module. In this case, the Julia module "Interpolations"<sup>196</sup> was used to provide a highly optimised and efficient linear interpolation algorithm to use in its place. Lastly, this interpolation step was further optimised by removing it from the qbare function and moving it instead into the function that calls qbare to calculate spectra for each radius of particle. Because the permittivity spectrum is fixed for a given material, there was no reason for this interpolation to be repeated every time the function was called, so the code was changed to allow the interpolation to occur outside the mean free path correcting function thus ensuring it would only have to be performed a single time instead of every time mean free path correction was performed. This gave a significant further increase to the speed of the computation and was the final optimisation made.

### 5.2.3 Overview of the Structure of the Program

The program created (Appendix 6 - Appendix 12) is structured into 3 separate modules. These modules each contain code used for different purposes and are organised as follows:

- `miemfp.jl` (Appendix 10): This module contains code based on the previous work of Bohren and Huffman and Hais et al.
- `nanoconc.jl` (Appendix 11): This module contains the new code for applying the algorithms in `bhmie` to particle enumeration and other tools for managing a database of material data that can be easily called upon.
- `quantumcalc.jl` (Appendix 12): This module contains a collection of functions useful for performing quantum physics calculations such as those described in Section 5.1.4. These were separated from the rest of the program to reduce the complexity of the `nanoconc` module and increase its readability through abstraction.

When examined from a top-down perspective the design of the program is relatively straightforward (Figure 71). The program incorporates an interface for managing a rudimentary database of materials and their properties (in `nanoconc.jl`) which the user can then call upon when performing a calculation. Before using the program, the information for the desired material must be added to the material database.

The program begins when the function “particlecount” (Appendix 6) is called from the “`nanoconc.jl`” module. When called upon the program begins by reading the UV/Vis and DLS data it is given, storing them. It then proceeds by loading the required material properties data for the desired material. The program then normalises the DLS data to a total relative amount of 1.0. The program then begins the calculation process, entering a loop that repeats once for every size of particle present (that we will call Loop A).

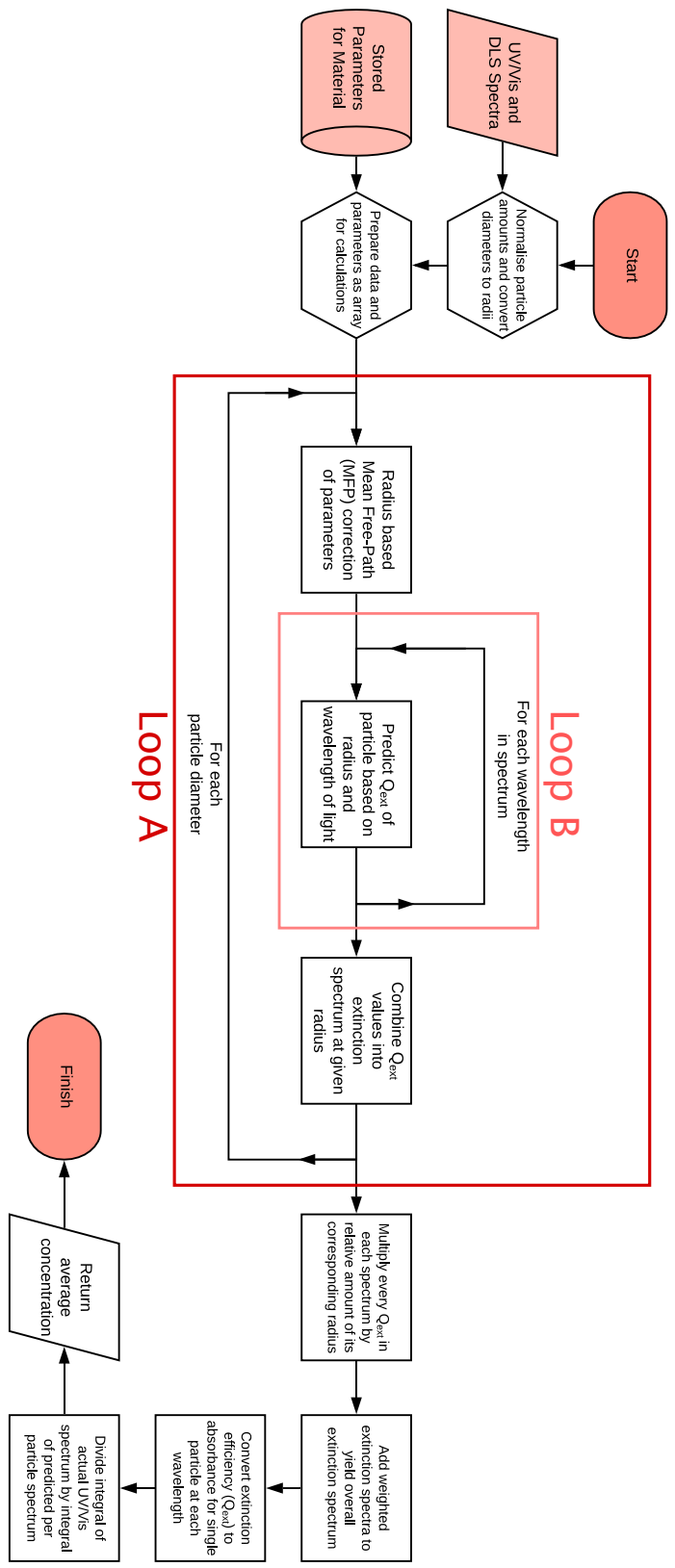


Figure 71. A high-level flowchart summarising the design of the particle counting program.

Loop A begins by passing the data to the function “qbare” (Appendix 7) in the miemfp.jl module. Qbare then begins by performing a mean free path correction (as described in Section 5.1.2) on the input parameters by calling the function “mfp” (Appendix 8). It then feeds this corrected data into another nested loop (that we will call loop B) where the program calculates the extinction coefficient at a specific wavelength by calling the function “bhmie” (Appendix 9) in miemfp.jl, which performs this calculation as described in Section 5.1.1. The loop B repeats until its calculation has been performed for every wavelength in the desired spectrum. Once loop B has exited, the extinction coefficient values returned are organised into an array and this extinction spectrum is returned back to qpredict where it is added to an array of spectra. At this point, the calculation of the spectrum for the first particle size present is complete, and loop A proceeds to repeat for every particle size present.

Once loop A exits, the function qpredict now has an array of arrays containing extinction coefficient values for each particle size at each wavelength in the spectrum (effectively, an extinction spectrum for each particle size). It then calculates a weighted mean of these extinction spectra, weighted by the relative amount of each particle size present in the DLS. This mean spectrum is then returned to the function particlecount. The mean spectrum and the actual UV/Vis spectrum are then linearly interpolated, integrated and their integrals are divided to finally return a numeric count of the particles per mL.

#### 5.2.4 Empirical Verification of Program Accuracy

To verify the accuracy of the program an empirical test was planned. For this experiment, a stock nanoparticle colloid of known concentration would be used to prepare a dilution series which would then be analysed using the algorithm to compare both methods. The colloid of known concentration in question was a silver nanoparticle colloid purchased from Sigma-Aldrich (10nm by TEM, 0.02mg/mL, 730785-25ML). Although

the colloid being used in sensor tests throughout this project was a gold colloid the prohibitive cost of purchasing a suitable gold nanoparticle colloid from a supplier meant that a silver colloid was a preferable option.

Before testing, it was necessary to convert the known mg/mL concentration to a value in particles per mL. In converting this value, the mass per particle for 10nm silver nanoparticles is first required. Thus, the conversion begins by calculating the volume of a of a 10nm particle using a simple spherical volume formula (Equation (52)). Once the volume of the nanoparticle has been found the volume of the atoms comprising it can be found the packing efficiency formula (Equation (53)), where  $V_{An}$  is the volume of the atoms,  $V_{NP}$  is the volume of the nanoparticle and  $P$  is the packing efficiency). By dividing the volume occupied by atoms by the volume of a single atom (Equation (54)) and multiplying the resulting number by the mass of a single atom it is possible to find a formula describing the mass per nanoparticle (Equation (55)). Finally, by dividing the mass per mL by the mass per nanoparticle we can calculate the particles per mL (Equation (56)).

$$V = \frac{4}{3}\pi r^3 \quad (52)$$

$$P = \frac{V_{An}}{V_{NP}} \times 100$$

$$\Rightarrow V_{An} = \frac{PV_{NP}}{100} \quad (53)$$

$$n = \frac{V_{An}}{V_A}$$

$$\Rightarrow V_{An} = nV_A \quad (54)$$

$$m_{NP} = nm_A \quad (55)$$

$$C_{mg/mL} = m_{NP}C_{np/mL} \quad (56)$$

Using these mathematical formulae it was possible to calculate that the stock solution of 10nm silver nanoparticles at a 0.02mg/mL concentration corresponded to a concentration of 4.55E9 particles per mL.

To gather data to test the NanoConc program the stock silver colloid was first diluted to 80%, 60%, 40% and 20% (v/v) in deionised water before being analysed using DLS and UV/Vis spectroscopy. This DLS and UV/Vis data was then analysed using the nanoconc program to calculate a particles per mL concentration value. By comparing these values with the expected particles per mL (based on the concentration of the stock and the percentage v/v of the analyte) it was possible to examine the accuracy of the predictions of the program. The data from this simple dilution series test is presented in Table 11 and Figure 72, below.

Table 11. A table comparing the nominal, maximum and minimum particles per mL for the standard (as calculated based on the data reported by the supplier) and the output of the nanoconc program.

Percentage (v/v)	Standard (PPmL)	Standard Minimum (PPmL)	Standard Maximum (PPmL)	Nanoconc (PPmL)
20%	9.89E+11	5.44E+11	2.03E+12	8.82E+11
40%	1.98E+12	1.09E+12	4.06E+12	1.66E+12
60%	2.97E+12	1.63E+12	6.08E+12	2.51E+12
80%	3.96E+12	2.17E+12	8.11E+12	3.36E+12
100%	4.94E+12	2.72E+12	1.01E+13	4.19E+12

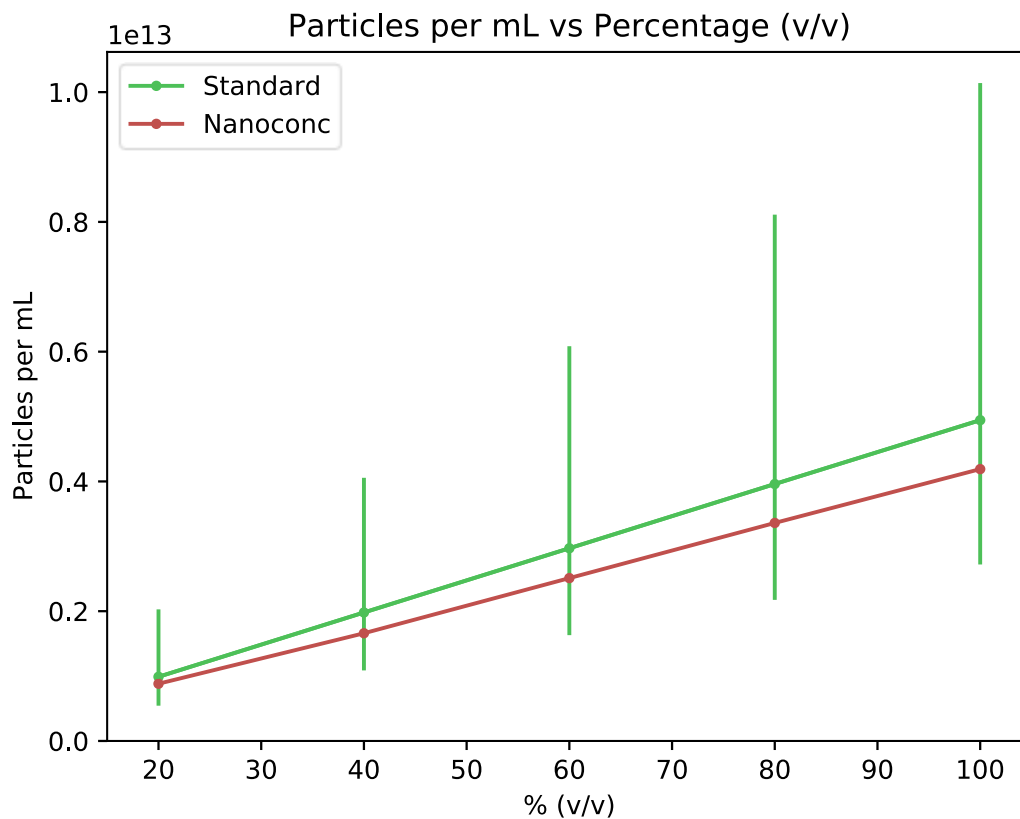


Figure 72. Plots of particles per mL vs % (v/v) of colloid as calculated based on the supplier's specifications (green, with error bands) and as returned by the NanoConc program (red). The output of the program is clearly well within the margin of error for the standard value.

From this data, it can be seen that the expected, calculated concentrations roughly correspond with the values according to the nanoconc program. The percentage difference that is present is likely due to either uncontrolled variables that influence the measurement of the data nanoconc relies on (such as temperature or turbidity) or inaccuracy in the concentration reported by the supplier of the colloid (which is a difficult hypothesis to test with available equipment).

### 5.2.5 Program Compatibility Tests

The final program was found to be capable of rapidly performing this calculation, producing a result for a 1,000 point spectrum predicted for a

dataset containing 10 particle sizes in an average of approximately 4.0 seconds for first execution, 1.6 seconds for second execution and 1.2 seconds for subsequent executions on an Intel i7-5600U CPU, a mid tier dual core laptop CPU that is several years old. As would be expected in a JIT compiled programming language, the first execution of the particlecount function is significantly slower than subsequent executions (although 4 seconds for such a complex calculation is still quite fast). The broad compatibility of the language chosen has also been tested, with the same calculation having been successfully performed on a wide variety of common operating systems covering most of the major operating system families and branches in common use today. The operating systems tested thus far (and their respective OS family branches) include:

- Windows 10 (Windows)
- Windows 8 (Windows)
- Windows 7 (Windows)
- Mac OS X Mavericks (Darwin)
- Mac OS X High Sierra (Darwin)
- FreeBSD 12.0 (Berkley Software Distribution)
- Android 8.1 Oreo x86 (Android)
- Lubuntu 19.04 (Ubuntu Linux)
- Linux Mint 19.2 "Tina" (Ubuntu Linux)
- Debian 10.1 "Buster" (Debian Linux)
- OpenSUSE Tumbleweed (SUSE Linux)
- Fedora 30 (Fedora Linux)
- CentOS 7 (Red Hat Enterprise Linux)
- Manjaro 18 (Arch Linux)
- Arch Linux (Arch Linux)
- Sabayon 19.03 (Gentoo Linux)
- Mageia 7.1 (Mandriva Linux)
- Solus 4 (Solus Linux)

In addition to these many software compatibility tests the program was also shown to work well on all of the most common CPU architectures currently in common use (x86, AMD64 and ARM). The code has been successfully statically compiled into .dll and .so files, two common types of widely compatible library accessible by most programming languages. Using included developer tools it is also possible to transpile the code into functioning C code, making it theoretically portable to any device with a C compiler. If, for some reason, compilation for a device is not possible Julia Computing Inc provide a free, cloud-based applet version of the Julia compiler<sup>197</sup> allowing scripts written in the language to be executed on any device with a browser that conforms to modern web 2.0 standards. Finally, interoperability tests have found that the code is also able to be easily called from other programming languages such as Python and C without the need for glue code, meaning it should be extremely easy to incorporate into other projects if needed. This extremely wide operating system, hardware and software compatibility of the program is important as it allows the program to be deployed as part of almost any platform likely to be encountered in a modern setting, ranging from old computers and high-end workstations to mobile phones and inexpensive single-board computers (such as the “Raspberry Pi” devices commonly used in research environments).

Although the choice of programming language has conferred this wide variety of benefits on the program it does also create a potential future inconvenience in the form of code deprecation. As Julia is a relatively young language it may be subject to major changes in the future as the language evolves. For example, during the development of the application (in the transition from Julia 0.7 to Julia 1.0) one such major syntax change was made modifying the syntax of iterative calculations, resulting in code breakage that could only be rectified with changes to the source code. If such a change affects a language feature used in the code this can deprecate it and cause it to need changes before it becomes executable

again. This can happen with any programming language, of course, but is far less likely to occur in older, more established and refined languages. At the time of writing, the current supported versions of Julia (1.1 and 1.2) has been confirmed to successfully execute the source code attached (Appendix 10 - Appendix 12) and the planned future changes to the language for Julia 1.3<sup>198</sup> and Julia 1.4<sup>197</sup> do not appear to list any changes that would be expected to cause code breakage.

### 5.2.6 Conclusions on the NanoConc Program

Based on the tests performed, it seems reasonable to conclude that through the application of Mie theory and computational methods the goal of developing a program capable of measuring the concentration of a nanoparticle colloid using readily available non-destructive methods has been achieved. Verification tests have suggested the program to be capable of measuring the concentration of a silver nanoparticle colloid to within at least an average of 6.14% of the actual value (based on the concentration reported by the supplier). For further verification, future work should ideally compare the results of analysis with the NanoConc program to those of a proven method instead of relying on unverified values reported by the supplier (such as nanoparticle tracking analysis<sup>199</sup>) if access to suitable equipment can be gained. In addition it will be important to expand tests to test the accuracy of the program with other metals besides silver, because although the calculation should theoretically be applicable to all metals this fact is in need of confirmation. Of course, the motivation for the development of this program was to quantify the concentration of gold colloids, but verifying the efficacy of the program with gold was not possible at this stage due to the prohibitive cost of gold nanoparticle colloids.

The final working program has been extensively tested to demonstrate its performance and wide ranging compatibility and adaptability. These features of the program are important, as a program of this nature has

many potential applications in research and thus should ideally be able to be easily deployed on a wide variety of platforms and incorporated into systems developed by future researchers. As the JIT compiler of the chosen programming language is further refined for better numeric computational performance the program can be expected to benefit from these improvements as no upcoming changes to the language are anticipated to break the source code or slow down performance critical functions. Finally, should code breakage occur, bugs be found or modifications needed the pythonic nature of the Julia programming language should make bugfixing and code maintenance/modification relatively simple for researchers with a modicum of programming experience.

## 6. Evaluation of Sensor Performance

To evaluate the performance of the final sensor platform design described in Section 4.3 it was first necessary to select a target analyte with which to experiment. For the sake of simplicity, it was decided to test the platform as a sensor for DNA. The DNA sequence to be used during testing was a small subsequence of exon 2 of the homo sapiens v-myc avian myelocytomatosis viral oncogene homolog (MYC) gene, also commonly known as the c-Myc gene. The c-Myc gene is responsible for many cell functions associated with cell proliferation, growth and death<sup>200,201</sup>. As might be suspected based on these functions, it is noted to be overexpressed in a wide variety of cancers<sup>200</sup> although it is most closely associated with Burkitt Lymphoma<sup>202</sup>. The gene has also been implicated as a possible contributing factor in many other cancers (as is evident by a brief examination of the NHGRI GWAS Catalog entries on the NCBI web page for the gene<sup>201</sup>). In addition to being a prolific cancer indicator overexpression of the c-Myc gene has also been noted (in the case of breast cancers, at least) to be strongly associated with more aggressive tumors and a negative prognosis<sup>200</sup>.

The short subsection of c-Myc exon 2 selected for testing had the following sequence:

GTCTTCCCCTACCCTCTCAACGACA

This sequence was selected as it provides a simple, easy to handle and relatively safe example of an oncogene sequence that can be used to demonstrate the potential usefulness of the sensor platform in cancer detection.

The most straightforward way to detect this sequence with a noble metal based sensor platform would be to functionalise the sensor with a thiolated DNA strand that is countersense to MYC exon 2 as a detection

molecule. Thus the sequence of the detection molecule (which will henceforth be referred to as the thio-DNA probe) to be used was:

TGTCGTTGAGAGGGTAGGGGAAGAC-thiol

Once an appropriate target analyte had been chosen, it was decided that a dose-response curve experiment should be performed for that analyte. To perform a dose-response curve test, the platform must first be incorporated into a sensor to detect the target analyte, then inoculated with varying concentrations of the target analyte. Once inoculated the response of the sensor to the analyte can be measured by analysing the sensor using a suitable characterisation technique. If the platform is suitable for use as a sensor an observable relationship between the amount of analyte added and the response observed would be expected. This relationship would then allow for the sensor to measure an unknown amount of analyte by simply measuring the response.

To examine a dose-response curve it is first important to select an appropriate response to measure. Based on previous experiments throughout Chapter 4 it was decided that the testing methods most likely to yield a useful response would be chronoamperometry, cyclic voltammetry and electrochemical impedance spectroscopy. As such, it was decided that experimentation should first begin by performing initial, simple dose-response tests using these methods to find the one that provides the most significant response. Following this, testing should proceed by determining the most reliable response and optimising a methodology before performing a final dose-response test to yield a dose-response curve for the sensor.

## 6.1 Testing of Analysis Techniques

As an initial test to determine the correct characterisation method for sensor measurements a simple dose-response curve experiment was performed using chronoamperometry, cyclic voltammetry and electrochemical impedance spectroscopy. Following these tests, the resulting datasets were compared to compare their usefulness and decide with which methods to proceed in future testing.

### 6.1a Testing of Analysis Techniques: Materials and Equipment

ZeonorFilm ZF14-188 (Zeon Chemical L.P. Japan) Cyclic Olefin Polymer (COP) was used as the CAP substrate. A 10 mm × 10 mm × 0.188 mm, 99.9% pure gold metal ablation target was prepared from a sputtering target (Agar Scientific, UK). For CAP, this target piece was then affixed to an ablation stage, fabricated using PlasClear photopolymer resin and a Freeform Pico (Asiga, CA, USA) SLA 3D printer. For PLAL the target was placed in an ablation cell fabricated from Verowhite polymer resin using a Stratasys Connex 1 polyjet 3d printer. All ablations were performed with a 1064 nm diode-pumped, solid state neodymium-doped yttrium aluminium garnet (Nd:YAG) laser. This laser was operated in TEM<sub>00</sub> mode, producing a beam with a Gaussian profile and a spot diameter of 140 μm at the focus. This beam was pulsed at a PRF of 10 kHz and with a pulse width of 700 ps. For CAP depositions, this laser beam was rastered across the target during sample production using a 2D scanning galvanometer (Raylase SS- 12, Germany). For PLAL production, the same galvanometer was used to trace a tight spiral on the target and an experimental prototype of a “Continuous Flow PLAL” setup was used. The target position in the beam waist was controlled using an M-404 4PD nano-position stage (PI, Germany).

Screen printing sensor fabrication steps were performed using Ercon E3178 Conductive Carbon Ink on a Dek 248 semi-automatic printer. The

reagents used during sensor fabrication were benzene-1,4-dithiol (99% GC, Sigma-Aldrich IE), 6-mercaptohexanol (97%, Sigma-Aldrich IE) and Phosphate Buffered Saline (PBS, tablet, Sigma-Aldrich IE). All DNA samples were sourced from Integrated DNA Technologies, Inc (IDT, USA).

The samples produced were electrochemically characterised using a Gamry Interface 1000E potentiostat. ANOVA analysis was performed with the aid of StatEase Design-Expert and analysis of electrochemical spectra was performed using Gamry eChem Analyst software. All other data analysis was performed in python based jupyter notebooks utilising the “Atom” IDE.

### 6.1b Testing of Analysis Techniques: Methodology

A number of sensors were prepared for the detection of the target analyte according to the following procedure:

1. 5mm × 5mm nanostructured gold squares were deposited on COP using CAP with the following parameters:
  - Laser Type: 1064nm Nd:YAG
  - Fluence: 0.79J/cm<sup>2</sup>
  - Repetition Rate: 10kHz
  - Pulse Width: 3.5μs
  - Scan Speed: 18mm/s
  - Scan Spacing: 50μm
  - Scan Type: Bidirectional
  - Vertical Spacing: 50μm
  - Target surface at focal point
2. Contacts were screen printed using Ercon E3178 Carbon Ink
3. Sensors were immersed in 0.1% (w/v) 1,4-dithiobenzene in a 50:50 water:ethanol solvent for 5 minutes (Figure 73a)
4. Sensors were then immersed in an aqueous gold nanoparticle colloid for 5 minutes (Figure 73b)

5. Immersed in 1,4-dithiobenzene again solution for 5 minutes
6. Immersed in nanoparticle colloid again for 5 minutes
7. Sensing surface was inoculated with 100 $\mu$ L of 10 $\mu$ M thio-DNA probe in PBS for 15 minutes (Figure 73c)
8. Sensing surface was inoculated with 100 $\mu$ L of 5% (v/v) 6-mercaptohexanol in 50:50 water:ethanol solvent as a passivator (Figure 73d)

The gold nanoparticle colloid used was produced using a continuous flow PLAL methodology currently being developed in the lab. It was produced on the same 1064nm ND-YAG laser used for the CAP depositions with the following continuous flow PLAL parameters:

- Fluence: 1.83J/cm<sup>2</sup>
- PRF: 10kHz
- Pulse Width: 500ps
- Ablation time: 30 mins
- Flow Rate: 140mL/min

This 83mL aqueous colloid batch was found to have a particle diameter of 18nm and a concentration of 6.84E11 particles per mL (according to the NanoConc program described in Section 5). Following each step involving exposure to a liquid solution the sensors were rinsed with a small amount of ethanol to minimise cross contamination of the reagents.

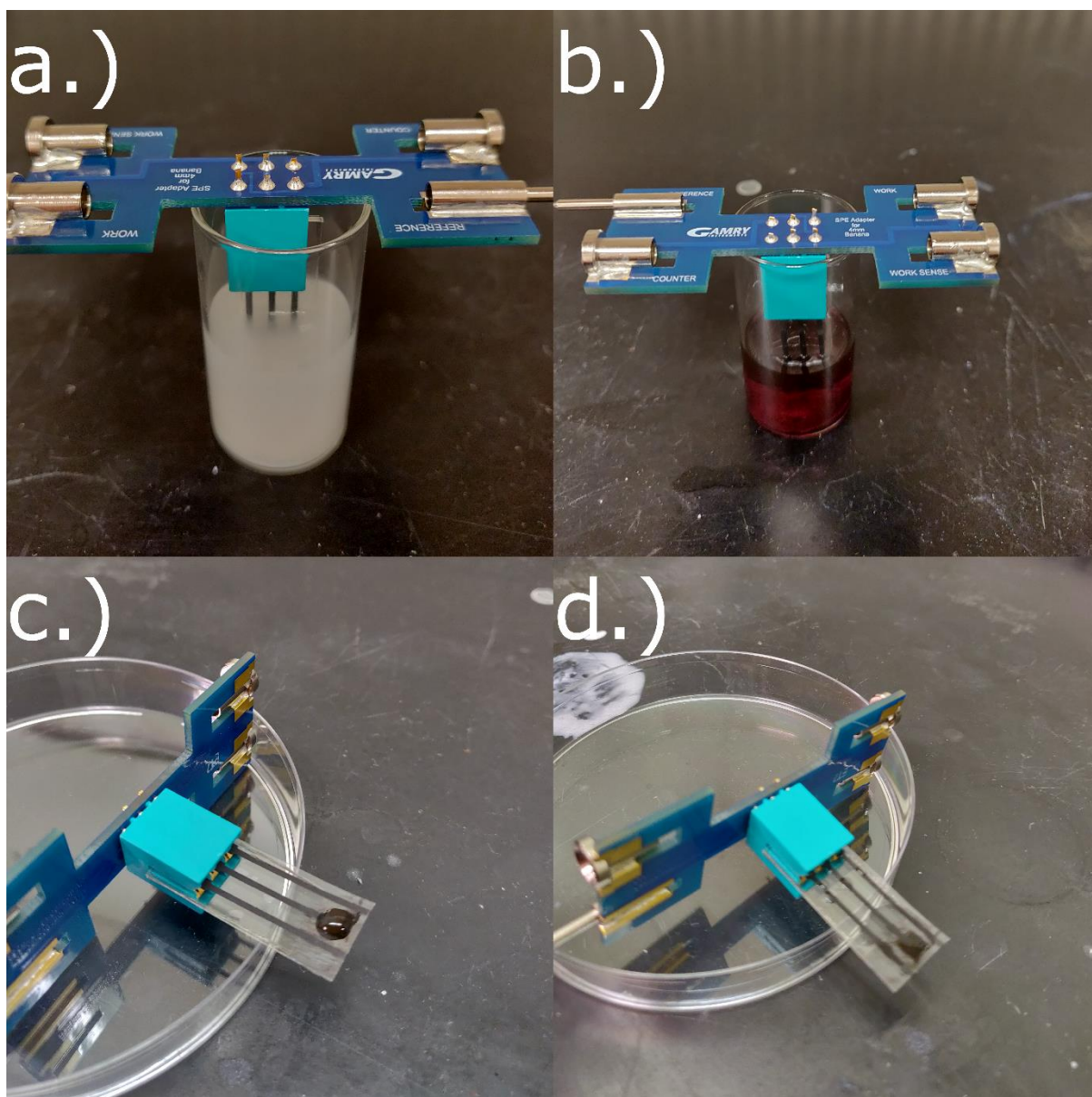


Figure 73. Photographs of the various steps of sensor fabrication following the screen-printing step. The steps pictured are (a) immersion in 1,4-dithiobenzene, (b) immersion in aqueous AuNP colloid, (c) inoculation with thio-DNA and (d) passivation with 6-mercaptohexanol.

For the first sensor test performed, the sensor was subjected to conductometric testing at each step to examine the effects of each fabrication step on the properties of the sensor. Following this, a batch of several sensors was prepared. Once this batch was prepared for use, the sensors were then inoculated with 100 $\mu$ L a various known concentrations

of c-Myc exon 2 for 30 minutes. The concentrations of the various c-Myc exon 2 solutions used were 1  $\mu\text{M}$ , 0.8  $\mu\text{M}$ , 0.6  $\mu\text{M}$ , 0.4  $\mu\text{M}$  and 0.2  $\mu\text{M}$ . After this inoculation, the sensors were then rinsed with ethanol to remove unbound DNA and subjected to conductometric testing in a PBS solution (Figure 74).



Figure 74. A photograph of conductometric testing being performed on the final sensor design. Sensors were immersed in PBS and subjected to conductometric testing both before and after inoculation with the target.

The conductometry data from this experiment was then analysed to understand the behaviour of these sensing surfaces during the fabrication process and in their final intended role as a biosensor.

## 6.1c Testing of Analysis Techniques: Results and Analysis

As previously mentioned in Section 6.1a, a sensor was subjected to conductometric testing during the fabrication process to examine its responses during fabrication (Appendix 13 - Appendix 20). This conductometric data shows very few obvious, major changes to the conductometric properties of the surface during fabrication until passivation occurs (between steps 3 and 7 of the fabrication process). Interestingly, a significant change in properties is observed when comparing the conductometric data (Figure 75) before and after the passivation step of the fabrication process (step 8).

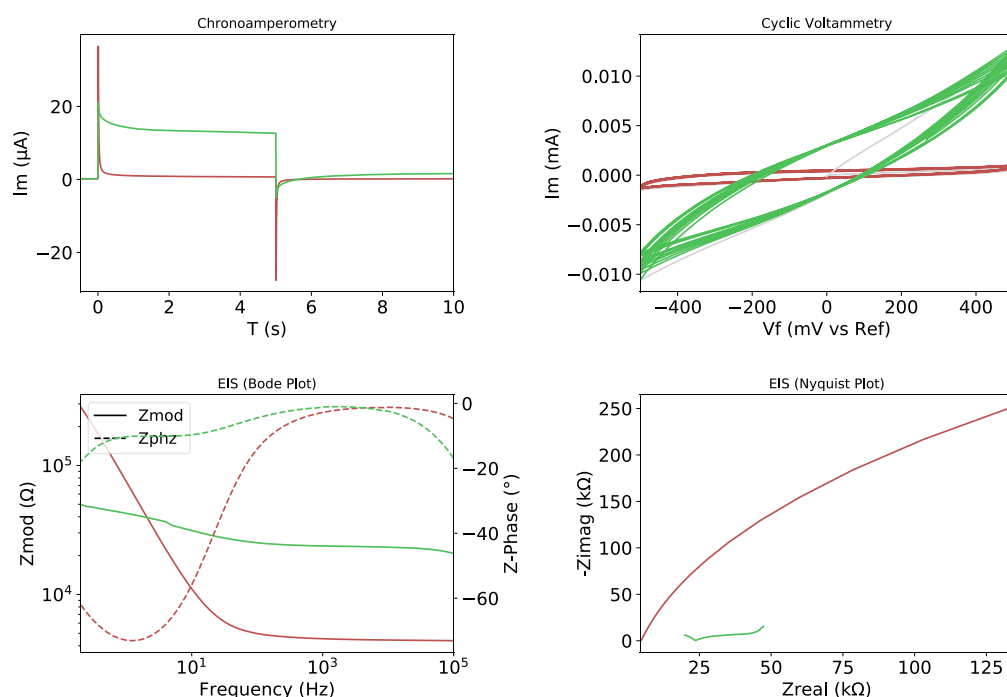


Figure 75. Overlaid graphs of several electrochemical tests for the sensor before (red) and after (green) passivation. Each plot shows a clear change in electrochemical properties following passivation.

For the chronoamperometry scan, A notable change in the intensity of the current peaks and the measured charge. This charge value is determined by calculating the integral of the plotted graph<sup>203</sup>. For each sample before

passivation, the charge was found to be between approximately 4  $\mu\text{C}$  and 5  $\mu\text{C}$  for each sample. Directly after passivation, the charge was found to have changed from 5.27  $\mu\text{C}$  (before) to a significantly larger value of 72.79  $\mu\text{C}$ . This shift would be indicative of a change in one of the parameters of the Cottrell equation for the sensor surface, although determining which one is not possible without further testing.

In the cyclic voltammetry scan, there is a clear shift in the slope of the line between the maximum and minimum voltage of the plot caused by the passivation step. There is also a clear increase in the area enclosed by the curves. As the scan rate and potential window for the CV scans were the same for both experiments this strongly suggests a significant increase in the capacitance of the sensor following passivation<sup>204</sup>. No clear peak anodic or cathodic current is present in either voltammogram. As these peaks are usually indicative of potentials at which reactions occur<sup>180,205</sup> which suggests that no significant redox reactions are occurring during the scan. This suggests that the sensors are reasonably stable under testing conditions, as they do not appear to be chemically reacting with the test solution.

In the EIS data obtained, there are clear changes in both the Bode plot and Nyquist plot of the sample caused by passivation. Most significantly, the Nyquist plot shows a clear change in both the real impedance and the direction of the curvature of the graph. In the Nyquist plot, the real impedance corresponds to the point at zero imaginary impedance<sup>203</sup>. While there is an obvious shift in real impedance during passivation as suggested by the Nyquist plots above, there is also an extremely clear shift in the range of real impedances across the frequency range swept. This suggests a change to the electrochemical properties of the system, although the exact nature of the change it implies is difficult to discern in the absence of EIS modelling.

Similarly, comparing the conductometric properties of the surface before and after its inoculation with c-Myc exon 2 (Figure 76) clearly shows a change.

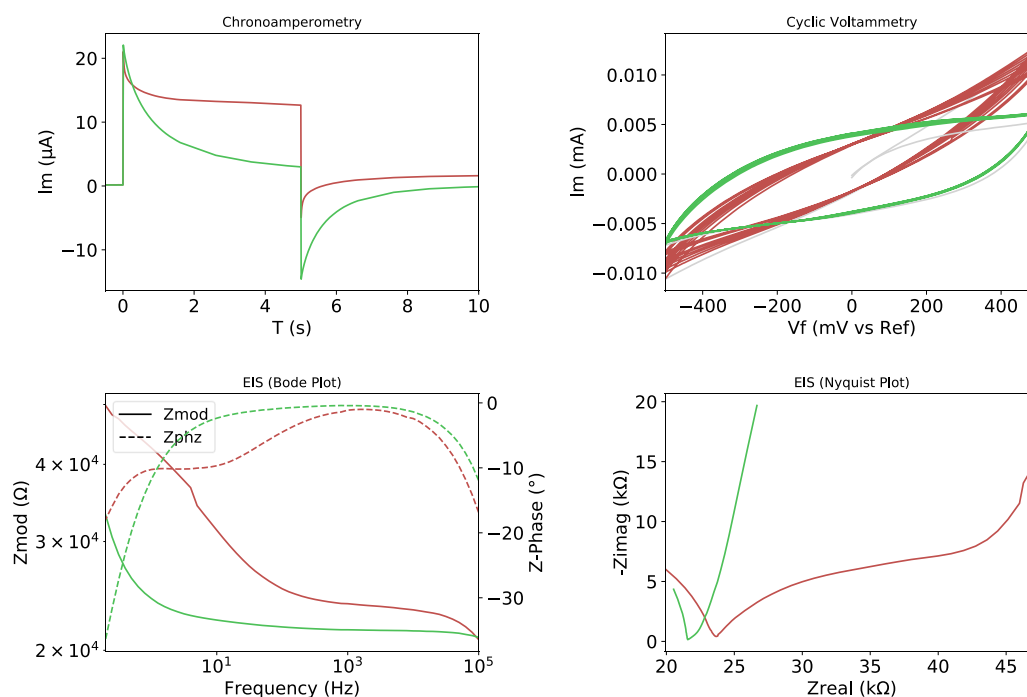


Figure 76. Overlaid graphs of several electrochemical tests for the sensor before (red) and after (green) exposure to c-Myc exon 2. Each plot shows a clear change in electrochemical properties following inoculation with the target.

Similar changes are visible here in the chronoamperometry and cyclic voltammetry plots to those observed before and after the passivation step. Also similar to above, a clear shift is observable in the Nyquist plot for the surface. These Nyquist plots before and after c-Myc exon 2 exposure show a definite difference in real impedance and the range of real impedances across the frequency range swept, suggesting an electrochemical change in the sensor in response to its intended target analyte.

Following this observation that the surface appeared to respond to the target analyte with a change in conductometric properties, a dilution series was prepared and a quick, naïve attempt was made to elucidate a dose-response curve. While the results of this dose-response test (Appendix 21 - Appendix 30) did show a variance in the features across the spectra obtained and a small unpredictable variation in real impedance, it was difficult to draw any conclusions from it. As such, rather than statistically analysing this data and attempting to find a significant dose-response model a decision was made to proceed by instead using it to refine a more accurate methodology for a future dose-response curve test.

Although all the EIS spectra for the inoculated samples differed from those obtained for the uninoculated samples the difference was small and the variance was high relative to that difference. This high percentage variance made the elucidation of a statistically significant trend near impossible. For future tests, it was decided it would be useful to increase response and decrease variance and appropriate changes to address this concern would be made in future experiments. In addition to this, it was clear that although the EIS data was giving an appreciable and readily quantifiable output the parameters used during this experiment were less than ideal. The real impedances found were generally occurring in regions extremely close to the edge of the spectrum and without a sharply defined minimum point, and thus were often difficult to identify as the real impedance with any degree of certainty. It was thus decided that before proceeding with another dose-response curve experiment better EIS parameters for the sample than the instrument default values would need to be found.

## 6.2 Dose-Response Curve of Sensor

Taking the lessons learned during the experiments described in Section 6.1, a slightly modified methodology for finding a dose-response curve for the sensor was devised. It was previously found that the data needed a larger response and smaller variance to determine if any quantifiable relationship was present between the amount of target analyte to which the sensor was exposed and its conductometric response. It was also suspected that the default EIS parameters used were not ideal for the analysis being performed. To address these issues, the methodology described below was applied in the next attempt at a dose-response measurement and the corresponding results are presented at the end of this Section.

### 6.1a Dose-Response Curve of Sensor: Materials and Equipment

ZeonorFilm ZF14-188 (Zeon Chemical L.P. Japan) Cyclic Olefin Polymer (COP) was used as the CAP substrate. A 10 mm × 10 mm × 0.188 mm, 99.9% pure gold metal ablation target was prepared from a sputtering target (Agar Scientific, UK). For CAP, this target piece was then affixed to an ablation stage, fabricated using PlasClear photopolymer resin and a Freeform Pico (Asiga, CA, USA) SLA 3D printer. For PLAL the target was placed in an ablation cell fabricated from Verowhite polymer resin using a Stratasys Connex 1 polyjet 3d printer. All ablations were performed with a 1064 nm diode-pumped, solid state neodymium-doped yttrium aluminium garnet (Nd:YAG) laser. This laser was operated in TEM00 mode, producing a beam with a Gaussian profile and a spot diameter of 140 μm at the focus. This beam was pulsed at a PRF of 10 kHz and with a pulse width of 700 ps. For CAP depositions, this laser beam was rastered across the target during sample production using a 2D scanning galvanometer (Raylase SS- 12, Germany). For PLAL production, the same galvanometer was used to trace a tight spiral on the target and an experimental prototype of a “Continuous Flow PLAL” setup was used. The

target position in the beam waist was controlled using an M-404 4PD nano-position stage (PI, Germany).

Screen printing sensor fabrication steps were performed using Ercon E3178 Conductive Carbon Ink on a Dek 248 semi-automatic printer. The reagents used during sensor fabrication were benzene-1,4-dithiol (99% GC, Sigma-Aldrich IE), 6-mercaptohexanol (97%, Sigma-Aldrich IE) and Phosphate Buffered Saline (PBS, tablet, Sigma-Aldrich IE). All DNA samples were sourced from Integrated DNA Technologies, Inc (IDT, USA).

The samples produced were electrochemically characterised using a Gamry Interface 1000E potentiostat. ANOVA analysis was performed with the aid of StatEase Design-Expert and analysis of electrochemical spectra was performed using Gamry eChem Analyst software. All other data analysis was performed in python based jupyter notebooks utilising the “Atom” IDE.

### 6.2b Dose-Response Curve of Sensor: Methodology

For the second attempt at a dose-response experiment, the sensors were fabricated and inoculated according to the same methodology as that used previously in Section 6.1. However, to increase the response observed, a decision was made to inoculate the sensor surface with c-Myc exon 2 samples of 10 times greater concentration, to increase the response to the analyte. Thus, in this repeat experiment the sensors were inoculated with 100  $\mu\text{L}$  of 10  $\mu\text{M}$ , 8  $\mu\text{M}$ , 6  $\mu\text{M}$ , 4  $\mu\text{M}$  and 3  $\mu\text{M}$  c-Myc exon 2 solutions. Furthermore, to reduce the observed variance in the responses, the experiment was conducted in duplicate (as 2 separate batches). These methodical modifications would be expected to yield a significant reduction in percentage variance, thus facilitating the elucidation of a statistically significant trend describing the concentration of the target analyte in terms of the conductometric response of the sensor.

Following a large amount of trial-and-error testing, an EIS parameter set was gradually approached wherein the real impedance observed in the Nyquist spectra were generally sharply discernible and features on the left hand side of the real impedance were more visible. The parameter set eventually decided upon for future EIS testing was:

- DC Voltage (V): 0 vs. Eref
- AC Voltage (mV rms): 10
- Initial Freq. (Hz): 1000000
- Final Freq. (Hz): 10
- Points/decade: 100
- Area (cm<sup>2</sup>): 0.25
- Conditioning: Off
- Init. Delay: Off

In this parameter set, the most significant improvement was given by increasing the resolution of the scan (by increasing the “points/decade” parameter). Increasing this value significantly showed that many of the initial difficulties in finding the real impedance were likely due to lack of resolution. However, this change also had the effect of significantly increasing the time required to conduct each EIS measurement. As such, a decision was made to focus on EIS data for this repeated dose-response measurement, as previous tests had shown the chronoamperometry and CV measurements to be of limited usefulness for this sensor type.

With this modified methodology in place, a repeat of the dose-response experiment was performed and the results are presented below.

### 6.2c Dose-Response Curve of Sensor: Results and Analysis

Analysis of the data obtained from the dose-response curve experiment began with the plotting of the EIS spectra obtained (visible in Appendix 31 - Appendix 50). At the new EIS parameter set the data exhibited some

of the features that would be more commonly expected in EIS spectroscopy (Figure 77) and, based on this, attempts were made to find an equivalent circuit suitable for analysis by circuit modelling. The data also showed a definite shift in samples before and after inoculation with c-Myc exon 2.

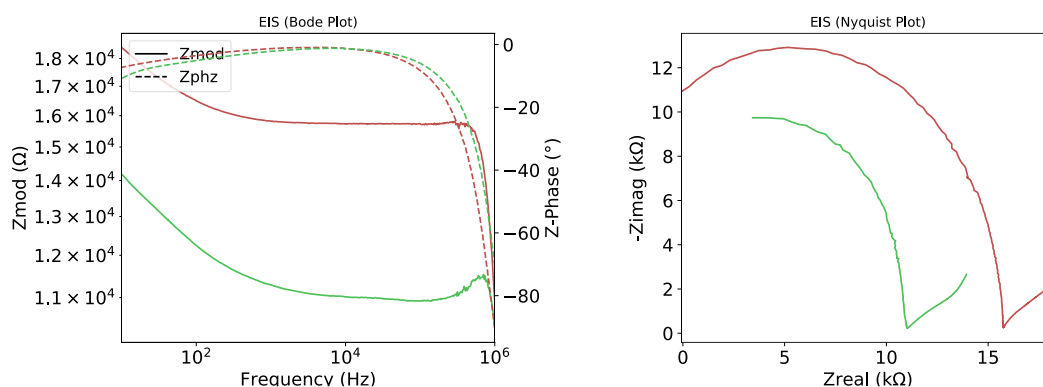


Figure 77. Example EIS plots for the sensor exposed to 10  $\mu$ M c-Myc exon 2 (red is before exposure and green is after exposure). There is a clearly visible change in the EIS spectrum for the sensor following inoculation with the target.

The clear semi-circular feature present in Figure 77 and several other of the spectra obtained is generally observed in diffusive electrode surfaces<sup>203</sup>. Sensor electrodes very often fall into this category<sup>206</sup> so they are generally modelled as such. Diffusive electrodes are commonly modelled as a Randles' circuit<sup>203,206</sup> (Figure 78). For this reason, initial modelling attempts were based on the Randles circuit but these models generally resulted in a somewhat poor fit.

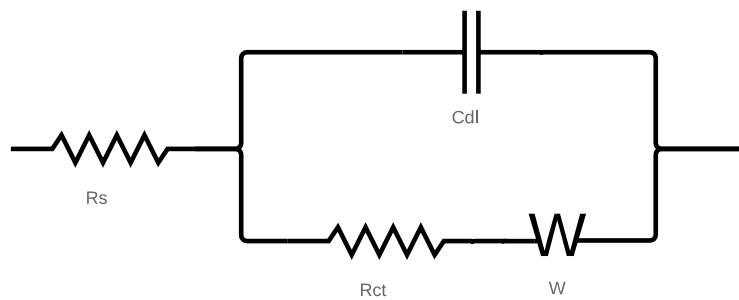


Figure 78. A diagram of the commonly modelled diffusive Randles' circuit. The “W” symbol represents a “Warburg element”, a type of constant phase element used to model diffusion in electrodes.

After significant experimentation and the exploration of various modified Randles circuits (for example, a variant replacing the capacitor  $C_{dl}$  with a constant phase element to account for surface roughness<sup>207</sup>) it was eventually found that the model which appeared to fit the data best consisted of 3 randles circuits in parallel (Figure 79). This equivalent circuit bears a resemblance to a “Transmission Line Model”, used as an alternative to the more common Randles’ cell in certain types of biosensor.

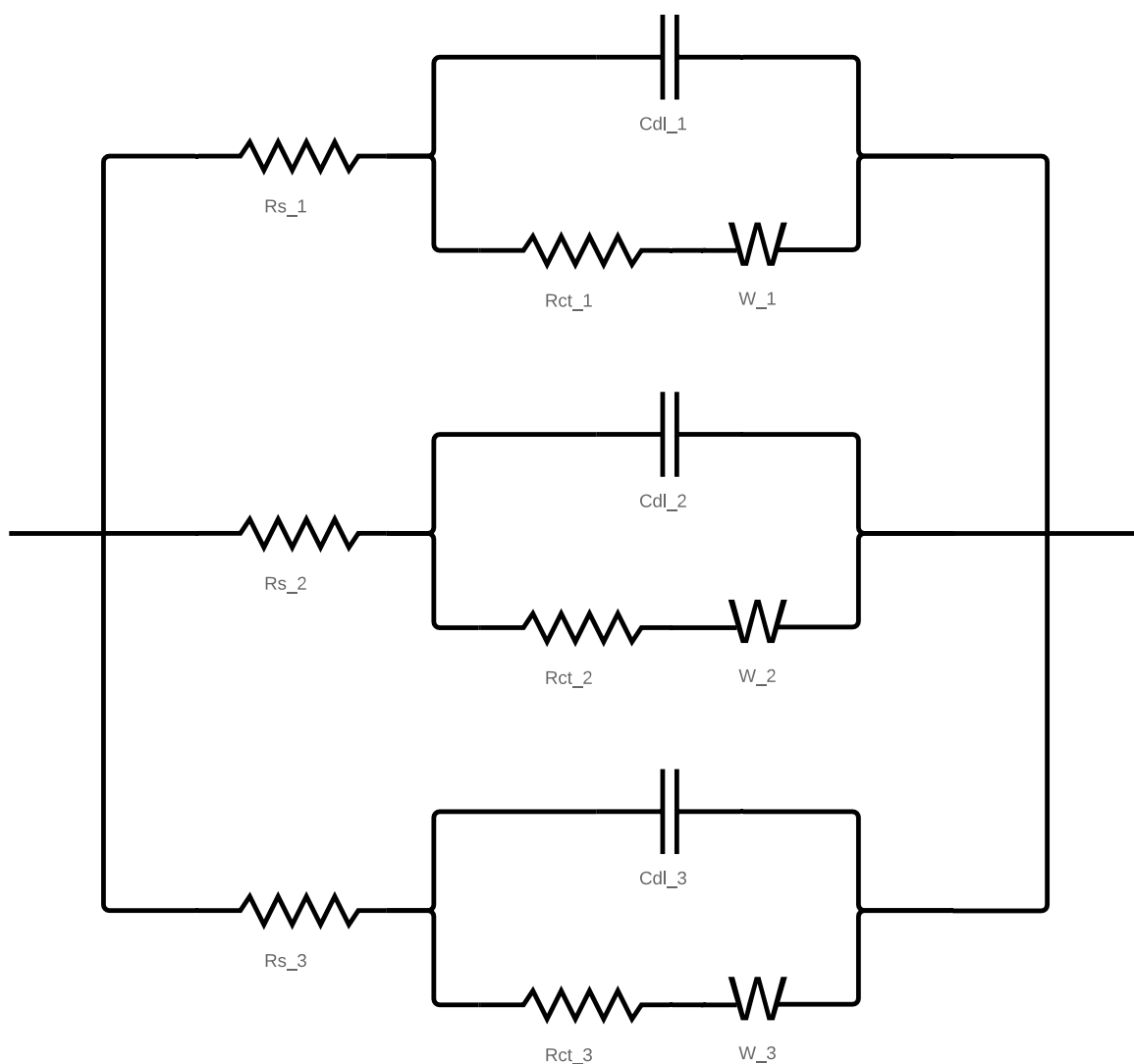


Figure 79. A diagram of the equivalent circuit found to most closely match the data obtained. Note that it is comprised of 3 Randles' circuits in parallel, with their elements labelled as being in Randles' circuit 1, 2 or 3

Once a model that appeared to describe the data was found, analysis of the results could begin. For the analysis the model above was fit to each spectrum in turn yielding equivalent resistivity, capacitance and Warburg admittances for each element labelled in Figure 79. Although this model fits the data, the large number of elements it has results in a high potential for inaccuracy as there are many, many degrees of freedom. To address this concern, it was decided that analysis would also include a

simpler measurement of real impedance from the Nyquist plots obtained as an alternative property of the circuit independent from the model.

Following the computation of this data for the spectra taken before and after inoculation a total resistivity, total capacitance and total Warburg admittance was calculated for each set of outputs from the model. This total was calculated in each case as it was difficult to ensure that the fitting algorithm was consistently treating each parallel Randles' element in the model consistently. For example, due to the simple purely mathematical and naïve nature of the fitting algorithm it is possible that for sample A it may return the values for the working electrode as Randles' element 1, whereas the values returned for element 1 in sample B could be those corresponding instead to the reference electrode. Despite this, we can expect that each of the electrodes in the sensor correspond to one of the Randles' circuits being modelled, even if it is difficult to be certain of which one without speculation. By adding together the data for all 3 Randles' circuits, this problem is avoided because the reference and counter electrodes wouldn't be expected to change their values significantly and this total value would include that of the working electrode.

Finally, to analyse the results a difference value and percentage difference values (for certain datasets, as will be discussed below) were calculated from the data obtained. These values were calculated to account for the inherent variance in the uninoculated sensor surfaces. As the fabrication process still results in some inconsistencies at this stage, there was some observed variance in the properties of the sensors before inoculation. This means that differences observed in the raw "after" dataset are caused by a combination of sensor variance and target analyte influence. Thus, by using differential values instead of the raw "after" values we can minimise the influence of sensor variance and isolate the effect of the target analyte on the sensor surface.

With all this data compiled (available in Appendix 51) it was then statistically analysed using Design-Expert 7 software. As the data was based on a single input parameter it was decided that the simplest way to being the analysis was by simply calculating the correlation coefficients for each of the most commonly used mathematical transforms in physical modelling. Analyses with these techniques found that the best correlated linear transfers appeared to occur for the “R-Total (diff)” (the differential of the total resistance from the model) and “Real Impedance (%diff)” (the percentage differential of the real impedance as measured by the Nyquist plot) output parameters. However, by examining these datasets more closely, it was found that there was a large divergence for both of the 4  $\mu\text{M}$  and 8  $\mu\text{M}$  concentrations across batches. For this reason, third tests were performed at the 4  $\mu\text{M}$  and 8  $\mu\text{M}$  datapoints and the correlation analysis was performed again. The complete results of this correlation analysis are presented in Appendix 52.

Similarly to the previous analysis, the second correlation analysis table shows a good (and appreciably improved) linear correlation for the “R-Total (diff)” (henceforth denoted as  $dR_T$ ) and “Real Impedance (%diff)” (henceforth denoted as  $dI_R$ ) outputs relative to the molar concentration ( $C_M$ ).

$$C_M = \frac{dR_T + 2.88744E^5}{35096} \quad (57)$$

$$C_M = \frac{dI_R + 100.831}{7.958} \quad (58)$$

At this point, a statistically significant model describing “R-Total (%diff)” ( $R^2=0.4643$ ,  $F=7.80$ ) also emerged but it was decided that it would be redundant in light of the existence of the “R-Total (diff)” model, and as its predicted  $R^2$  was significantly lower than its non-percentage counterpart (0.0571 vs 0.4654).

Table 12. A table of the ANOVA results for the initially derived fits (complete ANOVA tables are available in Appendix 53 - Appendix 54). These fits suggest predictable changes in sensor properties as a response to the target.

Response	Degrees of Freedom	Adjusted R <sup>2</sup>	Predicted R <sup>2</sup>	Adequate Precision	F Value
<b>R-Total (diff)</b>	1	0.6347	0.2850	8.682	18.38
<b>Real Impedance (%diff)</b>	1	0.4985	0.3312	8.021	4.55

Both of the correlations found (Table 12) show a positively sloped linear relationship between their respective measurement of resistance/impedance and the amount of target analyte inoculated. Thus, both the equivalent circuit modelling and the interpretation of the Nyquist plot imply in agreement that the sensor responds to the target analyte by proportionally increasing resistance.

Upon close statistical examination of both models it was noted that in the “R-Total (diff)” model the 4  $\mu\text{M}$  datapoint from batch 2 was a significant outlier skewing the fit. This was noticed by examination of the Cook’s Distance plot (Figure 80), a plot commonly used to identify outlying datapoints. The outlying point was previously identified as an apparent outlier (as discussed above) and repeated to increase the statistical accuracy of the 4  $\mu\text{M}$  sample subset.

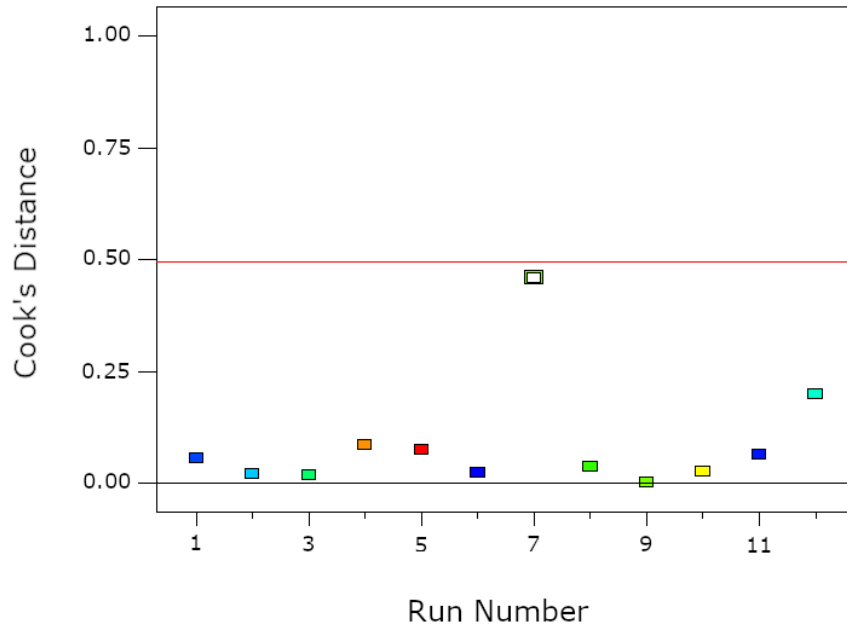


Figure 80. The Cook's Distance plot for the initially derived R-Total (diff) model. Note the highlighted outlier, signifying a point that significantly deviates from the observed trend.

A convenient way to quickly check if a sample in a bivariate dataset is likely to be an outlier is to use a simple confidence ellipse plot. As work so far had generally been performed at a 95% confidence interval, a confidence ellipse plot was made with a standard deviation of  $2\sigma$  standard deviation ellipse and the suspected outlier of interest was highlighted on the plot (Figure 81).

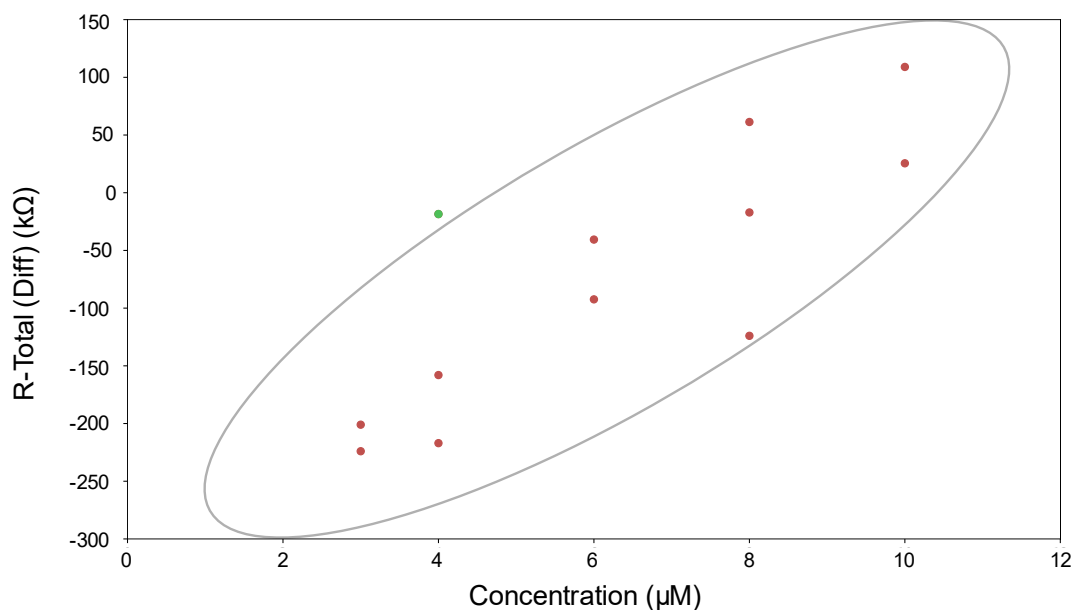


Figure 81. A  $2\sigma$  confidence ellipse plot for the R-Total (diff) dataset. The grey ellipse denoted the area of the plot wherein samples are less than 2 standard deviations from the trend. The suspected outlier of interest is highlighted in green and is clearly outside the  $2\sigma$  confidence range.

The confidence ellipse plot shows that the point does fall outside the  $2\sigma$  confidence boundary, further suggesting that the datapoint may be an outlier in the dataset. Based on this suspicion, the sensor used for the test described by the outlier datapoint was examined more closely to explore the possibility that the sensor may not have been deposited or printed correctly (Figure 82).

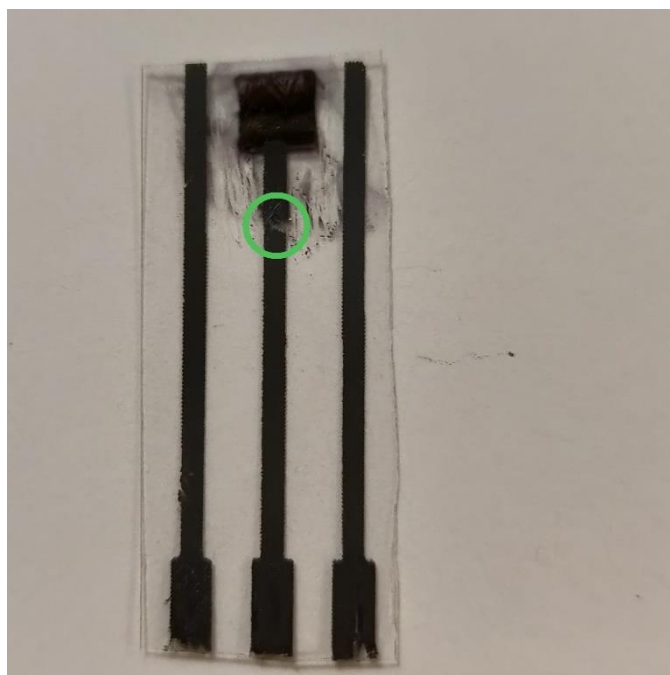


Figure 82. The sensor used for the 4um batch 2 datapoint of the dataset (the apparent outlier). An apparent break in the working electrode contact is highlighted with a green circle. This break is the most likely explanation for the unusually large standard deviation of the sample.

Upon examining the sensor, it was found that an apparent breakage was present in the contact for the working electrode. The origin of this breakage was difficult to discern; it may have been due to problems in the printing process but it may also be the result of damage as the breakage is also approximately the size of the tip of the tweezers used for sample handling. Whatever its root cause, this breakage offers a likely explanation for the statistically outlying datapoint this sensor produced.

Based on the statistical analysis and the reasonable justification discussed above it seems logical to conclude that this datapoint is likely an outlier. If it is an outlier, this then raises the question of whether or not it warrants exclusion from the dataset and rederivation of the model. As the underlying nature of the model would not be significantly altered by excluding the point (the models with and without the point are both positively sloped linear relationships) and an extra repetition of the

datapoint was obtained earlier in the experiment it makes sense to conclude that excluding the outlier is justifiable. Excluding this point would not fundamentally alter the conclusions drawn from the model, only change its accuracy (likely for the better if the point truly is an outlier).

With this outlying point excluded, the models were rederived and reanalysed and the results of this analysis can be seen in Table 13 (Appendix 55 - Appendix 56 for the full ANOVA tables). It can clearly be seen by comparing Table 12 and Table 13 that the removal of the outlier datapoint has resulted in a significant increase to the quality of the model, yielding a notable increase in all the major indicators of a good correlation.

Table 13. A table of the ANOVA results for the initially derived models (complete ANOVA tables are available in Appendix 55 - Appendix 56). These fits suggest predictable changes in sensor properties as a response to the target.

<b>Response</b>	<b>Degrees of Freedom</b>	<b>Adjusted R<sup>2</sup></b>	<b>Predicted R<sup>2</sup></b>	<b>Adequate Precision</b>	<b>F Value</b>
<b>R-Total (diff)</b>	1	0.8427	0.7767	13.602	49.23
<b>Real Impedance (%diff)</b>	1	0.7376	0.5870	10.847	26.29

The newly derived model describing the concentration of target analyte in terms of the R-Total (diff) measurement conformed to the following equation:

$$C_M = \frac{dR_T + 3.344E^5}{40390} \quad (59)$$

The  $R^2$  values for this model are quite good, and are accompanied by a high adequate precision and F value. Furthermore, the p-value of 0.0001 derived from the ANOVA analysis (Appendix 55) implies that this correlation has only a 0.01% chance of being a purely coincidental trend. This is quite a significant level of confidence in the model, although the actual correct probability of a coincidental trend is likely to be slightly higher as the calculated error bars resulting from the EIS model are not able to be taken into account by the statistical analysis software used.

The residuals of the actual data relative to the predicted model were found to be approximately normally distributed (as will be discussed further below) and the predicted vs actual plot shows clear agreement between the model and the empirical data (Figure 83). The normal plot of residuals for this model shows an extremely slight “double S-curve” shape, which suggests a slightly trimodal distribution. This could be due to small inaccuracies in the EIS model or variation in the quality of the sensors used for the experiment. One might hypothesize, for example, that a narrow normal distribution exists for high quality sensors superimposed on a wider normal distribution centered on the same point for sensors of slightly lower production quality. This would be expected to result in the kind of symmetrical double S-curve observed herein. However, as the amplitude of these double S-curve variations does not deviate much from the line representing a purely normal distribution, it makes sense to conclude that the data very closely approximates normally distributed data, and thus is normal enough to be treated as such.

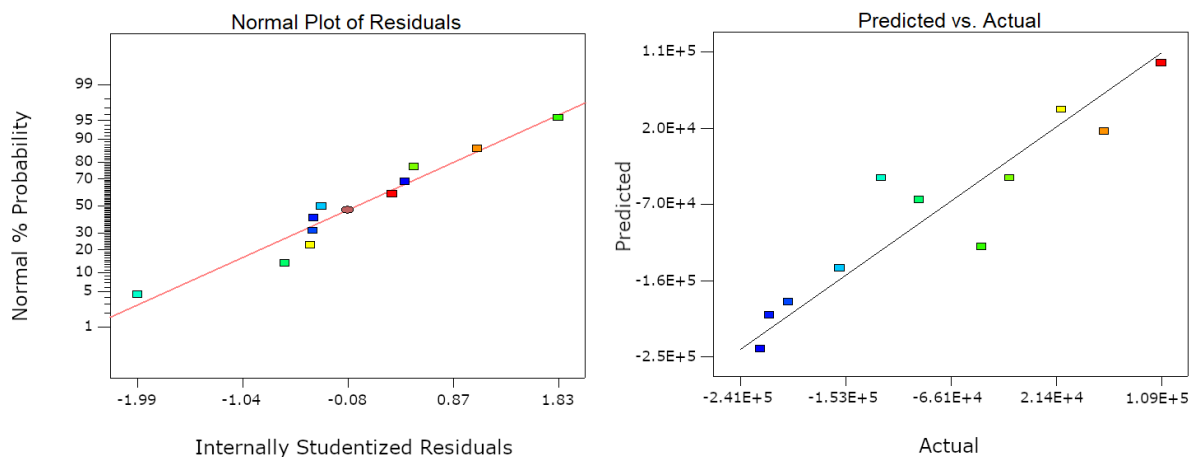


Figure 83. The normal plot of residuals and predicted vs actual plots for the R-Total (diff) model described by Equation (59).

By graphing the line described by the derived model (Equation (59)) and plotting the empirical data points (Figure 84) there is a noticeable agreement between the model and the observed reality. As can be seen, this relationship reveals one means of relating the concentration of the target analyte to the response of the sensor.

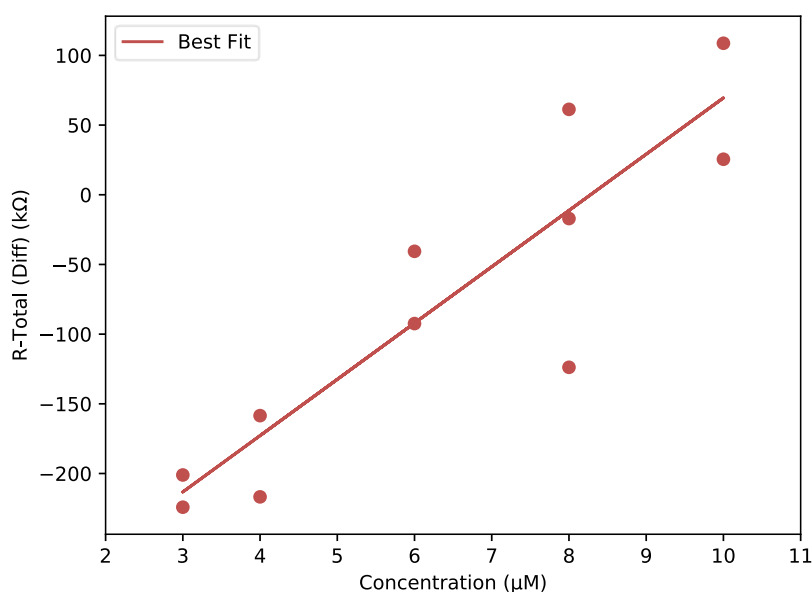


Figure 84. A plot of the empirical R-Total (diff) data obtained and the line described by Equation (59). The fitted line described by this equation aligns well with the empirical data.

As mentioned earlier, another potential method for using the sensor to quantify the target analyte is by measuring the percentage change in the real impedance according to the Nyquist plot (the “Real Impedance %diff” model in Table 13 and Appendix 56). Similar to the previously discussed model, this derived equation (Equation (60)) found a positively sloped linear relationship between the impedance of the sensor and the concentration of the target analyte.

$$C_M = \frac{dI_R + 107.19}{8.70} \quad (60)$$

The  $R^2$  values and other significant indicators such as adequate precision and F value are also quite good for this model although not quite as high as they were in the R-Total (diff) model described above. Despite this, it still shows a very significant p-value of 0.0009, suggesting a mere 0.09% chance of the correlation being due to pure coincidence.

For this model the residuals very closely obeyed a normal distribution and there is reasonable agreement evident in the predicted vs actual plot between the model and the empirical data obtained (Figure 85).

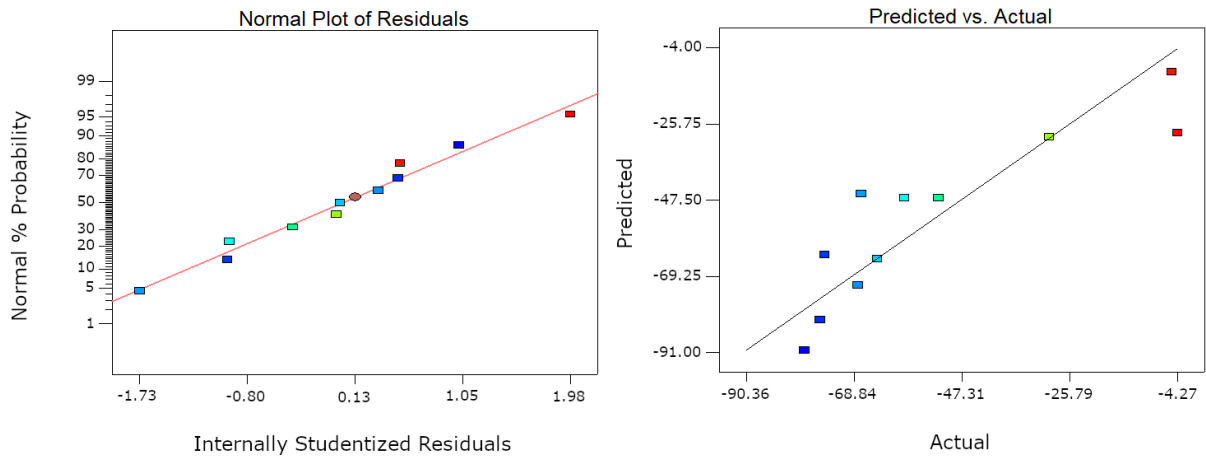


Figure 85. The normal plot of residuals and predicted vs actual plots for the Real Impedance (%diff) model described by Equation (60).

Again, by comparing the line described by the model (Equation (60)) with the empirical data we can see that the model does, indeed, describe a trend apparent in the sensor properties measured (Figure 86). This mathematical relationship provides a second means of relating the target analyte concentration to the observed change in the properties of the sensor.

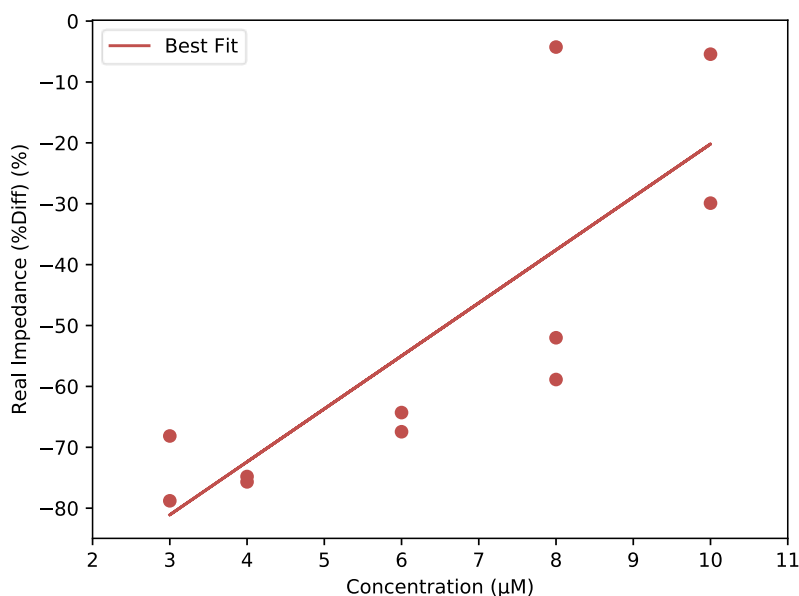


Figure 86. A plot of the empirical Real Impedance (%diff) data obtained and the line described by the Equation (60). The fitted line described by this equation aligns well with the empirical data.

Together, both of these models strongly suggest a mathematically quantifiable response of these electrodes to concentrations of target analyte, as would be required for their use as a sensor. Both models agree that there is a positively sloped linear correlation between the impedance of the sensor and the amount of analyte present. Furthermore, their p-values both imply that these models are very unlikely to have emerged through mere coincidence. Thus when taken together the agreement of these models and their p-values suggest an extremely low probability that the observed sensing activity is coincidental.

## 7. Summary and Conclusions

Throughout the course of this research project one constant trend was the repeated realisation that the path from an interesting discovery to an uninteresting and mundanely predictable process is, ironically, strewn with unpredictable obstacles. From the accidental discovery of the CAP process to its eventual application in a functioning sensor platform a number of interesting challenges presented themselves.

The work began with an extensive examination of the current state of biodiagnostics and sensor design (as discussed throughout Chapter 2). In addition to lending a familiarity with the field this process also allowed for a number of sensor design goals to be outlined for the sensor being developed. Based on the available literature (as discussed in Section 2.10) it was decided that the final sensor platform should ideally be the following:

- Label-free
- Inexpensive
- Mass producible
- Reusable
- Environmentally friendly to produce
- Conductometric
- DNA based

With these goals in mind, the development process began with the discovery of the CAP deposition process and the realisation that it could, potentially, be a useful fabrication method for achieving some of the goals outlined above.

Following its initial discovery as an accidental deposition during an unrelated experiment, the process of CAP was found to be a surprisingly

temperamental one. The chance occurrence that these accidentally incorrect parameters happened to fall within what we now know to be a narrow window wherein CAP deposition occurs and results in nanostructure formation was undoubtedly a lucky one. However, following this chance discovery the process was successfully refined to widen this narrow window of acceptable parameters and to increase the reliability of this inexpensive, rapid and environmentally friendly deposition process.

The refinement of the CAP process occurred in many incremental stages, as the understanding of the process gradually grew over time. Initially, it consisted of simple exploration of the capabilities of the technique and attempts to determine what may or may not influence nanoparticle depositions. During this stage, it was discovered that the technique was applicable to a wide variety of materials and it was decided that gold would be used in sensor development as it is easy to functionalise and well understood as a material from which to fabricate sensor platforms.

The first major optimisation to the reliability of the process was the discovery that interactions between the glass substrate initially used and the laser beam were interfering with the ablation and deposition process. By switching to COP as a deposition substrate, this initial source of variance was corrected. This first optimisation study also imparted an understanding that a large vertical spacing resulted in very poor deposition. Following this, the next optimisation study resulted in the realisation that large percentage variances in the vertical spacing between the deposition substrate and the target material appeared to be causing much of the observed remaining variance. Based on this, the final iteration of the CAP methodology was devised (Figure 21, Page 85) and this design was used throughout the rest of the project. At this stage, it was concluded that the CAP process had been optimised enough that it would likely be suitable for application in sensor fabrication. It had been

shown that several of the properties of surfaces deposited via the CAP process were controllable and the methodology had been refined into a repeatable process. At this stage work could progress to the next step of development.

The next stage in the development process involved the design of a suitable method for applying the CAP process as a sensor fabrication method. To this end, experiments to determine a suitable macroscale shape for the sensor design were undertaken. A variety of designs were tested including interdigitated designs. Although some major obstacles in the development of an interdigitated electrode design were successfully addressed (such as the noted existence of the “LIFT zone” around linear CAP depositions and, to a large extent, the ensurance of a contiguous deposition), the difficulty of reliably creating contacts for these designs and problems depositing conductive electrodes due to their miniscule thickness. For these reasons, the design eventually applied was a simple square electrode design for the working electrode of the sensor. Based on reading of the literature, if a square electrode design was to be used, the most reliable overall design would most likely be a 3-electrode design incorporating a counter electrode and a reference electrode in addition to the working electrode.

To make such a 3-electrode design work, a reliable set of CAP deposition parameters was decided upon. This set of parameters was noted to reliably result in the deposition of nanostructures but was found to have less than ideal conductivity for its application as a sensor surface. To remedy this, work began to develop a method for reliably increasing the conductivity of the sensors instead of trying to find a likely even narrower parameter range in which conductive nanostructures were reliably deposited. To this end, two separate methodologies were devised and tested for conductivity enhancement. The first (and simplest) of these methods was to laser sinter the surfaces after deposition (Figure 52, Page

153). Following testing, it was concluded that this method did result in conductivity enhancement but that the effect was extremely unpredictable and unreliable. This method would also have reduced the surface area of the nanostructures in the sensor, thus reducing the benefits of using the CAP process as a fabrication step. The second method for conductivity enhancement was crosslinking the adjacent nanostructures with conductive dithiol and nanoparticle “daisy chains” (Figure 55, Page 160). Once tested, it was found that this method resulted in a reliable conductivity increase without the disadvantage of reducing sensor surface area (in fact, it would be expected to increase it). As such, it was decided that this methodology was best suited for conductivity enhancement of the sensors.

In the fabrication of contacts for the working electrodes attempts were made to deposit contact using the CAP methodology at the same time as the initial sensor deposition. These tests were met with limited success and the creation of contacts using this method was quickly concluded to be too unreliable for application in final sensor design. Attempts were made to use the square electrodes as sensor without any specific contact point at a distance from the working electrode but this resulted in issues caused by directly clamping to the sensor surface (such as corrosion of the crocodile clip used). As a result, an alternative method for the fabrication of contacts and counter/reference electrode design based on screen printed contacts and the idea of screen printed counter/reference electrodes was eventually devised.

As discussed in Section 4.2.2, this screen printing based method for the fabrication of contacts was tested using conductive carbon ink and found to give a good contact between the sensor and the crocodile clip and (following some proof of concept tests) appeared to be suitable for use as a sensor based on some conductometric thiol exposure tests. Based on these results, a print screen was designed for this purpose (Figure 67,

Page 177). By utilising such a printing method it would still be possible to rapidly and inexpensively mass produce these sensor surfaces without the need for CAP deposition of these features. While this screen was waited for, it was decided that the time should be used to address a characterisation problem encountered earlier in the project.

During the development of the crosslinking based methodology for conductivity enhancement a gold nanoparticle colloid was used as the source of nanoparticles. Because gold nanoparticle colloids are generally expensive and environmentally unfriendly to produce and work with, an methodology called PLAL was used for in-house production of the particles as an inexpensive and green substitute for the usual chemical reduction based methodologies. Although the use of this colloid offered many advantages, it also presented the disadvantage of being extremely difficult to measure the concentration of with the equipment available. As such, a new methodology for particle counting based on the Mie model of light interaction by particles was devised (Section 5). This methodology makes use of UV/Vis spectroscopy and DLS measurement to count the number of particles by predicting their expected extinction coefficient from first principles. The methodology is based upon the earlier work of Bohren and Huffmann<sup>183</sup> and the extensions to their work done by Haiss et al<sup>184</sup>. The work of these researchers had resulted in a FORTRAN77 program capable of predicting the spectroscopic properties of a monodispersed nanoparticle colloid. With further modifications of this model, a program was made with the ability to predict the spectroscopic properties of a polydispersed colloid (such as those encountered in real life) and use those predicted properties with readily available empirical data to find an expected number of particles per mL for the colloid. In addition to extending the methodology of Haiss et al, the new program was also written in a more modern programming language, allowing for it to be more readily used, incorporated or modified by modern day researchers. The reimplementing of the program into the Julia

programming language also allowed it to take advantage of computing techniques that were in their infancy during the time of Haiss et al's original program allowing for increased performance through the use of optimisation methods such as multiprocessing and JIT compilation. The effectiveness of the newly developed program was verified using a silver nanoparticle colloid of known concentration and found to give a good approximation of the colloid concentration. With this new program developed, the focus of the project shifted back to the development of a sensor.

With the newly acquired screen printing screen, a large number of sensor surfaces were mass produced and these samples were subsequently used in the development of a final sensor platform. Using c-Myc exon 2 as a target analyte initial tests (in Section 6.1) appeared to suggest some kind of influence as a result of sensor interaction with the target. Based on these initial tests, it was decided that future tests would proceed using EIS as the conductometric testing method and tests were performed to find optimal EIS parameters. Finally, in Section 6.2 an EIS model was developed for the sensors being tested, and a final dose-response curve experiment was performed. This experiment resulted in the discovery of two different models relating the concentration of the target analyte to the conductometric response of the sensor. Thus, at this point, it was concluded that the use of the surfaces as a sensor had been demonstrated.

Based on the results obtained it can be concluded that the major aims of the project were achieved. As mentioned above, the primary goal of developing a new, novel methodology for the fabrication of biosensors was achieved. For the final sensor design, a number of goals were outlined at the beginning of this section and, at this stage, they have been achieved with the exception of reusability. Of course, the sensors

have not yet been tested for reusability at time of writing so it is yet to be seen how well this goal can be achieved.

With regards to more minor aims for the project that arose as a means towards the primary aim, they also appear to have been achieved. The CAP process was developed into a rapid, repeatable, inexpensive nanostructure deposition process. This process was further built upon with the development of post-processing techniques that allow for the fabrication of conductive nanostructured surfaces suitable for use in the sensor platform being developed or other uses such as printed electronics. Finally, a new methodology for particle enumeration in colloids was also developed, with the aim of characterising an important reagent in the fabrication process being developed.

As a final closing thought, the final results of this project offers many potential future avenues for further research in a variety of directions. Firstly, the further development of the CAP methodology as a deposition method seems promising. Future experiments to expand the range of materials, substrates and controlling parameters in the process as well as the fundamental physical understanding of this process could yield a plethora of end-uses ranging from flexible, printed, nanostructured electronics to voxel deposition or even the fabrication of surfaces with unique photonic activities. The nanoconc program developed also has a lot of room for future improvement, such as its expansion to include coated particles and non-metallic particles, or simply further validation of its accuracy as a methodology. Lastly (and most obviously), it offers a lot of room for potential future improvement of the final sensor platform. The fabrication process offers a wealth of possible parameters to tweak for the optimisation of sensitivity, reliability, reproducibility and cost. It has also been designed with the deliberate goal of being scalable to potential factory scale mass production and future work could yield progress towards this goal. Finally, the sensor still has room for further

development and validation of effectiveness through work such as tests with different analyte/detection molecule pairs, selectivity tests utilising a source of random DNA (such as is often sourced from herring sperm, for example), reusability tests by dehybridising the inoculated sensors before reinoculating and incorporation into a microfluidic platform. With such development, the eventual end-goal of a clinically usable, flexible and inexpensive (and thus massively multiplexable) sensor could be achievable.

## 9. Bibliography

- (1) De Flora, S.; Quaglia, A.; Bennicelli, C.; Vercelli, M. *FASEB J.* **2005**, *19* (8), 892.
- (2) Prentice, T. *Health, History and Hard Choices: Funding Dilemmas in a Fast-Changing World*; World Health Organization, 2006.
- (3) *Global Health Estimates 2014 Summary Tables: Deaths by Cause, Age and Sex, 2000-2012*; Geneva, Switzerland, 2014.
- (4) De Angelis, R.; Sant, M.; Coleman, M. P.; Francisci, S.; Baili, P.; Pierannunzio, D.; Trama, A.; Visser, O.; Brenner, H.; Ardanaz, E.; Bielska-Lasota, M.; Engholm, G.; Nennecke, A.; Siesling, S.; Berrino, F.; Capocaccia, R. *Lancet Oncol.* **2013**, *2045* (13), 1.
- (5) Newman, D. J.; Cragg, G. M. *J. Nat. Prod.* **2012**, *75* (3), 311.
- (6) Smith, R. A.; Manassaram-Baptiste, D.; Brooks, D.; Cokkinides, V.; Doroshenk, M.; Saslow, D.; Wender, R. C.; Brawley, O. W. *CA. Cancer J. Clin.* *64* (1), 30.
- (7) Garg, V.; Gu, N. Y.; Borrego, M. E.; Raisch, D. W. *Expert Rev. Pharmacoecon. Outcomes Res.* **2013**, *13* (3), 327.
- (8) Walker, A. Irish Cancer Society 2009,.
- (9) Kristensen, L. S.; Hansen, L. L. *Clin. Chem.* **2009**, *55* (8), 1471.
- (10) de Gramont, A.; Watson, S.; Ellis, L. M.; Rodón, J.; Tabernero, J.; de Gramont, A.; Hamilton, S. R. *Nat. Rev. Clin. Oncol.* **2014**, *12* (4), 197.
- (11) Watson, M. S. *Oncology*, 2nd ed.; Oxford University Press, 2006.
- (12) Hanahan, D.; Weinberg, R. A. *Cell* **2011**, *144* (5), 646.
- (13) Valdés-Mora, F.; Clark, S. J. *Oncogene* **2014**, No. April 2013, 1.
- (14) IARC. *IARC Monographs on the Evaluation on the Carcinogenic Risk of Cehmicals to Humans - Some Metals and Metallic Compounds*;

- Lyon, 1980.
- (15) Giuliano, A. R.; Kreimer, A. R.; de Sanjose, S. *J. Natl. Cancer Inst.* **2015**, *107* (6), djv128.
  - (16) Lemercier, C. *Cell. Mol. Life Sci.* **2015**, *72* (14), 2665.
  - (17) Winters, N.; Goldberg, M. S.; Hystad, P.; Villeneuve, P. J.; Johnson, K. *C. Sci. Total Environ.* **2015**, *526*, 153.
  - (18) Coghlin, C.; Murray, G. I. *J. Pathol.* **2010**, *222* (1), 1.
  - (19) Mehlen, P.; Puisieux, A. *Nat. Rev. Cancer* **2006**, *6* (6), 449.
  - (20) Cancer Types <http://www.cancer.gov/types> (accessed Jan 1, 2015).
  - (21) Freeman, S. *Biological Science*, 4th Editio.; 2010.
  - (22) Stockfleth, E.; Rosen, T.; Shumack, S. In *Managing Skin Cancer*; 2010; pp 17-35.
  - (23) Hainsworth, J. D.; Greco, F. A. In *Holland-Frei Cancer Medicine*; BC Decker, 2003.
  - (24) Farchoukh, L.; Milon, A.; Parwani, A. Case 858 -- A woman in her 70s with a bladder mass <http://path.upmc.edu/cases/case858.html> (accessed Jan 1, 2015).
  - (25) Burston, J.; Clay, R. D. *J. Clin. Pathol.* **1959**, *12* (1), 73.
  - (26) BENNETT, L. L.; SKIPPER, H. E.; STOCK, C. C.; RHOADS, C. P. *Cancer Res.* **1955**, *15* (7), 485.
  - (27) Liu, R.; Wang, X.; Aihara, K.; Chen, L. *Med. Res. Rev.* **2014**, *34* (3), 455.
  - (28) Choi, Y.-E.; Kwak, J.-W.; Park, J. W. *Sensors* **2010**, *10* (1), 428.
  - (29) Ferrara, N. *Arterioscler. Thromb. Vasc. Biol.* **2009**, *29* (6), 789.
  - (30) Shweiki, D.; Itin, A.; Soffer, D.; Keshet, E. *Nature* **1992**, *359* (6398), 843.
  - (31) Graeber, T. G.; Osmanian, C.; Jacks, T.; Housman, D. E.; Koch, C. J.;

- Lowe, S. W.; Giaccia, A. J. *Nature* **1996**, 379 (6560), 88.
- (32) Hockel, M.; Schlenger, K.; Aral, B.; Mitze, M.; Schaffer, U.; Vaupel, P. *Cancer Res.* **1996**, 56 (19), 4509.
- (33) Harris, A. L. *Nat. Rev. Cancer* **2002**, 2 (1), 38.
- (34) Shibata, A.; Nakagawa, K.; Tsuduki, T.; Miyazawa, T. *J. Nutr. Biochem.* **2015**, 26 (8), 832.
- (35) Polanski, M.; Anderson, N. L. *Biomark. Insights* **2007**, 1 (301), 1.
- (36) Miki, Y.; Swensen, J.; Shattuck-Eidens, D.; Futreal, P. A.; Harshman, K.; Tavtigian, S.; Liu, Q.; Cochran, C.; Bennett, L. M.; Ding, W. *Science* **1994**, 266 (5182), 66.
- (37) U.S. National Cancer Institute. Tumor Markers  
<http://www.cancer.gov/about-cancer/diagnosis-staging/diagnosis/tumor-markers-fact-sheet> (accessed Sep 9, 2015).
- (38) *Label-Free Biosensors*; Cooper, M. A., Ed.; Cambridge University Press, 2009.
- (39) Kuriyama, M.; Wang, M. C.; Papsidero, L. D.; Killian, C. S.; Shimano, T.; Valenzuela, L.; Nishiura, T.; Murphy, G. P.; Chu, T. M. *Cancer Res.* **1980**, 40 (12), 4658.
- (40) Hermann, N. *World J. Methodol.* **2014**, 4 (4), 219.
- (41) Oppermann, H.; Levinson, A. D.; Varmus, H. E.; Levintow, L.; Bishop, J. M. *Proc. Natl. Acad. Sci. U. S. A.* **1979**, 76 (4), 1804.
- (42) Held, L.; Eigentler, T. K.; Meier, F.; Held, M.; Röcken, M.; Garbe, C.; Bauer, J. *J. der Dtsch. Dermatologischen Gesellschaft* **2011**, 9 (7), 510.
- (43) Chan, P. C. R.; Wong, B. Y. L.; Ozcelik, H.; Cole, D. E. C. *Clin. Chem.* **1999**, 45 (8), 1285.
- (44) Nelson, H.; Huffman, L.; Fu, R.; Harris, E.; Walker, M.; Bougatsos, C. Centre for Reviews and Dissemination (UK) 2005,.

- (45) Dann, R. B.; DeLoia, J. A.; Timms, K. M.; Zorn, K. K.; Potter, J.; Flake, D. D.; Lanchbury, J. S.; Krivak, T. C. *Gynecol. Oncol.* **2012**, *125* (3), 677.
- (46) Yoshida, K.; Sanada, M.; Ogawa, S. *Jpn. J. Clin. Oncol.* **2013**, *43* (2), 110.
- (47) Vasiljević, N.; Ahmad, A. S.; Thorat, M. A.; Fisher, G.; Berney, D. M.; Møller, H.; Foster, C. S.; Cuzick, J.; Lorincz, A. T. *BMC Cancer* **2014**, *14*, 655.
- (48) King, W. H. *Anal. Chem.* **1964**, *36* (9), 1735.
- (49) Speight, R. E.; Cooper, M. A. *J. Mol. Recognit.* **2012**, *25* (9), 451.
- (50) Grieshaber, D.; MacKenzie, R.; Vörös, J.; Reimhult, E. *Sensors 2008*, *Vol. 8, Pages 1400-1458* **2008**, *8* (3), 1400.
- (51) Henstridge, M. C.; Laborda, E.; Rees, N. V.; Compton, R. G. *Electrochim. Acta* **2012**, *84*, 12.
- (52) Pejcic, B.; De Marco, R. *Electrochim. Acta* **2006**, *51* (28), 6217.
- (53) Pei, X.; Zhang, B.; Tang, J.; Liu, B.; Lai, W.; Tang, D. *Anal. Chim. Acta* **2013**, *758*, 1.
- (54) Gou, P.; Kraut, N. D.; Feigel, I. M.; Bai, H.; Morgan, G. J.; Chen, Y.; Tang, Y.; Bocan, K.; Stachel, J.; Berger, L.; Mickle, M.; Sejdíć, E.; Star, A. *Sci. Rep.* **2014**, *4*, 4468.
- (55) Xu, M.; Wang, R.; Li, Y. *Talanta* **2016**, *148*, 200.
- (56) Bruck, H. A.; Yang, M.; Kostov, Y.; Rasooly, A. *Methods* **2013**, *63* (3), 282.
- (57) Lee, D.; Cui, T. *Biosens. Bioelectron.* **2010**, *25* (10), 2259.
- (58) Wang, C.; Kim, J.; Zhu, Y.; Yang, J.; Lee, G.-H.; Lee, S.; Yu, J.; Pei, R.; Liu, G.; Nuckolls, C.; Hone, J.; Lin, Q. *Biosens. Bioelectron.* **2015**, *71*, 222.

- (59) Li, J.; Duan, Y.; Hu, H.; Zhao, Y.; Wang, Q. *Sensors Actuators B Chem.* **2015**, *219*, 65.
- (60) Trilling, A. K.; Beekwilder, J.; Zuilhof, H. .
- (61) Lepage, D.; Dubowski, J. J. *Biosensors* **2013**, *3* (2), 201.
- (62) Anker, J. N.; Hall, W. P.; Lyandres, O.; Shah, N. C.; Zhao, J.; Van Duyne, R. P. *Nat. Mater.* **2008**, *7* (6), 442.
- (63) Zeng, S.; Baillargeat, D.; Ho, H.-P.; Yong, K.-T. *Chem. Soc. Rev.* **2014**, *43* (10), 3426.
- (64) Carrascosa, L. G.; Calle, A.; Lechuga, L. M. *Anal. Bioanal. Chem.* **2009**, *393* (4), 1173.
- (65) Li, T.; Jo, E.-J.; Kim, M.-G. *Chem. Commun.* **2012**, *48* (17), 2304.
- (66) Schulz, H.; Baranska, M. *Vib. Spectrosc.* **2007**, *43* (1), 13.
- (67) Dalmay, C.; Leroy, J.; Pothier, A.; Blondy, P. *Procedia Eng.* **2014**, *87*, 54.
- (68) Jung, Y.; Jeong, J. Y.; Chung, B. H. *Analyst* **2008**, *133* (6), 697.
- (69) Kim, E.-S.; Shim, C.-K.; Lee, J. W.; Park, J. W.; Choi, K. Y. *Analyst* **2012**, *137* (10), 2421.
- (70) Janeway, C. A.; Travers, P.; Walport, M.; Shlomchik, M. J. In *Immunobiology: The Immune System in Health and Disease*; Garland Science, 2001.
- (71) Vidarsson, G.; Dekkers, G.; Rispens, T. *Front. Immunol.* **2014**, *5*, 520.
- (72) Nelson, A. L. *mAbs*. January 2010, pp 77–83.
- (73) Montenegro, J.-M.; Grazu, V.; Sukhanova, A.; Agarwal, S.; de la Fuente, J. M.; Nabiev, I.; Greiner, A.; Parak, W. J. *Adv. Drug Deliv. Rev.* **2013**, *65* (5), 677.
- (74) Mateo, C.; Grazu, V.; Palomo, J. M.; Lopez-Gallego, F.; Fernandez-

- Lafuente, R.; Guisan, J. M. *Nat. Protoc.* **2007**, *2* (5), 1022.
- (75) US Food and Drug Administration. 2003, pp 1-22.
- (76) Notomi, T. *Nucleic Acids Res.* **2000**, *28* (12), 63e.
- (77) Ni, X.; Castanares, M.; Mukherjee, A.; Lupold, S. E. *Curr. Med. Chem.* **2011**, *18* (27), 4206.
- (78) Bruno, J. G. *Molecules* **2015**, *20* (4), 6866.
- (79) Sun, H.; Zu, Y. *Small* **2015**, *11* (20), 2352.
- (80) Lakhin, A. V.; Tarantul, V. Z.; Gening, L. V. *Acta Naturae* **2013**, *5* (4), 34.
- (81) Arghir, I.; Spasic, D.; Verlinden, B. E.; Delport, F.; Lammertyn, J. *Sensors Actuators B Chem.* **2015**, *216*, 518.
- (82) Farid, S.; Meshik, X.; Choi, M.; Mukherjee, S.; Lan, Y.; Parikh, D.; Poduri, S.; Baterdene, U.; Huang, C.-E.; Wang, Y. Y.; Burke, P.; Dutta, M.; Stroschio, M. A. *Biosens. Bioelectron.* **2015**, *71*, 294.
- (83) Chen, A.; Yang, S. *Biosens. Bioelectron.* **2015**, *71*, 230.
- (84) Hänniger, T.; Wessels, H.; Fischer, C.; Paschke-Kratzin, A.; Fischer, M. *Anal. Chem.* **2014**, *86* (21), 10940.
- (85) Cox, J. C.; Ellington, A. D. *Bioorg. Med. Chem.* **2001**, *9* (10), 2525.
- (86) Yu, C.-C.; Chen, H.-L. *Microelectron. Eng.* **2015**, *132*, 98.
- (87) Verma, A.; Prakash, A.; Tripathi, R. *Opt. Commun.* **2015**, *357*, 106.
- (88) Zeng, S.; Yong, K.-T.; Roy, I.; Dinh, X.-Q.; Yu, X.; Luan, F. *Plasmonics* **2011**, *6* (3), 491.
- (89) Lei, W.; Si, W.; Xu, Y.; Gu, Z.; Hao, Q. *Microchim. Acta* **2014**, *181* (7-8), 707.
- (90) Ho, J. A.; Lin, Y.-C.; Wang, L.-S.; Hwang, K.-C.; Chou, P.-T. *Anal. Chem.* **2009**, *81* (4), 1340.
- (91) Lahiff, E.; Lynam, C.; Gilmartin, N.; O’Kennedy, R.; Diamond, D.

- Anal. Bioanal. Chem.* **2010**, 398 (4), 1575.
- (92) Lee, D.-W.; Lee, J.; Sohn, I. Y.; Kim, B.-Y.; Son, Y. M.; Bark, H.; Jung, J.; Choi, M.; Kim, T. H.; Lee, C.; Lee, N.-E. *Nano Res.* **2015**, 8 (7), 2340.
- (93) Bangar, M. A.; Chen, W.; Myung, N. V.; Mulchandani, A. *Thin Solid Films* **2010**, 519 (3), 964.
- (94) Tully, E.; Higson, S. P.; O’Kennedy, R. *Biosens. Bioelectron.* **2008**, 23 (6), 906.
- (95) Takamatsu, S.; Lonjaret, T.; Crisp, D.; Badier, J.-M.; Malliaras, G. G.; Ismailova, E. *Sci. Rep.* **2015**, 5, 15003.
- (96) Xie, H.; Luo, S.-C.; Yu, H.-H. *Small* **2009**, 5 (22), 2611.
- (97) du Toit, H.; Di Lorenzo, M. *Electrodeposited highly porous gold microelectrodes for the direct electrocatalytic oxidation of aqueous glucose*; 2014; Vol. 192.
- (98) Vessalli, B. A.; Zito, C. A.; Perfecto, T. M.; Volanti, D. P.; Mazon, T. J. *Alloys Compd.* **2017**, 696, 996.
- (99) Krishnan, J. N.; Kim, I. T.; Ahn, S.-H.; Kim, Z. H.; Cho, S.-H.; Kim, S. K. *BioChip J.* **2013**, 7 (4), 375.
- (100) Kahn, B. E. *Proc. IEEE* **2015**, 103 (4), 497.
- (101) Dumond, J. J.; Yee Low, H. *J. Vac. Sci. Technol. B, Nanotechnol. Microelectron. Mater. Process. Meas. Phenom.* **2012**, 30 (1), 010801.
- (102) Madou, M. J. *Fundamentals of Microfabrication: The Science of Miniaturization*, 2nd ed.; CRC Press, 2002.
- (103) Kumar, R.; Kumar, G.; Umar, A. *J. Nanosci. Nanotechnol.* **2014**, 14 (2), 1911.
- (104) Dhami, G.; Tan, B.; Venketakrishnan, K. *Opt. Lasers Eng.* **2011**, 49 (7), 866.

- (105) Kwok, H. .; Kim, H. .; Kim, D. .; Shen, W. .; Sun, X. .; Xiao, R. . *Appl. Surf. Sci.* **1997**, *109–110*, 595.
- (106) Adrian, F. J.; Bohandy, J.; Kim, B. F.; Jette, A. N.; Thompson, P. J. *Vac. Sci. Technol. B* **1987**, *5* (5), 1490.
- (107) Piqué, A.; Kim, H.; Auyeung, R. C. Y.; Beniam, I.; Breckenfeld, E. *Appl. Surf. Sci.* **2016**, *374*, 42.
- (108) Henley, S. J.; Carey, J. D.; Silva, S. R. P. *Phys. Rev. B - Condens. Matter Mater. Phys.* **2005**, *72* (19), 1.
- (109) Trice, J.; Thomas, D.; Favazza, C.; Sureshkumar, R.; Kalyanaraman, R. *Phys. Rev. B - Condens. Matter Mater. Phys.* **2007**, *75* (23), 1.
- (110) Ruffino, F.; Pugliara, A.; Carria, E.; Romano, L.; Bongiorno, C.; Spinella, C.; Grimaldi, M. G. *Nanotechnology* **2012**, *23* (4).
- (111) Lu, L.-X.; Wang, Y.-M.; Srinivasan, B. M.; Asbahi, M.; Yang, J. K. W.; Zhang, Y.-W. *Sci. Rep.* **2016**, *6* (1), 32398.
- (112) Pandey, P.; Kunwar, S.; Sui, M.; Bastola, S.; Lee, J. *IEEE Trans. Nanotechnol.* **2018**, *17* (2), 325.
- (113) Sperling, R. a; Parak, W. J. *Philos. Trans. A. Math. Phys. Eng. Sci.* **2010**, *368* (1915), 1333.
- (114) Atkins, P.; de Paula, J.; Keeler, J. *Atkins' Physical Chemistry*, 11th ed.; Oxford University Press, 2017.
- (115) Zhao, P.; Li, N.; Astruc, D. *Coord. Chem. Rev.* **2013**, *257* (3), 638.
- (116) Monic Shah, Vivek Badwaik, Yogesh Kherde, Hitesh Kumar Waghwani, Tulsi Modi, Zoraida P Aguilar, Hannah Rodgers, William Hamilton, Tamilselvi Marutharaj, Cathleen Webb, Matthew B. Lawrenz, R. D. **2014**, No. JUNE.
- (117) Frens, G. *Nat. Phys. Sci.* **1973**, *241* (105), 20.
- (118) Polte, J. *CrystEngComm* **2015**, *17* (36), 6809.

- (119) LaMer, V. K. *Ind. Eng. Chem.* **1952**, *44* (6), 1270.
- (120) LaMer, V. K.; Dinegar, R. H. *J. Am. Chem. Soc.* **1950**, *72* (11), 4847.
- (121) Finney, E. E.; Finke, R. G. *J. Colloid Interface Sci.* **2008**, *317* (2), 351.
- (122) Reiss, H. *J. Chem. Phys.* **1951**, *19* (4), 482.
- (123) Wen, T.; Brush, L. N.; Krishnan, K. M. *J. Colloid Interface Sci.* **2014**, *419*, 79.
- (124) Chow, M. K.; Zukoski, C. F. *J. Colloid Interface Sci.* **1994**, *165* (1), 97.
- (125) Ng, J. D.; Lorber, B.; Witz, J.; Théobald-Dietrich, A.; Kern, D.; Giegé, R. *J. Cryst. Growth* **1996**, *168* (1-4), 50.
- (126) Polte, J.; Eler, R.; Thünemann, A. F.; Emmerling, F.; Kraehnert, R. *Chem. Commun.* **2010**, *46* (48), 9209.
- (127) Polte, J.; Ahner, T. T.; Delissen, F.; Sokolov, S.; Emmerling, F.; Thünemann, A. F.; Kraehnert, R. *J. Am. Chem. Soc.* **2010**, *132* (4), 1296.
- (128) Polte, J.; Herder, M.; Eler, R.; Rolf, S.; Fischer, A.; Würth, C.; Thünemann, A. F.; Kraehnert, R.; Emmerling, F. *Nanoscale* **2010**, *2* (11), 2463.
- (129) Simo, A.; Polte, J.; Pfänder, N.; Vainio, U.; Emmerling, F.; Rademann, K. *J. Am. Chem. Soc.* **2012**, *134* (45), 18824.
- (130) Hendel, T.; Wuitschick, M.; Kettemann, F.; Birnbaum, A.; Rademann, K.; Polte, J. *Anal. Chem.* **2014**, *86* (22), 11115.
- (131) Brown, M. A.; Abbas, Z.; Kleibert, A.; Green, R. G.; Goel, A.; May, S.; Squires, T. M. *Phys. Rev. X* **2016**, *6* (1), 1.
- (132) Brust, M.; Walker, M.; Bethell, D.; Schiffrin, D. J.; Whyman, R. *J. Chem. Soc., Chem. Commun.* **1994**, No. 7, 801.
- (133) Perala, S. R. K.; Kumar, S. *Langmuir* **2013**, *29* (31), 9863.

- (134) Tripathi, S. C.; Kumar, M. *J. Radioanal. Nucl. Chem.* **2003**, *256* (3), 565.
- (135) Watanabe, M.; Takamura, H.; Sugai, H. *Nanoscale Res. Lett.* **2009**, *4* (6), 565.
- (136) Patel, K.; Kapoor, S.; Dave, D. P.; Mukherjee, T. *J. Chem. Sci.* **2005**, *117* (1), 53.
- (137) Guangnian, X.; Xueliang, Q.; Xiaolin, Q.; Jianguo, C. *RARE Met. Mater. Eng.* **2012**, *41* (3), 531.
- (138) Yakabuskie, P. A.; Joseph, J. M.; Keech, P.; Botton, G. A.; Guzonas, D.; Wren, J. C. *Phys. Chem. Chem. Phys.* **2011**, *13* (15), 7198.
- (139) Intartaglia, R.; Barchanski, A.; Bagga, K.; Genovese, A.; Das, G.; Wagener, P.; Di Fabrizio, E.; Diaspro, A.; Brandi, F.; Barcikowski, S. *Nanoscale* **2012**, *4* (4), 1271.
- (140) Bagga, K.; McCann, R.; Wang, M.; Stalcup, a.; Vázquez, M.; Brabazon, D. *J. Colloid Interface Sci.* **2015**, *447*, 263.
- (141) Streubel, R.; Bendt, G.; Gökce, B. *Nanotechnology* **2016**, *27* (20).
- (142) De Bonis, A.; Sansone, M.; D'Alessio, L.; Galasso, A.; Santagata, A.; Teghil, R. *J. Phys. D. Appl. Phys.* **2013**, *46* (44), 445301.
- (143) Lee, S.; Ahn, A.; Choi, M. Y. *Bull. Korean Chem. Soc.* **2015**, *36* (3), 832.
- (144) Reich, S.; Schönfeld, P.; Wagener, P.; Letzel, A.; Ibrahimkutty, S.; Gökce, B.; Barcikowski, S.; Menzel, A.; dos Santos Rolo, T.; Plech, A. *J. Colloid Interface Sci.* **2017**, *489*, 106.
- (145) Solati, E.; Dorrnian, D. *J. Clust. Sci.* **2015**, *26* (3), 727.
- (146) Kumar, B.; Thareja, R. K. *J. Appl. Phys.* **2010**, *108* (6).
- (147) Amans, D.; Malaterre, C.; Diouf, M.; Mancini, C.; Chaput, F.; Ledoux, G.; Breton, G.; Guillin, Y.; Dujardin, C.; Masenelli-Varlot, K.; Perriat, P. *J. Phys. Chem. C* **2011**, *115* (12), 5131.

- (148) Al-Mamun, S. A.; Nakajima, R.; Ishigaki, T. *J. Colloid Interface Sci.* **2013**, *392* (1), 172.
- (149) Streubel, R.; Barcikowski, S.; Gökce, B. *Opt. Lett.* **2016**, *41* (7), 1486.
- (150) *Microfluidics and Microfabrication*; Chakraborty, S., Ed.; Springer, 2010.
- (151) Neill, P. F. O.; Azouz, a Ben; Liu, J.; Marczak, S.; Slouka, Z.; Chang, H. C.; Diamond, D. *Biomicrofluidics* **2014**, *052112*.
- (152) CHEN, X.; CUI, D.; LIU, C.; LI, H. *Sensors Actuators B Chem.* **2008**, *130* (1), 216.
- (153) Chen, J.; Chen, D.; Yuan, T.; Chen, X.; Xie, Y.; Fu, H.; Cui, D.; Fan, X.; Khaing Oo, M. K. *Microelectron. Eng.* **2014**, *128*, 36.
- (154) Rhee, M.; Burns, M. a. *Lab Chip* **2008**, *8* (8), 1365.
- (155) Langelier, S. M.; Livak-Dahl, E.; Manzo, A. J.; Johnson, B. N.; Walter, N. G.; Burns, M. a. *Lab Chip* **2011**, *11* (9), 1679.
- (156) Temiz, Y.; Lovchik, R. D.; Kaigala, G. V.; Delamarche, E. *Microelectron. Eng.* **2014**, *132*, 156.
- (157) Guckenberger, D. J.; de Groot, T. E.; Wan, A. M. D.; Beebe, D. J.; Young, E. W. K. *Lab Chip* **2015**, *15* (11), 2364.
- (158) Farris, F. A. *Mathematics Magazine*. 1996, pp 185–189.
- (159) Stat-Ease. 2014,.
- (160) CERION Laser GmbH. Glass Frosting  
<http://glassprocessing.eu/applications-glass-frosting.htm> (accessed Jan 1, 2017).
- (161) Mattox, D. M. *Handbook of physical vapor deposition (PVD) processing*; William Andrew, 2010.
- (162) Sinclair, I. R. *Sensors and transducers*; Newnes, 2001.

- (163) Donnelly, T.; Lunney, J. G. *Appl. Surf. Sci.* **2013**, *282*, 133.
- (164) Schindelin, J.; Arganda-Carreras, I.; Frise, E.; Kaynig, V.; Longair, M.; Pietzsch, T.; Preibisch, S.; Rueden, C.; Saalfeld, S.; Schmid, B.; Tinevez, J.-Y.; White, D. J.; Hartenstein, V.; Eliceiri, K.; Tomancak, P.; Cardona, A. *Nat. Methods* **2012**, *9* (7), 676.
- (165) Yamaguchi, M.; Araga, S.; Mita, M.; Yamasaki, K.; Maekawa, K. *IEEE Trans. Components, Packag. Manuf. Technol.* **2015**, *5* (8), 1160.
- (166) Stathaki, T. *Image Fusion: Algorithms and Applications*, 1st ed.; Elsevier, 2008.
- (167) Gonzalez, R. C.; Woods, R. E. *Digital Image Processing*, 3rd ed.; Pearson, 2007.
- (168) Voigtman, E. *Anal. Chem.* **1997**, *69* (2), 226.
- (169) Patty, A.; Peijiang, Z. *Advances in Materials Sciences, Energy Technology and Environmental Engineering : Proceedings of the International Conference on Materials Science, Energy Technology and Environmental Engineering, MSETEE 2016, Zhuhai, China, May 28-29, 2016.*; CRC Press, 2016.
- (170) Huang, X.; El-Sayed, M. A. *J. Adv. Res.* **2010**, *1* (1), 13.
- (171) Gaspar, D.; Pimentel, A. C.; Mateus, T.; Leitão, J. P.; Soares, J.; Falcão, B. P.; Araújo, A.; Vicente, A.; Filonovich, S. A.; Águas, H.; Martins, R.; Ferreira, I. *Sci. Rep.* **2013**, *3* (1), 1469.
- (172) Akhtar, M.; Jabbar, A.; Ahmed, N.; Mehmood, S.; Umar, Z. A.; Ahmed, R.; Baig, M. A. *Laser Part. Beams* **2019**, *37* (01), 67.
- (173) Hrdlička, V.; Navrátil, T.; Barek, J.; Ludvík, J. *J. Electroanal. Chem.* **2018**, *821* (February), 60.
- (174) Hall Effect Measurements | NIST  
<https://www.nist.gov/pml/engineering-physics-division/popular-links/hall-effect> (accessed May 23, 2017).

- (175) Li, Y.; Galli, G.; Gygi, F. *ACS Nano* **2008**, 2 (9), 1896.
- (176) Milles, S.; Voisiat, B.; Nitschke, M.; Lasagni, A. F. *J. Mater. Process. Technol.* **2019**, 270 (July 2018), 142.
- (177) Diba, F. S.; Kim, S.; Lee, H. J. *Biosens. Bioelectron.* **2015**, 72, 355.
- (178) Tang, J.; Su, B.; Tang, D.; Chen, G. *Biosens. Bioelectron.* **2010**, 25 (12), 2657.
- (179) Kahyarian, A.; Achour, M.; Nestic, S. In *Trends in Oil and Gas Corrosion Research and Technologies*; Elsevier, 2017; pp 149–190.
- (180) Adams, R. N. *Electrochemistry at solid electrodes*, 1st ed.; 1969.
- (181) Hibbert, D. B. *Introduction to electrochemistry*; Macmillan Education UK: London, 1951.
- (182) Bustos, A. R. M.; Encinar, J. R.; Sanz-Medel, A. *Anal. Bioanal. Chem.* **2013**, 405 (17), 5637.
- (183) Bohren, C. F.; Huffman, D. R. *Absorption and Scattering of Light by Small Particles*; Wiley, 1998; Vol. 35.
- (184) Haiss, W.; Thanh, N. T. K.; Aveyard, J.; Fernig, D. G. *Anal. Chem.* **2007**, 79 (11), 4215.
- (185) Maye, M. M.; Han, L.; Kariuki, N. N.; Ly, N. K.; Chan, W. Ben; Luo, J.; Zhong, C. J. *Anal. Chim. Acta* **2003**, 496 (1–2), 17.
- (186) Mie, G. *Ann. Phys.* **1908**, 330 (3), 377.
- (187) Du, H. *Appl. Opt.* **2004**, 43 (9), 1951.
- (188) Fu Qiang; Sun, W. *Appl. Opt.* **2002**, 41 (18), 3545.
- (189) Kreibig, U.; Fragstein, C. v. *Zeitschrift für Phys.* **1969**, 224 (4), 307.
- (190) Ashcroft, N. W.; Mermin, N. D. *Solid State Physics*, 1st ed.; Holt, Rinehart, Winston, Eds.; Harcourt College Publishers: New York, 1976.
- (191) Greenwood, N. N.; Earnshaw, A. *Chemistry of the Elements*; Elsevier,

- 1997.
- (192) Norrby, L. J. *J. Chem. Educ.* **1991**, *68* (2), 110.
- (193) Weller, M.; Overton, T.; Rourke, J.; Armstrong, F. *Inorganic Chemistry*, 7th ed.; Oxford University Press, 2018.
- (194) Backus, J. *IEEE Ann. Hist. Comput.* **1998**, *20* (4), 68.
- (195) Bezanson, J.; Karpinski, S.; Shah, V. B.; Edelman, A. Why We Created Julia <https://julialang.org/blog/2012/02/why-we-created-julia> (accessed Jul 11, 2019).
- (196) Holy, T. 2019,.
- (197) Julia v1.4 Release Notes  
<https://github.com/JuliaLang/julia/blob/master/NEWS.md> (accessed Sep 26, 2019).
- (198) Julia v1.3 Release Notes  
<https://github.com/JuliaLang/julia/blob/v1.3.0-rc1/NEWS.md> (accessed Sep 26, 2019).
- (199) Filipe, V.; Hawe, A.; Jiskoot, W. **2010**, *27* (5), 796.
- (200) Elvan, P.; Tokgun, O.; Kurt, S.; Gaye, A.; Akca, H. *Gene* **2019**, *714* (December 2018), 143955.
- (201) NCBI. MYC MYC proto-oncogene, bHLH transcription factor [ Homo sapiens (human) ] <https://www.ncbi.nlm.nih.gov/gene/4609> (accessed Oct 2, 2019).
- (202) Mrdenovic, S.; Zhang, Y.; Wang, R.; Yin, L.; Chu, G. C. **2019**.
- (203) Rossiter, B. W.; Hamilton, J. F. *Physical Methods of Electrochemistry, Vol 2: Electrochemical Methods*, 2nd ed.; 1986.
- (204) Li, H.; Wang, J.; Chu, Q.; Wang, Z.; Zhang, F.; Wang, S. **2009**, *190*, 578.
- (205) ChemSpider - 4-aminopyridine  
<http://www.chemspider.com/Chemical->

Structure.1664.html?rid=63ddede8-173e-4d30-8b6f-c51b1a581600.

(206) Suni, I. I. *Trends Anal. Chem.* **2008**, 27 (7), 604.

(207) Xu, Y.; Li, C.; Mei, W.; Guo, M.; Yang, Y. *Med. Biol. Eng. Comput.* **2019**, 57 (7), 1515.

## 9. Appendices

Appendix 1. Complete ANOVA table for the particle area model .....	275
Appendix 2. Complete ANOVA table for the particle area standard deviation model.....	276
Appendix 3. Complete ANOVA table for the plasmonic peak position model.....	277
Appendix 4. Complete ANOVA table for the plasmonic peak integral model.....	278
Appendix 5. The complete ANOVA table for the line width model .....	279
Appendix 6. A flow diagram of the function particlecount in the nanoconc module.....	280
Appendix 7. A flow diagram of the function qbare in the miemfp module. ....	281
Appendix 8. A flow diagram of the function mfp in the miemfp module. ....	282
Appendix 9. A flowchart of the function bhmie in the miemfp module.	283
Appendix 10. The source code of the miemfp.jl module .....	284
Appendix 11. The source code of the nanoconc.jl module .....	294
Appendix 12. The source code of the quantumcalc.jl module .....	304
Appendix 13. Conductometric data for the unfunctionalised gold nanostructured surface tested in Section 16.1 (following step 2) .....	308
Appendix 14. Conductometric data for the sensor surface following its first dithiol exposure in Section 16.1 (following step 3) .....	309
Appendix 15. Conductometric data for the sensor surface following its first colloid exposure in Section 16.1 (following step 4).....	310

Appendix 16. Conductometric data for the sensor surface following its second dithiol exposure in Section 16.1 (following step 5) .....	311
Appendix 17. Conductometric data for the sensor surface following its second colloid exposure in Section 16.1 (following step 6).....	312
Appendix 18. Conductometric data for the sensor surface following its exposure to the thio-DNA probe in Section 16.1 (following step 7) .....	313
Appendix 19. Conductometric data for the sensor surface following its exposure to 6-mercaptohexanol as a passivating agent in Section 16.1 (following step 8) .....	314
Appendix 20. Conductometric data for the sensor surface following its exposure to 10 micromolar c-Myc exon 2 (the target analyte) in Section 16.1 .....	315
Appendix 21. Conductometric data for a sensor surface before inoculation with 1 micromolar c-Myc exon 2 .....	316
Appendix 22. Conductometric data for a sensor surface after inoculation with 1 micromolar c-Myc exon 2 .....	317
Appendix 23. Conductometric data for a sensor surface before inoculation with 0.8 micromolar c-Myc exon 2 .....	318
Appendix 24. Conductometric data for a sensor surface after inoculation with 0.8 micromolar c-Myc exon 2 .....	319
Appendix 25. Conductometric data for a sensor surface before inoculation with 0.6 micromolar c-Myc exon 2 .....	320
Appendix 26. Conductometric data for a sensor surface after inoculation with 0.6 micromolar c-Myc exon 2 .....	321
Appendix 27. Conductometric data for a sensor surface before inoculation with 0.4 micromolar c-Myc exon 2 .....	322
Appendix 28. Conductometric data for a sensor surface after inoculation with 0.4 micromolar c-Myc exon 2 .....	323

Appendix 29. Conductometric data for a sensor surface before inoculation with 0.2 micromolar c-Myc exon 2.....	324
Appendix 30. Conductometric data for a sensor surface after inoculation with 0.2 micromolar c-Myc exon 2 .....	325
Appendix 31. EIS plots for the batch 1 10 $\mu$ M sensor before inoculation .....	326
Appendix 32. EIS plots for the batch 1 10 $\mu$ M sensor after inoculation..	327
Appendix 33. EIS plots for the batch 1 8 $\mu$ M sensor before inoculation.	328
Appendix 34. EIS plots for the batch 1 8 $\mu$ M sensor after inoculation....	329
Appendix 35. EIS plots for the batch 1 6 $\mu$ M sensor before inoculation.	330
Appendix 36. EIS plots for the batch 1 6 $\mu$ M sensor after inoculation....	331
Appendix 37. EIS plots for the batch 1 4 $\mu$ M sensor before inoculation.	332
Appendix 38. EIS plots for the batch 1 4 $\mu$ M sensor after inoculation....	333
Appendix 39. EIS plots for the batch 1 3 $\mu$ M sensor before inoculation.	334
Appendix 40. EIS plots for the batch 1 3 $\mu$ M sensor after inoculation....	335
Appendix 41. EIS plots for the batch 2 10 $\mu$ M sensor before inoculation .....	336
Appendix 42. EIS plots for the batch 2 10 $\mu$ M sensor after inoculation..	337
Appendix 43. EIS plots for the batch 2 8 $\mu$ M sensor before inoculation.	338
Appendix 44. EIS plots for the batch 2 8 $\mu$ M sensor after inoculation....	339
Appendix 45. EIS plots for the batch 2 6 $\mu$ M sensor before inoculation.	340
Appendix 46. EIS plots for the batch 2 6 $\mu$ M sensor after inoculation....	341
Appendix 47. EIS plots for the batch 2 4 $\mu$ M sensor before inoculation.	342
Appendix 48. EIS plots for the batch 2 4 $\mu$ M sensor after inoculation....	343
Appendix 49. EIS plots for the batch 2 3 $\mu$ M sensor before inoculation.	344
Appendix 50. EIS plots for the batch 2 3 $\mu$ M sensor after inoculation....	345

Appendix 51. A table showing the compiled EIS data for the dose-response curve experiment.....	346
Appendix 52. A table showing the correlation values for linear, quadratic and cubic fits of each dataset against the concentration of the target analyte .....	353
Appendix 53. The ANOVA table for the initially derived R-Total (diff) model .....	358
Appendix 54. The ANOVA table for the initially derived Real Impedance (%diff) model .....	359
Appendix 55. The ANOVA table for the derived R-Total (diff) model with the outlier removed .....	360
Appendix 56. The ANOVA table for the derived Real Impedance (%diff) model with the outlier removed .....	361

Appendix 1. Complete ANOVA table for the particle area model

Particle Area						
Source	Sum of Squares	df	Mean Square	F Value	p-value Prob > F	
Model	2.630E-006	7	3.757E-007	4.50	0.0047	Significant
A-Scan Speed	2.089E-007	1	2.089E-007	2.50	0.1309	
B-Fluence	2.181E-007	1	2.181E-007	2.61	0.1233	
C-Scan Spacing	3.257E-008	1	3.257E-008	0.39	0.5399	
AB	2.090E-007	1	2.090E-007	2.51	0.1309	
AC	7.671E-007	1	7.671E-007	9.20	0.0072	
BC	3.267E-008	1	3.267E-008	0.39	0.5393	
ABC	7.671E-007	1	7.671E-007	9.20	0.0072	
Residual	1.502E-006	18	8.342E-008			
Cor Total	4.131E-006	25				
R <sup>2</sup>	0.6365			Predicted R <sup>2</sup>	0.2850	
Adjusted R <sup>2</sup>	0.4952			Adequate Precision	8.682	

Appendix 2. Complete ANOVA table for the particle area standard deviation model

Area Standard Deviation						
Source	Sum of Squares	df	Mean Square	F Value	p-value Prob > F	
Model	1.958E-004	7	2.797E-005	4.55	0.0045	Significant
A-Scan Speed	1.654E-005	1	1.654E-005	2.69	0.1183	
B-Fluence	2.173E-005	1	2.173E-005	3.53	0.0764	
C-Scan Spacing	3.176E-006	1	3.176E-006	0.52	0.4814	
AB	1.654E-005	1	1.654E-005	2.69	0.1183	
AC	3.312E-005	1	3.312E-005	5.39	0.0322	
BC	3.167E-006	1	3.167E-006	0.52	0.4821	
ABC	3.312E-005	1	3.312E-005	5.39	0.0322	
Residual	1.106E-004	18	6.146E-006			
Cor Total	3.064E-004	25				
R <sup>2</sup>	0.6389		Predicted R <sup>2</sup>		0.3312	
Adjusted R <sup>2</sup>	0.4985		Adequate Precision		8.021	

Appendix 3. Complete ANOVA table for the plasmonic peak position model

Plasmonic Peak Position						
Source	Sum of Squares	df	Mean Square	F Value	p-value Prob > F	
Model	1019.52	5	203.90	8.26	0.0002	Significant
A-Scan Speed	8.88	1	8.88	0.36	0.5554	
B-Fluence	784.14	1	784.14	31.77	<0.0001	
C-Scan Spacing	72.70	1	72.70	2.95	0.1016	
AC	89.72	1	89.72	3.63	0.0710	
BC	72.73	1	72.73	2.95	0.1015	
Residual	493.66	20	24.68			
Cor Total	1513.18	25				
R <sup>2</sup>	0.6738			Predicted R <sup>2</sup>	0.4085	
Adjusted R <sup>2</sup>	0.5922			Adequate Precision	9.528	

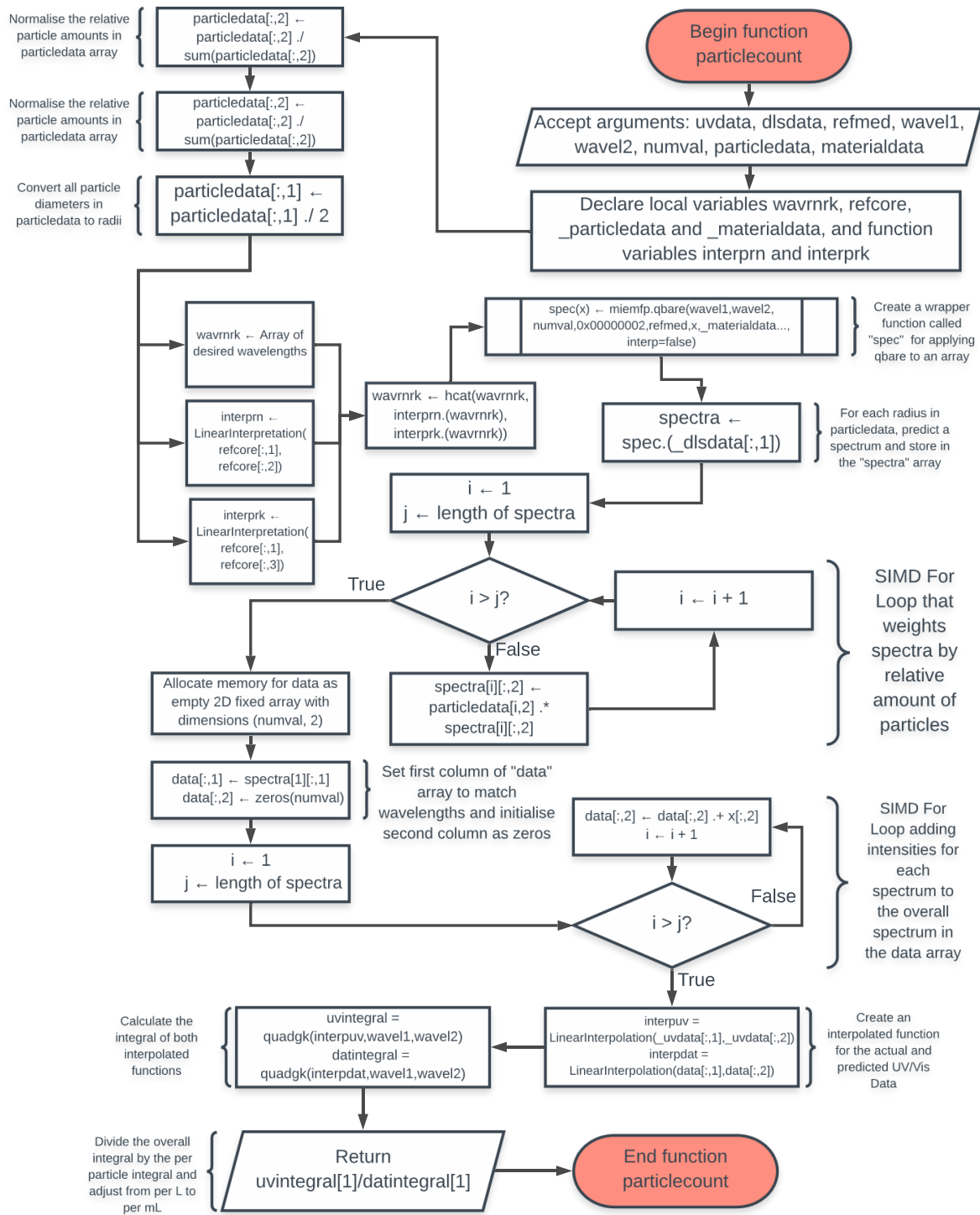
Appendix 4. Complete ANOVA table for the plasmonic peak integral model

Plasmonic Peak Integral						
Source	Sum of Squares	df	Mean Square	F Value	p-value Prob > F	
Model	15.22	2	7.61	19.67	<0.0001	Significant
B-Fluence	12.01	1	12.01	31.05	<0.0001	
C-Scan Spacing	3.21	1	3.21	8.29	0.0085	
Residual	8.90	23	0.39			
Cor Total	24.12	25				
R <sup>2</sup>	0.6310			Predicted R <sup>2</sup>	0.5380	
Adjusted R <sup>2</sup>	0.5990			Adequate Precision	12.440	

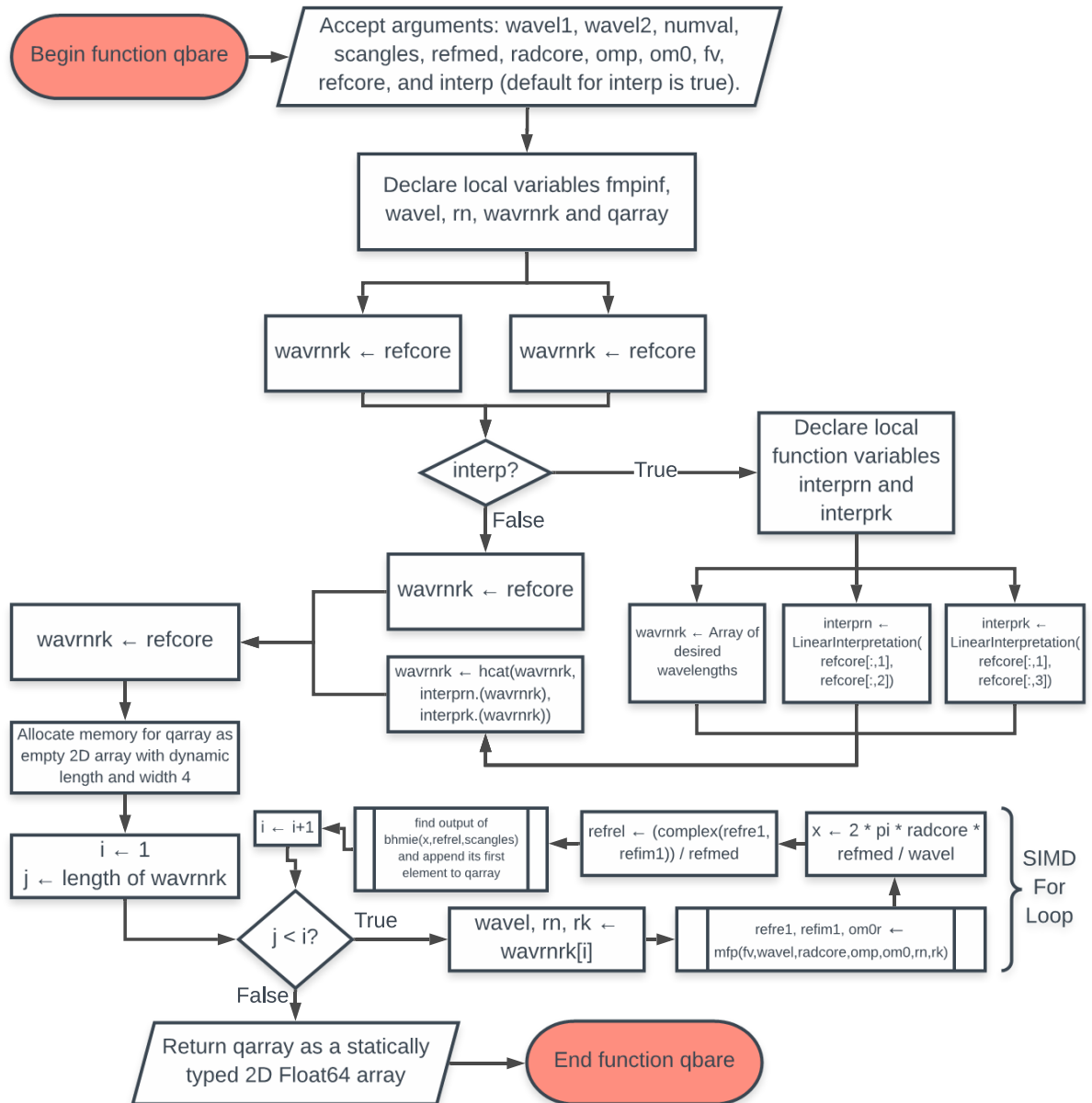
Appendix 5. The complete ANOVA table for the line width model

Line Width						
Source	Sum of Squares	df	Mean Square	F Value	p-value Prob > F	
Model	11.53	2	5.77	7.55	0.0054	significant
C-Laser Power	4.83	1	4.83	6.32	0.0239	
C <sup>2</sup>	4.83	1	4.83	6.32	0.0238	
Residual	11.46	15	0.76			
Cor Total	22.99	17				
R <sup>2</sup>	0.5016			Predicted R <sup>2</sup>	0.2823	
Adjusted R <sup>2</sup>	0.4351			Adequate Precision	5.434	

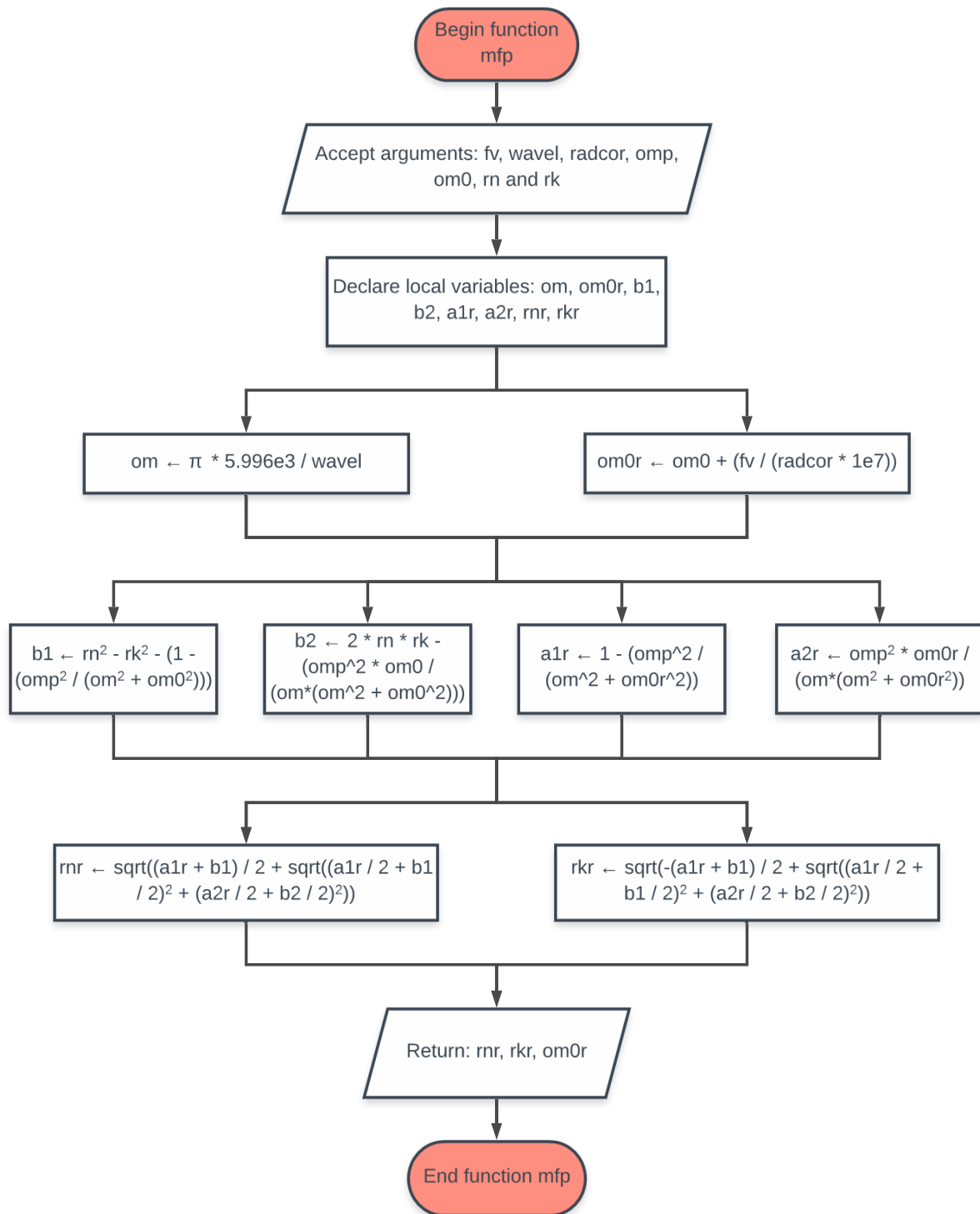
Appendix 6. A flow diagram of the function particlecount in the nanoconc module.



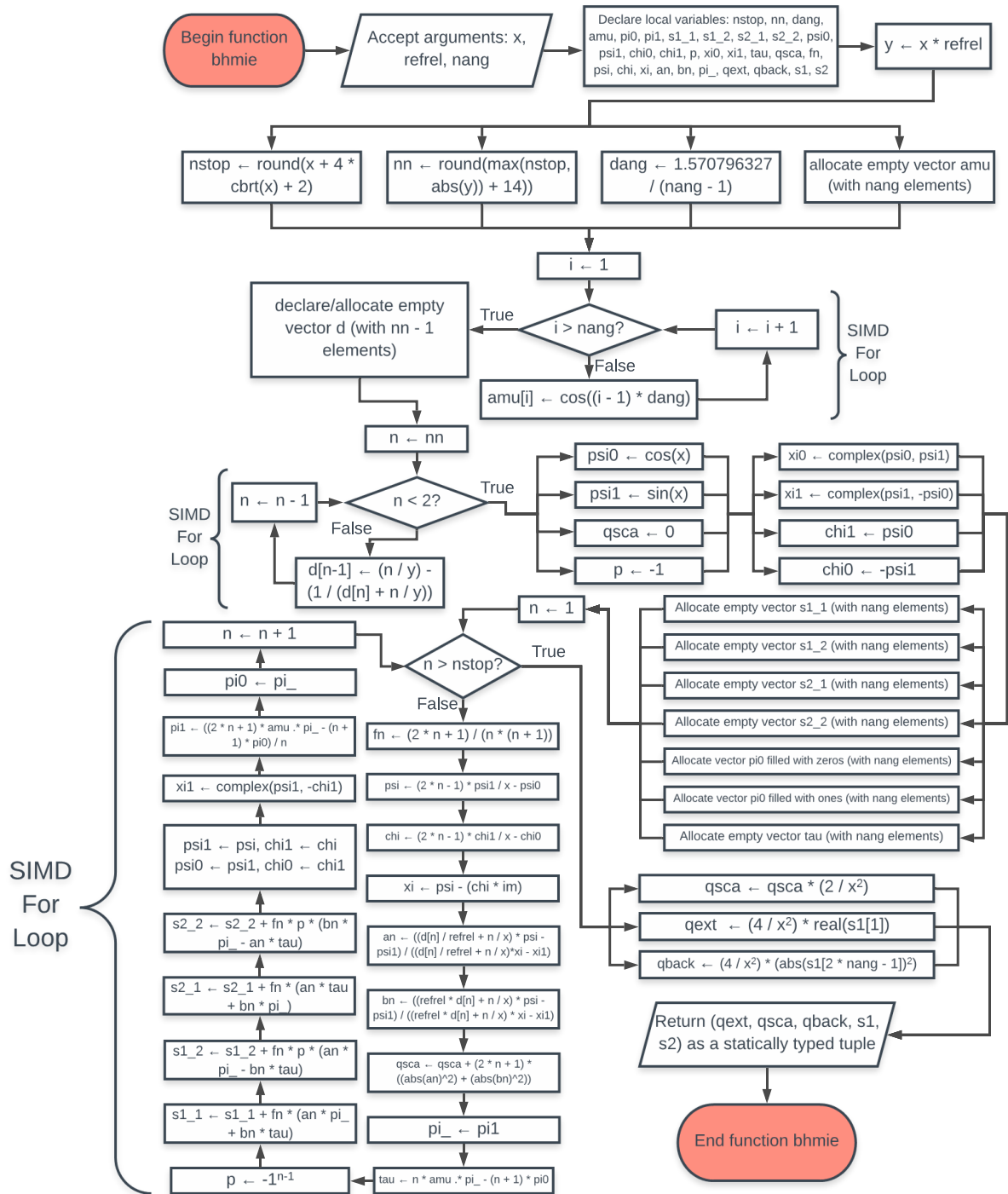
Appendix 7. A flow diagram of the function qbare in the miemfp module.



Appendix 8. A flow diagram of the function mfp in the miemfp module.



Appendix 9. A flowchart of the function `bhmie` in the `miemfp` module.



## Appendix 10. The source code of the miemfp.jl module

```
__precompile__()  
@doc """  
A module for calculating the expected extinction coefficients and  
backscattering  
parameters for coated/uncoated particles of a given size/material  
""" ->  
@fastmath module miemfp  
  
using Interpolations  
  
# an abstracted statype to allow interpolation object to be  
# declared without making extremely messy code  
const InterpFunc =  
Interpolations.Extrapolation{Float64,1,Interpolations.GriddedInterpolati  
on{Float64,1,Float64,Gridded{Linear},Tuple{Array{Float64,1}}},Gridded{Li  
near},Throw{Nothing}}  
  
@doc """  
Corrects refractive index and attenuation coefficient values to account  
for  
the mean free-path effect on the free conductance electrons in the  
particles  
""" ->  
function mfp(fv::Float64,wavel::Float64,radcor::Float64,omp::Float64,  
            om0::Float64,rn::Float64,rk::Float64)  
::Tuple{Float64,Float64,Float64}  
    local om::Float64, om0r::Float64, b1::Float64, b2::Float64  
    local a1r::Float64, a2r::Float64, rnr::Float64, rkr::Float64  
  
    @sync begin  
        om = pi * 5.996e3 / wavel  
        om0r = om0 + (fv / (radcor * 1e7))  
    end  
    @sync begin  
        b1 = rn^2 - rk^2 - (1 - (omp^2 / (om^2 + om0^2)))
```

```

    b2 = 2 * rn * rk - (omp^2 * om0 / (om*(om^2 + om0^2)))
    a1r = 1 - (omp^2 / (om^2 + om0r^2))
    a2r = omp^2 * om0r / (om*(om^2 + om0r^2))
end
@sync begin
    rnr = sqrt((a1r + b1) / 2 + sqrt((a1r / 2 + b1 / 2)^2 + (a2r / 2
+ b2 / 2)^2))
    rkr = sqrt(-(a1r + b1) / 2 + sqrt((a1r / 2 + b1 / 2)^2 + (a2r /
2 + b2 / 2)^2))
end
return (rnr, rkr, om0r)
end

@doc """
Solves for Qext accounting for the effect of particle coatings on
extinction
and scattering coefficients of particles
""" ->
function bhcoat(x::Float64,y::Float64,rfrel1::Complex,rfrel2::Complex
) ::Tuple{Float64,Float64,Float64}
    del::Float64 = 1e-8
    x1::Complex = rfrel1 * x
    x2::Complex = rfrel2 * x
    y2::Complex = rfrel2 * y
    nstop::UInt64 = UInt64(round(y + 4 * cbrt(y) + 1))
    refrel::Complex = rfrel2 / rfrel1

    d0x1::Complex = cos(x1) / sin(x1)
    d0x2::Complex = cos(x2) / sin(x2)
    d0y2::Complex = cos(y2) / sin(y2)
    psi0y::Float64, psi1y::Float64 = cos(y), sin(y)
    chi0y::Float64, chi1y::Float64 = -sin(y), cos(y)
    xi0y::Complex = complex(psi0y, -chi0y)
    xi1y::Complex = complex(psi1y, -chi1y)
    chi0y2::Complex, chi1y2::Complex = -sin(y2), cos(y2)
    chi0x2::Complex, chi1x2::Complex = -sin(x2), cos(x2)

```

```

qsca::

```

```

end
dnbar::Complex = (d1y2 - brack * chipy2) / (1. - brack * chiy2)
gnbar::Complex = (d1y2 - crack * chipy2) / (1. - crack * chiy2)
an::Complex = ((dnbar / rfrel2 + n / y) * psiy - psi1y) /
((dnbar / rfrel2 + n / y) * xiy - xi1y)
bn::Complex = ((rfrel2 * gnbar + n / y) * psiy - psi1y) /
((rfrel2 * gnbar + n / y) * xiy - xi1y)
qsca += (2 * n + 1) * (abs(an) * abs(an) + abs(bn) * abs(bn))
xback += (2 * n + 1) * (-1.)^n * (an - bn)
qext += (2 * n + 1) * (real(an) + real(bn))
psi0y, psi1y = psi1y, psiy
chi0y, chi1y = chi1y, chiy
xi1y = psi1y - chi1y * im
chi0x2, chi1x2 = chi1x2, chix2
chi0y2, chi1y2 = chi1y2, chiy2
d0x1, d0x2, d0y2 = d1x1, d1x2, d1y2
end
qsca = 2. / (y^2) * qsca
qext = 2. / (y^2) * qext
qback = real((1 / (y^2)) * (xback * conj(xback)))
return (qext, qsca, qback)
end

```

```
@doc """
```

```
Finds scattering parameters for uncoated particles.
```

```
""" ->
```

```
function bhmie(x::Float64, rfrel::Complex, nang::UInt32
)
::Tuple{Float64, Float64, Float64, Array{Complex, 1}, Array{Complex, 1}}
# nang must be greater than 1 and less than 4294967295
local nstop::UInt32, nn::UInt32, dang::Float64, amu::Vector{Float64}
local pi0::Vector{Float64}, pi1::Vector{Float64},
s1_1::Vector{Complex}
local s1_2::Vector{Complex}, s2_1::Vector{Complex},
s2_2::Vector{Complex}
local psi0::Float64, psi1::Float64, chi0::Float64, chi1::Float64,
p::Int8

```

```

    local xi0::Complex, xi1::Complex, tau::Vector{Float64},
qasca::Float64
    local fn::Float64, psi::Float64, chi::Float64, xi::Complex,
an::Complex
    local bn::Complex, pi_::Vector{Float64}, qext::Float64,
qback::Float64
    local s1::Vector{Complex}, s2::Vector{Complex}

y::Complex = x * refrel

@sync begin
    nstop = UInt32(round(x + 4. * cbrt(x) + 2.))
    nn = UInt32(round(max(nstop,abs(y)) + 14))
    dang = 1.570796327 / (nang - 1.)
    amu = Vector{Float64}(undef, nang)
end
@inbounds @simd for i in 1:nang
    amu[i]::Float64 = cos((i - 1.) * dang)
end
d::Vector{Complex} = fill(complex(0., 0.), nn + 1)
@inbounds @simd for n in nn:-1:2
    d[n-1]::Complex = (n / y) - (1. / (d[n] + n / y))
end

@sync begin
    psi0 = cos(x)
    psi1 = sin(x)
    qasca = 0.
    p = -1
end
@sync begin
    xi0 = complex(psi0, psi1)
    xi1 = complex(psi1, -psi0)
    chi1 = psi0
    chi0 = -psi1
end
@sync begin

```

```

s1_1 = fill(complex(0., 0.), nang)
s1_2 = fill(complex(0., 0.), nang)
s2_1 = fill(complex(0., 0.), nang)
s2_2 = fill(complex(0., 0.), nang)
pi0 = zeros(nang)
pi1 = ones(nang)
tau = Vector{Float64}(undef, nang)
end
@inbounds @simd for n in 1:nstop
    fn = (2 * n + 1) / (n * (n + 1))
    psi = (2 * n - 1) * psi1 / x - psi0
    chi = (2 * n - 1) * chi1 / x - chi0
    xi = psi - (chi * im)
    an = ((d[n] / refrel + n / x) * psi - psi1) / ((d[n] / refrel +
n / x)*xi - xi1)
    bn = ((refrel * d[n] + n / x) * psi - psi1) / ((refrel * d[n] +
n / x) * xi - xi1)
    qsca += (2 * n + 1) * ((abs(an)^2) + (abs(bn)^2))
    pi_ = pi1
    tau = n * amu .* pi_ - (n + 1) * pi0

    p = (-1)^(n-1)
    s1_1 += fn * (an * pi_ + bn * tau)
    s1_2 += fn * p * (an * pi_ - bn * tau)
    s2_1 += fn * (an * tau + bn * pi_)
    s2_2 += fn * p * (bn * pi_ - an * tau)

    psi0, chi0 = psi1, chi1
    psi1, chi1 = psi, chi
    xi1 = complex(psi1, -chi1)
    pi1 = ((2 * n + 1) * amu .* pi_ - (n + 1) * pi0) / n
    pi0 = pi_
end
@sync begin
    @inbounds s1 = vcat(s1_1, reverse(s1_2[1:length(s1_2)-1]))
    @inbounds s2 = vcat(s2_1, reverse(s2_2[1:length(s2_2)-1]))
end
end

```

```

@sync begin
    qsca *= (2. / (x^2))
    qext = (4. / (x^2)) * real(s1[1])
    qback = (4. / (x^2)) * (abs(s1[2 * nang - 1])^2)
end
return (qext,qsca,qback,s1,s2)
end

@doc """
Calculates the expected extinction coefficient spectrum for particles of
a given
size for uncoated particles (when directly passed attenuation spectrum
data)
""" ->
function
qbare(wavel1::Float64,wavel2::Float64,numval::UInt32,scangles::UInt32,

refmed::Float64,radcore::Float64,omp::Float64,om0::Float64,

fv::Float64,refcore::Array{Float64,2};interp::Bool=true
        ) ::Array{Float64,2}
    local fmpinf::Float64, wavel::Float64, rn::Float64, rk::Float64
    local wavrnrk::Array{Float64}, qarray::Array{Float64,2}

@sync begin
    fmpinf = fv*(1e-14/om0)
    qarray = Array{Float64}(undef,0,2)
end

    # if interpolation flag interpolate, otherwise assume refcore =
    desired wavrnrk
    if interp
        local interprn::InterpFunc, interprk::InterpFunc
        @sync begin
            wavrnrk = wavel1:(wavel2-wavel1)/(numval-1):wavel2
            interprn = LinearInterpolation(refcore[:,1],refcore[:,2])
            interprk = LinearInterpolation(refcore[:,1],refcore[:,3])

```

```

        end
        wavrnrk = hcat(wavrnrk,interpnrn.(wavrnrk),interpnrk.(wavrnrk))
    else
        wavrnrk = refcore
    end

    for (wavel, rn, rk) in eachrow(wavrnrk)
        refre1::Float64, refim1::Float64, om0r::Float64 =
mfp(fv,wavel,radcore,omp,om0,rn,rk)
        # calculate the size parameter for particles
        x::Float64 = 2 * pi * radcore * refmed / wavel
        # calculate relative refractive index between particles and
medium
        refrel::Complex = (complex(refre1, refim1)) / refmed
        # uses bhmie to find Qext and appends to qarray with wavelength
        qarray = vcat(qarray,[wavel bhmie(x,refrel,scangles)[1]])
    end
    return qarray
end
end

```

```
@doc """
```

Calculates the expected extinction coefficient spectrum for particles of a given

size for coated particles

```
""" ->
```

```
function
```

```
qcoat(wavel1::Float64,wavel2::Float64,numval::Int64,refmed::Float64,
      radcor::Float64,refre1::Float64,refim1::Float64,
      radcot::Float64,refre2::Float64,refim2::Float64,
```

```
omp::Float64,om0::Float64,fv::Float64,refcore::Array{Float64,2})
```

```
    # TODO later: Add static output!
```

```
    # refcore is an array containing the spectrum of refractive index vs
particle size
```

```
    tau::Float64 = (1/om0)*1e-14
```

```
    fmpinf::Float64 = fv*tau
```

```
    delta::Float64 = (wavel2-wavel1) / (numval-1)
```

```

wavrnrk::Vector{Tuple{Float64,Float64,Float64}} =
Vector{Tuple{Float64,Float64,Float64}}()
k::UInt32 = 1
@simd for i in 1:numval
    wavel::Float64 = wavel1 + (i-1)*delta
    # find values for refractive index of particles using linear
interpolation:
    if (wavel != refcore[1,1])
        while (refcore[k,1] < wavel)
            k += 1
        end
        push!(wavrnrk, (wavel,
            (refcore[k-1,2] + (wavel-refcore[k-1,1]) / (refcore[k,1]-
refcore[k-1,1]) * (refcore[k,2]-refcore[k-1,2])),
            (refcore[k-1,3] + (wavel-refcore[k-1,1]) / (refcore[k,1]-
refcore[k-1,1]) * (refcore[k,3]-refcore[k-1,3])))
        )
    end
end
qarray::Array{Float64} = Array{Float64}(\emptyset,4)
@inbounds @simd for vals in wavrnrk
    wavel::Float64, rn::Float64, rk::Float64 = vals
    # adjust for "mean free path effect" on free electrons in metal
core
    refre1, refim1, om0r = mfp(fv,wavel,radcor,omp,om0,rn,rk)
    # calculate relative size parameters x and y for core and
coating respectively
    x = 2 * pi * radcor * refmed / wavel
    y = 2 * pi * radcot * refmed / wavel
    # calculate complex refractive indices:
    rfrel1 = refre1 + (refim1*im) / refmed
    rfrel2 = refre2 + (refim2*im) / refmed
    # appends data to qarray as a row in the format [wavel qext qsca
qback]
    # bhcoat outputs are adjusted to be relative to core instead of
coating

```

```
        qarray = vcat(qarray, [wave1  
(bhcoat(x,y,rfrel1,rfrel2).*((radcot/radcor)^2))...])  
    end  
    return qarray  
end  
  
end
```

## Appendix 11. The source code of the nanoconc.jl module

```
__precompile__()  
@doc """  
A module that uses the functions contained in miemfp and quantumcalc to  
find the  
concentration of a nanoparticle colloid given enough information  
""" ->  
@fastmath module nanoconc  
  
include("miemfp.jl")  
include("quantumcalc.jl")  
  
using CSV, DataFrames, HDF5, Interpolations, QuadGK  
  
# an abstracted datatype to allow interpolation object to be  
# declared without making extremely messy code  
const InterpFunc =  
Interpolations.Extrapolation{Float64,1,Interpolations.GriddedInterpolati  
on{Float64,1,Float64,Gridded{Linear},Tuple{Array{Float64,1}}},Gridded{Li  
near},Throw{Nothing}}  
  
const matfile = "materials.h5" # this is the location of the material  
datafile  
  
@doc """  
Fetches info string for a saved material  
""" ->  
function fetchinfo(material::String) ::String  
    return string("\nMaterial:\t\t",material,  
        "\n- Valence:\t\t",h5readattr(matfile,material)["z"],  
        "\n- Atomic Mass:\t\t",h5readattr(matfile,material)["am"],  
        "amu\n- Density:\t\t",h5readattr(matfile,material)["rho"],  
        "g/cm^3\n-  
Resistivity:\t\t",h5readattr(matfile,material)["res"],  
        "Î©/m\nDerived values:\n- Plasma  
frequency:\t",h5readattr(matfile,material)["omp"],
```

```

        "e14Hz\n- Collision
frequency:\t",h5readattr(matfile,material)["om0"],
        "e14Hz\n- Fermi
Velocity:\t",h5readattr(matfile,material)["fv"],"cm/s\n",
        h5readattr(matfile,material)["info"],

"\nDescription:\n\"",h5readattr(matfile,material)["description"],
        "\"\n")
end

@doc """
Displays info for saved material
""" ->
function dispinfo(material::String)
    print(fetchinfo(material))
end

@doc """
stores material data for future use in the materials HDF5 data file with
the given
material name and description. Requires valence (z), atomic mass (am),
density (rho)(g/cm^3)
resistivity (res)(ohm*m) and a complex refractive index spectrum from a
file at filepath.
Refractive index data is taken from an appropriately formatted csv file
(formatted with
columns entitled "w","n" and "k" for wavelength in nm, n and k
respectively)
""" ->
function addmaterial(z::Float64,am::Float64,rho::Float64,res::Float64,

filepath::String,material::String,description::String;
                    disp::Bool=true)

    try
        flag = h5open(matfile, "r") do file has(file,material) end
    catch
        flag = false
    end
end

```

```

end

if !flag
    df::DataFrames.DataFrame = CSV.read(filepath)
    data::Array{Float64,2} =
(convert(Array{Float64,2},hcat(df[:w],df[:n],df[:k])))
    h5write(matfile,material,data)
    omp, om0, fv = quantumcalc.mieparams(z,am,rho,res)
    println(omp)
    println(om0)
    println(fv)
    h5writeattr(matfile, material, Dict(
        "z" => z,
        "am" => am,
        "rho" => rho,
        "res" => res,
        "omp" => omp,
        "om0" => om0,
        "fv" => fv,
        "description" => description,
        "info" => string("Wavelength Range:\t",minimum(data[:,1]),
            "nm-",maximum(data[:,1]),
            "nm\nNumber of datapoints:\t",
            size(data)[1])))

    if disp == true
        println("\nAdded material:")
        dispinfo(material)
    end
elseif disp == true
    println("\nMaterial ",material," Already exists!\n\nExisting
material:")
    dispinfo(material)
end
end

@doc """

```

An alternative version of the `addmaterial` function for materials with known mie

parameters. Requires input of plasma freq (`omp`) in Hz/1e14, collision freq (`om0`) in Hz/1e14 and

Fermi velocity (`fv`) in cm/s

""" ->

```
function addmaterial(omp::Float64,om0::Float64,fv::Float64,
filepath::String,material::String,description::String;
                    disp::Bool=true)

    try
        flag = h5open(matfile, "r") do file has(file,material) end
    catch
        flag = false
    end

    if !flag
        df::DataFrames.DataFrame = CSV.read(filepath)
        data::Array{Float64,2} =
        (convert(Array{Float64,2},hcat(df[:w],df[:n],df[:k])))
        h5write(matfile,material,data)
        println(omp)
        println(om0)
        println(fv)
        h5writeattr(matfile, material, Dict(
            "omp" => omp,
            "om0" => om0,
            "fv" => fv,
            "description" => description,
            "info" => string("Wavelength Range:\t",minimum(data[:,1]),
                "nm-",maximum(data[:,1]),
                "nm\nNumber of datapoints:\t",
                size(data)[1]))
        if disp == true
            println("\nAdded material:")
            dispinfo(material)
        end
    end
```

```

elseif disp == true
    println("\nMaterial ",material," Already exists!\n\nExisting
material:")
    dispinfo(material)
end
end

@doc """
This function loads the stored miemfp data for a saved material. omp,
om0, fv and
refractive index array are returned as a static tuple that can be
readily splatted
into the last few args of the miemfp.qbare and miemfp.qcoat functions
""" ->
function loadmaterial(material::String;disp::Bool=true
                    )
::Tuple{Float64,Float64,Float64,Array{Float64,2}}
    local output::Tuple{Float64,Float64,Float64,Array{Float64,2}}
    h5open(matfile, "r") do file
        data = d_open(file, material)
        output = (
            read(a_open(data, "omp")),
            read(a_open(data, "om0")),
            read(a_open(data, "fv")),
            read(data)
        )
    end
    if disp == true
        println("\nLoading material:")
        dispinfo(material)
        println()
    end
    return output
end

@doc """

```

This function lists all materials for which refractive index data is stored

```
""" ->
```

```
function listmaterials()
    h5open(matfile, "r") do file
        flag::Bool = false
        for i in file flag = true; break end
        if flag == true
            println("\nSaved materials:")
            for material in file
                println(name(material))
            end
        else
            println("\nNo materials saved!")
        end
    end
end
```

```
@doc """
```

This function deletes a material from the materials datafile

```
""" ->
```

```
function delmaterial(material::String; disp::Bool=true)
    h5open(matfile, "r+") do file
        if exists(file, material)
            if disp == true
                println("\nDeleting material:")
                dispinfo(material)
                println()
            end
            o_delete(file, material)
        else
            println("\nMaterial \"", material, "\" not found!")
        end
    end
end
```

```
@doc """
```

This function allows editing of specific parameters for a stored material

```
""" ->
```

```
function
```

```
editmaterial(material::String,param::String,value;disp::Bool=true)
```

```
    h5open(matfile,"r+") do file
```

```
        if !exists(file,material)
```

```
            if disp
```

```
                println("\nMaterial \"",material,"\" not
```

```
found!")
```

```
            end
```

```
            return
```

```
        end
```

```
    end
```

```
    matattr = h5readattr(matfile,material)
```

```
    matdata = h5read(matfile,material)
```

```
    if param == "refind"
```

```
        val0 = matdata
```

```
        value::typeof(matdata)
```

```
        matdata = value
```

```
    else
```

```
        val0 = matattr[param]
```

```
        value::typeof(val0)
```

```
        matattr[param] = value
```

```
    end
```

```
    h5open(matfile,"r+") do file
```

```
        o_delete(file,material)
```

```
    end
```

```
    h5write(matfile,material,matdata)
```

```
    h5writeattr(matfile, material, matattr)
```

```
    if disp
```

```
        println(material," Parameter ",param," changed from ",val0,"
```

```
to ",value)
```

```
    end
```

```
end
```

```
@doc """
```

This function takes DLS data and UV/Vis data and returns a corresponding particles per mL concentration measurement

```
""" ->
function
particlecount(uvdata::Array{Float64,2},dlsdata::Array{Float64,2},

refmed::Float64,wavel1::Float64,wavel2::Float64,numval::UInt32,

materialdata::Tuple{Float64,Float64,Float64,Array{Float64,2}},
                d0::Float64) ::Float64
    local wavrnrk::Array{Float64}, refcore::Array{Float64},
    _dlsdata::Array{Float64}
    local interprn::InterpFunc, interprk::InterpFunc,
    _materialdata::Tuple{Float64,Float64,Float64}

    # create a copy of the arrays to prevent global scope mutation
    _dlsdata, _uvdata = copy(dlsdata), copy(uvdata)
    # normalise relative amounts of particles to a total of 1
    _dlsdata[:,2] = _dlsdata[:,2] ./ sum(_dlsdata[:,2])
    # convert particle diameters in dlsdata to radii
    _dlsdata[:,1] = _dlsdata[:,1] ./ 2
    # convert absorption values in uv spectrum to absorbance values
    # separate material data parameters from refcore
    @sync begin
        _materialdata = materialdata[1:end-1]
        refcore = materialdata[end]
    end
    @sync begin
        wavrnrk = wavel1:(wavel2-wavel1)/(numval-1):wavel2
        interprn = LinearInterpolation(refcore[:,1],refcore[:,2])
        interprk = LinearInterpolation(refcore[:,1],refcore[:,3])
    end
    wavrnrk = hcat(wavrnrk,interprn.(wavrnrk),interprk.(wavrnrk))
    # define a wrapper function for later vectorised calculations
    spec(x) =
miemfp.qbare(wavel1,wavel2,numval,0x00000002,refmed,x,_materialdata...,w
avrnrk,interp=false)
```

```

    # note: the UInt32 above for "scangles" must be at least 2 for
accurate Qext. Higher "scangles"
    ##      does not increase Qext precision but will be important if
modding to also account for Qsca
    # perform vectorised spectrum prediction on dlsdata array
spectra = spec.(_dlsdata[:,1])
    # create a wrapper function for the conversion to absorbance
_predict(qext,avgr) = quantumcalc.predictabs(
    qext,
    avgr,
    d0
)
    # for each spectrum, multiply all values by their relative amounts
from the dlsdata array
@inbounds @simd for i in 1:length(spectra)
    spectra[i][:,2] = _dlsdata[i,2] .* spectra[i][:,2]
end
    # convert each weighted extinction efficient spectrum into an
absorbance spectrum
    # for 1 particle per L at path length
for i in 1:size(_dlsdata)[1]
    # create a subwrapper for vectorised conversion calculation
predict(qext) = _predict(qext,_dlsdata[i,1])
    # then perform the vectorised calculation
spectra[i][:,2] = predict.(spectra[i][:,2])
end
    # prep an array for final predicted spectrum
data::Array{Float64,2} = Array{Float64,2}(undef,numval,2)
data[:,1] = spectra[1][:,1]
data[:,2] = zeros(numval)
    # for each weighted spectrum, add it to the total spectrum in the
"data" array
    # this yields an overall mean spectrum for the "average" particle
present
@inbounds @simd for x in spectra
    data[:,2] = data[:,2] .+ x[:,2]
end

```

```
# create interpolation function for uvdata and returned data
interpuv = LinearInterpolation(_uvdata[:,1],_uvdata[:,2])
interpdat = LinearInterpolation(data[:,1],data[:,2])
# find integrals of both spectra
uvintegral = quadgk(interpuv,wavel1,wavel2)
datintegral = quadgk(interpdat,wavel1,wavel2)
return (uvintegral[1]/datintegral[1])
end

end
```

## Appendix 12. The source code of the quantumcalc.jl module

```
__precompile__()  
@doc """  
A module containing functions that apply various quantum physics  
formulae  
for use with "miemfp.jl" in spectrum prediction/concentration  
calculation  
""" ->  
@fastmath module quantumcalc  
  
# Planck's constant in JS according to the CODATA 2014 definition  
const h = 6.626070040e-34  
# Reduced Planck's Constant  
const hbar = h/(2*pi)  
# Fine structure constant based on the CODATA 2014 definition  
const alpha = 7.2973525664e-3  
# Speed of light in vacuum by the CODATA 2014 definition  
const c = 299752458  
# Elementary charge in C according to the CODATA 2014 definition  
const ec = 1.6021766208e-19  
# Boltzmann Constant in J/K according to CODATA 2014 definition  
const kb = 1.38064852e-23  
# Electron mass in kg according to the 2014 CODATA definition of 1amu  
and ref: DOI:10.1038/nature13026  
const me = 9.109383555654034e-31  
# Bohr radius in m  
const a0 = hbar/(me*c*alpha)  
# Avogadro's constant in mol^-1 according to the CODATA 2014 definition  
const A = 6.022140857e23  
  
@doc """  
Calculates the free electron density (ne) in m^-3 of an elemental  
material given  
its valence (z), atomic mass in amu (am) and mass density (rho) in  
g/cm^2  
Source: ISBN 0-03-083993-9 (page 4)
```

```

""" ->
function metalfed(z::Float64,rho::Float64,ma::Float64) ::Float64
    return (A*((z*rho)/ma)*1e6)
end

@doc """
Calculates the Fermi wave vector (kf) of electrons in a material given
electron density (ne)
Source: ISBN 0-03-083993-9 (page 36)
""" ->
function fermivec(ne::Float64) ::Float64
    return cbrt(3*ne*(pi^2))
end

@doc """
Calculates the Fermi velocity (fv) in m/s of electrons in a material
given Fermi
wave vector (kf)
Source: ISBN 0-03-083993-9 (page 36)
""" ->
function fermivel(kf::Float64;mstar::Float64=me) ::Float64
    return (hbar/mstar)*kf
end

@doc """
Calculates the electron sphere radius (rs) given its free electron
density (ne)
Source: ISBN 0-03-083993-9 (page 4)
""" ->
function spherad(ne::Float64) ::Float64
    return cbrt(3/(4*pi*ne))
end

@doc """
Calculates the plasma frequency (omp) of a material in Hz give its
electron
sphere radius (rs)

```

Source: ISBN 0-03-083993-9 (page 758)

""" ->

```
function plasmafreq(rs::Float64) ::Float64
    return 2*pi*11.44e15*(rs/a0)^(-3/2)
end
```

@doc """

Calculates the collision frequency ( $\omega_0$ ) in Hz for a material given its free

electron density ( $n_e$ ) and its resistivity ( $\text{res}$ )

Source: ISBN 0-03-083993-9 (page 8)

""" ->

```
function collfreq(ne::Float64,res::Float64;mstar::Float64=me) ::Float64
    return ((ec^2)*ne*res)/mstar
end
```

@doc """

Calculates the plasma freq ( $\omega_p$ ) in Hz/1e14, collision freq ( $\omega_0$ ) in Hz/1e14 and

Fermi velocity ( $v_f$ ) in cm/s of an elemental material given its valence ( $z$ ),

atomic mass ( $a_m$ ) in amu, mass density ( $\rho$ ) in g/cm<sup>2</sup> and its resistivity ( $\text{res}$ )

in Ohm\*m as a tuple of ( $\omega_p, \omega_0, v_f$ ) for use in Mie model algorithms contained in

the "miemfp" module

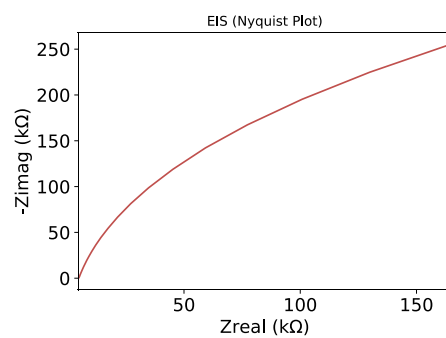
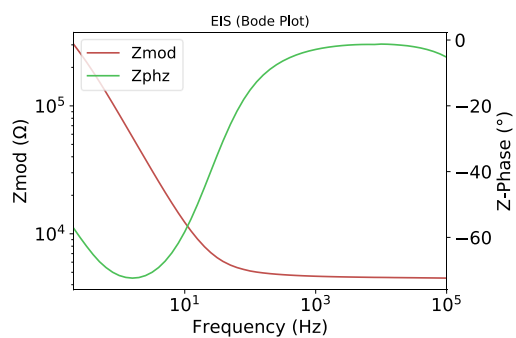
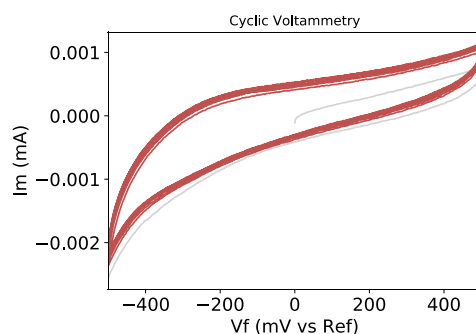
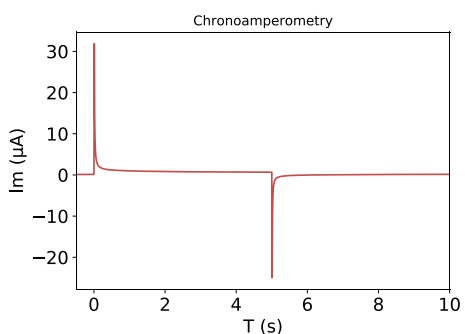
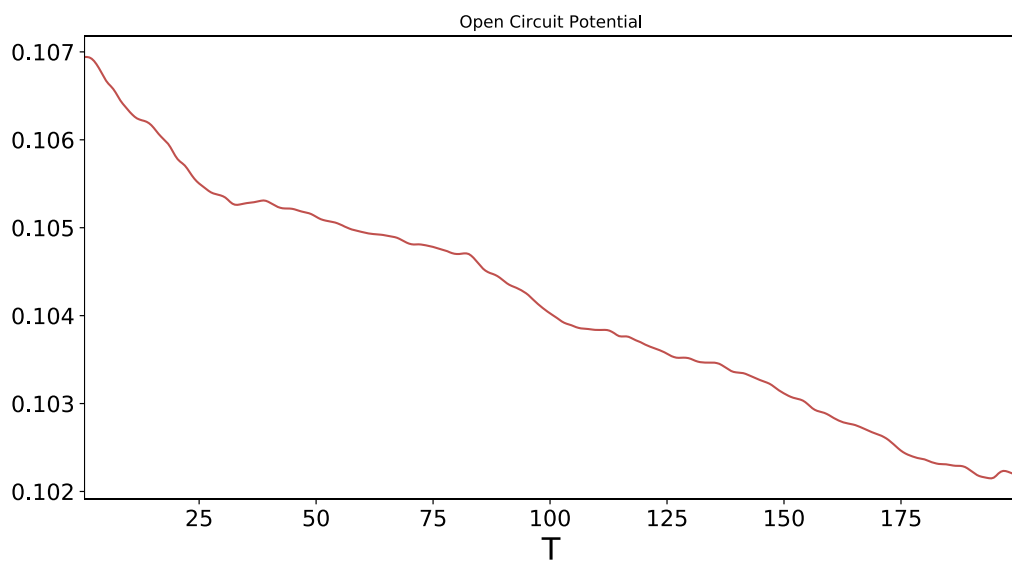
""" ->

```
function mieparams(z::Float64,am::Float64,rho::Float64,
                  res::Float64) ::Tuple{Float64,Float64,Float64}
    ne::Float64 = metalfed(z,rho,am)
    return (
        plasmafreq(spherad(ne))*1e-14,
        collfreq(ne,res)*1e-14,
        fermivel(fermivec(ne))*1e2
    )
end
```

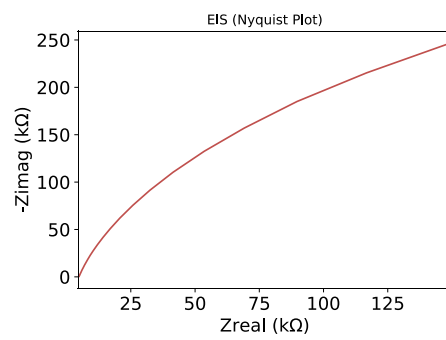
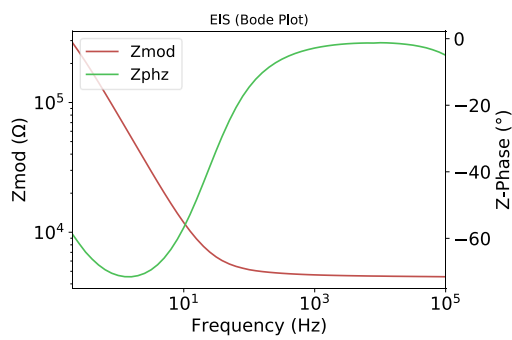
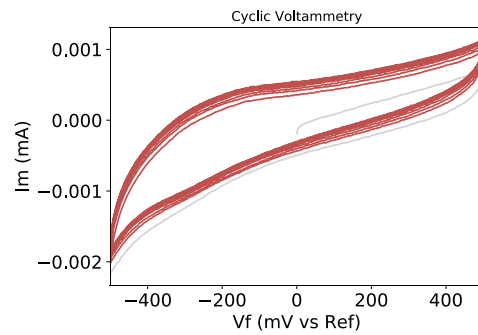
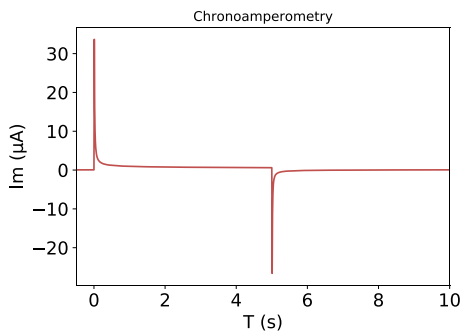
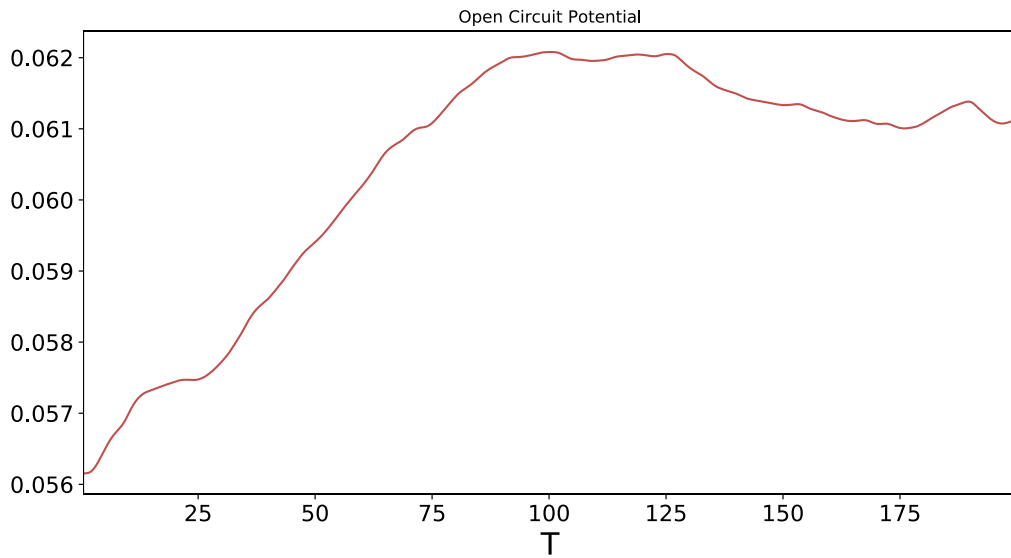
```
@doc """
Predicts the absorbance value of a single particle in 1L solvent from
the
extinction efficiency (qext), average particle radius (avgr), and path
length (l)
""" ->
function predictabs(qext::Float64,avgr::Float64,l::Float64) ::Float64
    return (pi * ((avgr*1E-7)^2) * (qext) * (l)) / 2.303
end

end
```

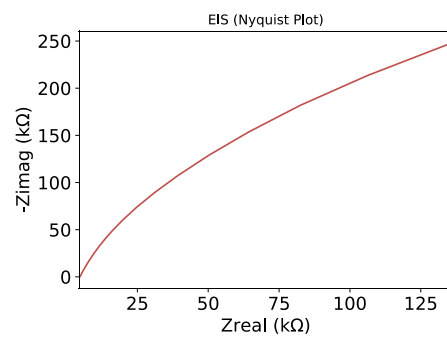
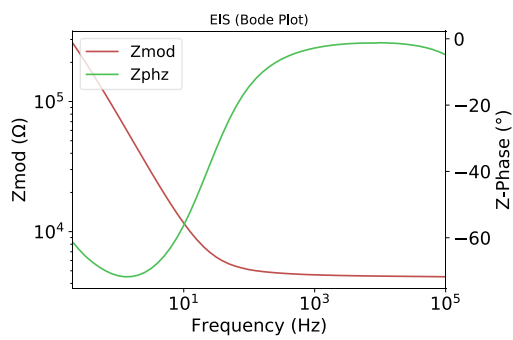
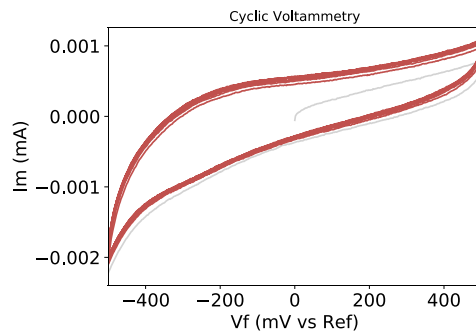
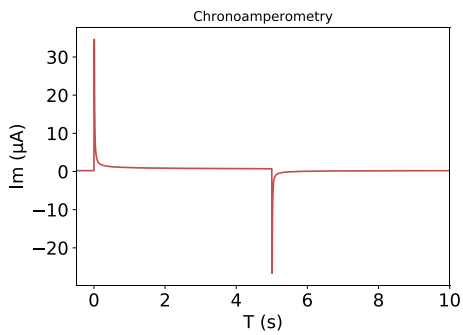
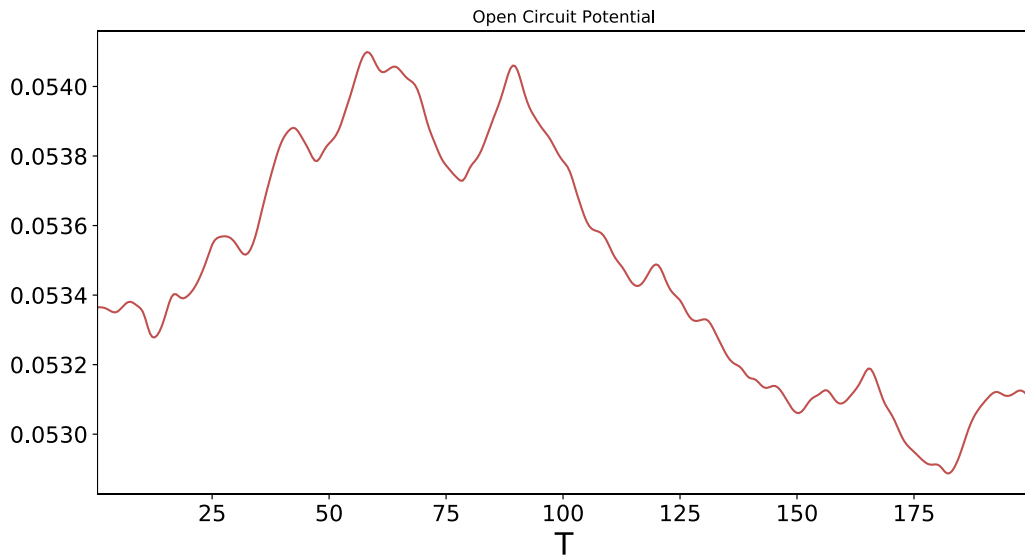
Appendix 13. Conductometric data for the unfunctionalised gold nanostructured surface tested in Section 16.1 (following step 2)



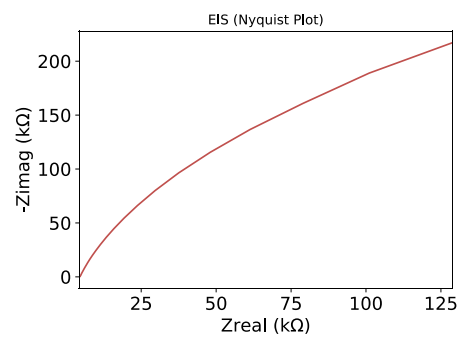
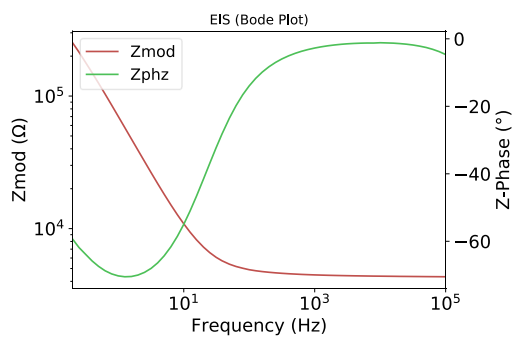
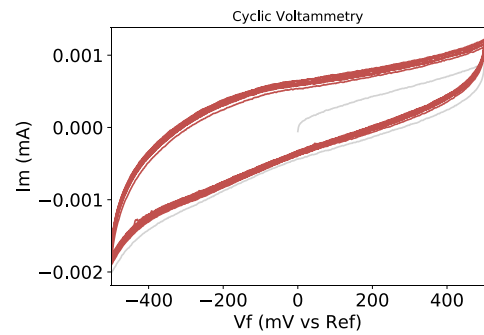
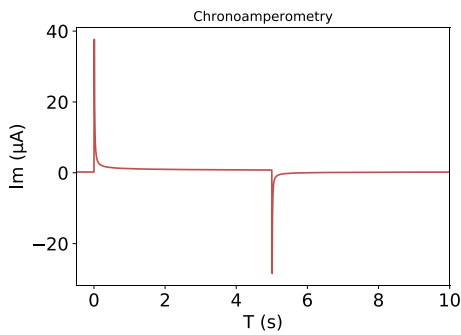
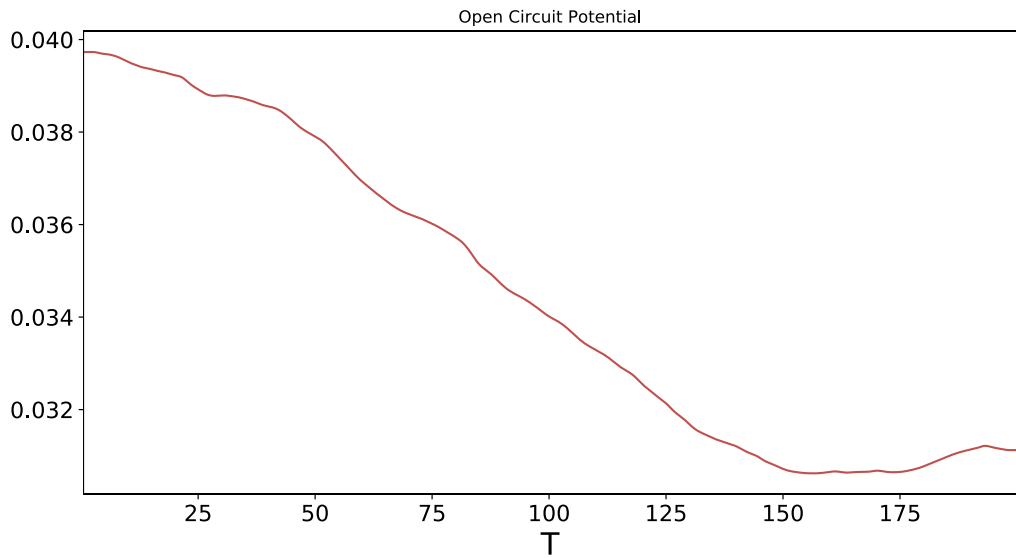
Appendix 14. Conductometric data for the sensor surface following its first dithiol exposure in Section 16.1 (following step 3)



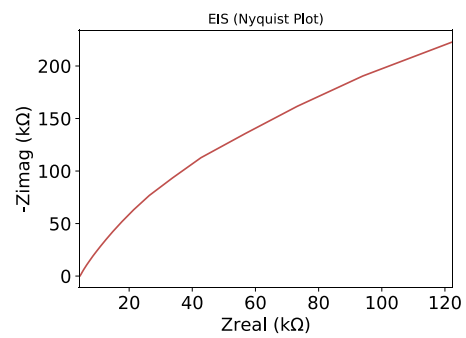
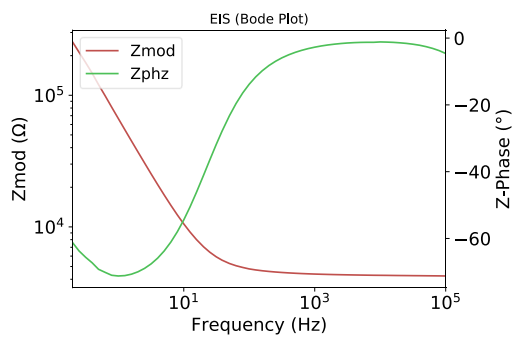
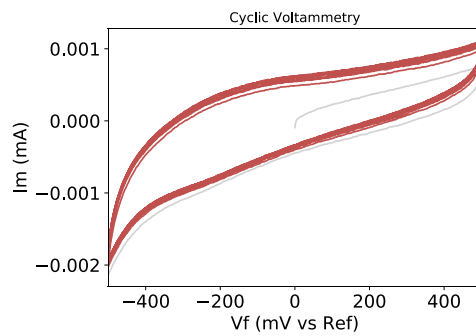
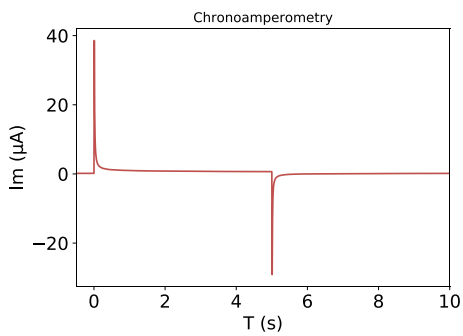
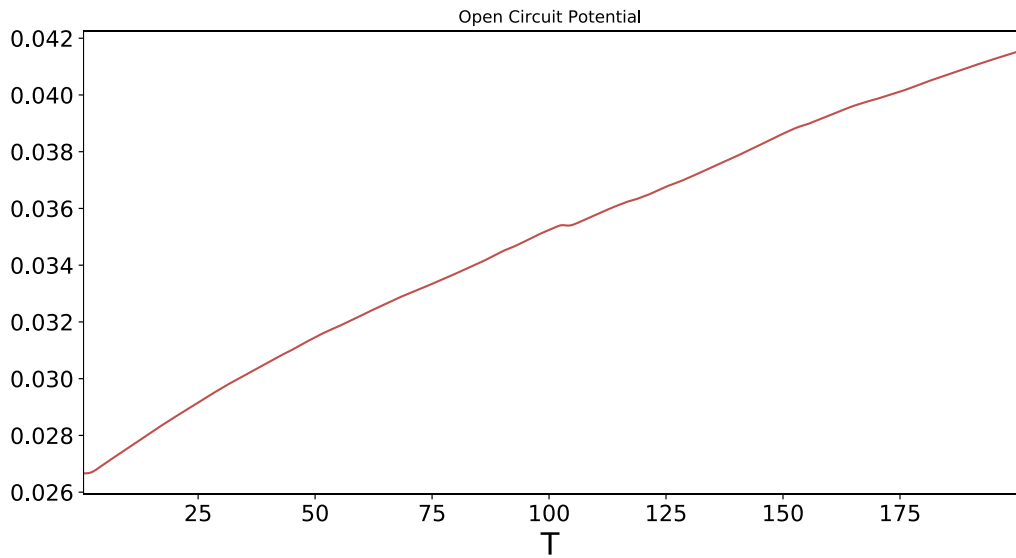
Appendix 15. Conductometric data for the sensor surface following its first colloid exposure in Section 16.1 (following step 4)



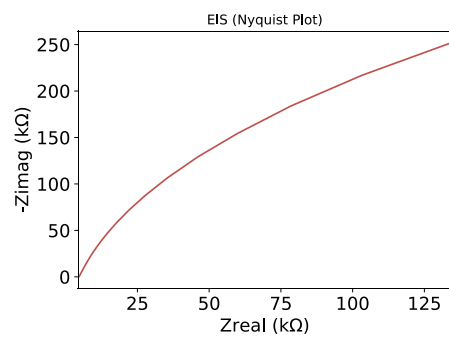
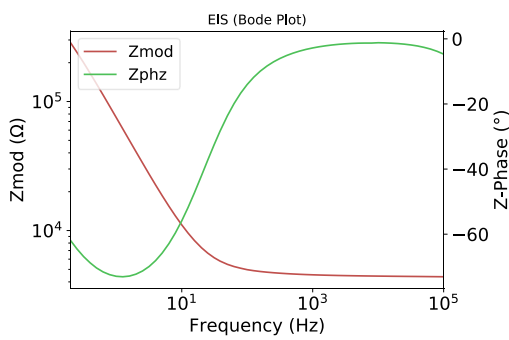
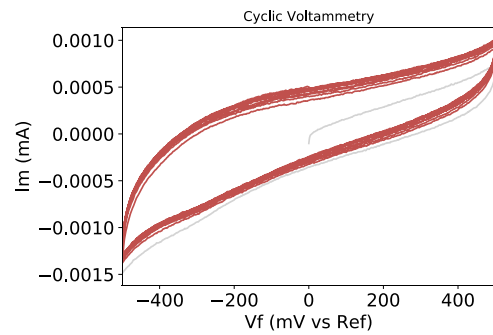
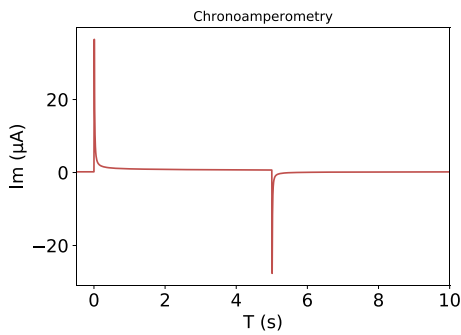
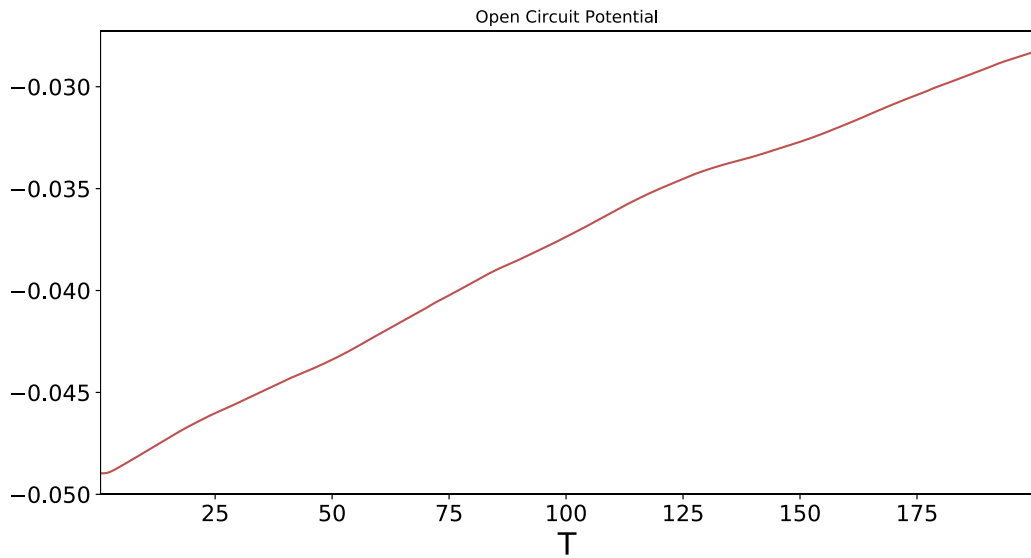
Appendix 16. Conductometric data for the sensor surface following its second dithiol exposure in Section 16.1 (following step 5)



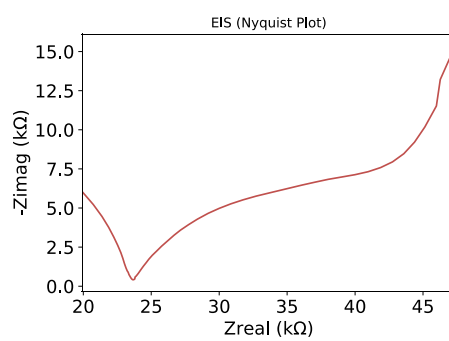
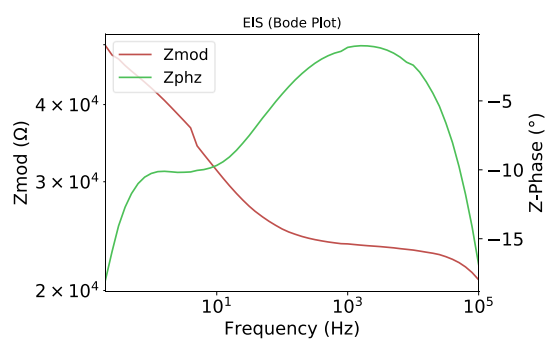
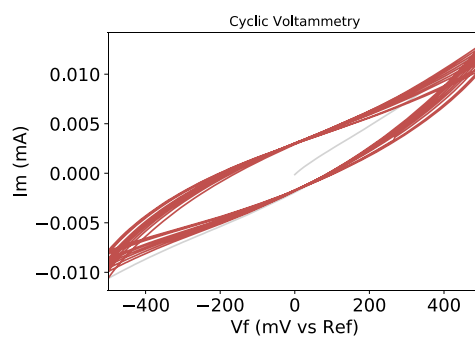
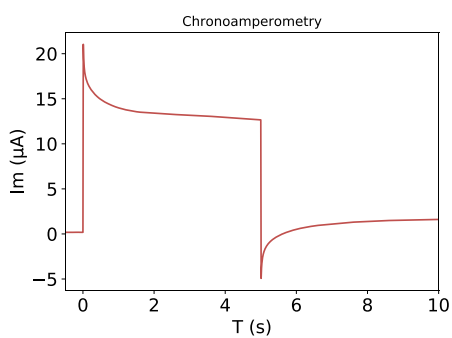
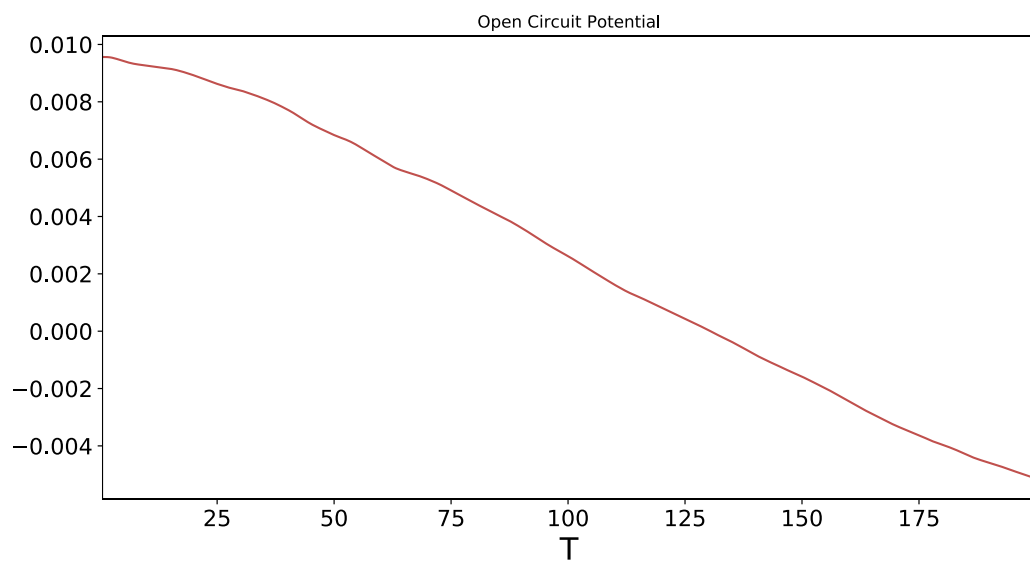
Appendix 17. Conductometric data for the sensor surface following its second colloid exposure in Section 16.1 (following step 6)



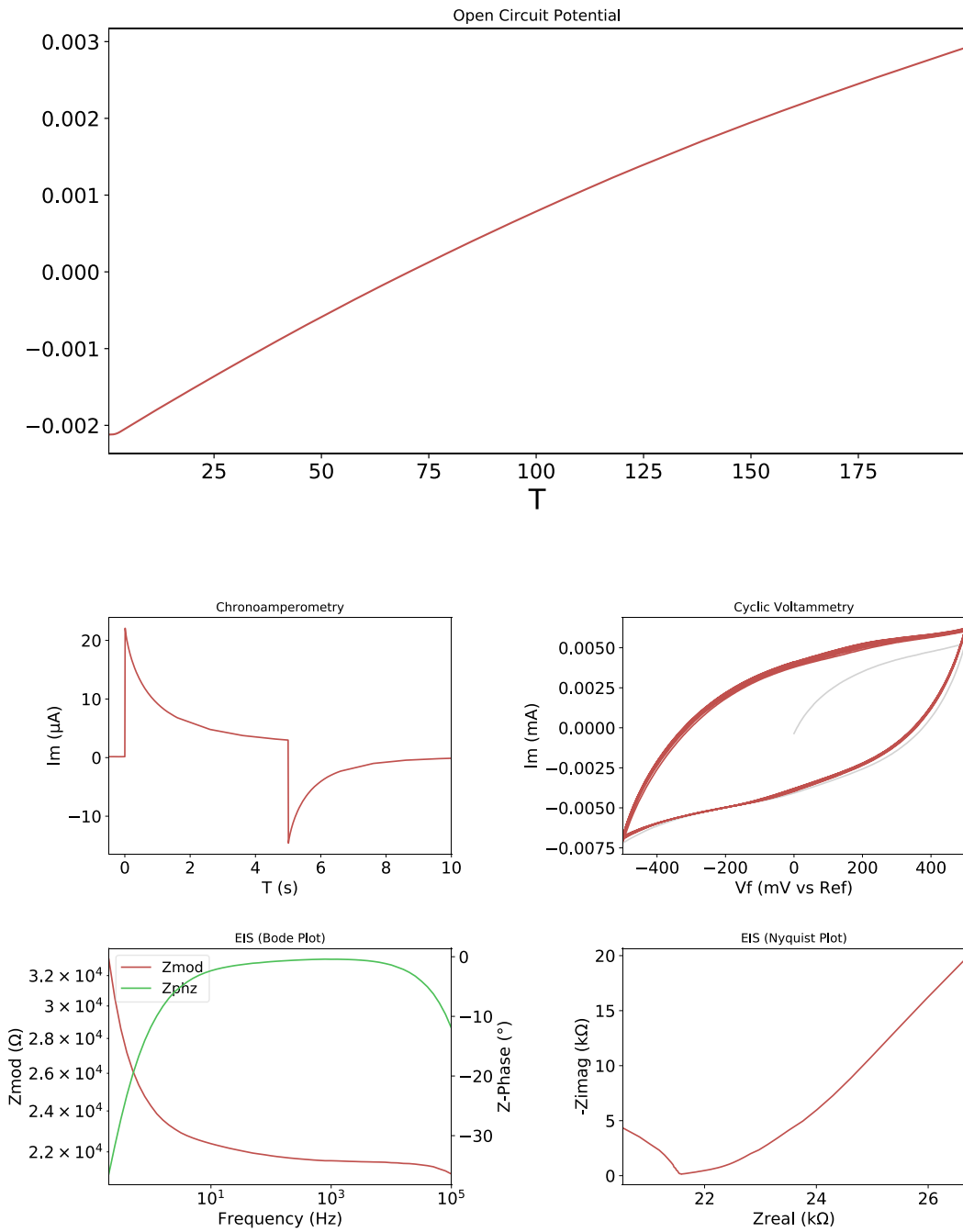
Appendix 18. Conductometric data for the sensor surface following its exposure to the thio-DNA probe in Section 16.1 (following step 7)



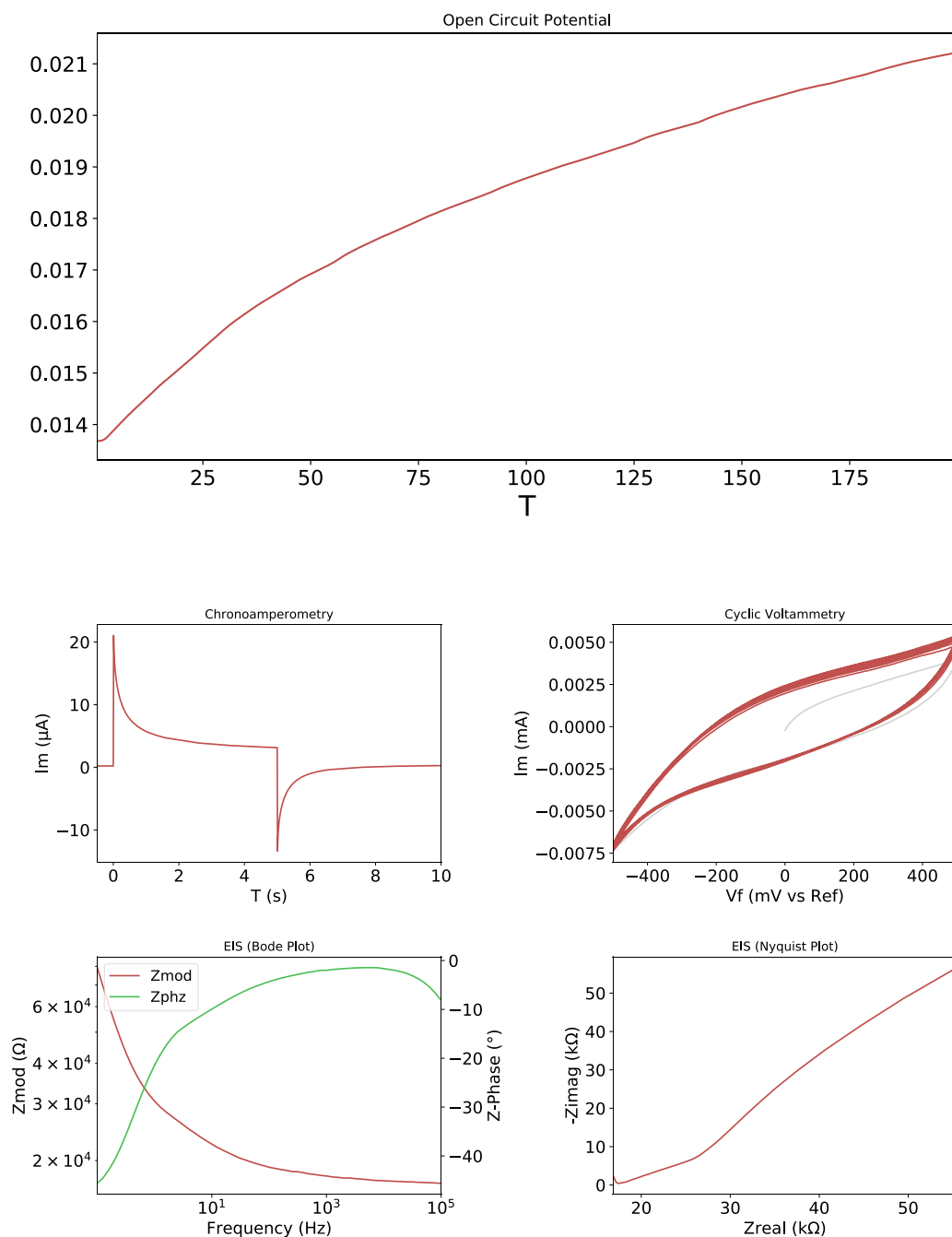
Appendix 19. Conductometric data for the sensor surface following its exposure to 6-mercaptohexanol as a passivating agent in Section 16.1 (following step 8)



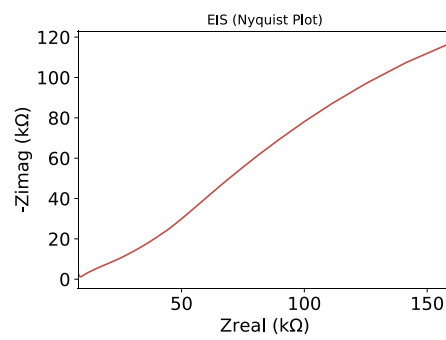
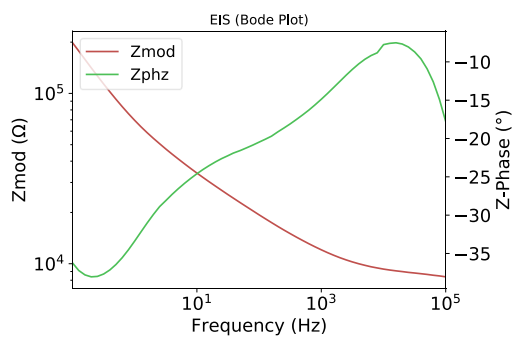
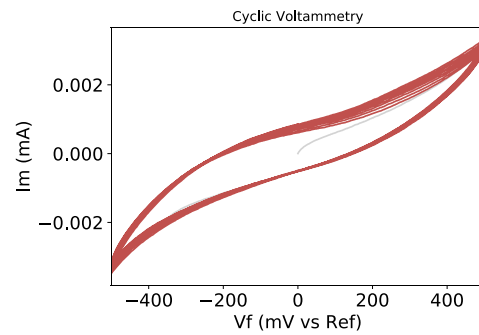
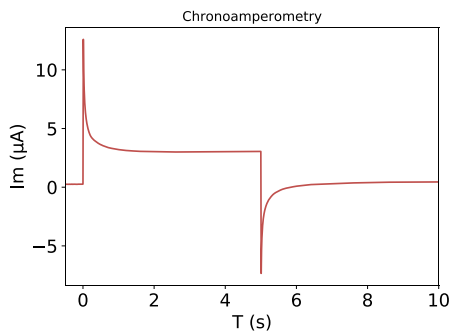
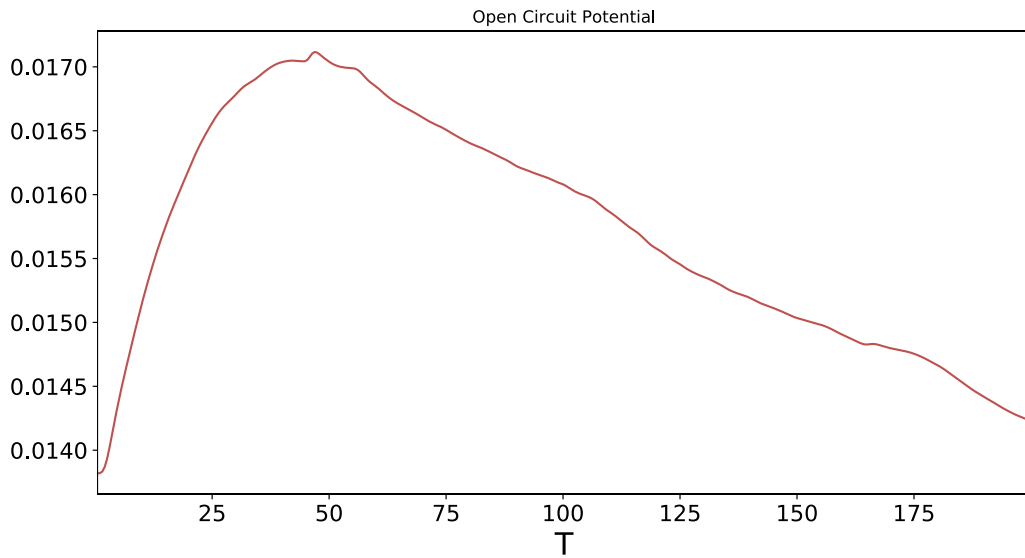
Appendix 20. Conductometric data for the sensor surface following its exposure to 10 micromolar c-Myc exon 2 (the target analyte) in Section 16.1



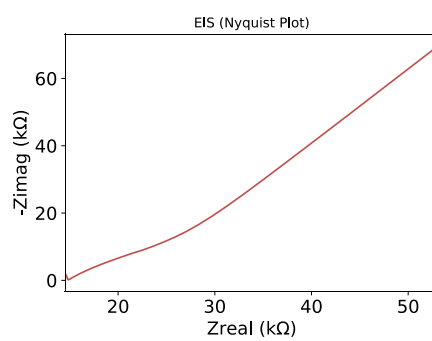
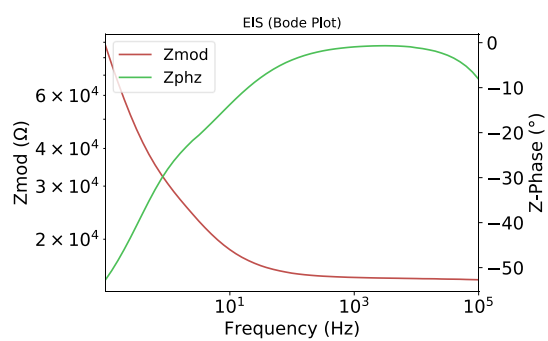
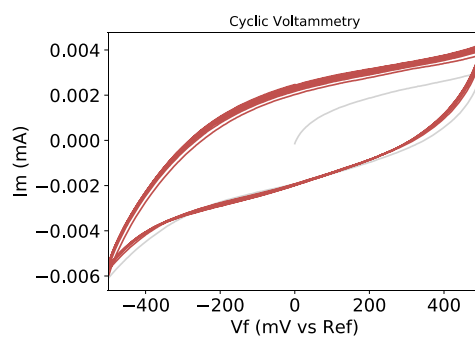
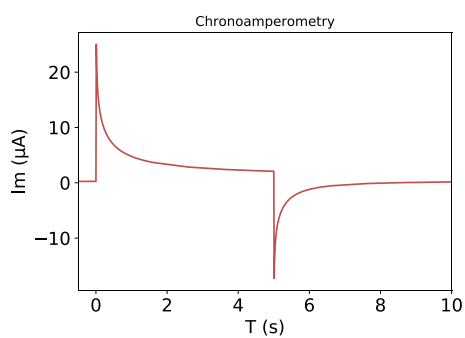
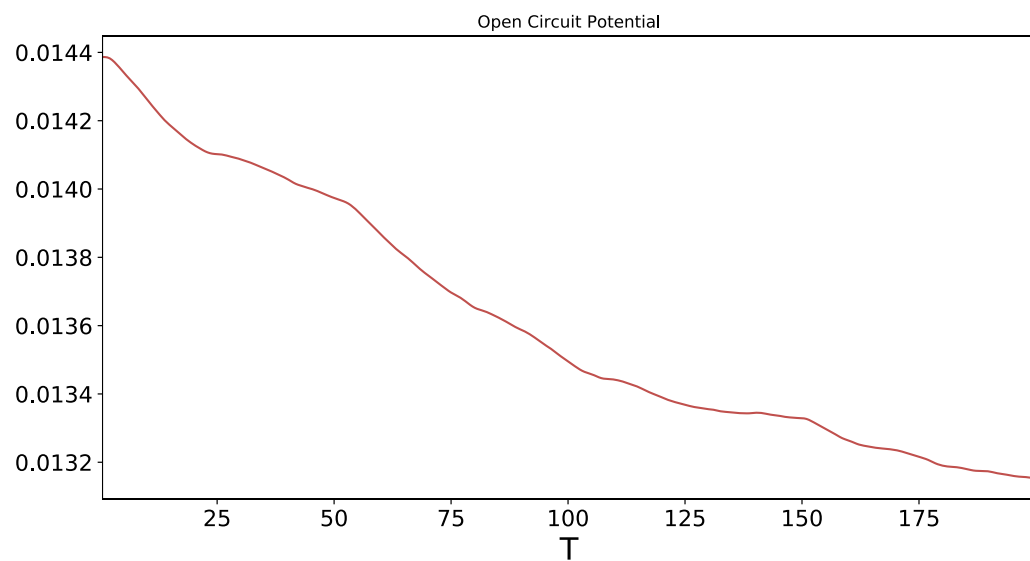
Appendix 21. Conductometric data for a sensor surface before inoculation with 1 micromolar c-Myc exon 2



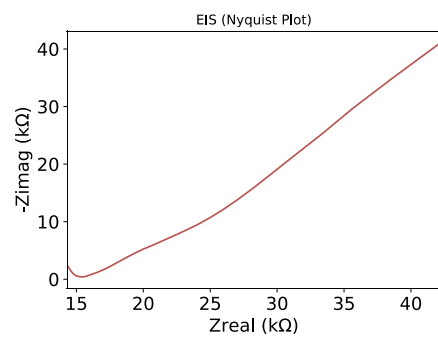
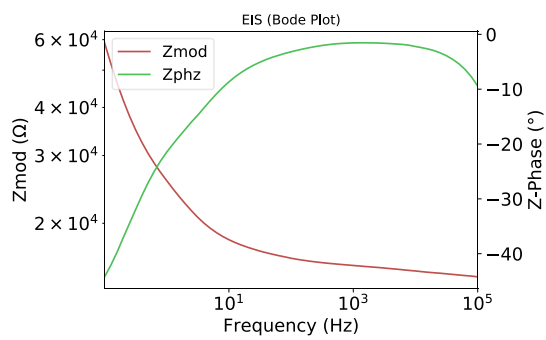
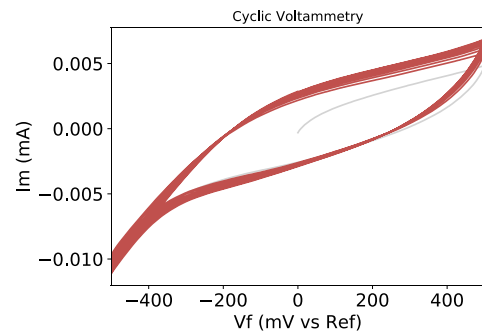
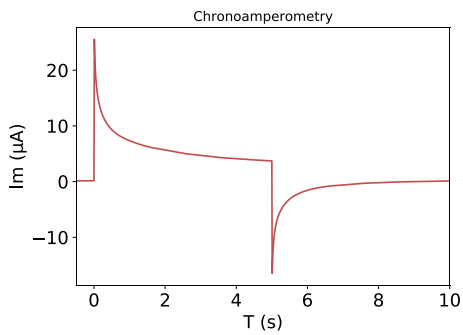
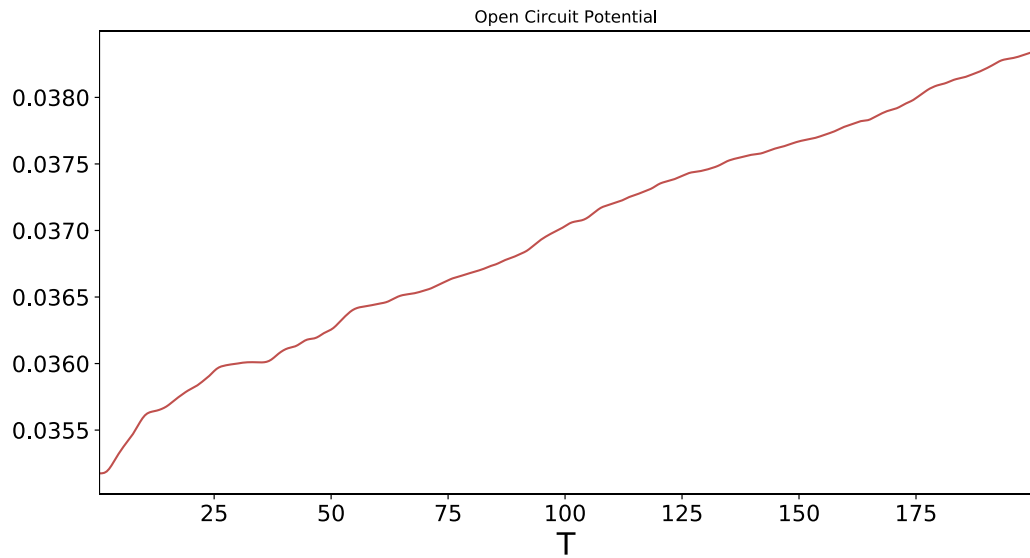
Appendix 22. Conductometric data for a sensor surface after inoculation with 1 micromolar c-Myc exon 2



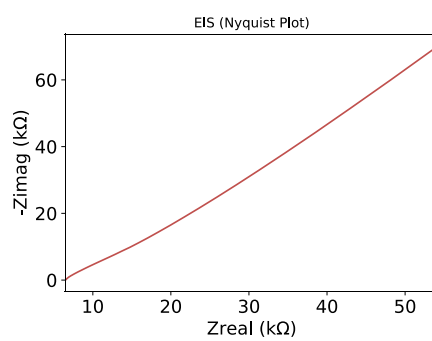
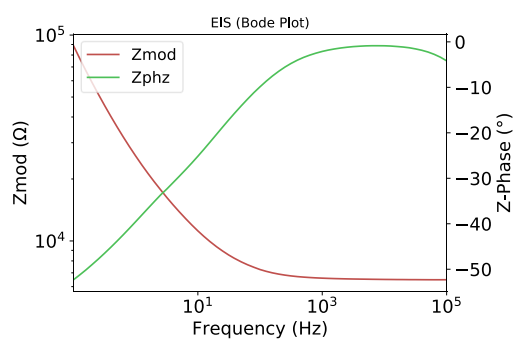
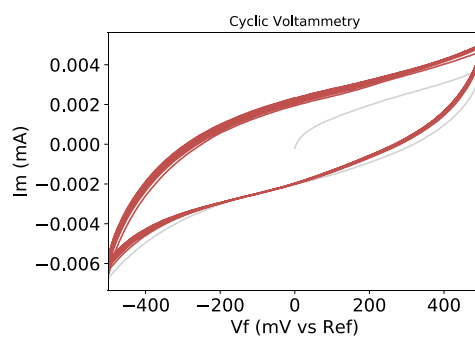
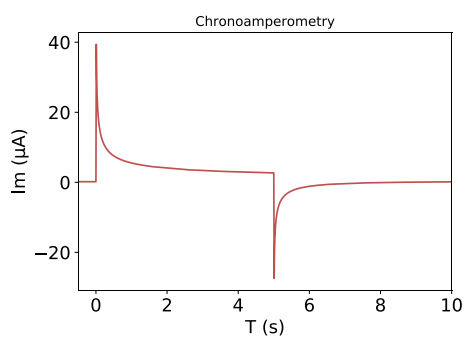
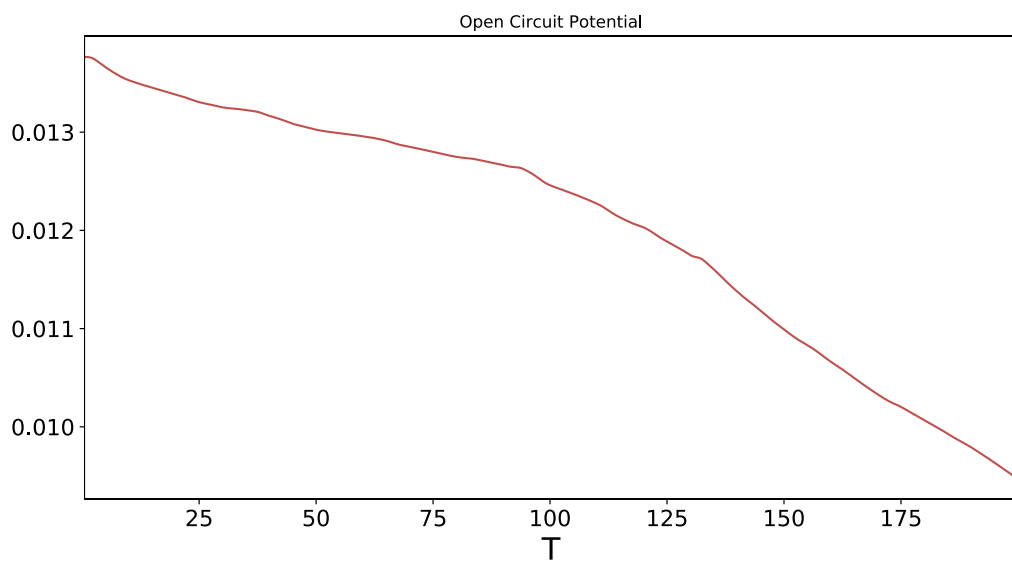
Appendix 23. Conductometric data for a sensor surface before inoculation with 0.8 micromolar c-Myc exon 2



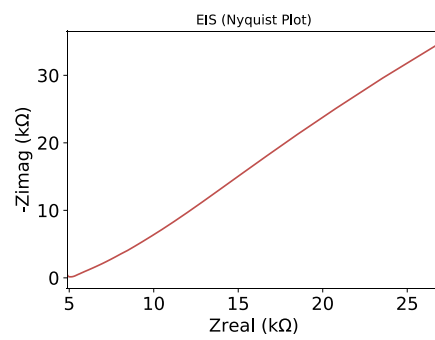
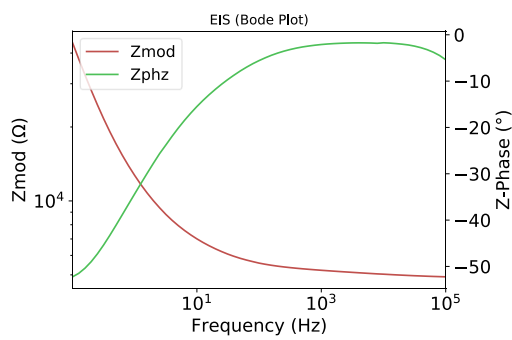
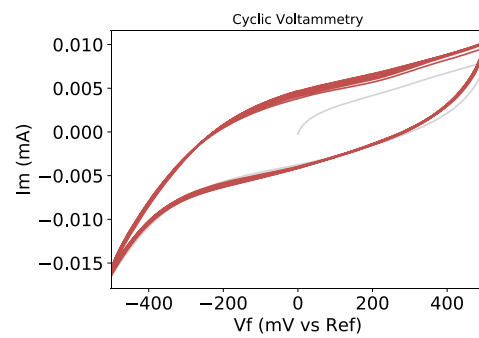
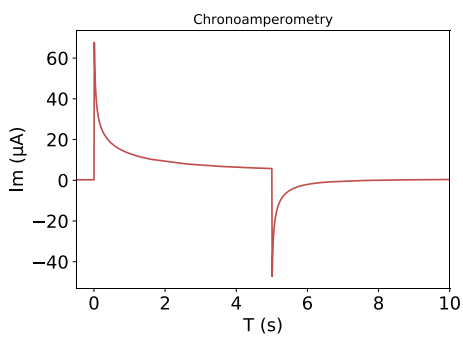
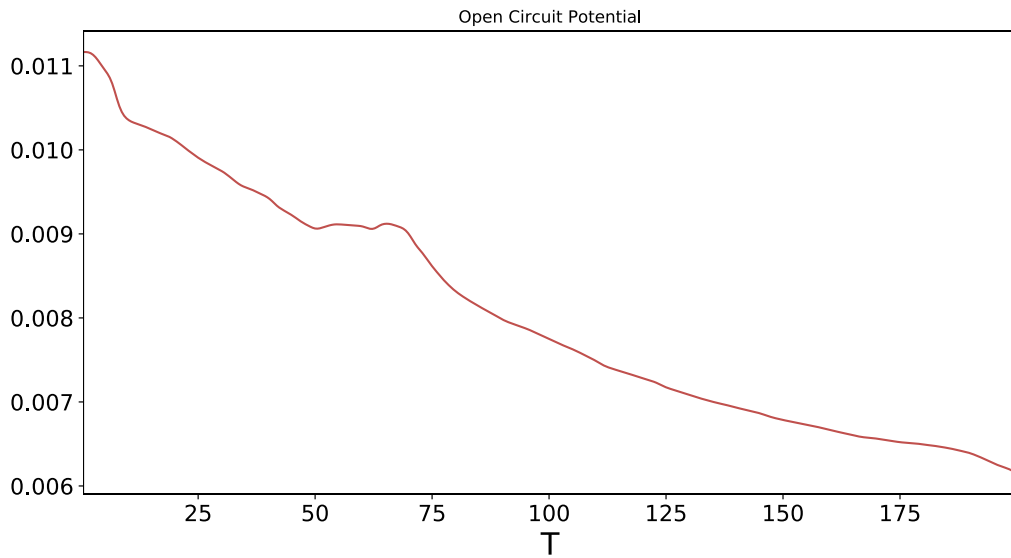
Appendix 24. Conductometric data for a sensor surface after inoculation with 0.8 micromolar c-Myc exon 2



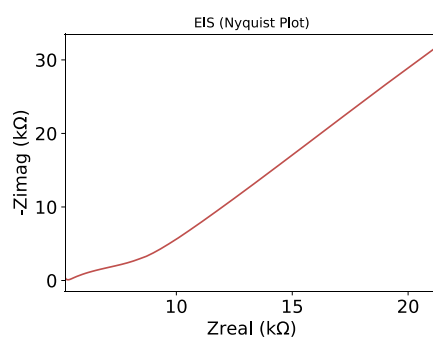
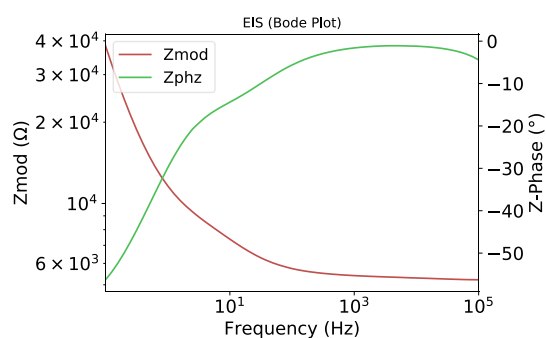
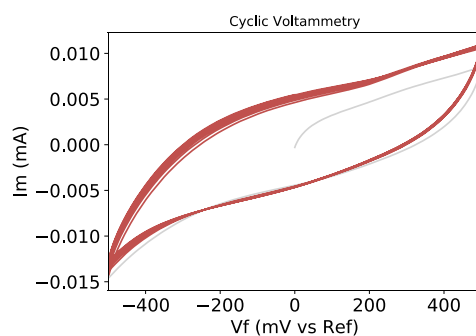
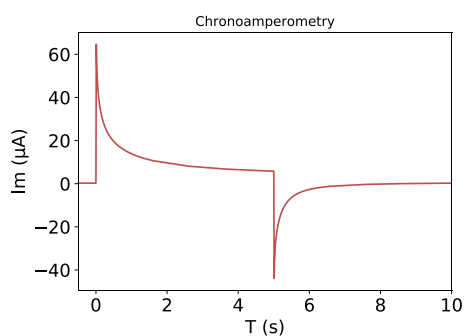
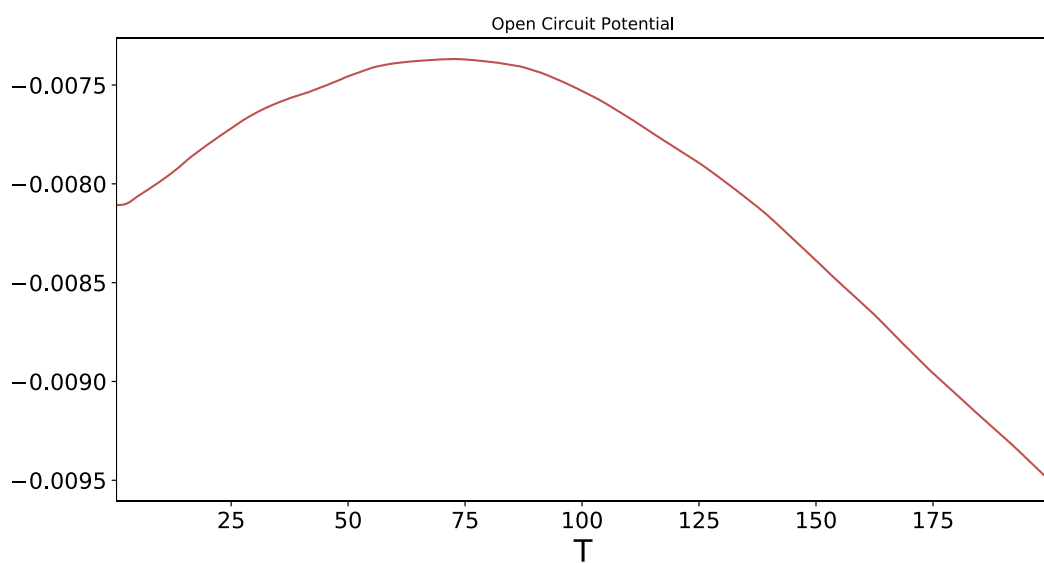
Appendix 25. Conductometric data for a sensor surface before inoculation with 0.6 micromolar c-Myc exon 2



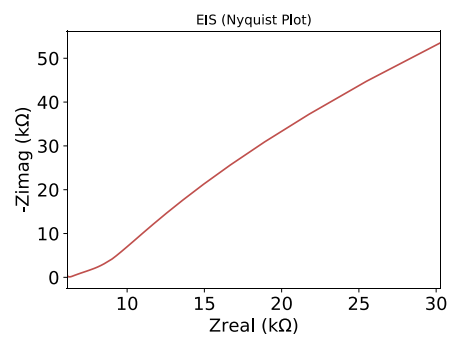
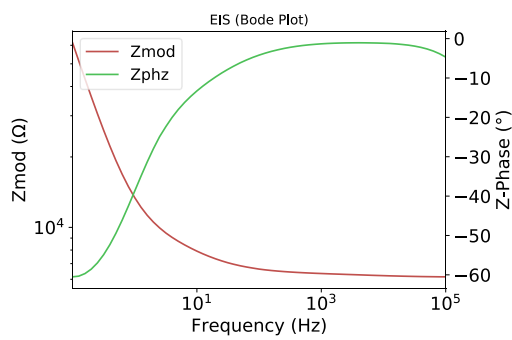
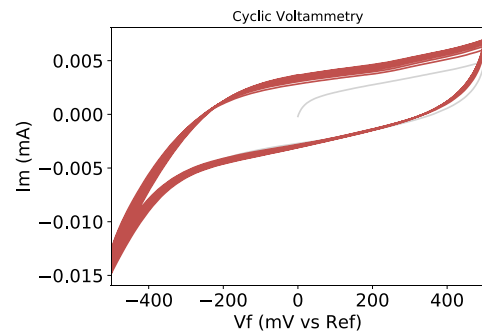
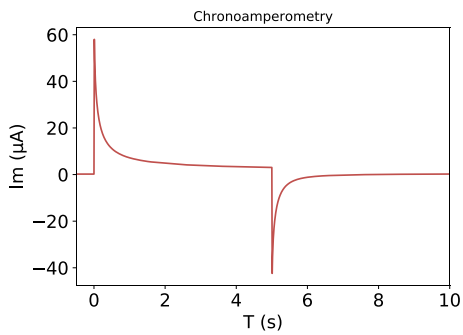
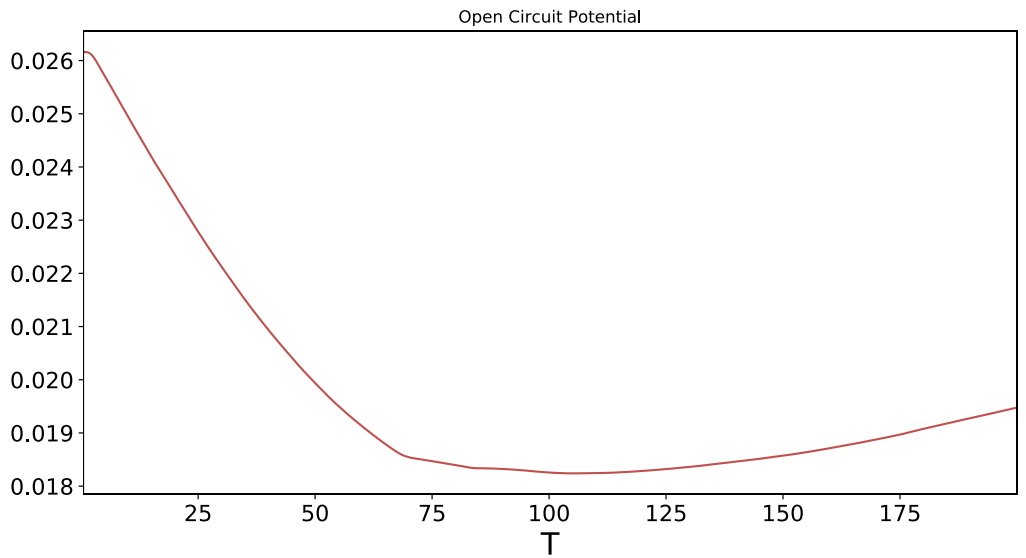
Appendix 26. Conductometric data for a sensor surface after inoculation with 0.6 micromolar c-Myc exon 2



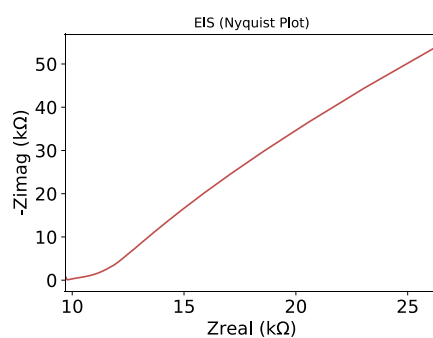
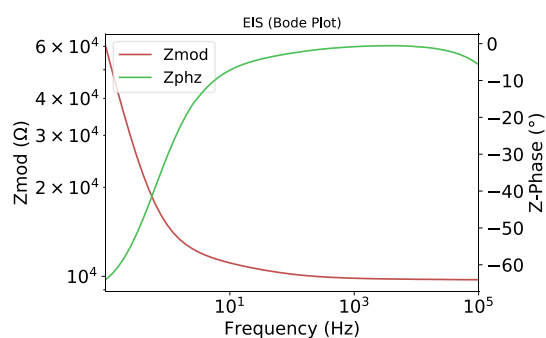
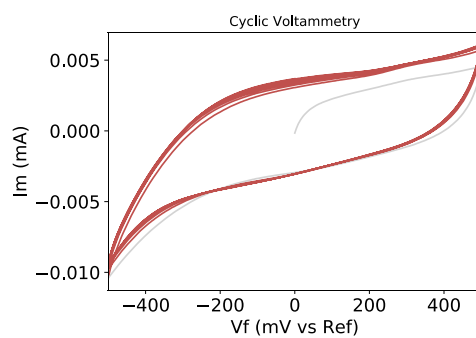
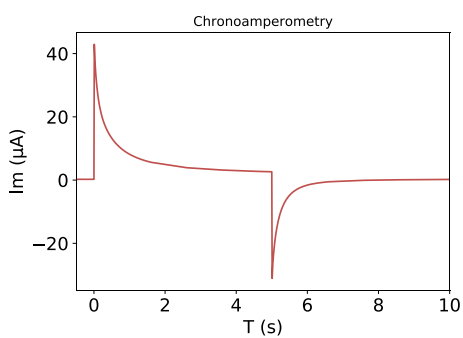
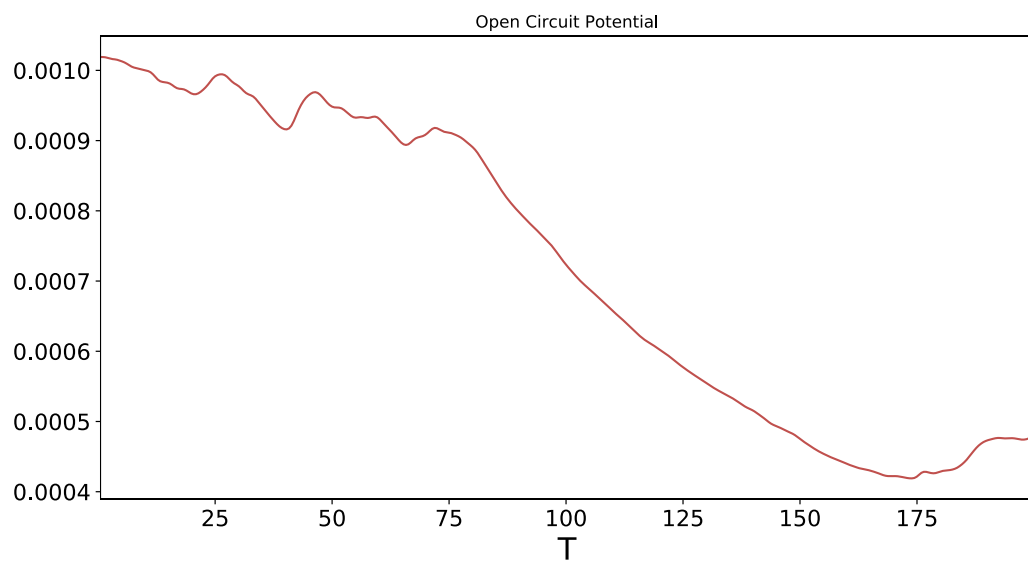
Appendix 27. Conductometric data for a sensor surface before inoculation with 0.4 micromolar c-Myc exon 2



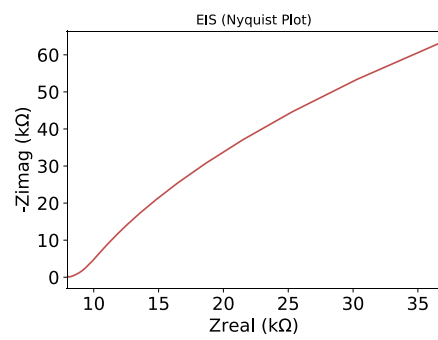
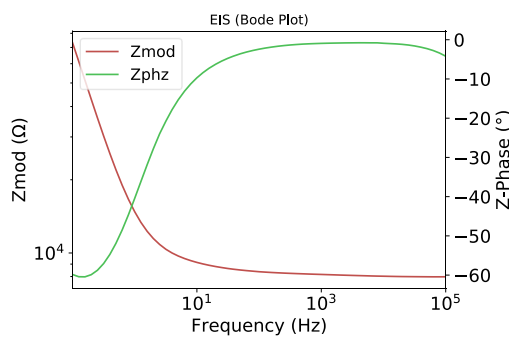
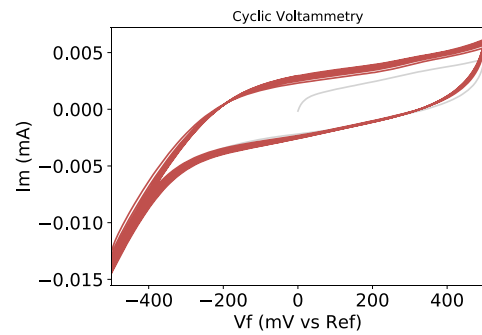
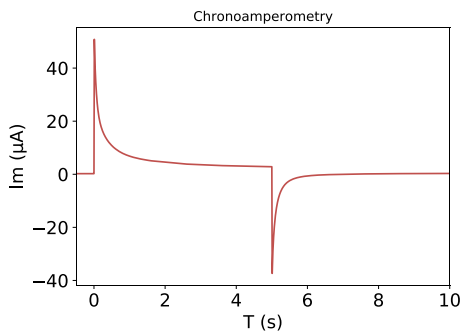
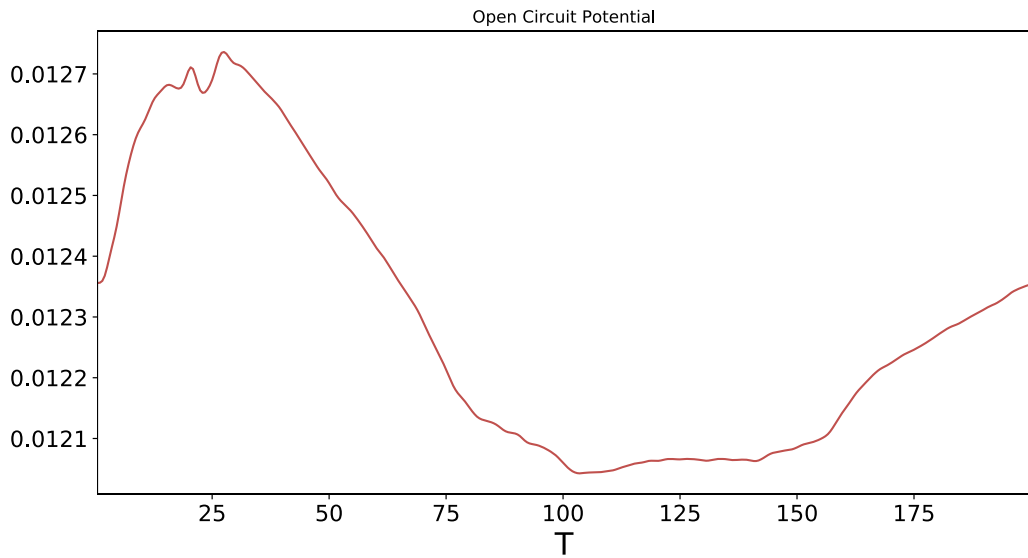
Appendix 28. Conductometric data for a sensor surface after inoculation with 0.4 micromolar c-Myc exon 2



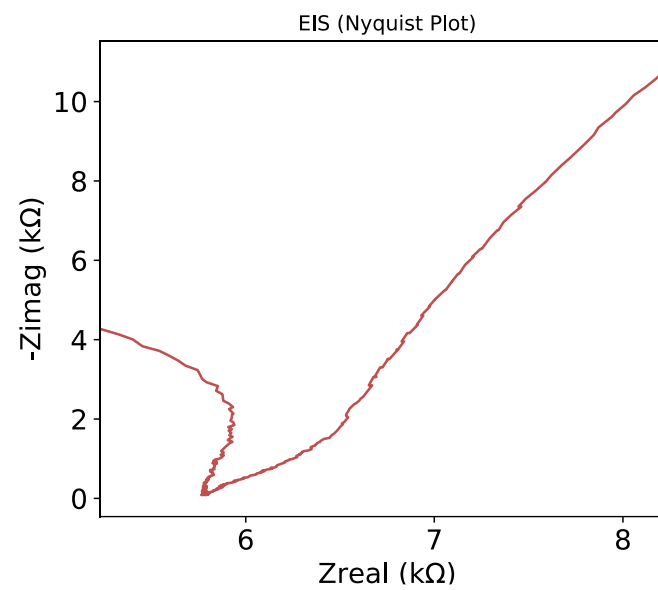
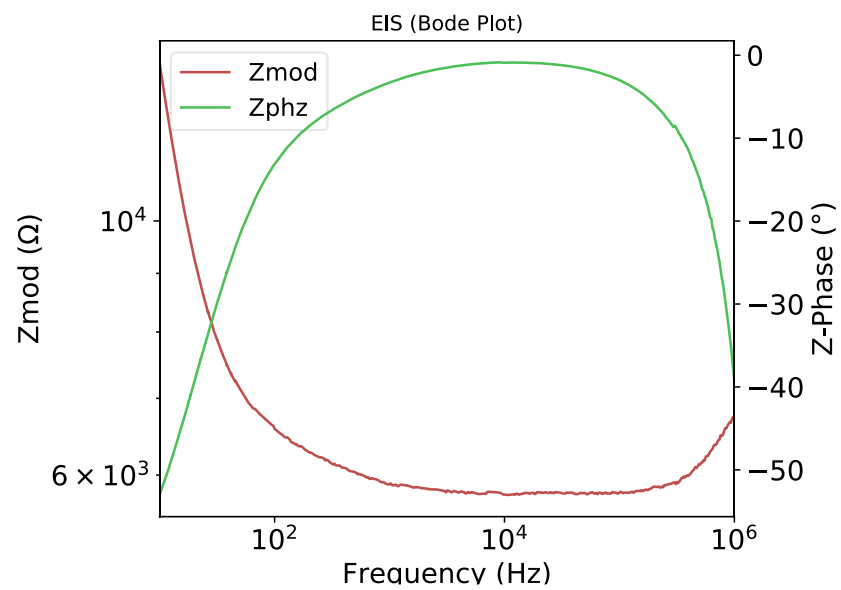
Appendix 29. Conductometric data for a sensor surface before inoculation with 0.2 micromolar c-Myc exon 2



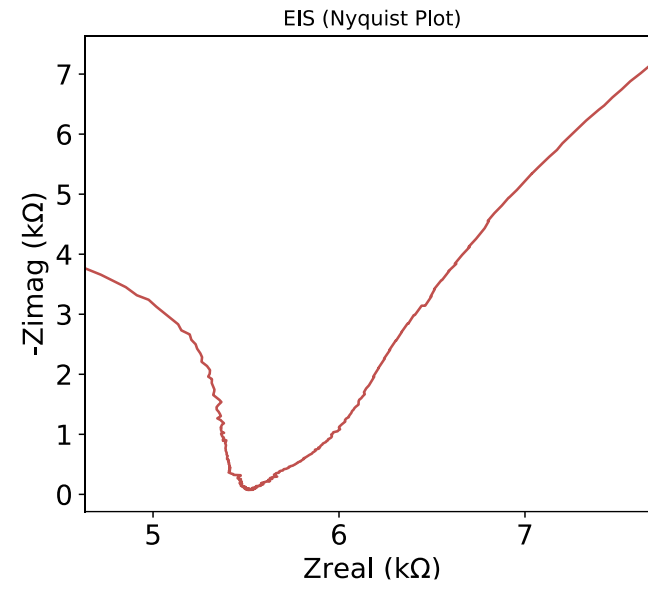
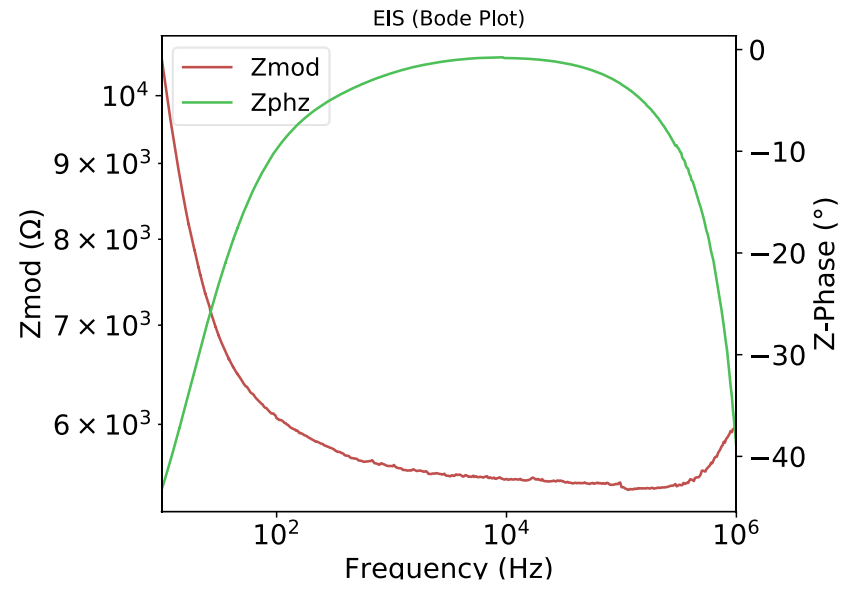
Appendix 30. Conductometric data for a sensor surface after inoculation with 0.2 micromolar c-Myc exon 2



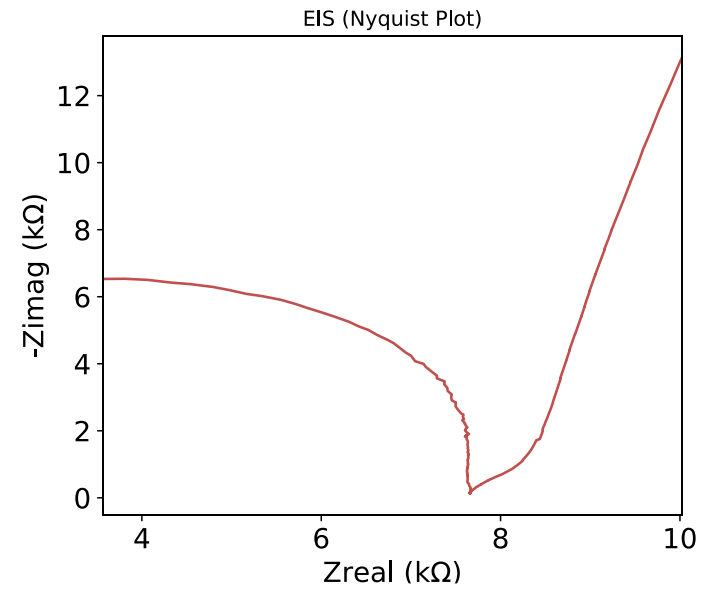
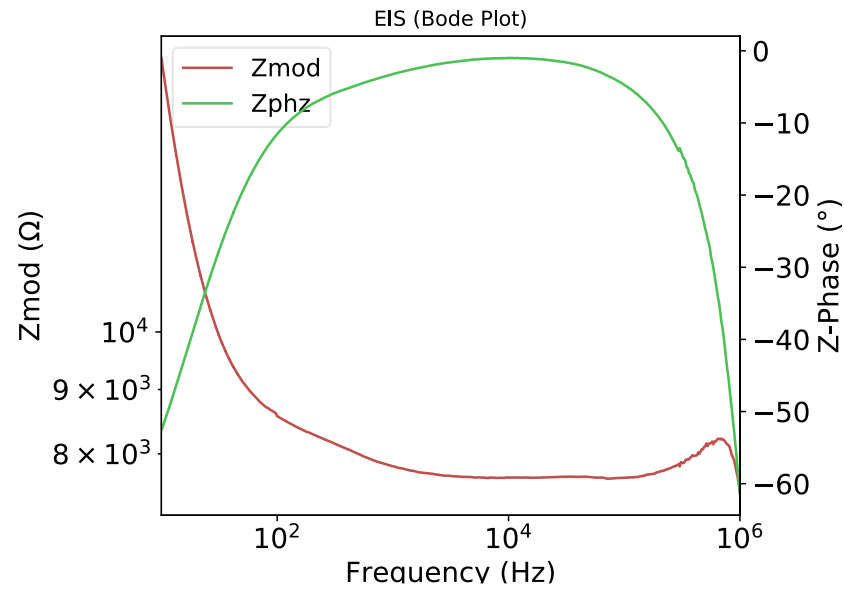
Appendix 31. EIS plots for the batch 1 10 $\mu$ M sensor before inoculation



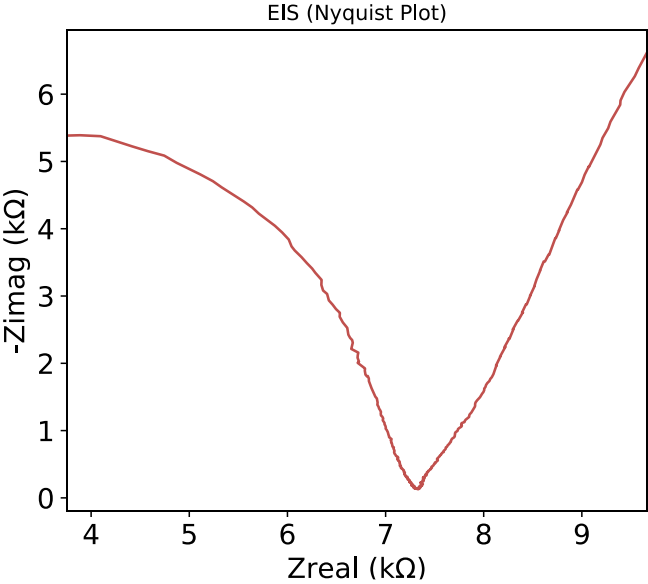
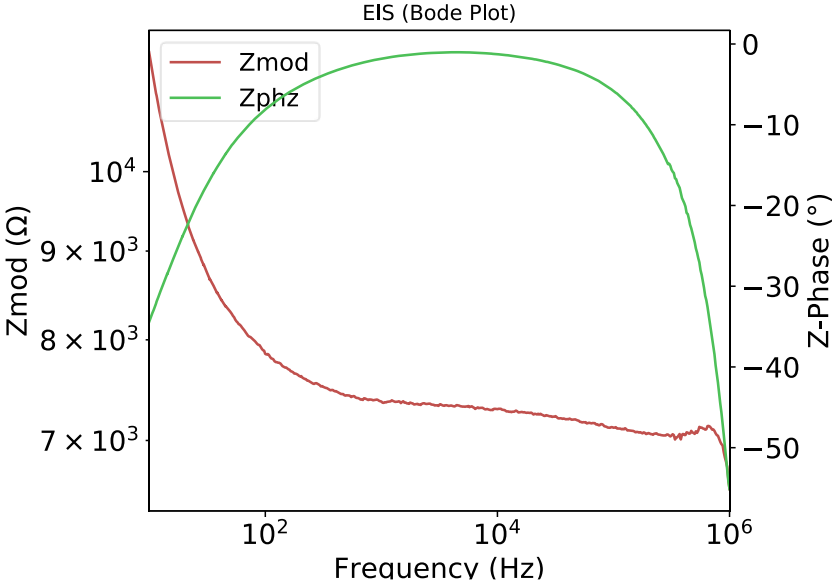
Appendix 32. EIS plots for the batch 1 10 $\mu$ M sensor after inoculation



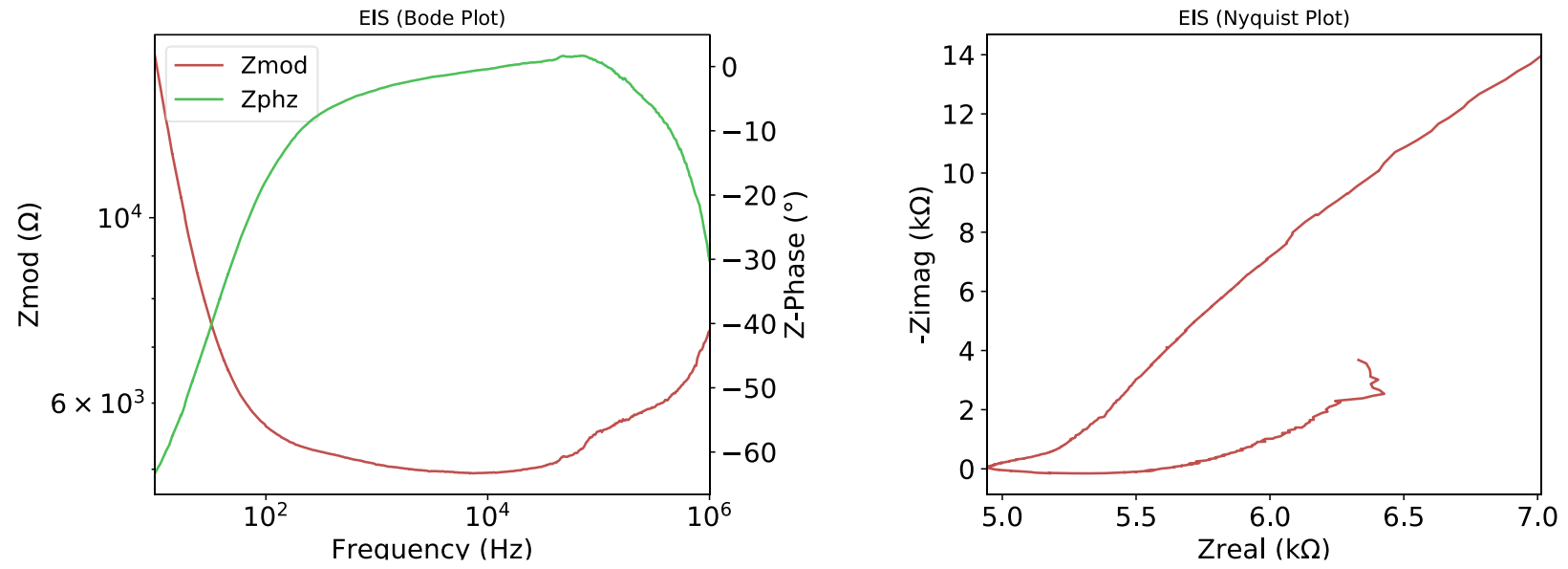
Appendix 33. EIS plots for the batch 1 8 $\mu$ M sensor before inoculation



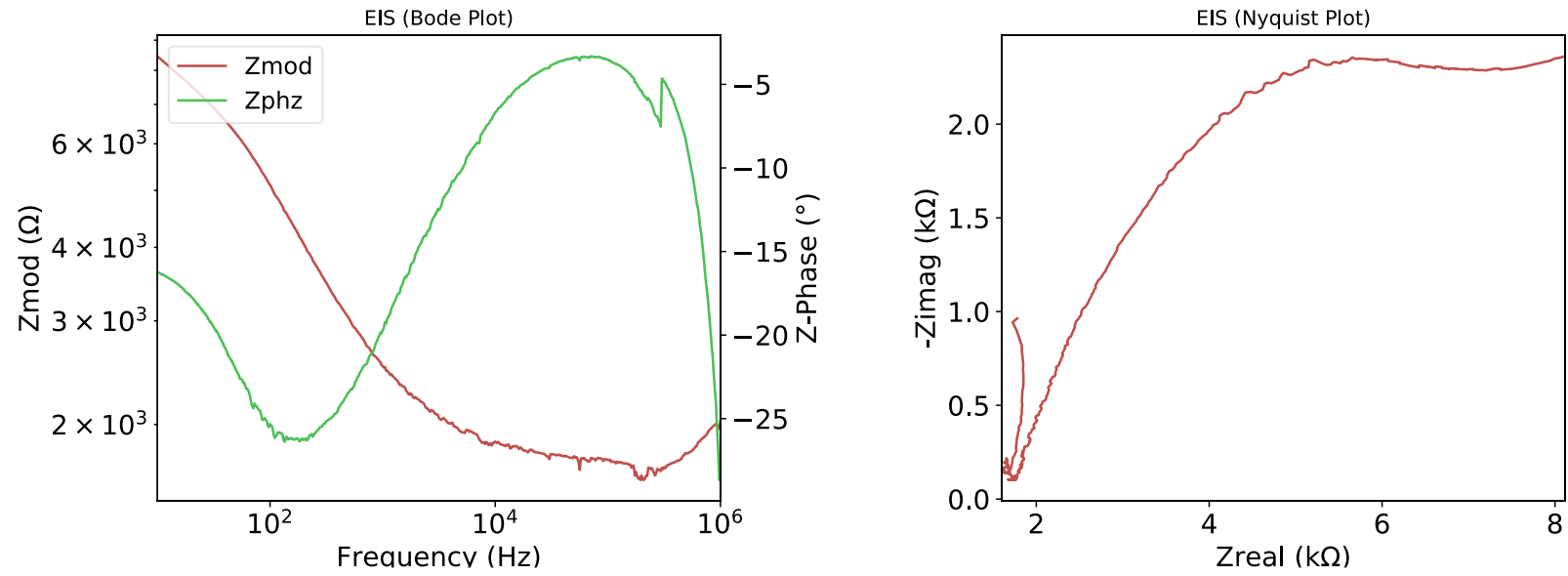
Appendix 34. EIS plots for the batch 1 8 $\mu$ M sensor after inoculation



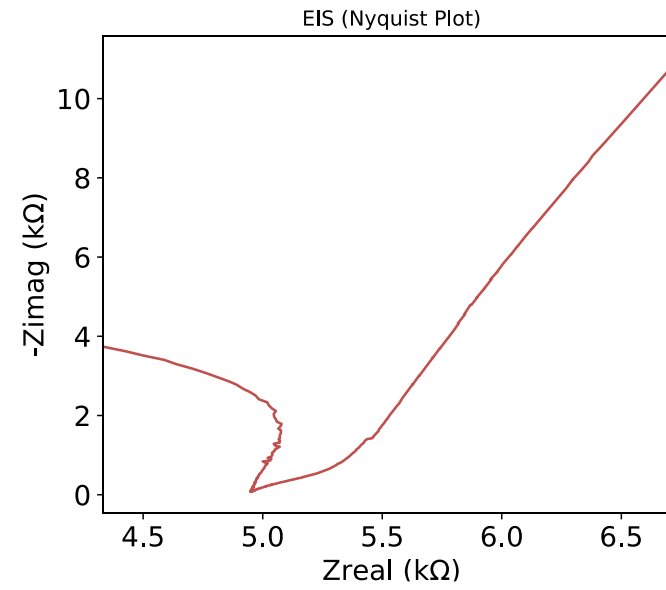
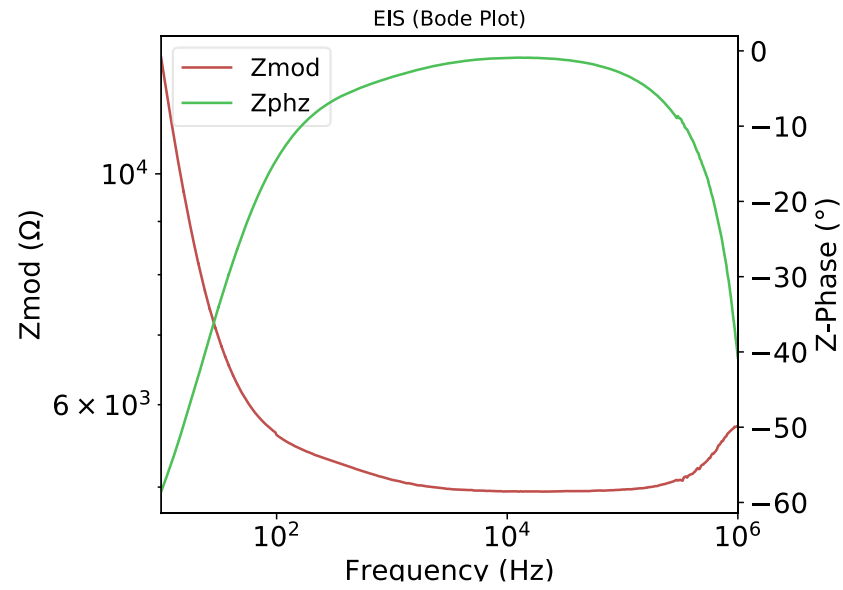
Appendix 35. EIS plots for the batch 1 6 $\mu$ M sensor before inoculation



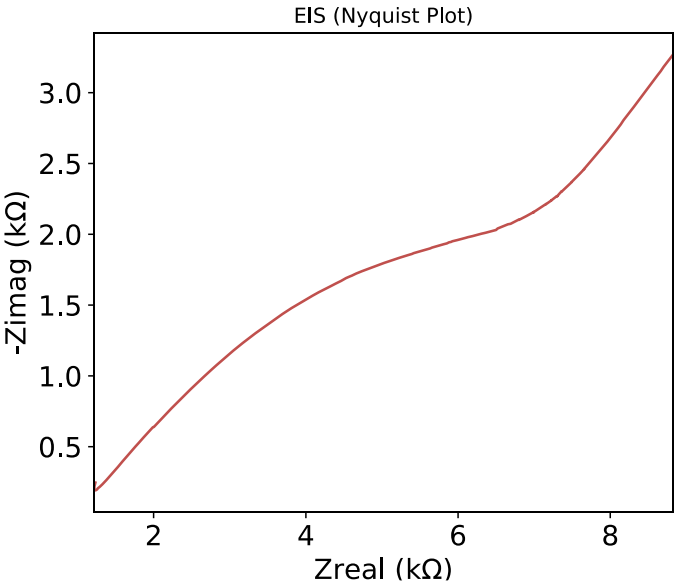
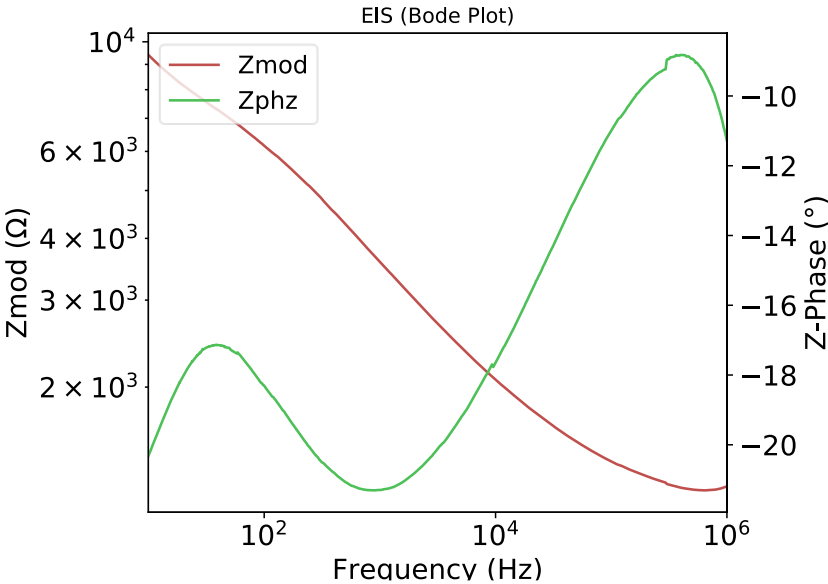
Appendix 36. EIS plots for the batch 1 6 $\mu$ M sensor after inoculation



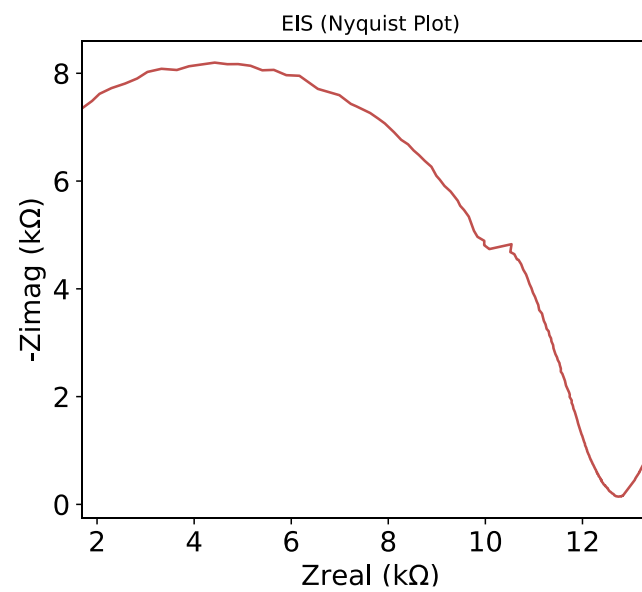
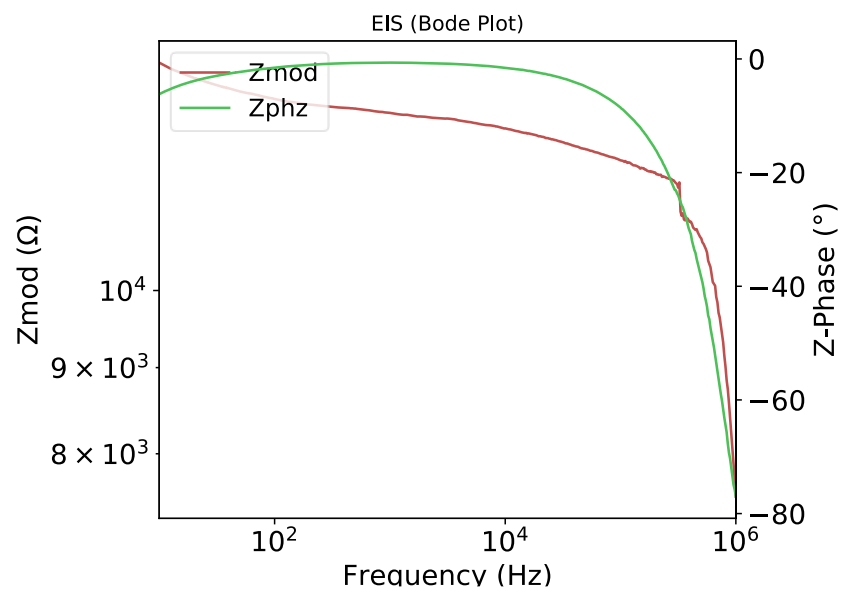
Appendix 37. EIS plots for the batch 1 4 $\mu$ M sensor before inoculation



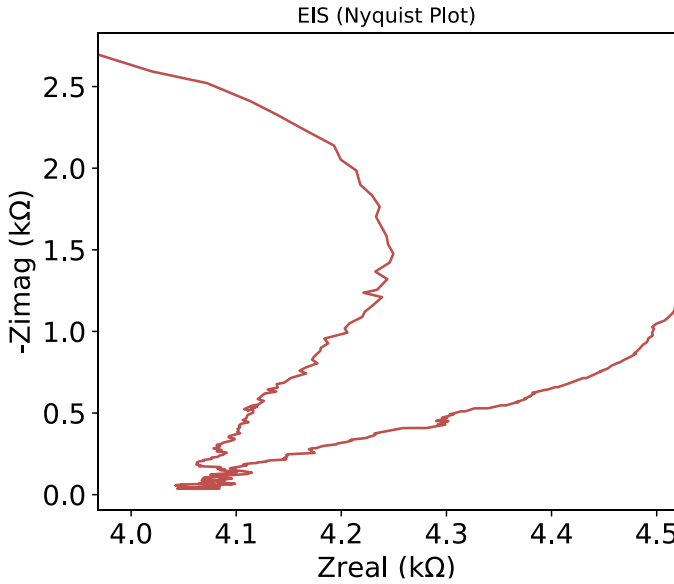
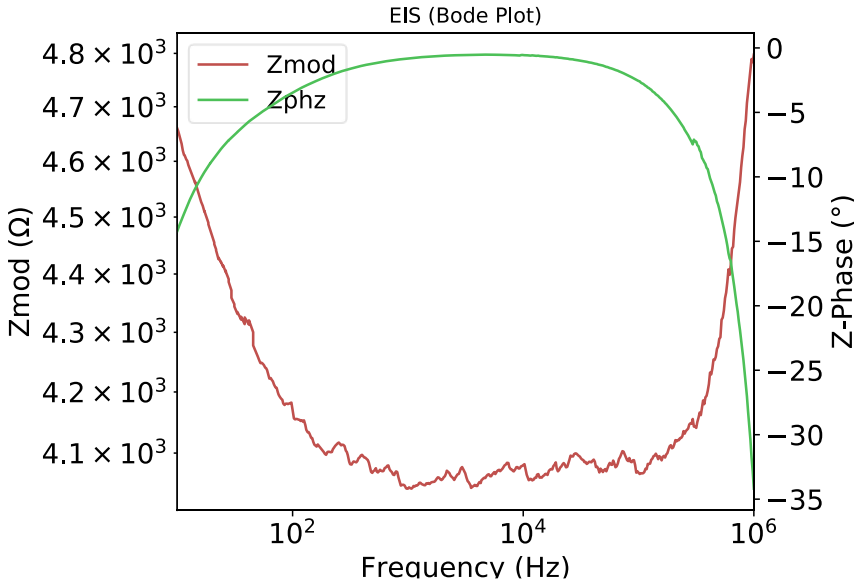
Appendix 38. EIS plots for the batch 1 4  $\mu$ M sensor after inoculation



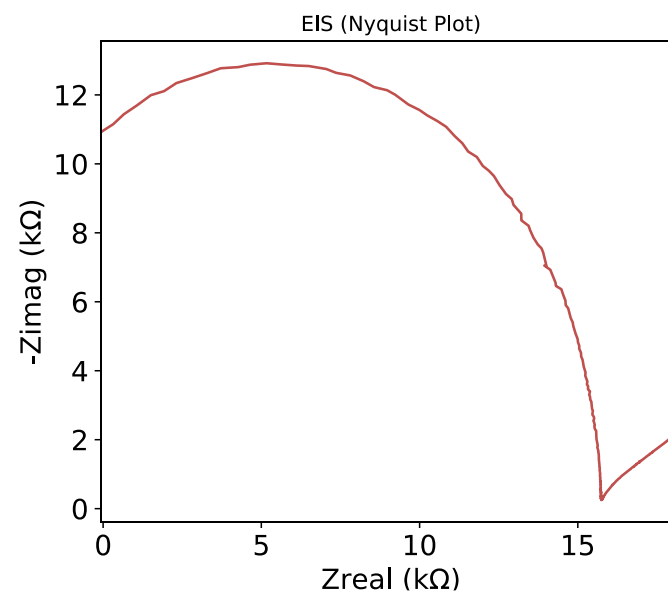
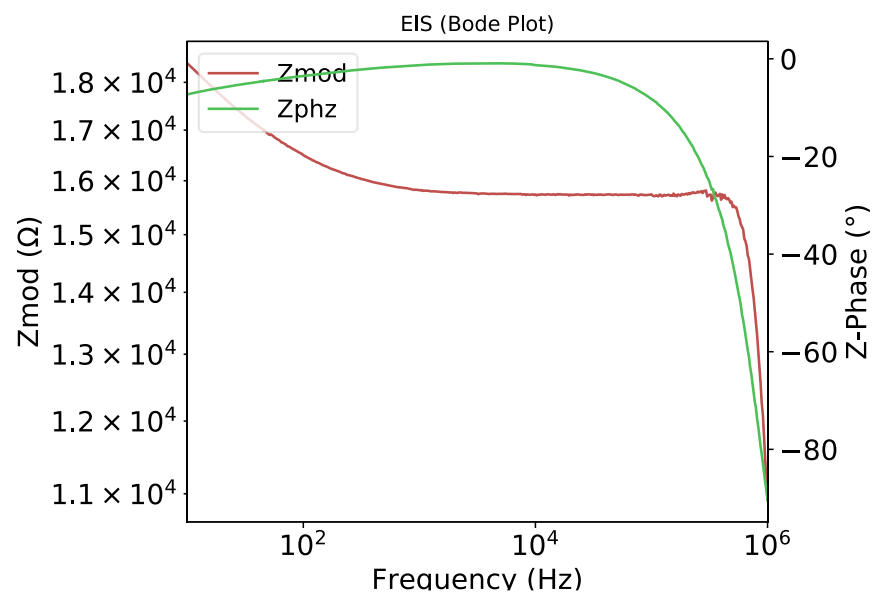
Appendix 39. EIS plots for the batch 1 3 $\mu$ M sensor before inoculation



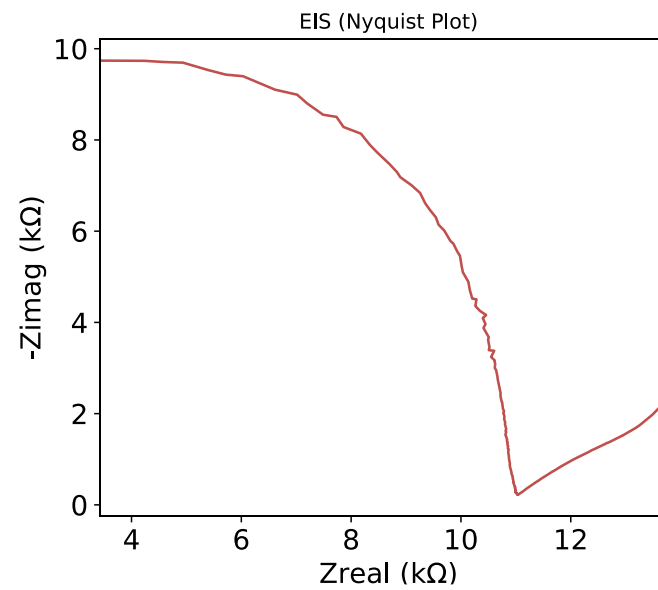
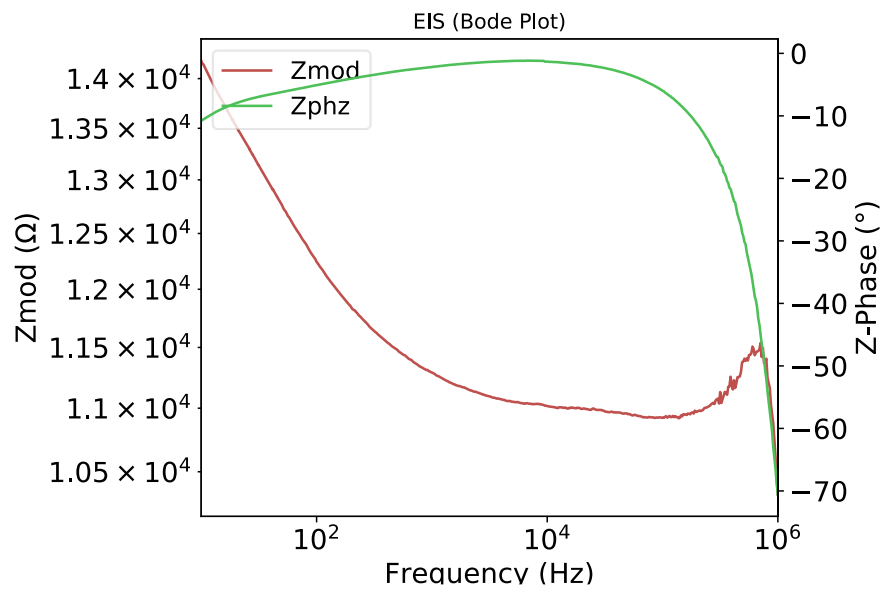
Appendix 40. EIS plots for the batch 1 3  $\mu\text{M}$  sensor after inoculation



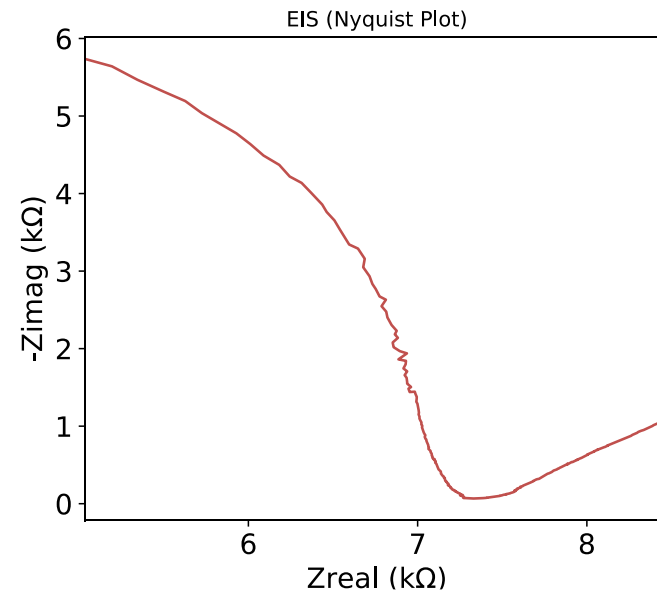
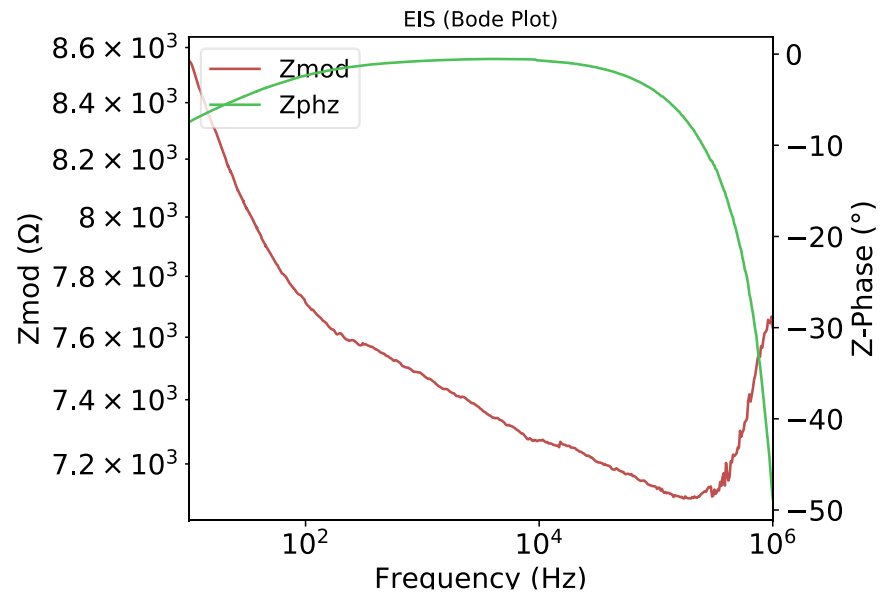
Appendix 41. EIS plots for the batch 2 10 $\mu$ M sensor before inoculation



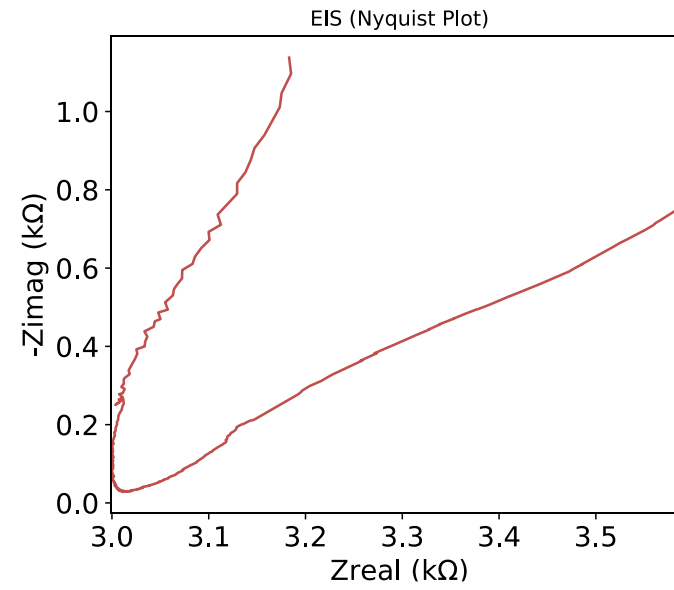
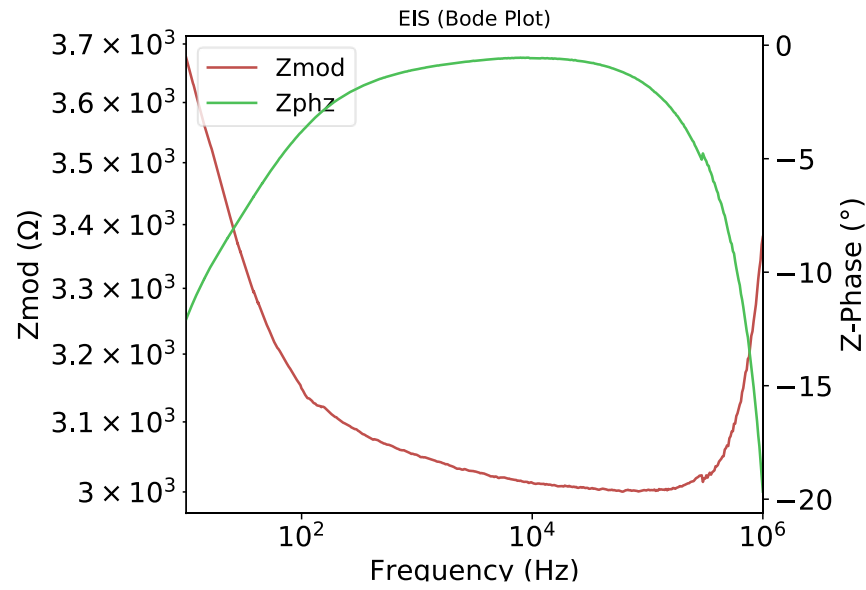
Appendix 42. EIS plots for the batch 2 10 $\mu$ M sensor after inoculation



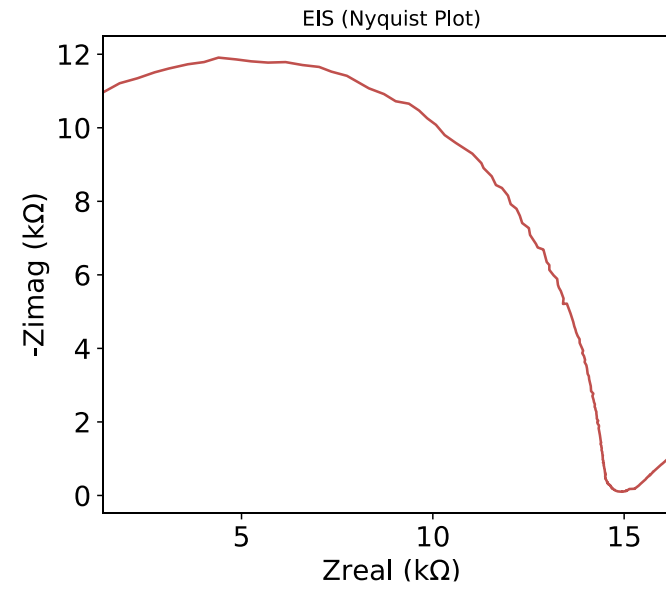
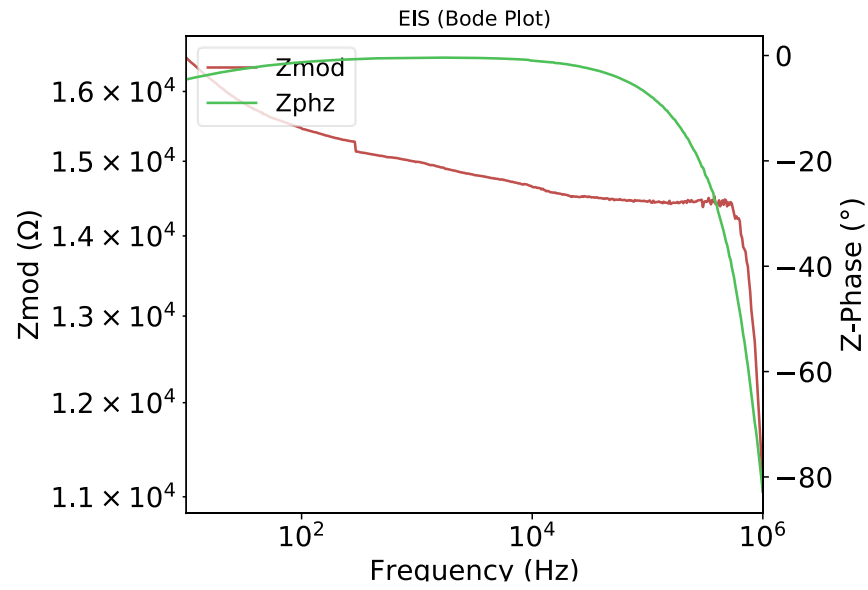
Appendix 43. EIS plots for the batch 2 8 $\mu$ M sensor before inoculation



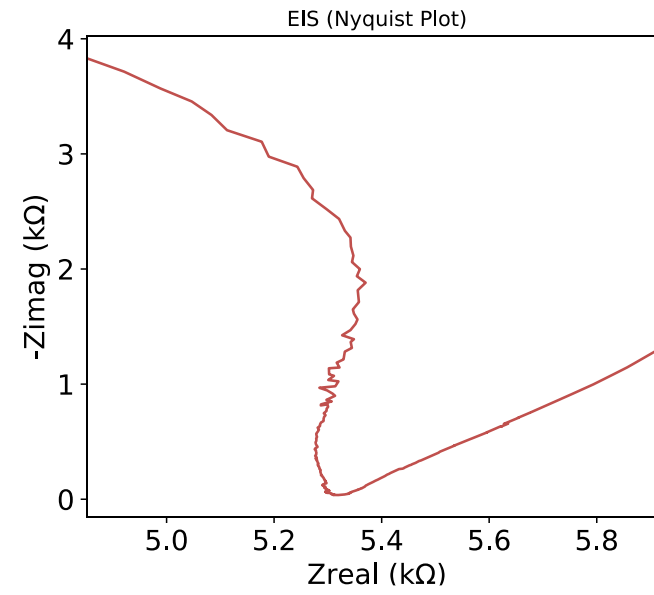
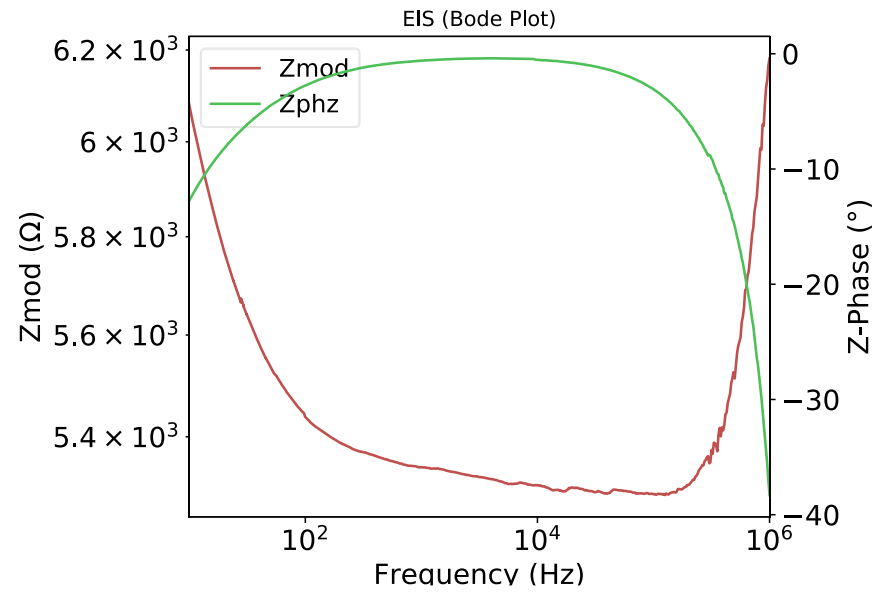
Appendix 44. EIS plots for the batch 2 8 $\mu$ M sensor after inoculation



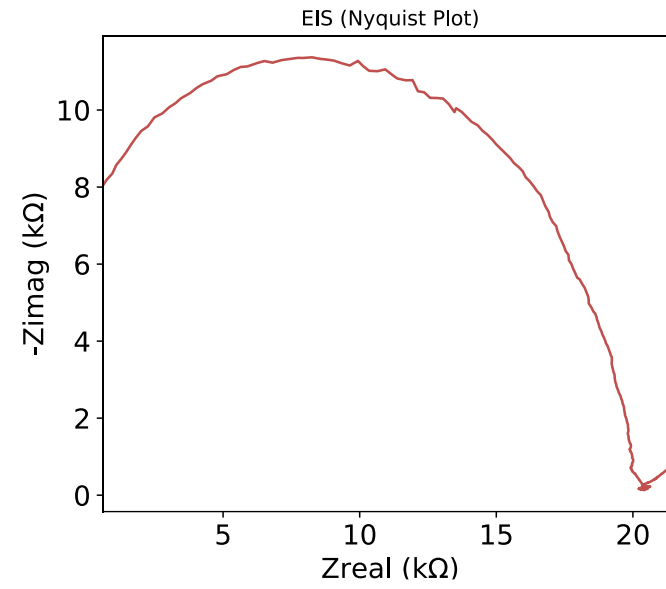
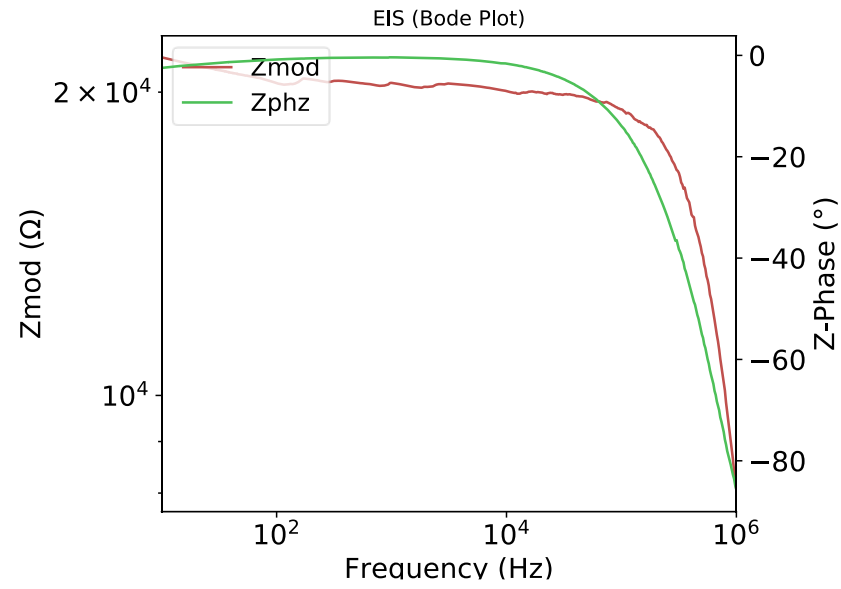
Appendix 45. EIS plots for the batch 2 6 $\mu$ M sensor before inoculation



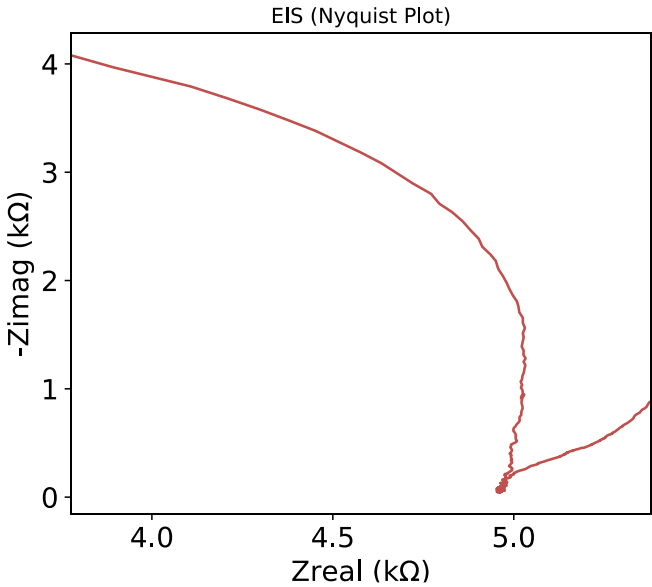
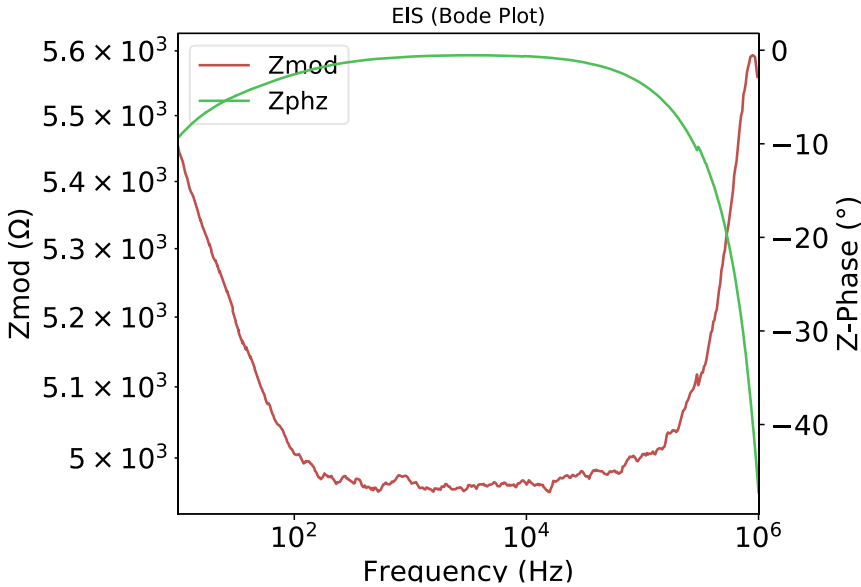
Appendix 46. EIS plots for the batch 2 6 $\mu$ M sensor after inoculation



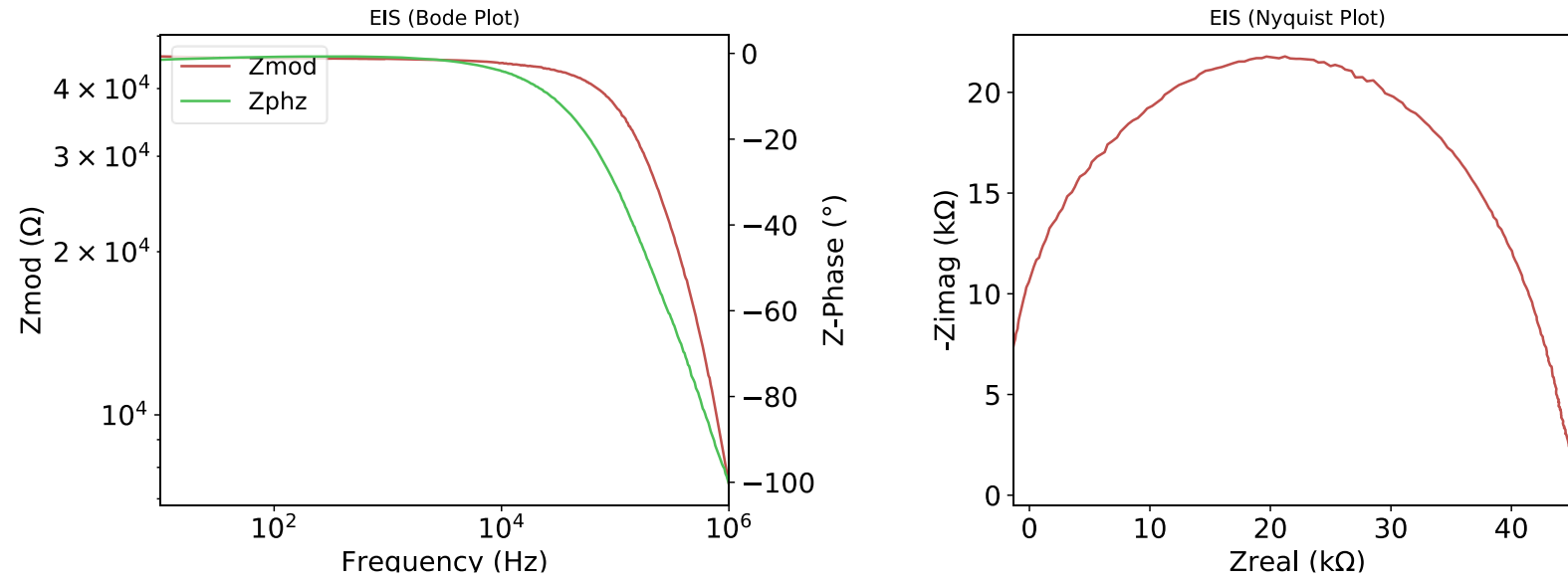
Appendix 47. EIS plots for the batch 2 4 $\mu$ M sensor before inoculation



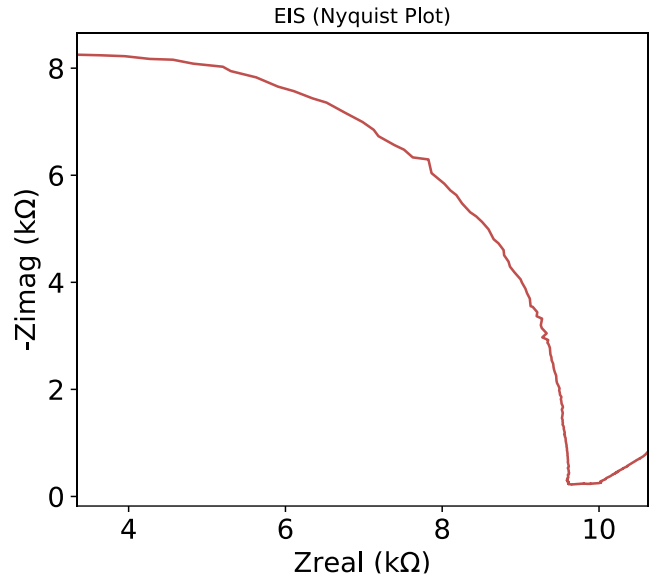
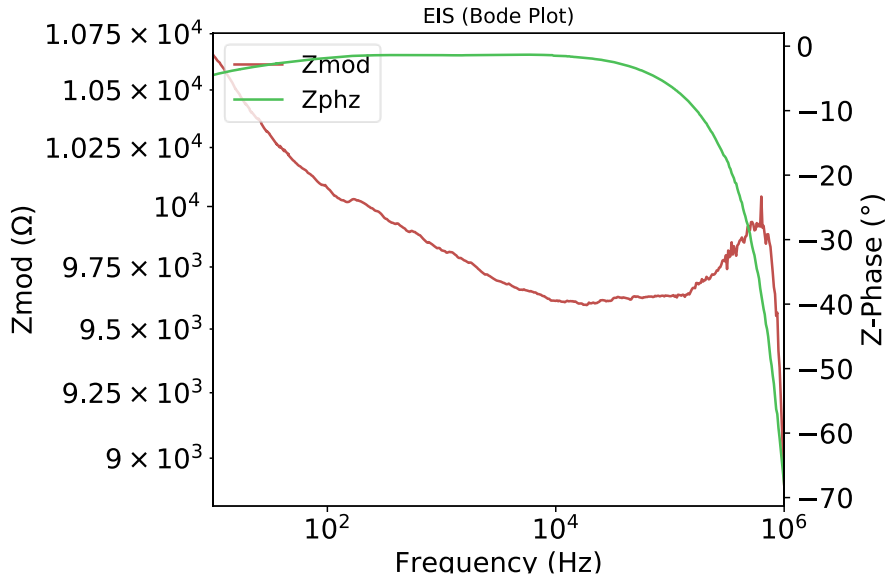
Appendix 48. EIS plots for the batch 2 4 $\mu$ M sensor after inoculation



Appendix 49. EIS plots for the batch 2 3 $\mu$ M sensor before inoculation



Appendix 50. EIS plots for the batch 2 3  $\mu$ M sensor after inoculation



Appendix 51. A table showing the compiled EIS data for the dose-response curve experiment

Batch	Batch 1					Batch 2					Repeats	
Conc ( $\mu\text{m}$ )	3	4	6	8	10	3	4	6	8	10	4	8
<b>Rs_1 (after) (<math>\Omega</math>)</b>	5.39E+03	1.01E+04	3.62E+03	2.84E+04	2.07E+04	1.56E+04	1.35E+04	1.14E+04	4.18E+03	3.14E+04	9.88E+03	1.34E+04
<b>Rct_1 (after) (<math>\Omega</math>)</b>	5.88E-02	3.81E+03	3.64E+02	7.04E+02	6.51E+04	1.41E+04	1.10E+03	7.22E-01	9.90E-02	1.33E+04	3.81E+00	2.37E+03
<b>Cdl_1 (after) (F)</b>	1.23E-05	3.74E-06	5.07E-08	5.89E-08	2.01E-06	1.23E-03	4.24E-09	2.14E-11	1.68E-05	2.73E-10	7.71E-07	1.54E-04
<b>W_1 (after) (S<math>\sqrt{s}</math>)</b>	1.36E-05	3.98E-05	2.91E-06	2.01E-06	-1.24E-06	4.92E-05	2.92E-05	-1.90E-08	1.69E-05	6.97E-07	2.33E-05	-1.90E-05
<b>Rs_2 (after) (<math>\Omega</math>)</b>	9.15E-02	1.42E+03	9.39E+02	3.44E+01	9.22E+03	2.24E+04	4.73E+03	1.23E+04	1.05E-02	5.26E+00	1.01E-01	5.73E-06
<b>Cdl_2 (after) (F)</b>	2.03E-11	7.80E-10	3.79E-11	1.97E-11	8.73E-07	3.07E-09	1.10E-05	3.74E-09	1.95E-11	2.11E-11	2.68E-11	2.49E-11
<b>Rct_2 (after) (<math>\Omega</math>)</b>	6.91E+03	4.39E+02	3.18E+03	1.18E+05	3.44E+04	2.80E+03	1.64E+00	1.56E+03	1.47E+02	1.30E+01	2.70E+00	8.79E+00
<b>W_2 (after) (S<math>\sqrt{s}</math>)</b>	-2.90E-09	3.09E-06	2.14E-06	9.87E-09	3.09E-07	1.05E-05	5.50E-05	2.88E-05	-1.24E-08	-1.85E-08	-1.91E-08	-1.23E-08
<b>Rs_3 (after) (<math>\Omega</math>)</b>	1.64E+04	9.49E+03	1.18E+04	9.96E+03	1.56E+00	1.14E-02	7.77E-02	8.59E+03	1.03E+04	1.39E+04	9.63E+03	4.77E+04
<b>Rct_3 (after) (<math>\Omega</math>)</b>	8.82E+00	1.05E+02	1.21E+01	6.74E+03	4.16E+04	1.01E+03	1.46E+01	2.80E+04	1.27E+02	6.08E+04	7.00E+02	1.80E-05
<b>Cdl_3 (after) (F)</b>	1.76E-07	4.46E-10	3.70E-05	1.68E-06	1.64E-11	2.11E-11	2.26E-11	6.25E-06	1.51E-08	5.33E-06	2.56E-05	6.03E-07

Batch	Batch 1					Batch 2					Repeats	
Conc ( $\mu\text{m}$ )	3	4	6	8	10	3	4	6	8	10	4	8
W_3 (after) (S√s)	7.46E-06	8.73E-08	-1.27E-04	4.40E-06	9.52E-07	-1.26E-08	-1.67E-08	5.95E-05	1.03E-05	-4.06E-06	3.50E-05	2.23E-06
Rs_1 (err) ( $\Omega$ )	8.70E+04	3.29E+02	6.03E+03	1.80E+05	7.76E+04	6.36E+04	1.89E+05	1.38E+03	1.67E+04	4.34E+03	5.50E+05	4.53E+04
Rct_1 (err) ( $\Omega$ )	1.62E+11	3.29E+03	1.57E+04	2.84E+05	4.47E+05	8.85E+09	3.08E+04	2.23E+08	2.29E+10	3.22E+03	5.78E+05	6.47E+06
Cdl_1 (err) (F)	3.00E+01	9.10E-07	1.34E-07	1.64E-06	9.50E-06	8.50E-01	1.11E-07	8.00E-08	6.50E+00	6.88E-11	3.69E-04	1.47E-02
W_1 (err) (S√s)	1.18E-04	3.32E-05	7.44E-06	2.77E-05	6.44E-06	9.51E+01	9.30E-04	1.03E-08	1.49E-04	1.85E-07	1.60E-03	3.89E-02
Rs_2 (err) ( $\Omega$ )	6.76E+04	5.07E+02	7.03E+03	8.27E+03	6.97E+03	1.31E+05	2.29E+04	3.11E+05	4.03E+03	9.25E+02	7.47E+02	3.50E+02
Cdl_2 (err) (F)	1.30E-09	6.54E-10	1.84E-10	7.77E-12	5.89E-06	3.68E-08	6.03E-02	1.91E-07	1.90E-09	3.17E-09	1.70E-08	2.93E-09
Rct_2 (err) ( $\Omega$ )	1.47E+08	8.12E+02	1.23E+04	3.07E+05	6.87E+07	3.52E+04	1.99E+07	8.47E+04	1.22E+07	9.29E+06	4.65E+07	1.92E+07
W_2 (err) (S√s)	3.55E-08	9.59E-07	9.08E-06	3.71E-08	1.96E-05	1.43E-04	5.62E-04	1.67E-03	3.58E-08	7.90E-09	6.35E-09	1.22E-09
Rs_3 (err) ( $\Omega$ )	8.00E+05	1.84E+04	3.55E+03	2.25E+04	3.11E+02	9.18E+02	2.37E+03	1.53E+05	1.00E+05	3.59E+02	5.22E+05	5.78E+05
Rct_3 (err) ( $\Omega$ )	1.09E+07	3.22E+07	7.47E+05	1.85E+05	3.26E+05	3.38E+05	3.66E+07	2.32E+06	2.00E+03	8.91E+04	1.98E+07	1.43E+12
Cdl_3 (err) (F)	5.99E-04	2.45E-07	1.24E-02	2.39E-06	4.04E-13	5.76E-11	1.02E-08	1.94E-04	3.86E-07	6.69E-07	2.15E-02	7.13E+00

Batch	Batch 1					Batch 2					Repeats	
Conc ( $\mu\text{m}$ )	3	4	6	8	10	3	4	6	8	10	4	8
W_3 (err) (S√s)	5.34E-04	1.07E-06	1.36E-03	2.07E-05	1.51E-05	4.96E-09	2.33E-08	3.02E-03	1.58E-04	1.88E-05	3.69E-03	4.79E-05
Goodness of fit (after)	1.98E-05	4.49E-05	1.11E-04	4.82E-06	1.36E-03	2.52E-03	3.69E-04	8.40E-04	3.03E-04	2.51E-03	1.34E-03	2.51E-03
Rs_1 (before) ( $\Omega$ )	5.97E+04	4.26E-02	1.91E+04	8.58E-02	1.14E+04	1.69E-03	1.26E+04	6.59E+04	1.13E+04	5.07E+04	2.12E+04	6.73E-03
Rct_1 (before) ( $\Omega$ )	9.57E+03	2.21E+04	9.50E+03	4.28E+04	8.91E-01	1.86E-03	1.76E+03	7.59E+03	4.64E-05	1.54E+04	9.46E+04	6.66E-01
Cdl_1 (before) (F)	2.80E-07	1.55E-11	4.77E-07	1.60E-11	8.00E-07	2.48E-11	2.55E-05	5.05E-10	3.91E-05	3.25E-10	9.83E-04	2.95E-11
W_1 (before) (S√s)	6.61E-06	2.04E-06	-2.29E-06	8.47E-07	-1.16E-06	-9.43E-09	2.56E-05	6.17E-07	-1.06E-06	1.03E-06	-1.23E-03	-2.42E-08
Rs_2 (before) ( $\Omega$ )	8.87E+01	9.42E+03	5.73E+04	1.45E+04	7.52E+03	9.19E+04	2.11E+04	1.74E+04	1.98E+04	1.98E+04	6.50E-02	4.18E+04
Cdl_2 (before) (F)	1.78E-11	9.47E-07	1.74E-11	7.24E-07	2.37E-11	7.04E-11	4.52E-09	2.14E-05	8.20E-09	8.55E-06	2.73E-11	6.21E-11
Rct_2 (before) ( $\Omega$ )	1.44E+05	1.92E+04	1.63E+04	9.77E+03	2.25E+04	1.35E+05	1.86E+03	3.34E-05	7.44E+02	6.54E+03	1.47E+00	1.20E+05
W_2 (before) (S√s)	2.14E-08	-5.18E-07	-1.63E-08	-7.32E-07	3.04E-06	8.13E-07	1.58E-05	-9.61E-06	7.47E-06	1.51E-04	-2.29E-08	6.45E-08

Batch	Batch 1					Batch 2					Repeats	
Conc ( $\mu\text{m}$ )	3	4	6	8	10	3	4	6	8	10	4	8
<b>Rs_3 (before) (<math>\Omega</math>)</b>	1.65E+04	1.91E+04	6.71E+03	2.53E+04	1.93E+04	5.36E+04	2.81E-03	3.84E-06	1.13E-06	1.37E+00	4.37E+04	2.27E+04
<b>Rct_3 (before) (<math>\Omega</math>)</b>	4.43E-01	1.14E+05	3.57E+03	1.02E+04	1.71E+03	7.06E-01	5.18E+02	1.40E+02	4.50E-02	1.53E+03	7.75E+04	2.91E+03
<b>Cdl_3 (before) (F)</b>	1.08E-05	2.23E-07	4.62E-07	2.22E-07	7.92E-08	1.96E-05	2.10E-11	1.87E-11	1.76E-11	1.99E-11	5.85E-11	1.26E-05
<b>W_3 (before) (<math>S\sqrt{s}</math>)</b>	1.02E-05	8.77E-07	5.74E-06	2.47E-06	2.82E-06	-2.06E-06	-1.40E-08	-1.17E-08	-5.64E-09	-1.41E-08	7.03E-08	3.06E-04
<b>Rs_1 (err) (<math>\Omega</math>)</b>	9.90E+07	8.74E+03	1.41E+04	5.45E+03	2.32E+04	1.06E+02	9.39E+05	1.30E+04	7.37E+03	1.53E+04	1.75E+02	5.13E+02
<b>Rct_1 (err) (<math>\Omega</math>)</b>	3.17E+07	5.17E+04	3.62E+03	2.48E+05	3.35E+10	3.70E+10	3.31E+06	8.66E+03	9.13E+14	1.42E+04	2.95E+10	9.76E+07
<b>Cdl_1 (err) (F)</b>	8.97E-04	1.24E-11	2.72E-07	4.33E-12	4.52E-02	3.29E-06	6.12E-04	7.59E-10	1.02E+03	2.94E-10	3.21E-02	5.71E-08
<b>W_1 (err) (<math>S\sqrt{s}</math>)</b>	2.40E-02	9.54E-06	5.26E-07	1.02E-05	7.76E-06	1.01E-09	5.07E-03	3.14E-07	9.66E-04	1.15E-06	4.42E+05	1.02E-08
<b>Rs_2 (err) (<math>\Omega</math>)</b>	3.77E+03	7.53E+04	1.83E+04	7.97E+04	1.73E+04	7.30E+05	2.63E+06	7.61E+02	2.19E+04	2.73E+03	6.18E+02	1.20E+04
<b>Cdl_2 (err) (F)</b>	1.87E-12	5.77E-06	3.42E-12	3.45E-06	1.10E-10	1.10E-09	1.13E-06	5.54E+02	3.57E-08	8.13E-06	2.98E-08	1.78E-11
<b>Rct_2 (err) (<math>\Omega</math>)</b>	8.45E+04	8.43E+05	6.04E+03	4.29E+05	2.54E+05	3.67E+06	4.84E+05	6.00E+12	2.45E+03	2.84E+04	5.69E+07	5.88E+04

Batch	Batch 1					Batch 2					Repeats	
Conc ( $\mu\text{m}$ )	3	4	6	8	10	3	4	6	8	10	4	8
W_2 (err) (S $\sqrt{s}$ )	4.48E-08	1.44E-05	2.79E-09	7.27E-06	6.52E-05	2.32E-05	4.27E-03	1.52E-04	1.92E-05	4.85E-03	1.21E-08	1.78E-08
Rs_3 (err) ( $\Omega$ )	7.61E+06	3.38E+05	1.76E+03	3.21E+05	1.78E+05	2.46E+05	9.60E+02	8.99E+02	2.44E+03	8.37E+02	1.67E+04	2.45E+02
Rcl_3 (err) ( $\Omega$ )	1.55E+10	8.14E+06	6.71E+03	4.71E+05	4.30E+04	2.36E+13	5.09E+05	2.78E+06	2.07E+11	1.18E+05	3.75E+04	7.32E+03
Cdl_3 (err) (F)	1.61E+00	5.47E-06	1.46E-07	2.70E-06	1.56E-06	1.00E+02	1.04E-10	3.81E-10	6.57E-06	2.71E-11	2.00E-11	7.43E-06
W_3 (err) (S $\sqrt{s}$ )	1.36E-02	2.05E-05	1.13E-06	1.37E-05	5.48E-05	1.49E-03	5.52E-09	5.10E-09	1.05E-08	4.55E-09	1.29E-08	6.28E-03
Goodness of fit (before)	1.19E-05	5.51E-05	4.57E-04	7.95E-05	5.55E-05	2.45E-03	1.50E-03	3.81E-03	1.43E-03	4.59E-03	8.68E-04	2.49E-03
Rs_1 (diff) ( $\Omega$ )	-5.43E+04	1.01E+04	-1.54E+04	2.84E+04	9.34E+03	1.56E+04	9.30E+02	-6.59E+04	-7.08E+03	-1.93E+04	-1.13E+04	1.34E+04
Rct_1(diff) ( $\Omega$ )	-9.57E+03	-1.82E+04	-9.14E+03	-4.21E+04	6.51E+04	1.41E+04	-6.59E+02	-7.59E+03	9.89E-02	-2.11E+03	-9.46E+04	2.37E+03
Cdl_1 (diff) (F)	1.20E-05	3.74E-06	-4.26E-07	5.89E-08	1.21E-06	1.23E-03	-2.55E-05	-4.84E-10	-2.23E-05	-5.21E-11	-9.82E-04	1.53E-04
W_1 (diff) (S $\sqrt{s}$ )	6.99E-06	3.77E-05	5.21E-06	1.16E-06	-7.70E-08	4.92E-05	3.68E-06	-6.36E-07	1.79E-05	-3.32E-07	1.25E-03	-1.89E-05
Rs_2 (diff) ( $\Omega$ )	-8.86E+01	-8.00E+03	-5.63E+04	-1.44E+04	1.70E+03	-6.95E+04	-1.64E+04	-5.18E+03	-1.98E+04	-1.98E+04	3.65E-02	-4.18E+04
Cdl_2 (diff) (F)	2.52E-12	-9.46E-07	2.06E-11	-7.23E-07	8.72E-07	2.99E-09	1.10E-05	-2.14E-05	-8.18E-09	-8.55E-06	-4.90E-13	-3.72E-11

Batch	Batch 1					Batch 2					Repeats	
Conc ( $\mu\text{m}$ )	3	4	6	8	10	3	4	6	8	10	4	8
<b>Rct_2 (diff) (<math>\Omega</math>)</b>	-1.37E+05	-1.87E+04	-1.31E+04	1.08E+05	1.19E+04	-1.32E+05	-1.86E+03	1.56E+03	-5.97E+02	-6.53E+03	1.23E+00	-1.20E+05
<b>W_2 (diff) (<math>\text{S}\sqrt{\text{s}}</math>)</b>	-2.43E-08	3.61E-06	2.16E-06	7.41E-07	-2.73E-06	9.73E-06	3.92E-05	3.84E-05	-7.48E-06	-1.51E-04	3.77E-09	-7.68E-08
<b>Rs_3 (diff) (<math>\Omega</math>)</b>	-1.70E+02	-9.60E+03	5.09E+03	-1.53E+04	-1.93E+04	-5.36E+04	7.49E-02	8.58E+03	1.03E+04	1.39E+04	-3.41E+04	2.51E+04
<b>Rct_3 (diff) (<math>\Omega</math>)</b>	8.38E+00	-1.14E+05	-3.56E+03	-3.49E+03	3.99E+04	1.01E+03	-5.03E+02	2.79E+04	1.27E+02	5.93E+04	-7.68E+04	-2.91E+03
<b>Cdl_3 (diff) (F)</b>	-1.06E-05	-2.22E-07	3.65E-05	1.46E-06	-7.92E-08	-1.96E-05	1.62E-12	6.24E-06	1.51E-08	5.33E-06	2.56E-05	-1.20E-05
<b>W_3 (diff) (<math>\text{S}\sqrt{\text{s}}</math>)</b>	-2.73E-06	-7.90E-07	-1.32E-04	1.94E-06	-1.86E-06	2.05E-06	-2.69E-09	5.95E-05	1.03E-05	-4.05E-06	3.49E-05	-3.04E-04
<b>R-total (after) (<math>\Omega</math>)</b>	2.87E+04	2.53E+04	1.99E+04	1.64E+05	1.71E+05	5.59E+04	1.94E+04	5.04E+04	1.48E+04	1.19E+05	2.02E+04	6.35E+04
<b>R-total (before) (<math>\Omega</math>)</b>	2.30E+05	1.84E+05	1.12E+05	1.03E+05	6.23E+04	1.46E+05	3.60E+04	9.10E+04	3.11E+04	8.74E+04	2.37E+05	6.74E+04
<b>R-total (diff) (<math>\Omega</math>)</b>	-2.01E+05	-1.58E+05	-9.24E+04	6.13E+04	1.09E+05	-2.24E+05	-1.85E+04	-4.06E+04	-1.71E+04	2.55E+04	-2.17E+05	-1.24E+05
<b>C-total (after) (F)</b>	3.74E-06	3.70E-05	1.74E-06	2.88E-06	0.00E+00	1.23E-03	1.10E-05	6.25E-06	1.68E-05	5.33E-06	2.64E-05	1.54E-04
<b>C-total (before) (F)</b>	1.10E-05	1.17E-06	9.39E-07	9.46E-07	8.79E-07	1.96E-05	2.55E-05	2.14E-05	3.91E-05	8.55E-06	9.83E-04	1.26E-05
<b>C-total (diff) (F)</b>	1.41E-06	2.57E-06	3.61E-05	7.96E-07	2.00E-06	1.21E-03	-1.45E-05	-1.52E-05	-2.22E-05	-3.22E-06	-9.57E-04	1.42E-04

Batch	Batch 1					Batch 2					Repeats	
Conc ( $\mu\text{m}$ )	3	4	6	8	10	3	4	6	8	10	4	8
W-total (after) (S $\sqrt{s}$ )	2.11E-05	4.30E-05	-1.22E-04	6.42E-06	2.29E-08	5.97E-05	8.42E-05	8.83E-05	2.71E-05	-3.38E-06	5.82E-05	-1.67E-05
W-total (before) (S $\sqrt{s}$ )	1.68E-05	2.40E-06	3.43E-06	2.58E-06	4.70E-06	-1.26E-06	4.13E-05	-9.01E-06	6.40E-06	1.52E-04	-1.23E-03	3.06E-04
W-total (diff) (S $\sqrt{s}$ )	4.24E-06	4.06E-05	-1.25E-04	3.84E-06	-4.67E-06	6.10E-05	4.29E-05	9.73E-05	2.07E-05	-1.56E-04	1.29E-03	-3.23E-04
Real impedance (before) (k $\Omega$ )	12.76	4.893	4.949	7.659	5.791	45.44	8.247	14.89	7.328	15.75	20.4	22.13
Real impedance (after) (k $\Omega$ )	4.065	1.233	1.611	7.332	5.476	9.638	3.601	5.316	3.014	11.04	4.961	10.62
Real impedance (diff) (k $\Omega$ )	-8.695	-3.66	-3.338	-0.327	-0.315	-35.802	-4.646	-9.574	-4.314	-4.71	-15.439	-11.51
R-total (%diff) (%)	-87.516	-86.211	-82.272	59.760	174.393	-154.067	-51.324	-44.587	-54.932	29.165	-91.472	-183.725
Real impedance (%diff) (%)	-68.143	-74.801	-67.448	-4.269	-5.439	-78.790	-56.336	-64.298	-58.870	-29.905	-75.681	-52.011

Appendix 52. A table showing the correlation values for linear, quadratic and cubic fits of each dataset against the concentration of the target analyte

Transform	Linear					Quadratic					Cubic				
Fit data	Std. Dev	R <sup>2</sup>	Adj R <sup>2</sup>	Pred R <sup>2</sup>	Press	Std. Dev	R <sup>2</sup>	Adj R <sup>2</sup>	Pred R <sup>2</sup>	Press	Std. Dev	R <sup>2</sup>	Adj R <sup>2</sup>	Pred R <sup>2</sup>	Press
<b>Rs_1 (after)</b>	9.23E+03	0.269	0.187	-0.255	1.31E+09	8.05E+03	0.505	0.381	-0.200	1.26E+09	8.59E+03	0.507	0.296	-0.647	1.73E+09
<b>Rct_1 (after)</b>	1.73E+04	0.239	0.155	-0.744	6.14E+09	1.35E+04	0.584	0.480	-0.662	5.85E+09	1.37E+04	0.625	0.465	-0.972	6.94E+09
<b>Cdl_1 (after)</b>	3.46E-04	0.139	0.044	-0.603	2.00E-06	3.37E-04	0.272	0.090	-0.892	2.36E-06	3.13E-04	0.451	0.216	-1.292	2.87E-06
<b>W_1 (after)</b>	1.48E-05	0.526	0.473	0.162	3.48E-09	1.43E-05	0.607	0.508	0.122	3.65E-09	1.51E-05	0.614	0.449	-0.234	5.13E-09
<b>Rs_2 (after)</b>	7.30E+03	0.067	-0.036	-0.839	9.45E+08	7.37E+03	0.156	-0.055	-1.382	1.22E+09	7.86E+03	0.158	-0.203	-2.257	1.67E+09
<b>Cdl_2 (after)</b>	3.31E-06	0.053	-0.052	-0.555	1.62E-10	3.51E-06	0.054	-0.182	-0.699	1.77E-10	3.53E-06	0.163	-0.196	-0.844	1.92E-10
<b>Rct_2 (after)</b>	3.08E+04	0.133	0.037	-0.551	1.53E+10	3.22E+04	0.157	-0.054	-0.858	1.83E+10	3.17E+04	0.287	-0.019	-1.077	2.05E+10
<b>W_2 (after)</b>	1.62E-05	0.130	0.034	-0.415	3.82E-09	1.69E-05	0.152	-0.060	-0.550	4.19E-09	1.65E-05	0.298	-0.004	-0.554	4.20E-09
<b>Rs_3 (after)</b>	1.35E+04	0.053	-0.052	-0.653	2.85E+09	1.37E+04	0.135	-0.081	-0.825	3.15E+09	1.33E+04	0.281	-0.027	-1.082	3.59E+09
<b>Rct_3 (after)</b>	1.66E+04	0.461	0.401	0.005	4.60E+09	1.39E+04	0.666	0.583	0.272	3.36E+09	1.14E+04	0.804	0.721	0.469	2.45E+09
<b>Cdl_3 (after)</b>	1.32E-05	0.013	-0.097	-0.642	2.61E-09	1.29E-05	0.160	-0.050	-0.825	2.90E-09	1.23E-05	0.333	0.047	-0.686	2.68E-09

Transform	Linear					Quadratic					Cubic				
Fit data	Std. Dev	R <sup>2</sup>	Adj R <sup>2</sup>	Pred R <sup>2</sup>	Press	Std. Dev	R <sup>2</sup>	Adj R <sup>2</sup>	Pred R <sup>2</sup>	Press	Std. Dev	R <sup>2</sup>	Adj R <sup>2</sup>	Pred R <sup>2</sup>	Press
W_3 (after)	4.33E-05	0.003	-0.108	-0.653	2.80E-08	4.50E-05	0.044	-0.195	-1.316	3.92E-08	4.78E-05	0.053	-0.353	-1.758	4.67E-08
Rs_1 (before)	2.65E+04	0.001	-0.110	-0.852	1.17E+10	2.79E+04	0.021	-0.224	-1.505	1.59E+10	2.91E+04	0.064	-0.338	-2.396	2.15E+10
Rct_1 (before)	2.98E+04	0.038	-0.069	-0.589	1.32E+10	3.14E+04	0.048	-0.190	-0.711	1.42E+10	3.25E+04	0.111	-0.270	-1.064	1.71E+10
Cdl_1 (before)	2.89E-04	0.073	-0.030	-0.511	1.23E-06	3.07E-04	0.073	-0.159	-0.635	1.33E-06	3.10E-04	0.169	-0.187	-0.806	1.47E-06
W_1 (before)	3.68E-04	0.068	-0.036	-0.515	1.98E-06	3.90E-04	0.068	-0.165	-0.626	2.13E-06	3.95E-04	0.162	-0.197	-0.797	2.35E-06
Rs_2 (before)	2.82E+04	0.028	-0.080	-0.729	1.28E+10	2.99E+04	0.029	-0.214	-1.388	1.76E+10	3.03E+04	0.126	-0.249	-2.137	2.31E+10
Cdl_2 (before)	6.61E-06	0.028	-0.079	-0.403	5.68E-10	6.86E-06	0.072	-0.160	-0.855	7.51E-10	6.92E-06	0.173	-0.181	-1.027	8.21E-10
Rct_2 (before)	5.87E+04	0.129	0.032	-0.534	5.46E+10	5.72E+04	0.264	0.080	-0.532	5.45E+10	3.94E+04	0.695	0.564	0.227	2.75E+10
W_2 (before)	4.07E-05	0.231	0.145	-0.636	3.17E-08	3.57E-05	0.472	0.340	-1.094	4.05E-08	3.61E-05	0.529	0.326	-1.437	4.72E-08
Rs_3 (before)	1.79E+04	0.155	0.061	-0.476	5.05E+09	1.81E+04	0.237	0.046	-0.749	5.99E+09	1.82E+04	0.319	0.027	-1.194	7.51E+09
Rct_3 (before)	3.78E+04	0.134	0.038	-0.586	2.35E+10	3.99E+04	0.140	-0.075	-0.779	2.64E+10	3.80E+04	0.319	0.027	-0.688	2.50E+10
Cdl_3 (before)	6.77E-06	0.148	0.053	-0.479	7.17E-10	6.67E-06	0.265	0.081	-0.570	7.61E-10	4.57E-06	0.698	0.569	0.145	4.14E-10

Transform	Linear					Quadratic					Cubic				
Fit data	Std. Dev	R <sup>2</sup>	Adj R <sup>2</sup>	Pred R <sup>2</sup>	Press	Std. Dev	R <sup>2</sup>	Adj R <sup>2</sup>	Pred R <sup>2</sup>	Press	Std. Dev	R <sup>2</sup>	Adj R <sup>2</sup>	Pred R <sup>2</sup>	Press
<b>W_3 (before)</b>	9.22E-05	0.052	-0.054	-0.520	1.23E-07	9.51E-05	0.103	-0.122	-0.663	1.34E-07	9.38E-05	0.238	-0.089	-0.887	1.52E-07
<b>Rs_1 (diff)</b>	4.74E+04	0.003	-0.108	-0.865	3.79E+10	5.03E+04	0.003	-0.246	-1.262	4.59E+10	5.36E+04	0.009	-0.415	-2.069	6.23E+10
<b>Rct_1 (diff)</b>	3.71E+04	0.142	0.047	-0.613	2.33E+10	3.62E+04	0.275	0.094	-0.654	2.39E+10	3.85E+04	0.281	-0.027	-1.133	3.08E+10
<b>Cdl_1 (diff)</b>	5.21E-04	0.012	-0.098	-0.732	4.29E-06	5.33E-04	0.083	-0.146	-0.992	4.93E-06	4.93E-04	0.313	0.018	-1.150	5.33E-06
<b>W_1 (diff)</b>	3.68E-04	0.084	-0.018	-0.489	1.98E-06	3.90E-04	0.084	-0.145	-0.599	2.13E-06	3.97E-04	0.173	-0.181	-0.775	2.36E-06
<b>Rs_2 (diff)</b>	2.51E+04	0.010	-0.100	-0.724	9.90E+09	2.65E+04	0.022	-0.222	-1.360	1.35E+10	2.64E+04	0.148	-0.218	-1.893	1.66E+10
<b>Cdl_2 (diff)</b>	7.96E-06	0.055	-0.050	-0.408	8.50E-10	8.30E-06	0.088	-0.140	-0.785	1.08E-09	8.79E-06	0.103	-0.281	-1.149	1.30E-09
<b>Rct_2 (diff)</b>	6.84E+04	0.204	0.116	-0.412	7.46E+10	6.60E+04	0.341	0.176	-0.311	6.93E+10	6.23E+04	0.487	0.267	-0.411	7.46E+10
<b>W_2 (diff)</b>	4.48E-05	0.286	0.206	-0.512	3.83E-08	3.93E-05	0.512	0.391	-0.923	4.87E-08	4.17E-05	0.520	0.314	-1.342	5.93E-08
<b>Rs_3 (diff)</b>	2.76E+04	0.052	-0.053	-0.812	1.31E+10	2.71E+04	0.186	-0.018	-1.008	1.45E+10	2.84E+04	0.218	-0.117	-1.580	1.87E+10
<b>Rct_3 (diff)</b>	4.12E+04	0.351	0.278	-0.195	2.81E+10	4.14E+04	0.418	0.273	-0.157	2.72E+10	4.31E+04	0.448	0.211	-0.365	3.21E+10
<b>Cdl_3 (diff)</b>	1.68E-05	0.006	-0.104	-0.694	4.32E-09	1.59E-05	0.210	0.012	-0.734	4.42E-09	1.22E-05	0.588	0.412	-0.038	2.65E-09

Transform	Linear					Quadratic					Cubic				
Fit data	Std. Dev	R <sup>2</sup>	Adj R <sup>2</sup>	Pred R <sup>2</sup>	Press	Std. Dev	R <sup>2</sup>	Adj R <sup>2</sup>	Pred R <sup>2</sup>	Press	Std. Dev	R <sup>2</sup>	Adj R <sup>2</sup>	Pred R <sup>2</sup>	Press
<b>W_3 (diff)</b>	1.06E-04	0.049	-0.057	-0.510	1.59E-07	1.07E-04	0.127	-0.092	-0.606	1.69E-07	1.09E-04	0.208	-0.132	-0.933	2.04E-07
<b>R-total (after)</b>	4.12E+04	0.533	0.481	0.183	2.67E+10	3.80E+04	0.646	0.557	0.220	2.55E+10	4.01E+04	0.654	0.506	-0.047	3.42E+10
<b>R-total (before)</b>	5.48E+04	0.450	0.389	0.064	4.60E+10	5.52E+04	0.505	0.381	0.058	4.63E+10	5.89E+04	0.506	0.294	-0.197	5.88E+10
<b>R-total (diff)</b>	7.03E+04	0.671	0.635	0.465	7.22E+10	7.43E+04	0.673	0.592	0.397	8.14E+10	7.62E+04	0.700	0.571	0.285	9.66E+10
<b>C-total (after)</b>	3.41E-04	0.150	0.055	-0.586	1.95E-06	3.33E-04	0.280	0.100	-0.880	2.32E-06	3.13E-04	0.444	0.206	-1.334	2.88E-06
<b>C-total (before)</b>	2.85E-04	0.078	-0.025	-0.502	1.19E-06	3.02E-04	0.078	-0.153	-0.621	1.29E-06	3.07E-04	0.170	-0.185	-0.799	1.43E-06
<b>C-total (diff)</b>	5.11E-04	0.013	-0.097	-0.732	4.12E-06	5.23E-04	0.081	-0.149	-1.007	4.77E-06	4.87E-04	0.302	0.002	-1.205	5.24E-06
<b>W-total (after)</b>	4.89E-05	0.198	0.109	-0.343	3.61E-08	5.02E-05	0.249	0.062	-0.799	4.83E-08	5.34E-05	0.256	-0.063	-1.168	5.82E-08
<b>W-total (before)</b>	3.90E-04	0.118	0.020	-0.450	2.25E-06	4.14E-04	0.119	-0.102	-0.578	2.45E-06	4.13E-04	0.233	-0.096	-0.689	2.63E-06
<b>W-total (diff)</b>	3.97E-04	0.151	0.057	-0.408	2.35E-06	4.21E-04	0.152	-0.061	-0.563	2.61E-06	4.18E-04	0.265	-0.050	-0.686	2.81E-06
<b>Real impedanc e (before)</b>	9.87E+00	0.152	0.058	-0.514	1.56E+03	9.32E+00	0.327	0.159	-0.509	1.56E+03	8.48E+00	0.513	0.304	-0.594	1.65E+03

Transform	Linear					Quadratic					Cubic				
Fit data	Std. Dev	R <sup>2</sup>	Adj R <sup>2</sup>	Pred R <sup>2</sup>	Press	Std. Dev	R <sup>2</sup>	Adj R <sup>2</sup>	Pred R <sup>2</sup>	Press	Std. Dev	R <sup>2</sup>	Adj R <sup>2</sup>	Pred R <sup>2</sup>	Press
Real impedance (after)	2.97E+00	0.185	0.095	-0.407	1.37E+02	2.78E+00	0.366	0.208	-0.352	1.32E+02	2.57E+00	0.527	0.324	-0.313	1.28E+02
Real impedance (diff)	7.57E+00	0.354	0.282	-0.178	9.39E+02	7.33E+00	0.461	0.326	-0.276	1.02E+03	6.89E+00	0.584	0.405	-0.469	1.17E+03
R-total (%diff)	7.19E+01	0.464	0.405	0.057	8.18E+04	6.99E+01	0.549	0.436	0.047	8.26E+04	6.61E+01	0.648	0.497	0.014	8.55E+04
Real impedance (%diff)	1.52E+01	0.692	0.657	0.479	3.52E+03	1.54E+01	0.720	0.650	0.422	3.90E+03	1.63E+01	0.724	0.606	0.252	5.05E+03

Appendix 53. The ANOVA table for the initially derived R-Total (diff) model

R-Total (diff)						
Source	Sum of Squares	df	Mean Square	F Value	p-value Prob > F	
Model	9.072E+010	1	9.072E+010	18.38	0.0020	significant
A- Concentration	9.072E+010	1	9.072E+010	18.38	0.0020	
Residual	4.443E+010	9	4.936E+009			
Cor Total	1.380E+011	11				
R <sup>2</sup>		0.6310		Predicted R <sup>2</sup>		0.5380
Adjusted R <sup>2</sup>		0.5990		Adequate Precision		12.440

Appendix 54. The ANOVA table for the initially derived Real Impedance (%diff) model

Real Impedance (%diff)						
Source	Sum of Squares	df	Mean Square	F Value	p-value Prob > F	
Model	4665.07	1	4665.07	20.18	0.0015	significant
A- Concentration	4665.07	1	4665.07	20.18	0.0015	
Residual	2080.99	9	231.22			
Cor Total	7437.13	11				
R <sup>2</sup>	0.6915		Predicted R <sup>2</sup>		0.4788	
Adjusted R <sup>2</sup>	0.6573		Adequate Precision		9.292	

Appendix 55. The ANOVA table for the derived R-Total (diff) model with the outlier removed

R-Total (diff)						
Source	Sum of Squares	df	Mean Square	F Value	p-value Prob > F	
Model	1.114E+011	1	1.114E+011	49.23	0.0001	significant
A- Concentration	1.114E+011	1	1.114E+011	49.23	0.0001	
Residual	1.811E+010	8	2.263E+009			
Cor Total	1.346E+011	10				
R <sup>2</sup>		0.8602	Predicted R <sup>2</sup>		0.7767	
Adjusted R <sup>2</sup>		0.8427	Adequate Precision		13.602	

Appendix 56. The ANOVA table for the derived Real Impedance (%diff) model with the outlier removed

Real Impedance (%diff)						
Source	Sum of Squares	df	Mean Square	F Value	p-value Prob > F	
Model	5163.90	1	5163.90	26.29	0.0009	significant
A- Concentration	5163.90	1	5163.90	26.29	0.0009	
Residual	1571.11	8	196.39			
Cor Total	7424.99	10				
R <sup>2</sup>	0.7667		Predicted R <sup>2</sup>		0.5870	
Adjusted R <sup>2</sup>	0.7376		Adequate Precision		10.847	